Effects of Increased Energy and Particulate Damping on Rocket

William. Anderson
PURDUE UNIVERSITY

11/19/2015
Final Report

REPORT DOCUMENTATION PAGE

The public reporting burden for this collection of information is estimated to average 1 hour per response, including the time for reviewing instructions, searching existing data sources, gathering and maintaining the data needed, and completing and reviewing the collection of information. Send comments regarding this burden estimate or any other aspect of this collection of information, including suggestions for reducing the burden, to Department of Defense, Washington Headquarters Services, Directorate for Information Operations and Reports (0704-0188), 1215 Jefferson Davis Highway, Suite 1204, Arlington, VA 22202-4302. Respondents should be aware that notwithstanding any other provision of law, no person shall be subject to any penalty for failing to comply with a collection of information if it does not display a currently valid OMB control number.
PLEASE DO NOT RETURN YOUR FORM TO THE ABOVE ADDRESS.

1. REPORT DATE (DD-MM-YYYY)	2. REPORT TYPE	3. DATES COVERED (From - To)
	Final Technical	08/01/11 - 04/30/11

4. TITLE AND SUBTITLE

Fuel Chemistry And Combustion Distribution Effects On Rocket Engine Combustion Stability

5a. CONTRACT NUMBER

5b. GRANT NUMBER

FA9550-10-1-0431

5c. PROGRAM ELEMENT NUMBER

6. AUTHOR(S)

William E Anderson
Stephen D Heister
Steven S Son

5d. PROJECT NUMBER

5e. TASK NUMBER

5f. WORK UNIT NUMBER

7. PERFORMING ORGANIZATION NAME(S) AND ADDRESS(ES)

Purdue University Sponsored
Program Services Young
Hall, 302 Wood Street West
Lafayette, IN 47907

8. PERFORMING ORGANIZATION REPORT NUMBER

9. SPONSORING/MONITORING AGENCY NAME(S) AND ADDRESS(ES)

AF Office of Scientific Research
875 N. Randolph St. Room 3112
Arlington, VA 22203

10. SPONSOR/MONITOR'S ACRONYM(S)

AFOSR

11. SPONSOR/MONITOR'S REPORT NUMBER(S)

12. DISTRIBUTION/AVAILABILITY STATEMENT

Approved for Public Release; Distribution Unlimited

13. SUPPLEMENTARY NOTES

14. ABSTRACT

The goal of the project was to understand how changes in the rate of energy addition can be used to alter the combustion instability characteristics of liquid rocket engines. Fuels with increased energy, either due to higher heats of formation or energetic additives, presumably result in higher performance. This study seeks to understand how changes in combustion rate, due to fuel chemistry changes, might be used to develop high-performing, stable rocket engines. The overall objective of the project was to develop a fundamental understanding of how the spatial distribution of combustion and its temporal response to pressure oscillations depends on kinetic rates, flammability limits, and energy release density. The study combines basic drop combustion experiments, an in situ study using a spontaneously unstable model rocket combustor, and associated modeling of particles in combustion chamber gas flows.

15. SUBJECT TERMS

energetic propellants, combustion stability, particulate dynamics

16. SECURITY CLASSIFICATION OF:			17. LIMITATION OF ABSTRACT	18. NUMBER OF PAGES	19a. NAME OF RESPONSIBLE PERSON
a. REPORT	b. ABSTRACT	c. THIS PAGE			William Anderson
			UU		19b. TELEPHONE NUMBER (Include area code)
					765-496-2658

FUEL CHEMISTRY AND COMBUSTION DISTRIBUTION EFFECTS ON ROCKET ENGINE COMBUSTION STABILITY

The goal of the project was to understand how changes in the rate of energy addition can be used to alter the combustion instability characteristics of liquid rocket engines. Fuels with increased energy, either due to higher heats of formation or energetic additives, presumably result in higher performance. This study seeks to understand how changes in combustion rate, due to fuel chemistry changes, might be used to develop high-performing, stable rocket engines. The overall objective of the project was to develop a fundamental understanding of how the spatial distribution of combustion and its temporal response to pressure oscillations depends on kinetic rates, flammability limits, and energy release density. The study combines basic drop combustion experiments, an *in situ* study using a spontaneously unstable model rocket combustor, and associated modeling of particles in combustion chamber gas flows.

1.   Additives

1.1   Introduction

Nanofluids (liquids with nanoscale particles) have existed for the past several years yielding improved heat transfer properties. Recently nanofluids have been considered in combustion environments. In the following we summarize work that has examined the effect of addition of nanoscale fuel particles in liquids. We have considered both individual droplet combustion, as well as combustor studies.

Three publications are being submitted from this work, two are nearly ready for submission and a third is in preparation. A M.S. student (Mark Pfeil) published and defended a thesis on this work and another M.S. student (Alex Troiani) is completing his M.S. with this funding.

1.2   Experimental Setup

A. Atmospheric Experiments

Droplets were suspended on quartz rods with beads formed at the end, a method previously used by other researchers [1],[2]. Quartz was chosen due to its relatively low thermal conductivity, resulting in minimal heat transfer to the droplet. Several droplets of neat ethanol were burned on each rod before burning a droplet containing additives. The rods were cleaned

between each droplet burn using a butane flame. The rod was changed after the combustion of one or two droplets containing additives to avoid buildup of combustion products on the rod.

The quartz rods were suspended in a clear acrylic box with an aluminum bottom and an open top. This configuration was used to minimize convection effects on the droplet while allowing it to burn in atmospheric air. A coiled 30 gauge Nichrome wire was inserted through a hole in the acrylic box and positioned near the droplet. A voltage was applied across the wire causing it to heat and ignite the droplets. After ignition, the Nichrome wire was retracted away from the droplet in order to avoid interaction with the combustion. Backlighting was provided by a halogen lamp placed behind an Interfit translucent light reflector, producing a contrasting, white background. A Vision Research Phantom V. 7.3 high speed camera was used to record the droplet surface as it burned. The high speed camera was operated at a frame rate of up to 5000 fps with a 14 bit image depth. The lens on the high speed camera was an Infinity Photo-Optical Company K2 Long Distance Microscope. A schematic diagram of this experimental system is shown in Fig. 1. The videos obtained using the high speed camera were analyzed using MATLAB software [3] to determine the equivalent diameter of the droplet from the droplet cross-section as a function of time. A Vision Research Phantom V. 7.3 color high speed camera, with the same Infinity Photo-Optical Company K2 Long Distance Microscope, was also used to record general combustion behavior, primarily to observe flame color during combustion.
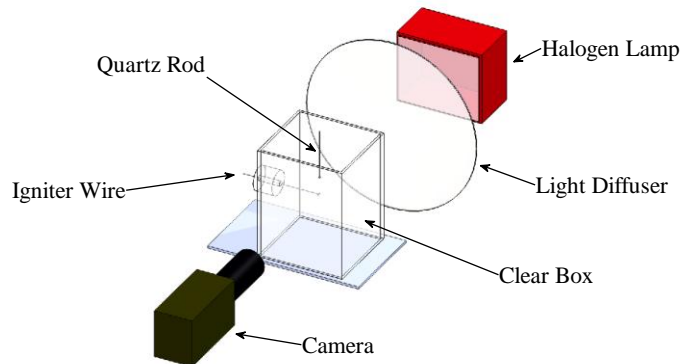

Fig. 1 Setup of droplet experiments performed at atmospheric conditions.

B. Experiments at Elevated Pressures

The windowed pressure vessel (Crawford bomb) has been used to perform droplet combustion experiments in a high pressure air atmosphere. The configuration of the bomb is shown in Fig. 2.

Droplets are suspended from a droplet holder inside the Crawford bomb, which was sealed from the surrounding atmosphere. The droplet holder was a quartz rod with a circular ring on the end, ranging from 1.6 to 3.6 mm, allowing for droplets of equivalent diameters of 2.5 to 4.5 mm. The chamber was then pressurized, and the Nichrome wire ignited a propellant igniter mix, which quickly ignited the droplet in the holder. The propellant was made up of a mix of 25 μm Ni-Al powder, Longshot powder, and nitrocellulose binder. The propellant ignition charge lasted between 0.1-0.2 seconds. The droplet burn was recorded by using a high speed phantom camera from 200 to 2500 fps. A halogen lamp was used to provide a backlight to allow viewing of the droplet throughout the burn lifetime. A 486 nm notch filter was placed on the phantom camera with the Nikon lens to allow for the viewing of the AlO radicals which occur during the droplet combustion [12]. This allowed the direct viewing of aluminum combustion throughout the droplet lifetime.

(a)   (b)
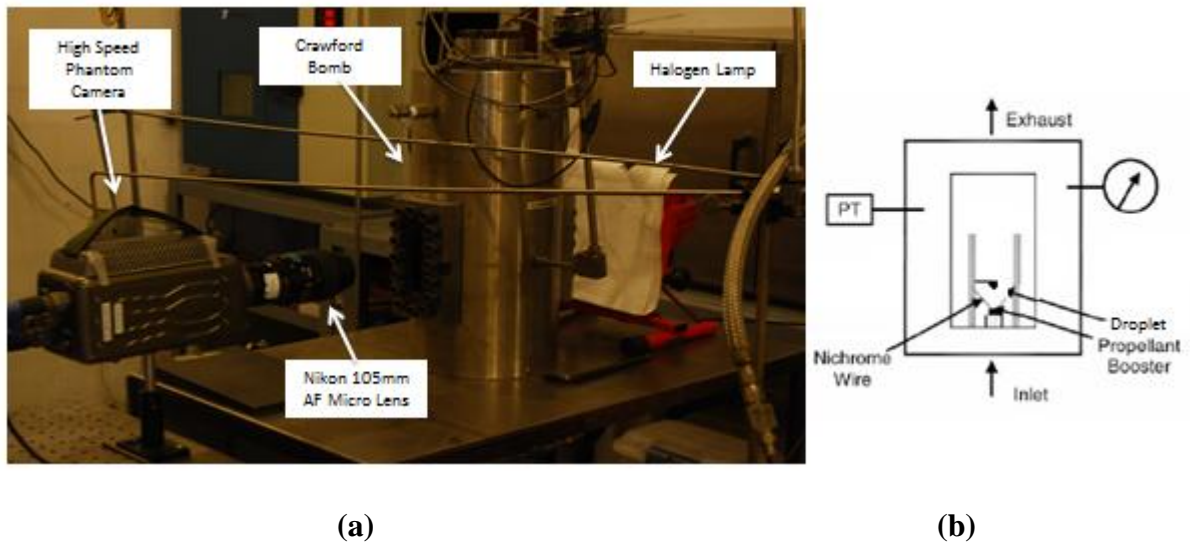
Fig. 2 High pressure droplet combustion experiment. Part (a) shows the setup of the Crawford bomb, Phantom camera, and the halogen lamp, which was used for a backlight source. Part (b) is a diagram of the interior of the Crawford bomb, and shows the droplet holder, droplet, and the ignition system for the experiment.

C. High Speed Planar Laser Induced Fluorescence (PLIF) System

A brief description of the high speed planar laser induced fluorescence (PLIF) system is given here. For further details about the system, the reader is referred to the work of Hedman *et. al* [4]. A Sirah Credo (CREDO-DYE) dye laser was pumped at a repetition rate of 5 kHz by an

Edgewave Nd:YAG (IS811-DZ) solid state laser. The pulse energy of the frequency-doubled 283.23 nm beam from the dye laser was measured to be 0.15 mJ/pulse. The beam was expanded vertically and horizontally using a negative spherical lens (f = -75 mm, clear aperture (C.A.) = 21.3 mm) and expanded further horizontally using another negative cylinder lens (f = 50 mm, C.A. = 21.3 mm). The beam was then focused using a positive spherical lens (f = 500 mm, C.A. = 50.0 mm) resulting in a well collimated beam having a large circular cross section of approximately 5 cm. A thin sheet was then produced after the light was focused through a square cylindrical lens (f = 250 mm, C.A = 43.2 mm * 43.2 mm). The distance between these lenses was adjusted to change the sheet height and width. The width of the beam was smaller than the droplet initial diameters and was tall enough to capture the diffusion flame around the droplet. The laser wavelength was set to 283.2 nm to excite the Q1(7) OH line. Experiments were also performed at a laser wavelength of 283.1 nm that does not excite the OH radical, thus allowing us to distinguish between broadband fluorescence and the OH radical. Experiments performed using the wavelength of 283.1 nm will be referred to as *"detuned"* in the present work.

The OH signal was recorded using a UV intensifier, high speed camera assembly. A Video Scope International high speed image intensifier (VS4-1845HS), capable of operating at 100 kHz with a gain of up to 80,000, was attached to the Vision Research Phantom V. 7.3 camera. A UV-grade lens (UKA Optics - UV1054B 105mm F/4.0 Quartz Lens) was attached to the UV intensifier. A Semrock interference filter (FF01-320/40-25) that had a transmission of 74% at 310 nm was used to transmit OH fluorescence and block broadband flame emission and scattered laser light. This camera assembly was placed perpendicular to the laser plane as shown in the schematic diagram in Fig. 3.

Images acquired using this setup were post processed with MATLAB software [3]. Droplet diameter and OH intensity distributions were recorded. The laser caused the droplet to fluoresce, allowing the droplet diameter to be determined as well. The light emission immediately around the droplet was removed in MATLAB before finding the droplet size to provide a more accurate measurement. Quartz rods were placed within the laser sheet and a drop was deposited on the bead. The amount of time the droplet was exposed to the laser before ignition was minimized to reduce evaporation prior to ignition.
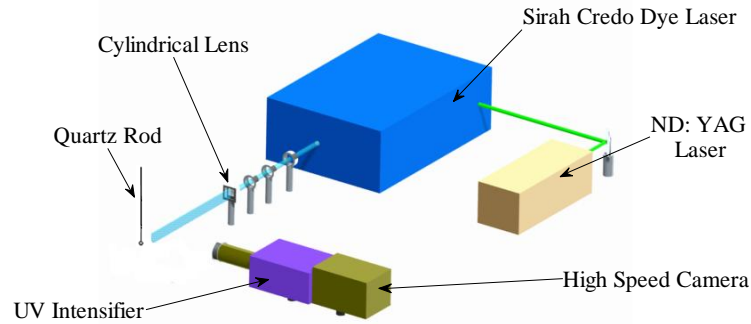
Fig. 3 High speed planar laser induced fluorescence (PLIF) schematic.

1.2 Fuels/Additives

A. Additives

Currently, the method of bringing H_2 into a combustor is to store it separately from the fuel and inject it into the combustor or fuel line. While acceptable for research purposes, this method is impractical for many applications due to the large volumes required to store gaseous H_2, or the cryogenic requirements of using liquid H_2. One possible solution involves introducing H_2 through additives with high hydrogen content into the fuel. These materials would not only be a practical pathway of introducing H_2 but also have the potential of increasing energy density and potentially overall fuel performance. There is strong potential that the additive can influence the combustion behavior of a system as well.

Ammonia borane (AB) was selected for investigation in the present work for both droplet combustion and rocket combustor experiments due to its relatively high hydrogen content. AB consists of 19.6 wt.% hydrogen and can be dissolved into fuels ranging from alcohols to ethers. When AB is heated in its solid state, it begins to decompose and release H_2 gas at several different temperatures, depending on the heating rate. If AB is kept at a constant elevated temperature for an extended period of time, decomposition will begin to occur at a temperature of 355 K, near the boiling point of ethanol (351 K). For higher heating rates, the first step of AB decomposition will begin to occur at temperatures below 385 K, releasing primarily H_2 with small amounts of borazine [5]. In this first step, the release of 7.2 wt.% of the hydrogen as H_2 of the 19.6 wt.% contained in AB was reported [6]. No significant amount of other products are formed until temperatures exceed 400 K, at which point H_2 gas is formed releasing up to 14.4 wt.% hydrogen in total for temperatures under 500 K [6]. However, Baitalow *et. al* [6] noted

that the total amount of H_2 gas formed was independent of the heating rate for the heating rates tested.

Other research shows that decomposition temperatures vary depending on the solvent [7] and that the amount of H_2 released, along with the rate of dehydrogenation at lower temperatures, increases when mixed with an ionic liquid [8],[9]. Due to conflicting trends, it is not apparent at what temperature AB will begin to decompose when dissolved in ethanol; however, the proximity of the boiling point of ethanol and the decomposition temperatures of AB indicate that AB will decompose and release H_2 gas while ethanol is burning. This makes AB a strong candidate to influence the combustion behavior of the fuel through hydrogen combustion and is therefore one of the additives selected for this study.

Two types of AB were used for these experiments including AB from Sigma Aldrich that has a 97% purity and AB produced at Purdue University through a process developed by Ramachandran *et. al* [10] that yields a 98% purity AB.

Nano aluminum (nAl) was also selected for investigation in both droplet combustion and rocket combustor experiments. The primary reason for selecting aluminum was its previous use in solid rocket motor systems to suppress combustion instabilities. Since small concentrations of nAl had significant influence in the combustion behavior of solid motors, there was a good probability that it might have a similar effect in liquid rockets. Nano sized aluminum was selected because its increased ease of suspension at low concentrations when compared to micron sized aluminum. Nano Aluminum was purchased from the company Novacentrix with a reported average diameter of 80 nm.

B. Liquid Fuels

Ethanol was chosen as a liquid fuel for both nano aluminum (nAl) and AB additives. Ethanol can dissolve a significant amount of AB compared to other fuel candidates (6.5% by weight compared to 4% and 1% in isoproponal and isobutanol respectively [11]) allowing 1.3 wt.% of the fuel to be hydrogen. Methanol and tetrahydrofuran [11] can also dissolve a significant amount of AB but were not used due to the rapid AB decomposition in methanol and toxicity of tetrahydrofuran. Ethanol was also effective at suspending nAl without the use of surfactants for sufficient time to perform experiments. Additionally, neat ethanol has been characterized in the liquid rocket combustion configuration used in the present work to use for baseline comparison.

One drawback to selecting ethanol for the fuel with AB additives was that once dissolved, the mixed fuel reacts slowly over a period of months producing ammonia. While this phenomena may make the AB-ethanol fuel combination impractical for actual application, the fundamental information gained from this fuel-additive system on the effects of H_2 and additives is still of interest.

JP-8 was chosen as a liquid fuel for nAl. While nAl did not suspend without the use of a surfactant in JP-8, it had higher energy content than ethanol which makes it more practical for liquid rocket application. Neat JP-8 had also been well characterized in the combustor configuration used in the present work, thus baseline data for comparison was already available.

Nitromethane was also chosen as a liquid fuel for nAl motivated by research efforts conducted by Sabourin et al, in which gelled nitromethane with suspended nAl was burned in a strand burner [13]. Sabourin reported that increasing the concentration of aluminum in the mixture increased the burning rate dramatically. A residue of aluminum was not left behind, indicating that the aluminum participated in the combustion. This is in sharp contrast from past work in droplet combustion, in that aluminum has only ever been seen to participate in combustion by being released from the droplet in a microexplosion event at the end of the droplet lifetime, often times leaving a residue behind [14]. Nitromethane was investigated to determine the extent to which the aluminum would participate in the combustion in a droplet configuration.

C. Fuel Mixtures

The AB/ethanol fuels were prepared by dissolving 3 and 6 wt.% AB into ethanol. To avoid loss of hydrogen content in the fuel mixture from ammonia production, AB/ethanol mixtures were used within several days of preparation. The nAl/ethanol and nAl/JP8 fuels both contained 1 wt.% nAL. Because neat JP8 was unable to suspend nAL for any duration of time, an additional 3 wt.% of a surfactant called Neodol was added to aid in particle suspension.

For the droplet experiments, both nAL fuels were mixed for 30 seconds using a Branson Sonicator, model 102 (CE), operated at 50% power with a cycle of 0.2 seconds off and 0.8 seconds mixing. This sonicator mixes by applying ultrasonic energy at a high frequency to the fluid and its constituents causing the clumped nAl particles to break apart and suspend in the fluid.

For experiments performed in the rocket combustor, a Resodyn LabRam resonant mixer was used for short time intervals, after which the fuel was visually inspected. The fuel mixture was mixed at an intensity of 50 for the first time interval and then at 100 for the following intervals. The fuel was mixed for four or five intervals until no nano particles were left on the bottom of the mixing container. Sample intensity and the corresponding G's imparted to the mixture during mixing for ethanol with nAl is shown in Fig. 4. The two different mixing methods were used based on the amount of fuel needed for the experiment. The sonicator produces very local mixing making it difficult to mix large quantities of liquid fuels that were needed for the rocket combustor; therefore, in these cases, the Resodyn mixer was used.
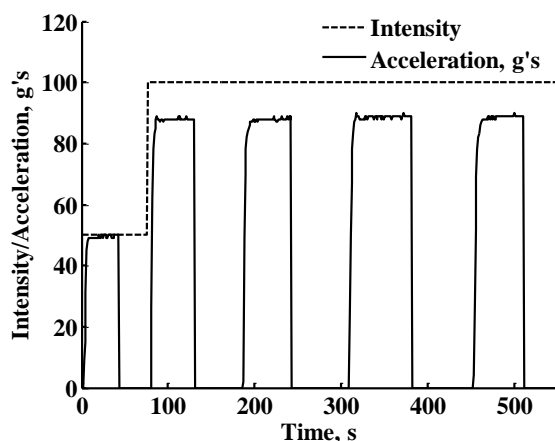

Fig. 4 Sample mixing Resodyn LabRam data for ethanol with 1 wt.% nAl.

As observed in previous studies, prolonged suspension of the nAl in the liquids has proven to be a challenge as the nAl particles will agglomerate over time and begin to precipitate out. Precipitation of the nAl for the JP-8 and Neodol fuel as well as the ethanol fuel was observed after 10 minutes. Mixing with the sonicator or the Resodyn mixer resulted in similar suspension times. To ensure good suspension of particles, the combustion experiments were performed within minutes of mixing. The fuels were also shaken by hand between mixing and performing of the experiments to help inhibit settling of the nAl.

For gelled droplet mixtures involving Aerosil 380, the Resodyn mixer was used to ensure the even distribution of particles throughout the solution. The vial sample was placed in the Resodyn for 5 minutes at 60% intensity after the additives were placed in the fuel. Immediately prior to combustion testing, the sample was placed in a Cole-Parmer 8890 Ultrasonic Cleaner for 2 minutes to ensure an even distribution for the combustion tests.

1.4 Droplet Results

A. Atmospheric Experiments

The results obtained from the experiments involving the additive AB are detailed in paper soon to be submitted to the journal Combustion and Flame. The draft form of this paper is provided in the appendix of this report for further information about this additive and its influence on the combustion behavior of droplets.

Nano aluminum had very little impact on the combustion behavior of an individual droplet burning. Nano aluminum was observed to participate in the combustion process only at the end of the droplet lifetime. The results of this section show very little difference between the neat fuel and the fuel with the additive. General observations are presented first, followed by more detailed discussion of the combustion process.

The addition of nAl to ethanol produced little deviation from the combustion behavior of neat ethanol. The only significant difference was the presence of a relatively large agglomerate of nAl left on the quartz rod after the liquid was consumed. As the droplet burned, the convective force of gas leaving the droplet was not sufficient to drive nAl from the surface; thus, as the combustion process proceeded, the concentration of nAl within the liquid increased, eventually leaving a large agglomerate of nAl. Since very little oxygen was able to diffuse to the surface of the fuel droplet, it is unlikely that the nAl reacted at the droplet surface, meaning that little to no nAl participated in the combustion process of ethanol. The remaining agglomerate of nAl reacted with the surrounding air to form aluminum oxide once the liquid fuel had been consumed.

Neat JP-8 burned uniformly during combustion and followed the nearly D^2 law behavior. A bright, sooty, yellow flame was present during the combustion process that notably extended above the droplet in the presence of gravity due to natural convection. This behavior persisted till the fuel was consumed and the droplet extinguished.

The addition of 3 wt.% Neodol to JP-8 produced little difference in the flame color or brightness; however, gas generation within the droplet that lead to bubble formation was observed. Bubble formation became more frequent toward the end of the droplet lifetime as the fuel was consumed. At this point, gas generation occasionally lead to droplet shattering, shown in Fig. 5 for a typical case.
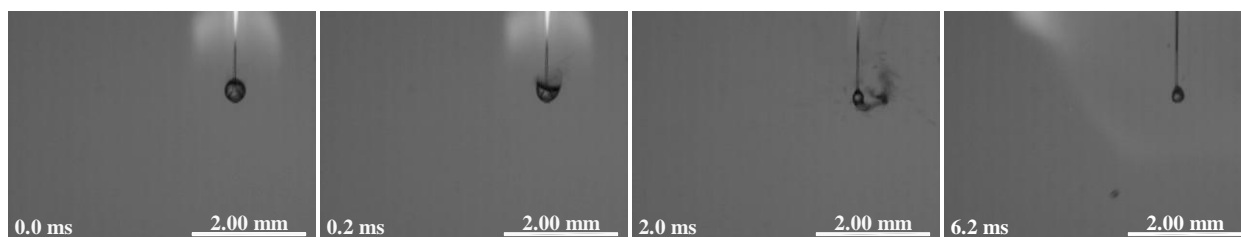
Fig. 5 Shattering of a JP-8 and 3 wt.% Neodol droplet at the end of the droplet lifetime.

Adding nAl to the JP-8/Neodol mixture had no effect on the quasi-steady combustion behavior of the fuel droplet.   The nAl was not observed to participate until bubble formation began within the droplet.   After that, as bubbles reach the surface and burst, nAl was occasionally expelled and reacted near the flame envelop of the droplet where the temperatures were the highest.   Bubble formation and eruption may have caused the droplet to shatter, resulting in wide dispersion and rapid combustion of the nAl, shown in Fig. 6. This behavior was very similar to droplets that contained JP-8/Neodol, suggesting that nAl would not participate in the combustion process if it were not for the presence of the surfactant microexplosion.
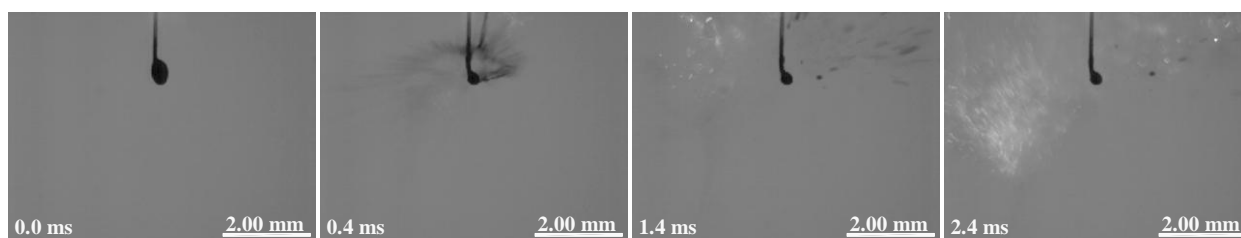

Fig. 6 Shattering of a JP-8, 3 wt.% Neodol, and 1 wt.% nAl droplet at the end of the droplet lifetime.

The droplet size history for both ethanol and JP-8 based fuels were recorded throughout the droplet combustion process. The D^2 law coefficient was determined for these fuels during the quasi-steady combustion period, shown in Table 1. The effect of adding nAl to ethanol produced a slight increase in the regression rate of the fuel; however, these measurements were within the standard deviation, making it inconclusive if nAl was affecting the regression rate of ethanol. Adding Neodol and nAl produced similar, inconclusive results.

Table 1 D^2 Law Coefficient Rates for Fuels Containing Nano Aluminum

Fuel	Additive	D^2 Law Coefficient,	Standard Deviation
Ethanol		0.80	±0.05
Ethanol	1 wt.% nAl	0.83	±0.03
JP-8		1.08	±0.04
JP-8	1 wt.% nAl/3 wt.% Neodol	1.05	±0.03

JP-8/nAl fuels were also investigated using PLIF imaging. As the addition of nAl to ethanol in all other experiments had provided no significant change to any aspect of the combustion behavior, ethanol droplets containing nAl were not studied with PLIF. The flame structure for JP-8, JP-8/Neodol, and JP-8/Neodol/nAl all had very similar characteristics. A band of OH was present during the quasi-steady burning portion which had similar intensity on all sides of the droplet except above the droplet where the intensity dropped significantly.

However, differences were noticed in the combustion behavior of the JP-8/Neodol/nAl fuel when bubble generation occurred. The eruption of a bubble within the droplet caused bright signal emission to leave the surface of the fuel droplet that diffused outwards towards the enveloping flame. As the bright light emission approached the diffusion flame, the intensity of the signal weakened. The outer diffusion flame in the path of this ejection became distorted as the gaseous fuel pushed the flame outwards. This behavior is shown in Fig. 7. Since similar behavior was noted in the combustion of JP-8/Neodol fuels, it is suspected that the bright light emission is a result of large concentrations of gaseous fuel fluorescing.
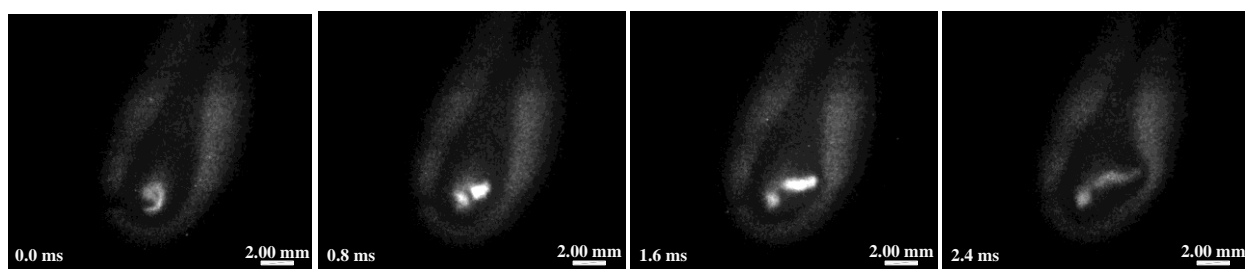

Fig. 7 High speed PLIF measurements of a JP-8/3 wt.% Neodol/3 wt.% nAl droplet.

B. Experiments at Pressure

The base fuel mixture considered for this study was a baseline nitromethane mixture with 4 wt.% 80 nm nano-aluminum 1 wt.% Aerosil 380 (fumed silica gellant). The combustion behavior of this fuel was characterized in compressed air at 1000 psig, along with variations to

the mixture in the areas of aluminum particle size, aluminum particle loading, and Aerosil 380 loading. The base mixture followed, in general, a two stage burning behavior, as illustrated in Fig. 8. The first stage was dominated by a nitromethane and air flame, which is largely filtered out by the 486 nm lens that indicates AlO. This indicates little aluminum combustion in this stage. It appears to be localized in a few areas. Aluminum particles can be seen coming off the droplet and burning. The second stage has a much more intense aluminum reaction, indicated by high intensity of the filtered light emission. A bright aluminum flame occurs at the bottom of the droplet, which quickly spreads up to enshroud the entirety of the droplet. This two stage combustion behavior is also be observed in most of the other mixtures, except for the case where micron sized aluminum particles were used.

**(a)**   **(b)**
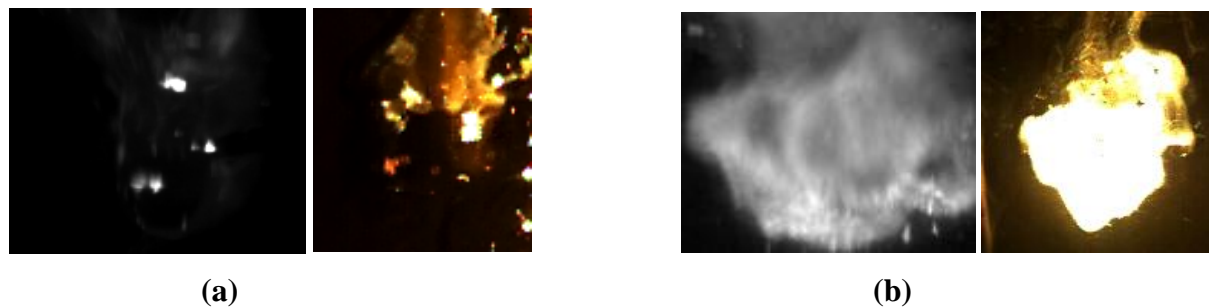
Fig. 8 Phases of combustion of the 4 wt.% 80 nm Al 1 wt.% Aerosil 380 Nitromethane through the 486 nm notch filter (left) and the full color spectrum (right). Part (a) shows the first stage of the burn, with light aluminum participation, while part (b) shows the typical second stage of the burn, which had a much more extensive aluminum participation in the burn.

Analysis of the emission (or radiation) of the burning baseline fuel mixture through the 486 nm notch filter (AlO emission) showed an instability (specifically an oscillatory emission) in the burning aluminum during the second phase of the burn. This self-oscillation can be seen in Fig. 9 (for our baseline material) below that shows the average intensity of the light emission. The oscillations occur at about 35 Hz. Light emission plots for each type of mixture used in a systematic study are shown in Fig. 10. The captions list the materials considered.
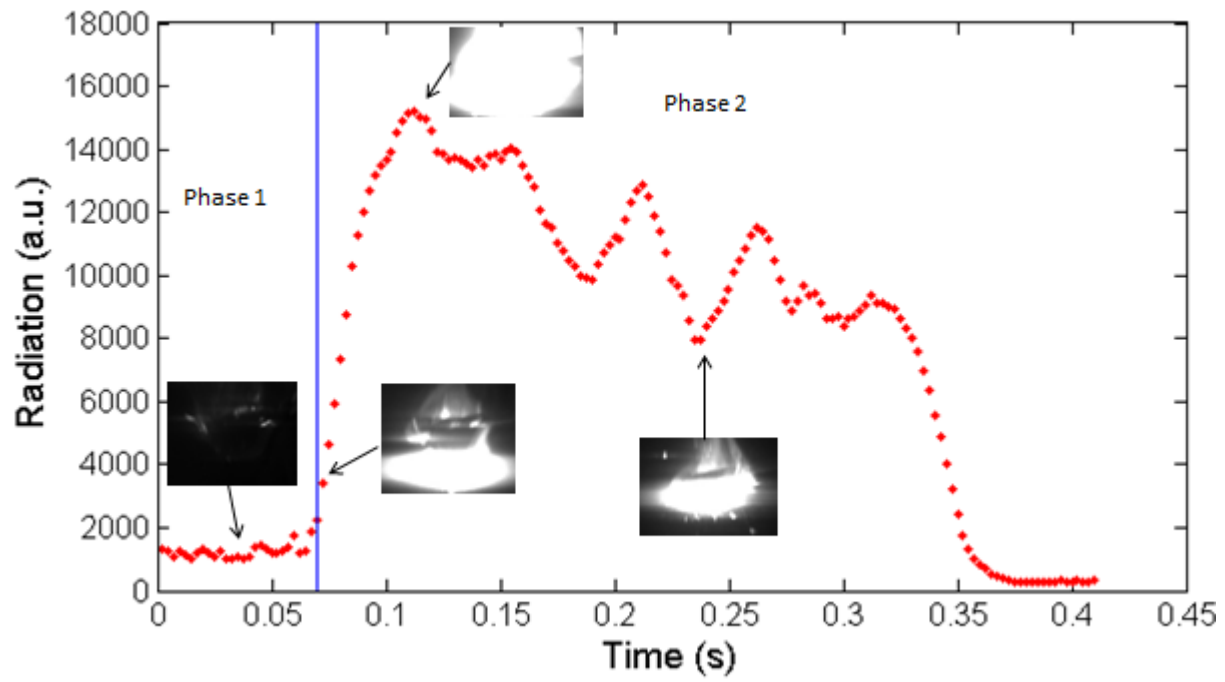
Fig. 9 Radiation (light emission) plot over time for the combustion of a 4 Wt.% 80 nm Al 1 wt.% Aerosil 380 Nitromethane droplet. The second phase instability can clearly be seen.
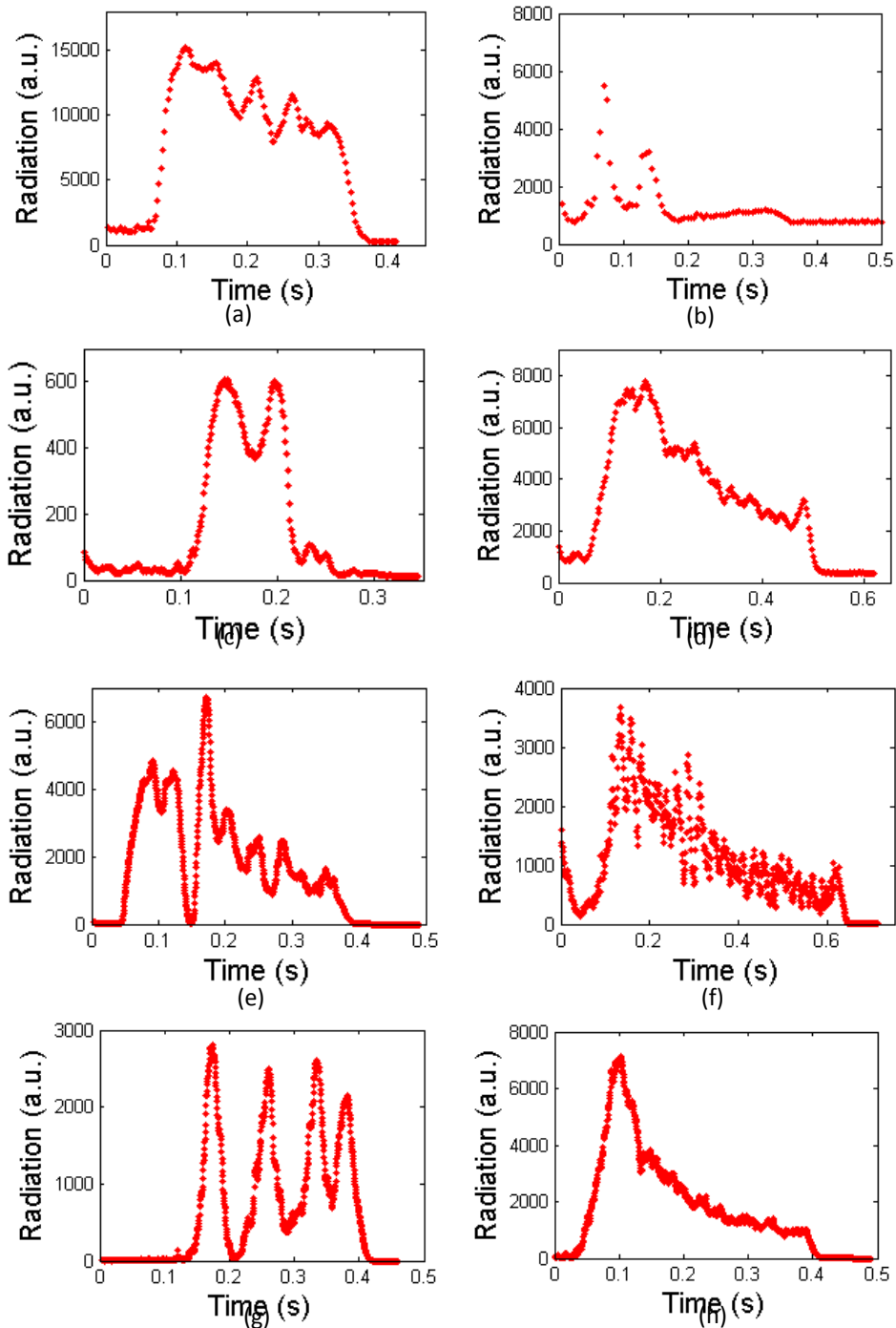
Fig. 10 AlO emission (radiation) plots over time for droplets burning in compressed air at 1000 psi for all fuel mixture variations used in systematic study. All mixtures are nitromethane with the following loadings: (a) baseline mixture (4 wt.% 80 nm Al 1 wt.% Aerosil 380) (b) 4 wt.% 30 μm Al 1 wt.% Aerosil 380 (c) 4 wt.% 100 nm Al 1 Wt.% Aerosil 380 (d) 4 wt.% 38 nm Al 1 wt.% Aerosil 380 (e) 6 wt.% 80 nm Al 1 wt.% Aerosil 380 (f) 2 wt.% 80 nm Al 1 wt.% Aerosil 380 (g) 4 wt.% 80 nm Al and no Aerosil 380 (h) 4 wt.% 80 nm Al 2 wt.% Aerosil 380.

The effect of aluminum particle size on the combustion was explored by replacing the baseline 80 nm aluminum with 38 nm, 100 nm and 30 μm aluminum. The micron sized mixture exhibited infrequent particle participation as indicated by the low light emission, as well as a failure to enter the second stage as shown in Fig. 10 (b). In addition, the peak and duration of the intensity is far less indicating incomplete combustion is likely. The 38 nm mixture (Fig. 10 (d)) burned less intensely and had a lower burning rate than the 80 nm mixture, taking an additional 60 ms for a droplet with an equivalent diameter of about 3.5 mm to be consumed. This can be attributed to a lower active aluminum content. The 38 nm particles have an aluminum content of only 54.3%, while an 80 nm particle has an active content ranging from 76-80%. The self-oscillations are lower in amplitude, but the frequency is higher than the baseline. The 100 nm nAl (Fig. 10 (c)) mixture burns comparably to the 80 nm solution, however, the instability in the second phase tended towards a slightly higher frequency of around 48 Hz, rather than the 80 nm solution's 35 Hz.

The effect of the aluminum loading of the mixture on the droplet combustion was explored by varying the aluminum weight percent from baseline 4 wt.% to either 2 or 6 wt.%. Changing the aluminum loading altered the burn time. This change is illustrated in Fig. 11, showing that an increased aluminum content decreased the total burn time. The 6 wt.% solution also possessed some dramatic oscillations, as indicated by the emission, in the second phase burning, while the 2 wt.% solution shows smaller amplitudes and a much higher frequency, as seen in Fig. 10, parts (e) and (f).
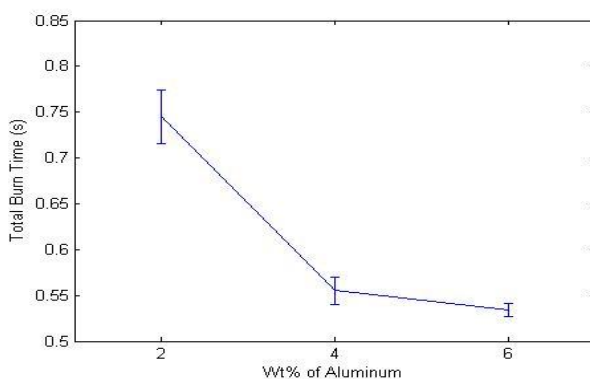

Fig. 11 Comparison of total burn times for varying aluminum loadings for 1 wt.% Aerosil 380 nitromethane mixtures. Increasing the aluminum concentration decreases the total burn time.

The effect of the fumed silica (Aerosil 380) loading of the mixture on the droplet combustion was explored by varying the Aerosil 380 weight percent from the baseline 1 wt.% to either no Aerosil 380 or 2 wt.% (Fig. 10 (g) and (h), respectively). For droplets initial droplets ranging from 3 to 3.8 mm, the droplets with higher particle loading reached the second stage combustion sooner, as shown in Fig. 12. This relation may partially be a result of improved conduction brought about from the higher particle loading, allowing faster heating of the droplet. Also, as first stage burning continues the remaining material increases in solids loading. Consequently it would not be surprising that starting with a higher solids loading causes a transition to the second stage of burning sooner. From observing the light emission (radiation) plots in
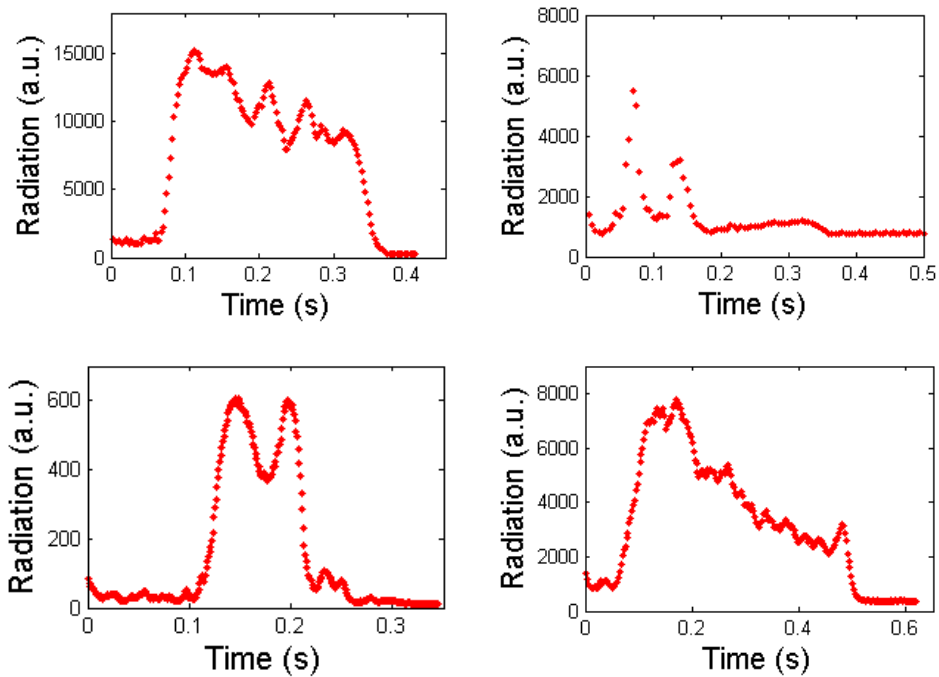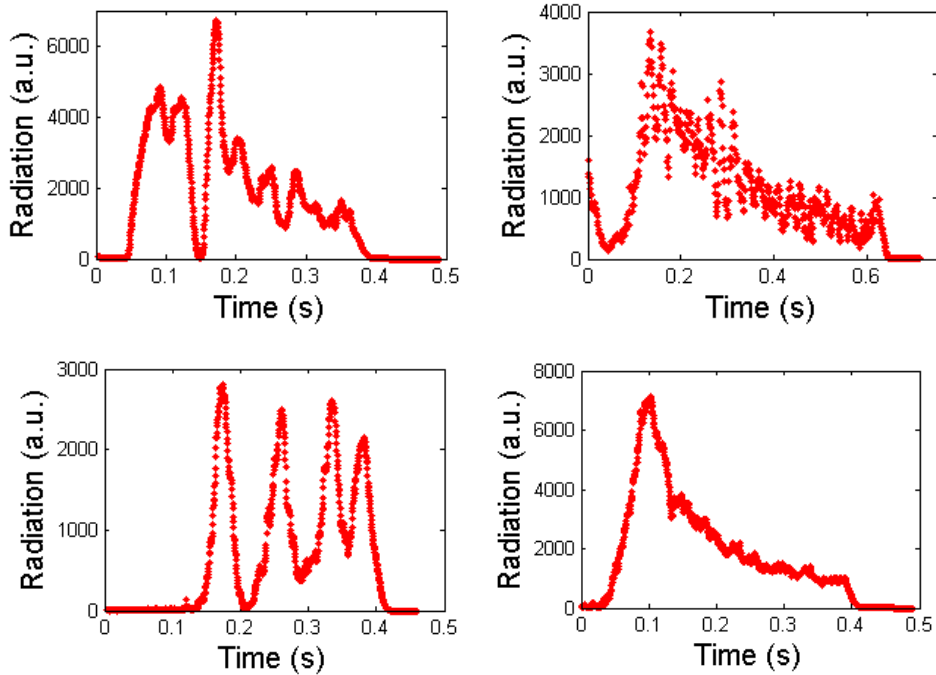
Fig. 10 (g), it can be seen that the solution without Aerosil 380 showed a very large amplitude in its second stage instability, while the mixture with 2 wt.% Aerosil 380 (Fig. 10 (h)) exhibited a dramatically smaller amplitude in its oscillatory emission, and emission slowly decreased over time.
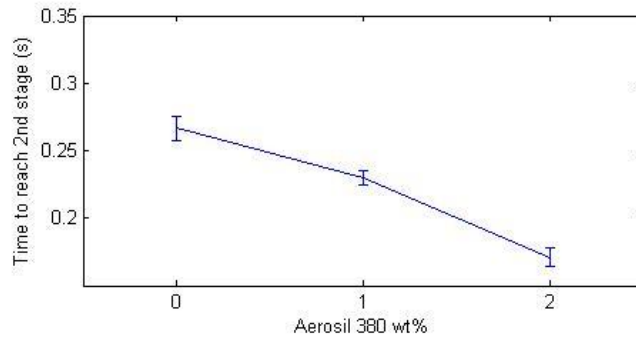
Fig. 12 Comparison of time required to reach the second burn stage for varying Aerosil loadings in a 4 wt.% aluminum nitromethane solution. The inverse relation may be a result of the improved conduction of the higher loading in the droplets, allowing a faster heating in the droplet; or it reflects a more fully gelled fluid.

The effect of pressure was also examined. The baseline fuel of the systematic study (4 wt.% 80 nm nano-aluminum 1 wt.% Aerosil 380 nitromethane) was burned at pressures varying from

one atmosphere to 1000 psig in air. Three pressure regimes were noted for the droplet combustion behavior. An AlO emission (radiation) plot with an example of each of the regimes is shown in Fig. 13. The higher pressure regime ranged from 400 to 1000 psig, in which droplet combustion behavior was much like that observed in the baseline pressure (1000 psig). The two stage flame behavior was observed. The first phase consisted of a nitromethane flame with some relatively discrete aluminum participation. This stage lasted longer for lower pressures because the burning was slower. The second stage had characteristically significant aluminum participation, and oscillations can be observed in the AlO emission plots. The droplet burn lifetime is much shorter than the other two regimes.
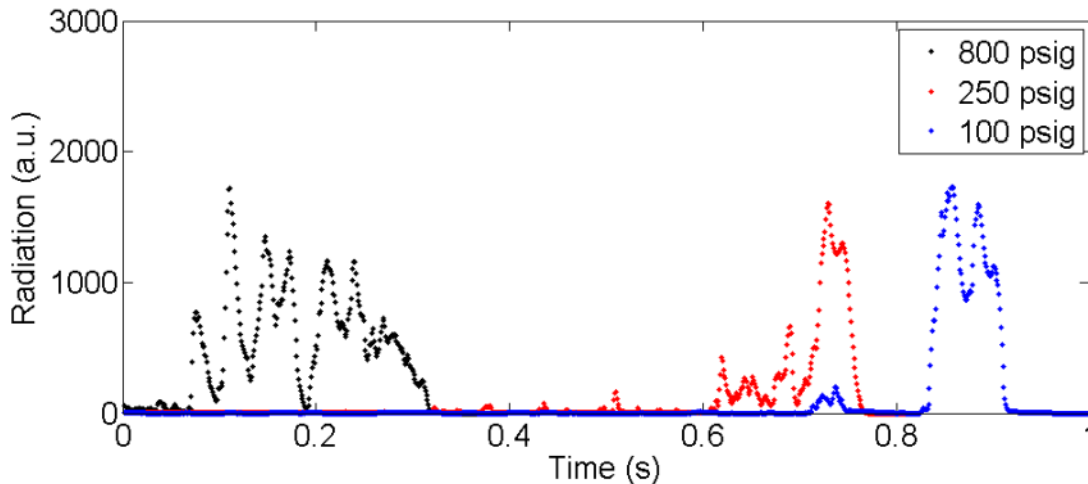
Fig. 13 AlO radiation plot of 4 wt.% 80 nm Al 1 wt.% Aerosil 380 Nitromethane at 800 psig, 250 psig and 100 psig. Each shows the characteristic burning behavior of their respective pressure regime.

The second pressure regime ranged from about 200 to 400 psig. This case represents a transition stage. The two stage burning is still present to some extent. However, a very long first stage occurs, with very weak discrete aluminum participation, followed by a short second stage with its characteristic instability. Most of the nitromethane then is consumed, forming a final residue, which falls off of the rod and burns brightly at the end. A typical case is shown for the 250 psig case shown in Fig. 13.

The third pressure regime occurred below about 200 psig. A typical case is shown for the 100 psig case shown in Fig. 13. In these cases, as nitromethane in the droplet burned, an occasional

discrete aluminum reactions for most of the droplet lifetime. When nearly all the nitromethane is consumed it leaves a final residue, which finally reacts brightly.

The following preliminary conclusions can be drawn from the pressurized combustion tests. The baseline case and many of its variations burn in two stages at higher pressure: a largely nitromethane flame stage with light aluminum participation, and a second stage characterized by significant aluminum participation. Droplets with a higher particle loading (either silica gallant or nAl) reached the second stage of burning more rapidly. Increasing aluminum loading in these mixtures also increases the droplet burning rate. Mixtures with higher active aluminum content, or lower Aerosil 380 content experienced greater amplitudes in their burning self-oscillations. Aluminum participated (either in the first mode with discrete burning particles or with significant participation in the second stage) in the entirety of the droplet combustion in compressed air at pressures above 400 psig. At pressures lower than 400 psig the primary aluminum reaction occurred in the residue stage.

These results appear to show that the timing of the participation of the nAl in the heat release can be modified with gelling or nAl loading. This may be useful in the modification of combustor instabilities. Interestingly, increased solids loading is shown to increase Al participation in the reaction and can greatly increase the reaction rate. Generally, gelling a liquid hampers reaction rates. A more fully gelled liquid (higher solid loadings) appears to inhibit the liquid from participating separately from the solids in the reaction so instead they both react. If solids loading is light (poorly gelled) then primarily liquid participates in the initial stage combustion and the solids are left behind until the resulting solid loading becomes high enough the mixture is gelled and then both solids and liquids participate fully. Pressure also plays a significant role. Since nitromethane is a fuel-rich monopropellant its regression rate is strongly dependent on pressure. At lower pressures the mass flux is too low evidently for the nAl to participate until it burns as a residue. This raises a question about whether a pure liquid fuel (not a monopropellant) would have a high enough mass flux to result in significant nAl participate before a residue is left. Our hypothesis that a sufficient burning rate is needed to have the aluminum participate in reactions. Monopropellants, such as nitromethane, have greatly increased burning rates with pressures. Pure fuels are much less affected by pressure. To test this hypothesis, an oxygen concentrated environment is needed, a higher volatility fuel, or an externally heated droplet should be considered.

1.5   Model Combustor Results

A. Ammonia Borane

The results from the combustor experiments involving the additive AB are also detailed in technical note soon to be submitted to the Journal of Propulsion and Power. The draft of this paper is provided in the appendix of this report for further information about this additive and its influence on the combustion behavior of the model combustor system.

B. Nano Aluminum

Experiments were performed using both ethanol and JP-8 as the base fuel and nAl as the additive. Experiments were carried out at a fixed oxidizer post length of 19.1 cm using combustor Config. 1. One neat ethanol and two neat JP-8 experiments provided a base line for comparison. One ethanol/nAl and two JP-8/Neodol/nAl experiments were conducted, the parameters for which are listed in Table 2 and indicate relatively similar test conditions for each base fuel.

Table 2 Nano Aluminum Experiment Parameters

Fuel	Additive	Mean Pressure, kPa	O/F
Ethanol		1482 (215)	7.10
Ethanol	1 wt.% nAl	1551 (225)	7.29
JP-8		1517 (220)	6.89
JP-8		1551 (225)	6.81
JP-8	1 wt.% nAl/3 wt.% Neodol	1551 (225)	6.87
JP-8	1 wt.% nAl/3 wt.% Neodol	1551 (225)	6.99

Only pressure data at various locations in the combustor was recorded for these tests. Thus, only the magnitude and frequency of the instability were analyzed. As will be shown in the following sections, nAl had relatively little influence on the combustion stability of the system and combustion behavior of the fuels. This result is consistent with the observations from droplet experiments. Since the aluminum did not react until the liquid fuel had been consumed, it was expected that the aluminum in the combustor would also not react till the liquid fuel had been spent. This results in large agglomerates of aluminum that are difficult to combust before exiting the combustion chamber. The lack of heat release from the aluminum within the chamber will lead to very small effects, if any, on the combustion process of the fuel.

The frequency of the different acoustical modes of the system is shown in Fig. 14. These plots show the power spectral density of the pressure data obtained by the kullite that was 1.27 cm

downstream from the injector face for both neat fuels and fuels with nAl. It was difficult to observe the difference in frequency of the instability for the 1st mode for the ethanol tests, Fig. 14 (a); however, the increase in the frequency of the instability for the higher acoustical modes was apparent with the addition of nAl. A closer look at the first mode of the instability does show an increase in the frequency of the instability of around 60 Hz. This was possibly caused by the combustion of a portion of the nAl that raised the temperature of the reacting gaseous flow allowing for faster propagation of sound waves in the combustor.
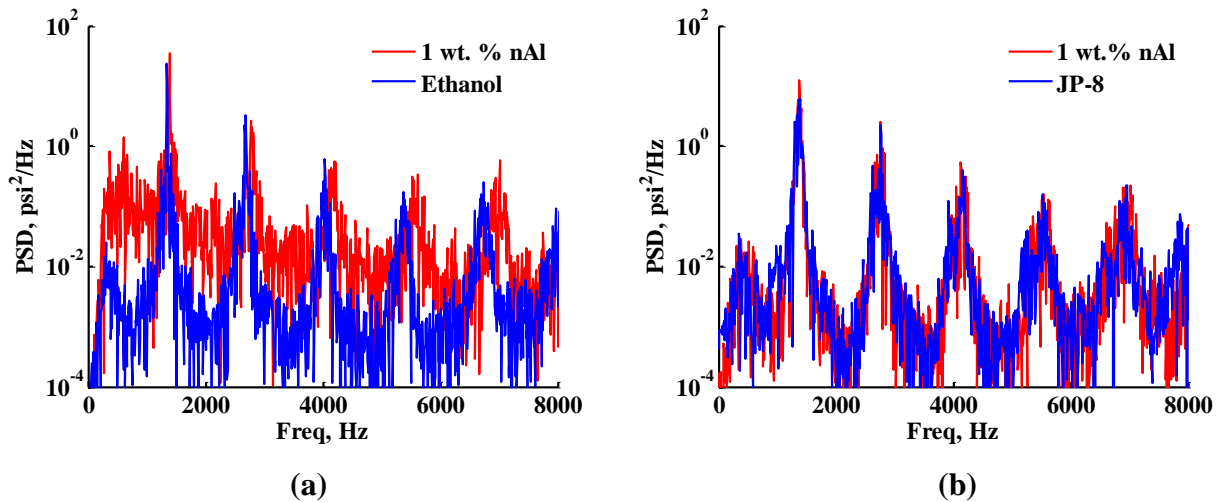

Fig. 14 Power spectral density measurements of fuels with and without nAl with a fixed oxidizer post length of 19.1 cm. (a) Ethanol. (b) JP-8.

The addition of nAl and Neodol to JP-8 had no noticeable impact on the frequency of the instability of the system, Fig. 14(b). This is an indication that the nAl was passive in the combustion process of JP-8 and most likely did not react until it had exited the combustion chamber if it reacted at all.

The amount of energy in each acoustical mode is depicted in Fig. 14. It is difficult to note changes in the amount of energy present in each mode from this figure. Fig. 15 provides additional analysis of the instability magnitude and shows the pressure data taken by the kullite that is 1.27 cm downstream from the injector face that has been filtered by a 15% band pass filter around the 1st mode of the instability. The pressure oscillations for the ethanol experiments exhibited an increase in the magnitude of the peak to peak pressure oscillations when nAl was introduced to the fuel. The fluctuations in pressure swings, for the data passed through a high pass filter, showed max pressure oscillations increasing up to 40% with the addition of nAl.

These results are tabulated in Table 3 which lists the maximum peak to peak pressure oscillations for a portion of the test. The increased magnitude of the instability could be caused by the hotter combustion temperatures noted previously and result in higher sound speeds. The increased speed of sound can cause the unsteady heat release and the pressure oscillations to become more in phase temporally and thus account for the increase in the magnitude of the pressure oscillations.

(a)   (b)
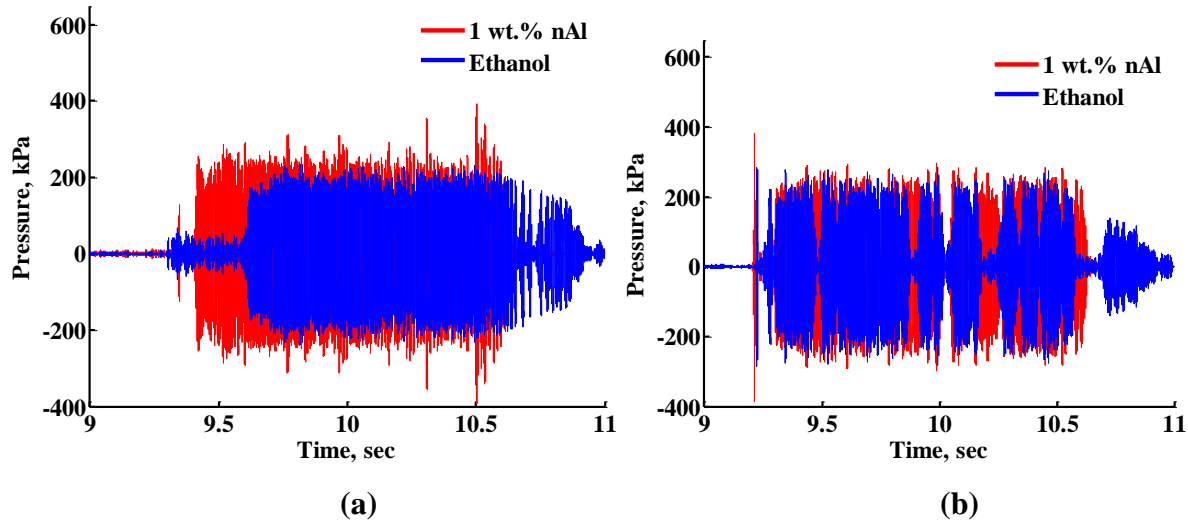
Fig. 15 Pressure oscillations traces of the pressure data filtered through a band pass around the 1st acoustical mode of fuels with and without nAl with a fixed oxidizer post length of 19.1 cm. (a) Ethanol. (b) JP-8.

The addition of nAl to JP-8 again had no noticeable effect on the combustion behavior of the system. Pressure oscillations in the 1st mode, shown in Fig. 15, showed no variation with the addition of nAl. A 5-20% increase in the max peak to peak pressure fluctuations was noted, see Table 3; however, it is difficult to determine the cause of the increase since no other variations were observed when nAl with Neodol were added to JP-8.

Table 3 Nano Aluminum Experiments Pressure Fluctuations

Fuel	Additive	Max Pressure Oscillation, kPa
Ethanol		738 (107)
Ethanol	1 wt.% nAl	1020 (148)
JP-8		814 (118)
JP-8		848 (123)
JP-8	1 wt.% nAl/3 wt.%	924 (134)
JP-8	1 wt.% nAl/3 wt.%	972 (141)

1.6   References

[1] G. A. E. Godsave, Burning of Fuel Droplets, *Symposium (International) on Combustion*, Vol, 4, Combustion Institute, September 1953, pp. 818-830.

[2] S. Kumagai and H. Isoda, Combustion of Fuel Droplets in a Falling Chamber, *Symposium (International) on Combustion*, Vol 6, Combustion Institute, August 1957, pp. 726-731.

[3] MATLAB, version 7.11.0 (R2010b), The MathWorks Inc., Natick, Massachusetts, 2010.

[4] T.D. Hedman, K.Y. Cho, A. Satija, L.J. Groven, R.P. Lucht, and S.F. Son, Experimental Observation of the Flame Structure of a Bimodal Ammonium Perchlorate Composite Propellant Using 5 kHz PLIF, *Combustion and Flame*, Vol. 159, 2012, pp. 427-437.

[5] G. Wolf, J. Baumann, F. Baitalow, and F. P. Hoffmann, Calorimetric Process Monitoring of Thermal Decomposition of B-N-H Compounds, *Thermochimica Acta*, Vol. 343, 2000, pp. 19-25.

[6] F. Baitalow, G. Wolf, J. Baumann, K. Jaenicke-Rößler, and G. Leitner, Thermal Decomposition of B-H-N Compounds Investigated by Using Combined Thermoanalytical Method, *Thermochimica Acta*, Vol. 391, 2002, pp. 159-168.

[7] J. S. Wang and R. A. Geanangel, B NMR Studies of the Thermal Decomposition of Ammonia-Borane in Solution, *Inorganica Chimica Acta*, Vol. 148, December 1987, pp. 185-190.

[8] S. Basu, Y. Zheng, and J. P. Gore, An Experimental Study of Neat and Ionic Liquid-Aided Ammonia Borane Thermolysis, *Journal of Power Sources*, Vol. 196, 2011, pp. 734-740.

[9] Martin E. Bluhm, Mark G. Bradley, Robert Butterick III, Upal Kusari, and Larry G. Sneddon, Amineborane-Based Chemical Hydrogen Storage: Enhanced Ammonia Borane Dehydrogenation in Ionic Liquids, *Journal of the American Chemical Society*, Vol. 128, 2006, pp. 7748-7749.

[10] P. Ramachandran and P. Gagare, Preparation of Ammonia Borane in High Yield and Purity, Methanolysis, and Regeneration, *Inorganic Chemistry*, Vol. 46, 2007, pp. 7810-7817.

[11] P. A. Storozhenko, R. A. Svitsyn, V. A. Ketsko, A. K. Buryak, and A. V. Ul'yanov. *Russian Journal of Inorganic Chemistry*, Vol. 50, 2005, pp. 980-985.

[12] Moore, S Son, and B Asay, *Propellants, Explosives, Pyrotechnics*, Vol. 29, 2004, pp. 106-111.

[13] J Sabourin, R Yetter, B Asay, J Lloyd, V Sanders, G Risha, S Son, *Propellants, Explosives, Pyrotechnics*, Vol. 34, 2009, pp. 385-393.

[14] Y Gan, L Qiao, *Combustion and Flame*, Vol. 158, 2011, pp. 354-368.

2   Hydrogen Addition Effects on Unstable Methane Combustion

2.1   Introduction

Combustion instability was studied using a continuously varying resonance combustor (CVRC) at Purdue University. The capability exists to vary the length of the oxidizer post during a test, thus changing the resonant acoustic frequencies of the combustion chamber. In this way, it has been shown in the past at Purdue that with 100% methane as the fuel, combustion begins stable at an ox-post length (LOP) of 7.5 in, and then spontaneously transitions to unstable combustion as the post decreases in length. Combustion again spontaneously transitions back to stable combustion once the post has decreased in length to near 4.5 in.

It has been suggested that the addition of hydrogen to the fuel will have an effect on the stability of combustion because of the increased flame speed observed with hydrogen. Chen et al. determined that for a certain percent of hydrogen in methane, the flame speed increases as shown in Figure 2.1.
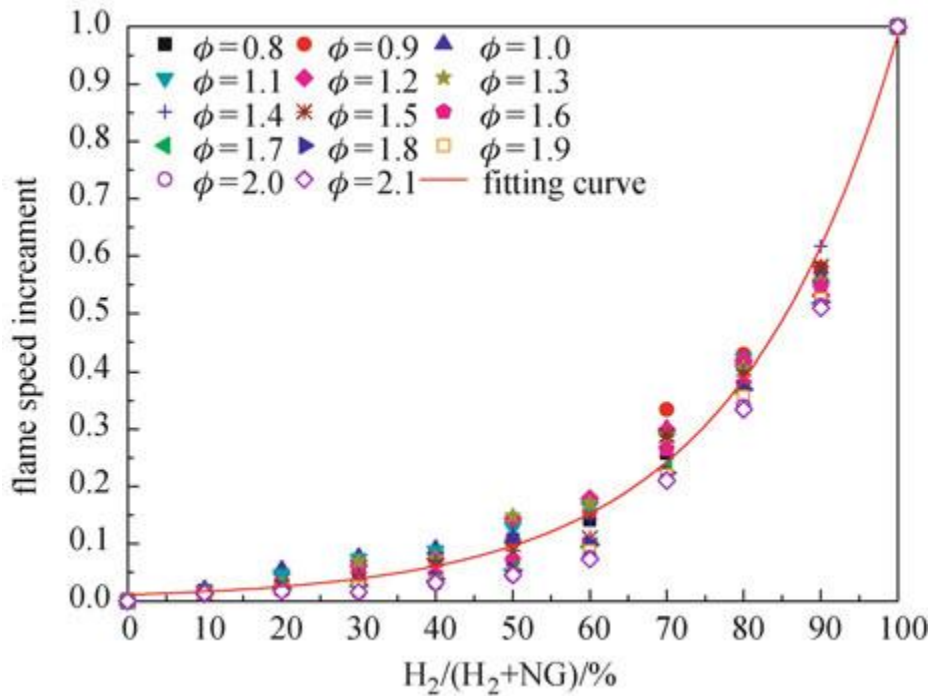
Figure 2.1: Experimental study on the laminar flame speed of hydrogen/natural gas/air mixtures (Chen Dong, Xi'an Jiaotong University, Xi'an 710049, China) © Higher Education Press and Springer-Verlag Berlin Heidelberg 2010).

To determine the effect of hydrogen on combustion instability, the CVRC was operated at baseline cases of 0% hydrogen and 100% hydrogen as well as an intermediate case of 80%

hydrogen addition by volume. 80% hydrogen was chosen because it is at this mixture that there is a significant increase in flame speed.

2.2 Experimental Setup

The present work builds off work previously done at Purdue University by utilizing the Continuously Variable Resonance Combustor (CVRC), a naturally unstable rocket combustor, as a test bed for studying combustion instabilities. The CVRC allows for repeatable instabilities to be created and studied in the laboratory. The experiment has the unique ability of continuously varying the geometry of the oxidizer post during hot fire, thus changing the resonance of the system and creating a varying range of combustion instabilities while maintaining constant inlet conditions. The oxidizer post length will be varied during the course of each test, translating between lengths of 7.5 *in* and 3.5 *in*. This translation takes place over a sufficient time so that the system can be considered "quasi-steady" at each post length.

The CVRC, shown in Figure 2.2, was previously used to test liquid fuels but has been adapted to be able to test gaseous fuels. The system consists of a gas generator used to decompose the liquid H_2O_2 into hot oxygen and steam, an oxidizer injector mounted on a shaft that can translate during the course of the test, a co-axial fuel injector, and a dump combustor. The system is instrumented with thermocouples and two types of pressure sensors that take measurements at 500 Hz and 100 kHz. The chamber has three sections, the first of which is removable and interchangeable with a quartz chamber that is used to view combustion at the head end of the combustor. Care was taken to create a system with conditions that are easy for CFD modelers to duplicate.
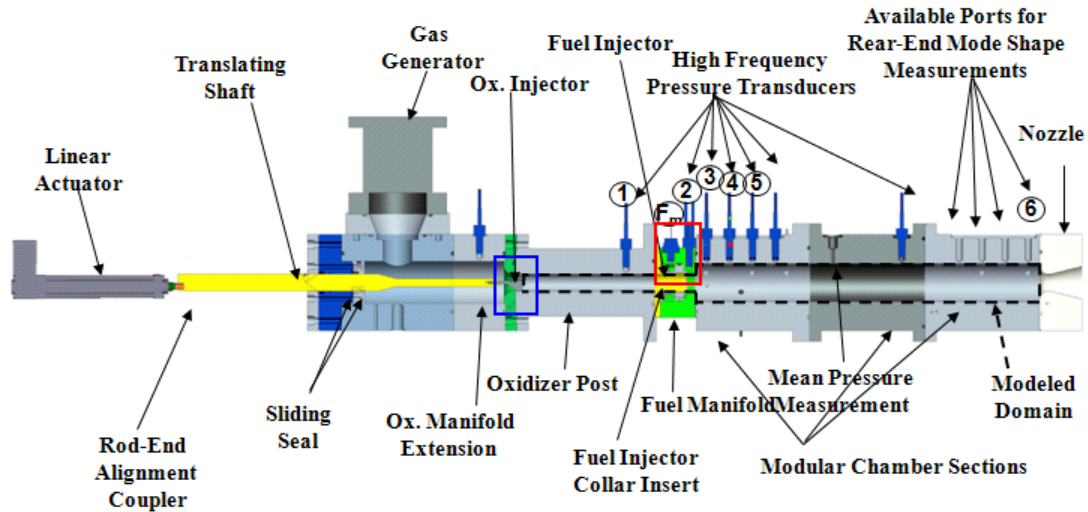
Figure 2.2. Experimental setup of the CVRC combustor. The linear actuator moves the translating shaft providing the variable length oxidizer post. The gas generator is a catalyst bed for the hydrogen peroxide. Pressure is measured along the length of the CVRC by both high and low frequency pressure transducers.

The combustor was originally designed to operate without an igniter by taking advantage of auto-ignition between decomposed hydrogen peroxide and the JP-8 fuel. It has not been possible to achieve auto-ignition with gaseous methane and decomposed hydrogen peroxide, so a small amount of JP-8 is added to the fuel line just upstream of the main methane valve. This JP-8 is pushed into the chamber by the methane fuel and ignites with the peroxide. This starting technique has worked consistently for methane-fueled tests. For hydrogen tests, JP-8 ignition was not enough to ignite the hydrogen fuel so a more complicated startup sequence was used. First, a slug of JP-8 is pushed into the combustor by methane gas. Once the JP-8 ignites the methane gas, the hydrogen valve is opened and the hydrogen ignites from the burning methane. In the case of the 100% hydrogen test, once hydrogen ignition is achieved, the methane valve is closed. The startup sequence is quick and can be seen in the pressure data. All data used for this study was taken after the startup transient.

2.3 Light Emission from Combustion

High speed videos were taken with a Phantom camera at 10,000 *frames/s* with an exposure of 10 μs. Each frame contains 184 pixels by 320 pixels, allowing images to be taken across the

entire diameter of the combustor and from the injector face to 5.0 in downstream of the injector face. High speed videos of the light intensity were filmed through the optical chamber made of a quartz tube inserted in an acrylic housing.

Chemiluminesence is light emitted by molecules in an excited state when they radiatively relax to a lower energy state. Common high energy chemiluminescent species in hydrocarbon flames include CH*, OH*, C_2*, and CO_2*. CH*, emitting at 432 *nm*, was chosen as the radical to measure for this study because it is present only during the high temperature regions associated with combustion. Therefore, the light emitted by this radical can serve as a qualitative measure of local heat release.

A Semrock 432/17 narrow band filter with a transmittance of greater than 0.90 for wavelengths in the range of 423-444 *nm* was used on the high speed camera to capture the light emitted during combustion process. The intensity of the light fluctuates with the combustion and is used as an approximation for the unsteady heat release. The videos obtained are line of sight measurements. This induces a degree of uncertainty into the measurements as the light from all sides of the chamber is being recorded.

Local pressure fluctuation values were not recorded during the optical tests because the optical chamber had no instrumentation ports. The local pressure fluctuations for each pixel location were estimated by applying a time shift and amplitude scaling factor to the pressure measurements made at the aft end of chamber. Prior experimental data were used to verify that the estimations were accurate.

2.4 Data Acquisition and Instrumentation

Two sets of data were acquired remotely for each test through the use of National Instruments Labview program. Mean pressure and temperature were recorded at 500 Hz, and high frequency pressure oscillations were recorded at a minimum of 100 kHz. The 500 Hz data included pressure in both the fuel and oxidizer tanks, before and after the oxidizer catalyst bed, upstream of the cavitating and sonic venturis, in the fuel and oxidizer manifolds, in the oxidizer post, and in the combustion chamber. These measurements were used to obtain the mean pressure data, as they are not capable of collecting data fast enough to capture the high frequency pressure oscillations. Figure 2.3 shows selected pressures recorded during a typical methane test.

The data show the oxidizer is turned on first and allowed 3.0 *s* to reach a steady operating condition. The fuel is then turned on and the pressure in the chamber rises. The odd bump in the oxidizer manifold pressure is caused by the changing volume of the oxidizer manifold as the post translates. This is consistent and is seen in every test. The high oscillations in the oxidizer manifold (at 14 *s*) mark the point where the system runs out of oxidizer. This happens after the test has been completed and the fuel turned off. The rise in chamber pressure is seen right as the fuel turns corresponds to when the JP-8 enters the chamber. The system is allowed to reach a steady operating condition before the post begins to translate.

Figure 2.4 shows the measured flow rates of oxidizer and fuel. Both flow rates are level indicating the fuel and oxidizer flow was consistent throughout the test. The fuel flow rate shows a small spike at about 8 s. This corresponds to when the JP-8 is going through the venturi. Figure 2.4 also shows the length of the oxidizer post as a function of time. This is a typical forward translating test. The length of the post is indicated in grey on the plot and begins at a length of 7.5 *in* and translates at 2.0 *in/s* until it reaches a length of 3.5 *in*.
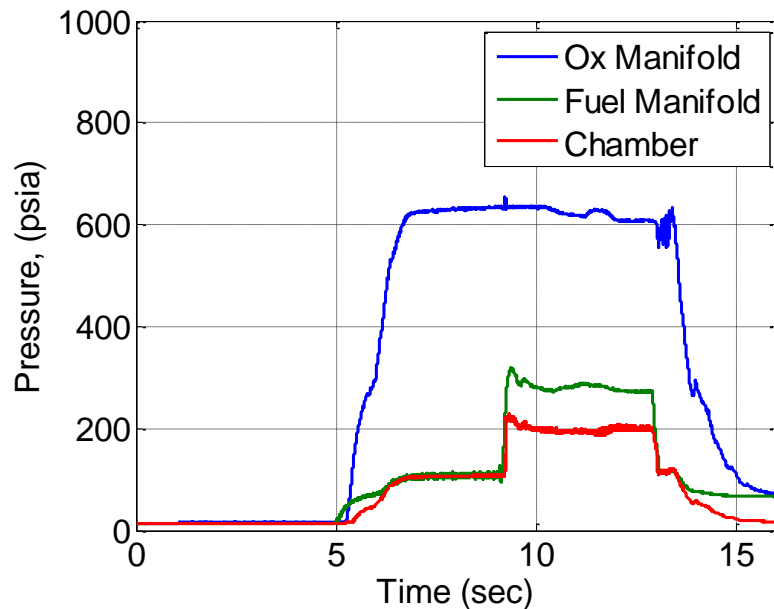
Figure 2.3. Pressure data obtained at 500 Hz for a typical methane test.
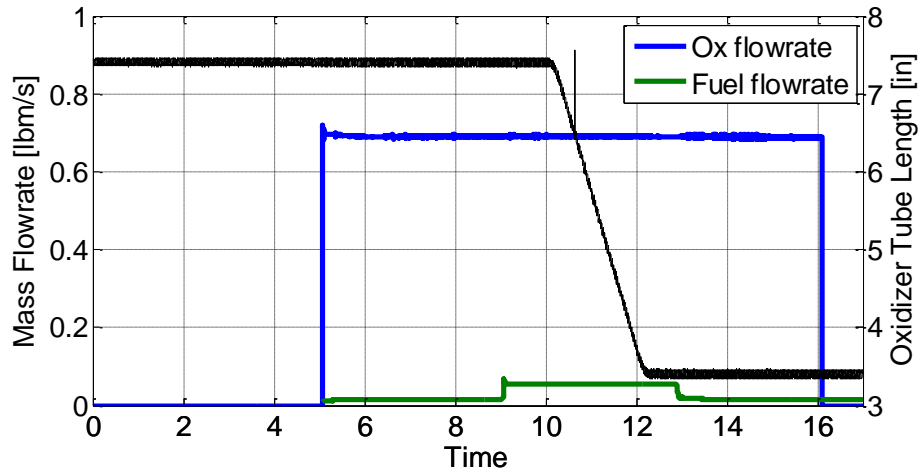
Figure 2.4. Mass flow rate of the fuel and oxidizer and length of the oxidizer post vs. time for a typical methane test.

To analyze the high frequency pressure measurements obtained during each test, waveform shape, PSD plots, and spectrogram plots were created. Because it is not possible to measure pressure inside the optical section, all pressure measurement analysis will be done using data obtained from the 14.5" location (near the nozzle) which is present during optical and non-optical tests. This way, pressure data can be directly compared between optical and non-optical tests.

2.5   Pressure Measurements

The pressure signal can be high-pass filtered at 150 Hz to get rid of any electrical noise in the signal. The high-passed signal can then be analyzed in the frequency domain by obtaining the Power Spectral Density of the signal (PSD). The data used to perform the PSD is taken from 0.1s of data. 0.1 seconds corresponds to a post movement of .2 inches. Because of the small length change during this period of time, a quasi-steady assumption is taken for the 0.1 second sample of data. A typical PSD is shown below in Figure 2.5.
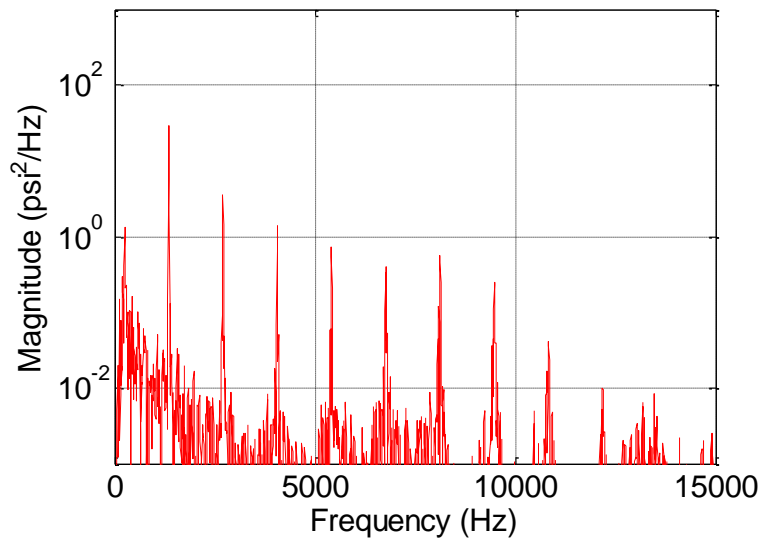
Figure 2.5. Power Spectral Density plot of the pressure signal from the 14.5" location

It is of interest to see how this PSD taken for 0.1s of data changes throughout the test as the oxidizer post length changes. To do this, a PSD is calculated at each 0.1 second interval and the peak amplitude value corresponding to the first mode is taken at each interval. This value is recorded and then plotted against the oxidizer post length (Lop). An example of this PSD vs. Lop plot is shown below in Figure 2.6.
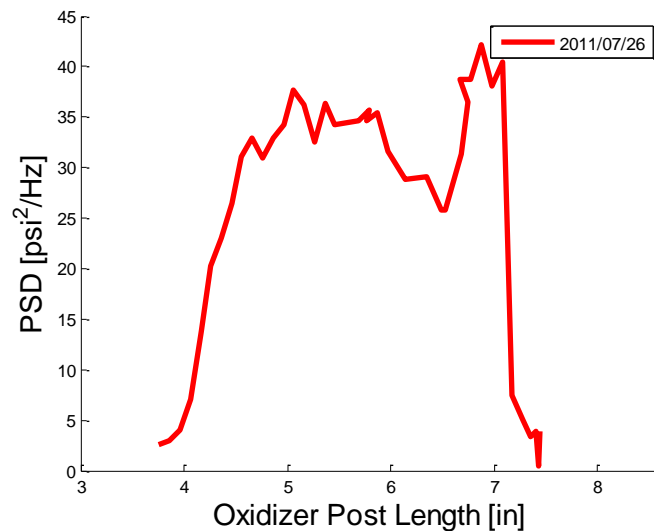
Figure 2.6. PSD vs. Lop for the 14.5" location.

In this particular test, combustion instability as measured from each PSD peak starts off stable at Lop=7.5" As the post transitions, the instability level increases dramatically near Lop=7.0". Different levels of instability are observed throughout the test and the levels decrease back to a stable condition starting near Lop=4.5". In addition to recording each PSD peak amplitude, the corresponding frequency at which the peak occurs can also be recorded and plotted against the oxidizer post length. An example of this PSD(freq) vs. Lop plot is shown below in Figure 2.7.
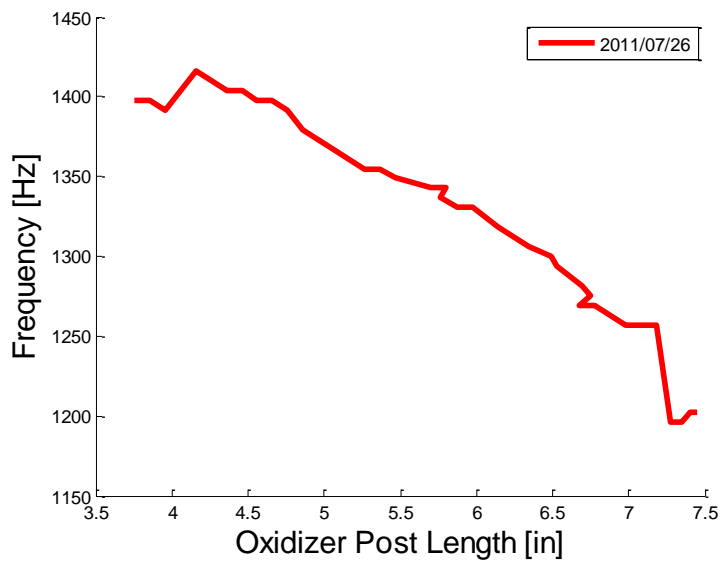
Figure 2.7. PSD(freq) vs. Lop. Showing how the frequency of the first mode changes with a changing oxidizer post length.

Once again, note that the test begins at an oxidizer post length of 7.5". Here we see the 1st mode frequency starts near 1200 Hz and transition to higher values throughout the test as the oxidizer post length decreases. It is also worth noting the large jump in frequency near Lop=7.0" which corresponds to the same oxidizer post length at which the test transitioned to unstable combustion. This jump is typical and is seen in the other tests.

2.6 High Speed Optical Measurements

In addition to obtaining pressure measurements, each test was performed with the instrumented chamber section replaced with an optically accessible quartz chamber section. To analyze and compare this optical data for different hydrogen concentrations, the following analysis was performed: Averaged Light Intensity, Total RMS Intensity, and 1st Mode RMS Intensity. Because of the large amount of data contained in the high speed image files, the high speed video was broken up into sets of 230 frames. These sets were taken at various times corresponding to various oxidizer post lengths. The 230 frame set contains approximately 30 pressure cycles. The quasi-steady assumption is again made because the post moves only 0.046" during each frame set. In all optical results shown, flow will be from left to right (the injector is on the left).

To obtain the average light intensity, the average of each pixel is taken over the entire frame set. The average light is an indication of where combustion is taking place in the chamber. Because of the problems with the line of sight measurements, the average light intensity is most useful in determining the distance from the injector face that combustion occurs in the chamber.

To determine where the largest fluctuations are occurring in the combustion, the root-mean-squared (RMS) value at each pixel in the frame set is determined from the raw pixel intensity signal. Like the total RMS intensity plots, the 1st Mode RMS intensity plots are created by determining the RMS value for each pixel. This time, instead of determining the RMS value from the raw intensity signal, the light intensity signal is first band-passed around the first mode frequency. The RMS value is then taken from the resulting band-passed signal. The 1st Mode RMS intensity plot shows where the light is fluctuating the most at the same frequency as the pressure.

2.7 Test Conditions

Tests were performed for hydrogen concentrations by volume of 0%, 80%, and 100%. The operating conditions for each test are presented below in Table 2.1 The nominal operating conditions are a chamber pressure of 200 psi and an overall equivalence ratio of 0.8.

Table 2.1. Summary of experimental test conditions.

Test Number	1.1	1.2	2.1	2.2	3.1	3.2
Hydrogen Percent (Vol.)	0%	0%	80%	80%	100%	100%
Optical?	No	Yes	No	Yes	No	No
Chamber Pressure (psi)	200.00	200.00	204.00	215.00	212.00	210.00
H_2O_2 flow rate (lbm/s)	0.6900	0.7000	0.70	0.71	0.701	0.696
CH_4 Flow Rate (lbm/s)	0.0550	0.0560	0.0285	0.0308	0	0
Oxidizer to Fuel Ratio	12.5	12.5	16.7	15.8	21.5	20.2
Equivalence Ratio (Φ)	0.751	0.754	0.748	0.790	0.872	0.927
Test Date	7/14/2011	7/26/2011	10/24/2011	10/26/2011	4/6/2010	7/6/2011

Because there is no CH* emission when burning pure hydrogen with hydrogen peroxide, no optical data was taken for the 100% hydrogen case. The results for each analysis outlined in the previous chapter will now be compared for each of the three cases of hydrogen concentration. The 100% hydrogen tests presented in this study produced very stable combustion as expected. There were however some tests that produced unexpected results. It was observed that changes in the fuel line upstream of the fuel injector caused some of the hydrogen tests to produce strong instabilities. These instabilities were unique in that the unstable mode changed during the tests. The first mode appears strong during startup, after the post moves a small amount, the first mode dies out and the second mode becomes strong, as the post translates even further, the second mode dies out and the third mode becomes strong. This new "mode switching" behavior is unique and warrants further study in the future. Because this behavior appears to be directly related to upstream plumbing, and stable tests can be run consistently when the upstream plumbing is installed in a certain way, the results and analysis included in this report use data obtained from the stable 100% hydrogen tests.

2.8 High Frequency Pressure Results

First the high frequency pressure measurements from each hydrogen concentration will be compared. Because it would be difficult to make comparisons directly from the PSD plot alone, the PSD vs. Lop plots are shown below for PSD peaks and corresponding frequencies in Figures 2.8 and 2.9, respectively.
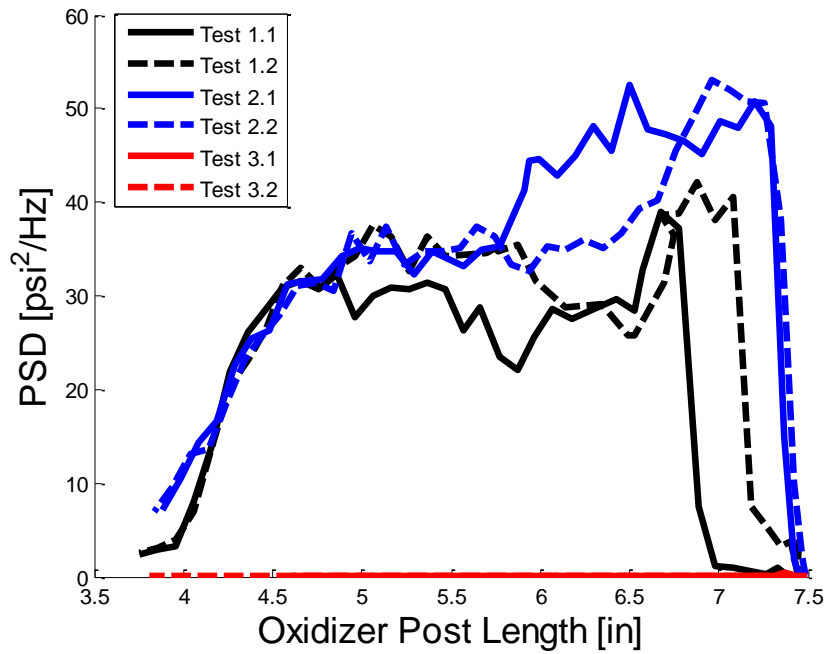
Figure 2.8. PSD vs. Lop comparing all six tests.
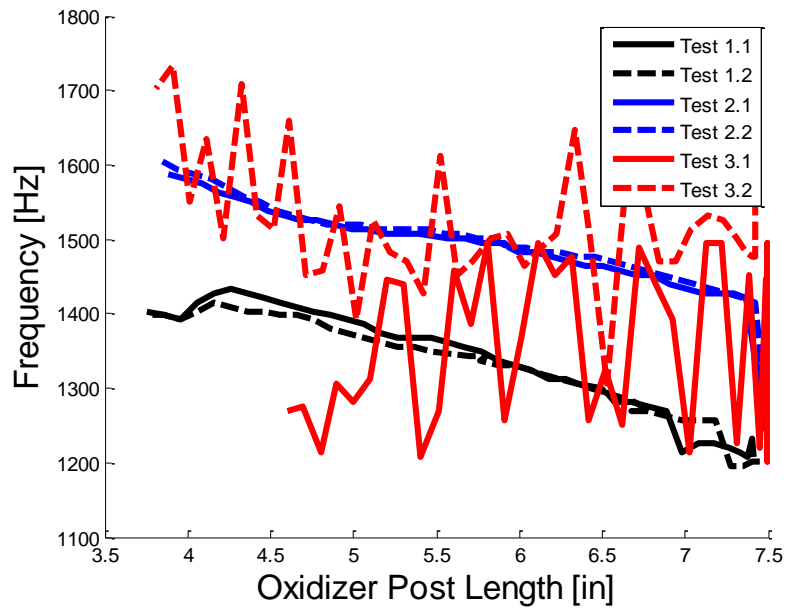
Figure 2.9. PSD(freq) vs. Lop comparing the frequency as a function of oxidizer post length for all six tests.

Again, the legend shows the test number and for simplicity in visualization, black lines are for 0% hydrogen, blue lines are for 80% hydrogen, and red lines are for the 100% hydrogen

cases. In the amplitude plot, it is clear that the hydrogen case is not unstable. Because there are no peaks in the PSD plot for 100% hydrogen, it is not possible to pick out a frequency and that is why the frequency appears to jump around in the PSD frequency plot. The PSD does not yield any insightful data for the 100% hydrogen case except that it is stable.

The PSD vs. Lop does however provide useful information about the 0% and 80% hydrogen addition cases. The 80% hydrogen cases both appear to transition to unstable combustion much sooner than the 0% cases. The 80% hydrogen cases reach a similar, yet slightly higher amplitude than that of pure methane suggesting that the addition of hydrogen at 80% by volume actually increases unstable behavior. The trend throughout the test is very similar for both cases. The high instability levels slowly decrease as the oxidizer post decreases in length and then dramatically start to transition back to stable combustion around and oxidizer post length of 4.5".

The PSD(freq) vs. Lop plot shows that the two cases for 0% and 80% hydrogen have similar trends as the oxidizer post decreases. Both cases show an increase in frequency at a similar rate. Both cases also show a dramatic increase in frequency at the point where the test transitions from stable to unstable combustion. The 80% hydrogen case has a frequency that is roughly 160 Hz higher than the 0% hydrogen case as expected due to the change in sound speed within the chamber.

A spectrogram from each test is shown below in Figure 2.10. The test numbers are indicated above each sub-figure. Once again, it is clear right away that the 100% hydrogen case was stable throughout the duration of the post movement. There is however one discrepancy in the 100% hydrogen case. During test 3.2, the hydrogen case actually appears to be operating unstable prior to the movement of the post. This behavior was not captured by the PSD because it did not examine what happened prior to post movement. As soon as the post begins to move, Test 3.2 immediately becomes stable and this behavior continues until the end of the test. This behavior is likely due to the presence of methane and JP-8 that are used to ignite the hydrogen.

The 0% and 80% hydrogen cases show very similar behavior. During each test, there are initial disturbances due to the ignition of the propellants which die out. Next, the amplitude of instability increases almost instantaneously at a certain oxidizer post length (this length varies depending on the test). At this time, even higher order modes, up to nine of them, appear. As the post continues to translate, the instabilities begin to disappear one by one starting with the higher order modes and working down to the first mode. Throughout the transitioning portion of the

test, it is once again noticed that the frequency of the instabilities slowly increases with decreasing oxidizer post length.

Note that the spikes observed in the oxidizer post length represented by the blue line are due to electrical noise and are not real. The post transitions smoothly from 7.5" down to 3.5" at a rate of 2" per second.

Test 1.1

Test 1.2

Test 2.1

Test 2.2

Test 3.1

Test 3.2
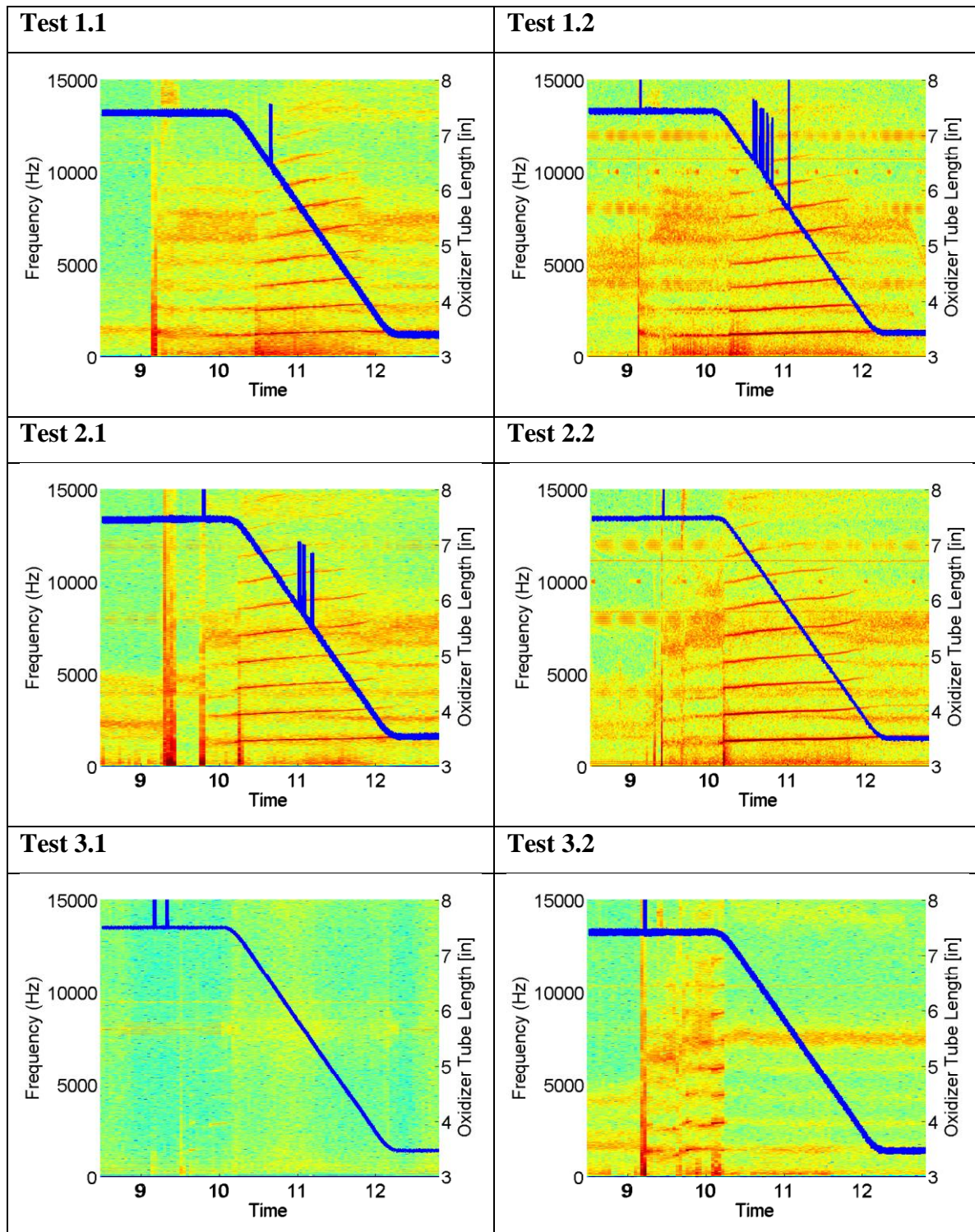
Figure 2.10. Spectrograms from all six tests.

2.10   High Speed Optical Results

Now that the pressure data for each case has been compared, an investigation into the effects of hydrogen addition using the optical results can be performed. Once again, note that because there is no CH* emission when pure hydrogen is burned with hydrogen peroxide, only optical results for Tests 1.2, and 2.2 will be shown. (Test 1.1 and Test 2.1 did not have the optical chamber installed). Average light intensity plots for Test 1.2 and Test 2.2 are shown below in Figures 2.11 and 2.12 respectively. The light intensity is presented without units to emphasize that there is no direct calibration between camera intensity and heat release. Apart from the apparent difference in intensity magnitude, the two tests appear to behave similarly. Initially, combustion is taking place away from the injector face. As the test transitions from stable to unstable, the main combustion zone moves back closer to the injector face. Likewise, as the test begins to transition to stable combustion, the region of combustion moves back away from the face.

The total RMS plots show the first signs of distinction between the two cases. During the 0% hydrogen test, light oscillations appear only near the head end of the injector. Conversely, during the 80% hydrogen test, the oscillations as indicated by RMS intensity are spread across the entire width of the optical section. At an oxidizer post length of 4.5" (corresponding to near the location where the combustion began a transition to stable combustion), the RMS intensity appears near the injector face and at the downstream end of the optical section, leaving an area in the middle that has low levels of RMS intensity. The total RMS intensity is plotted for Test 1.2 and Test 2.2 in Figures 2.13 and 2.14 respectively. In both cases, the level of oscillations in light are low at the beginning and end of the test. Higher RMS values are seen during the unstable portion of the test. Figures 2.15 and 2.16 show the RMS of the light intensity signal after it has been band-pass filtered around the first mode for Test 1.2 and Test 2.2 respectively. These plots appear very similar to the total RMS plots shown previously which indicates that nearly all of the combustion light oscillation occurs at the first mode frequency.

In summary, a significant amount of hydrogen was mixed with gaseous methane in a single element longitudinal combustor. While there were some noticeable changes of the location of light intensity oscillation, the overall stability of the combustor was not improved. In fact, pressure oscillation levels actually increased in magnitude with the addition of 80% Hydrogen by volume.
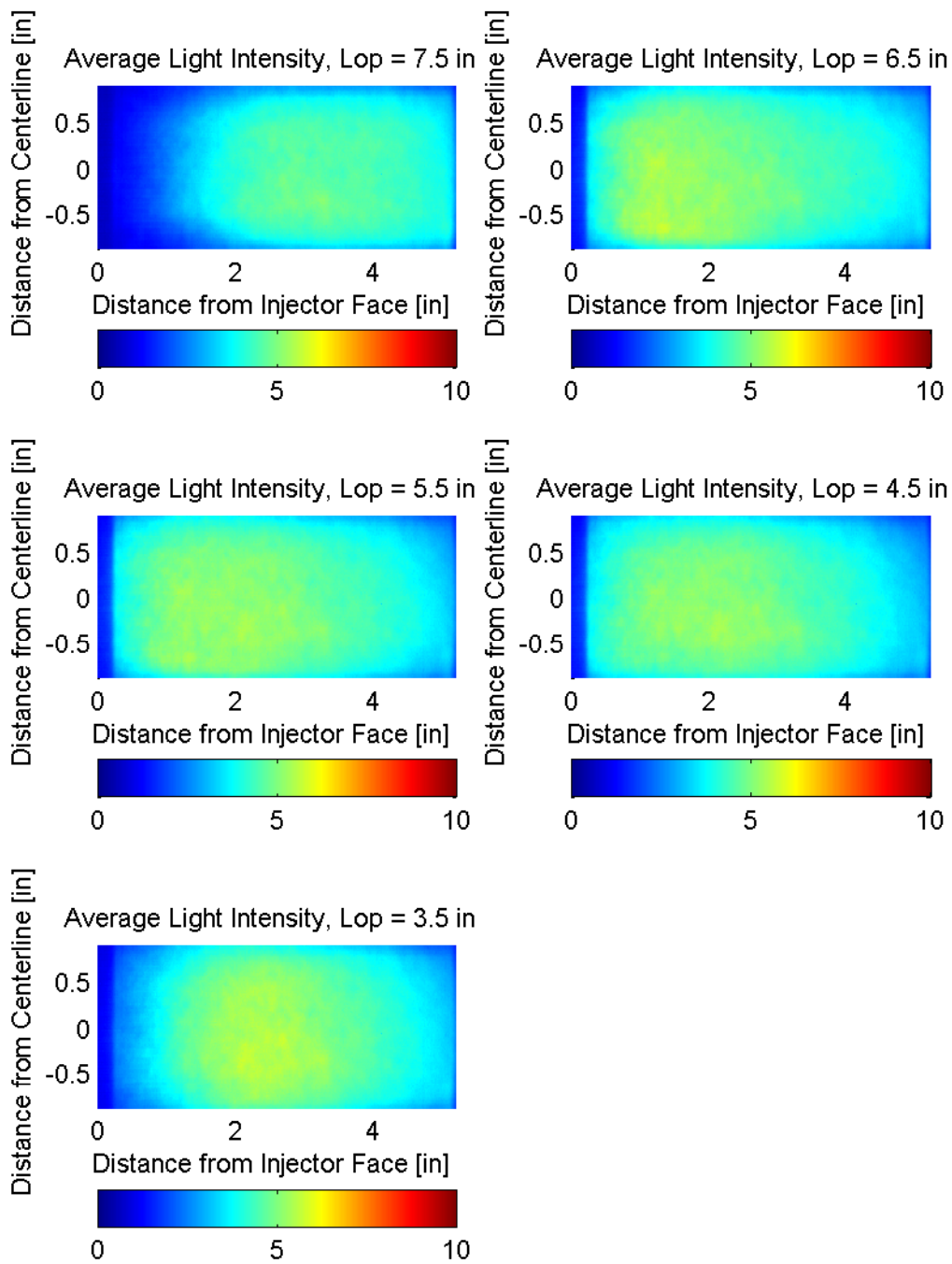
Figure 2.11. Test 1.2 Average light intensity plots for various oxidizer post lengths. 0% hydrogen.
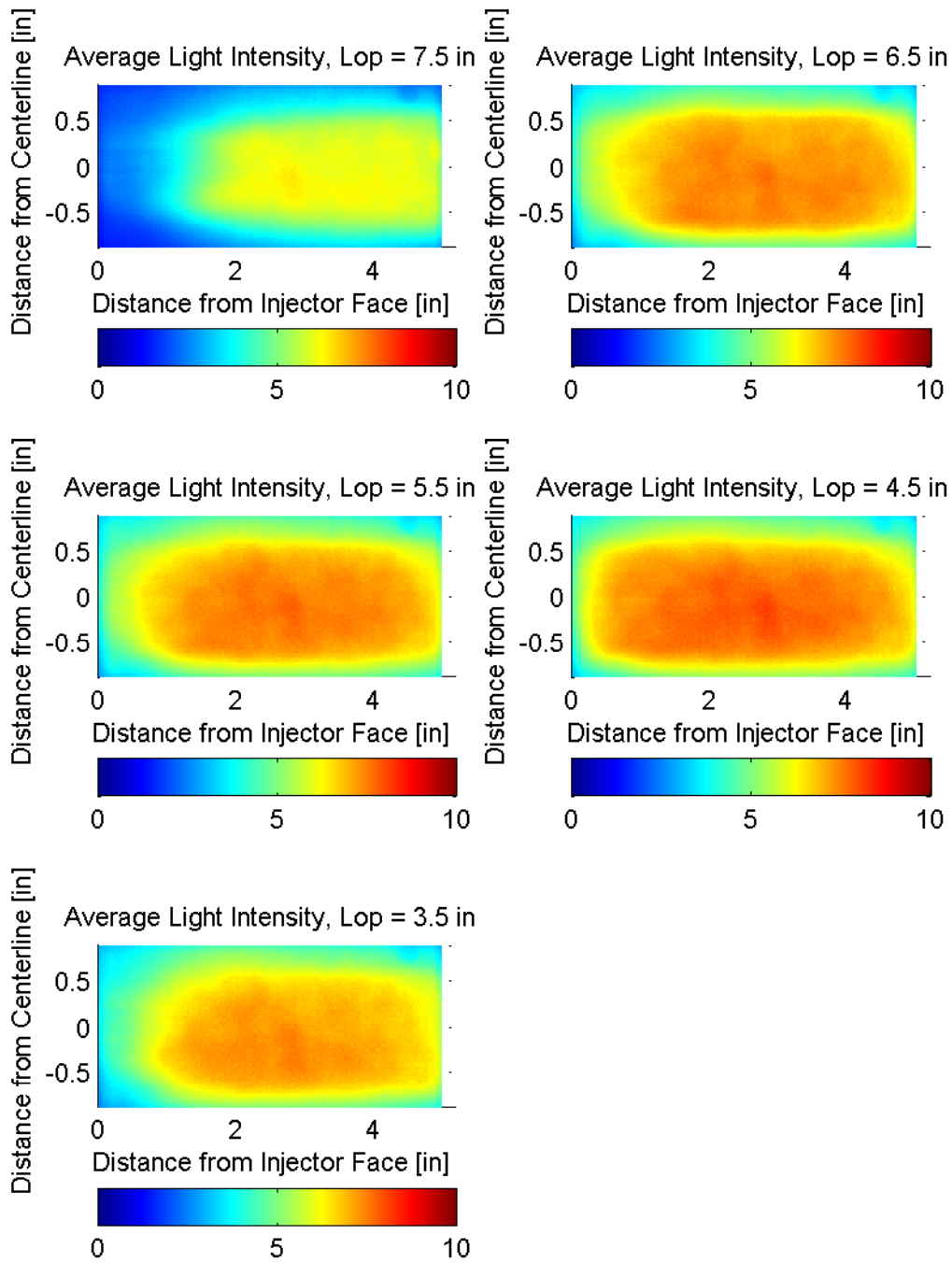
Figure 2.12. Test 1.2 Average light intensity plots for various oxidizer post lengths. 80% hydrogen.
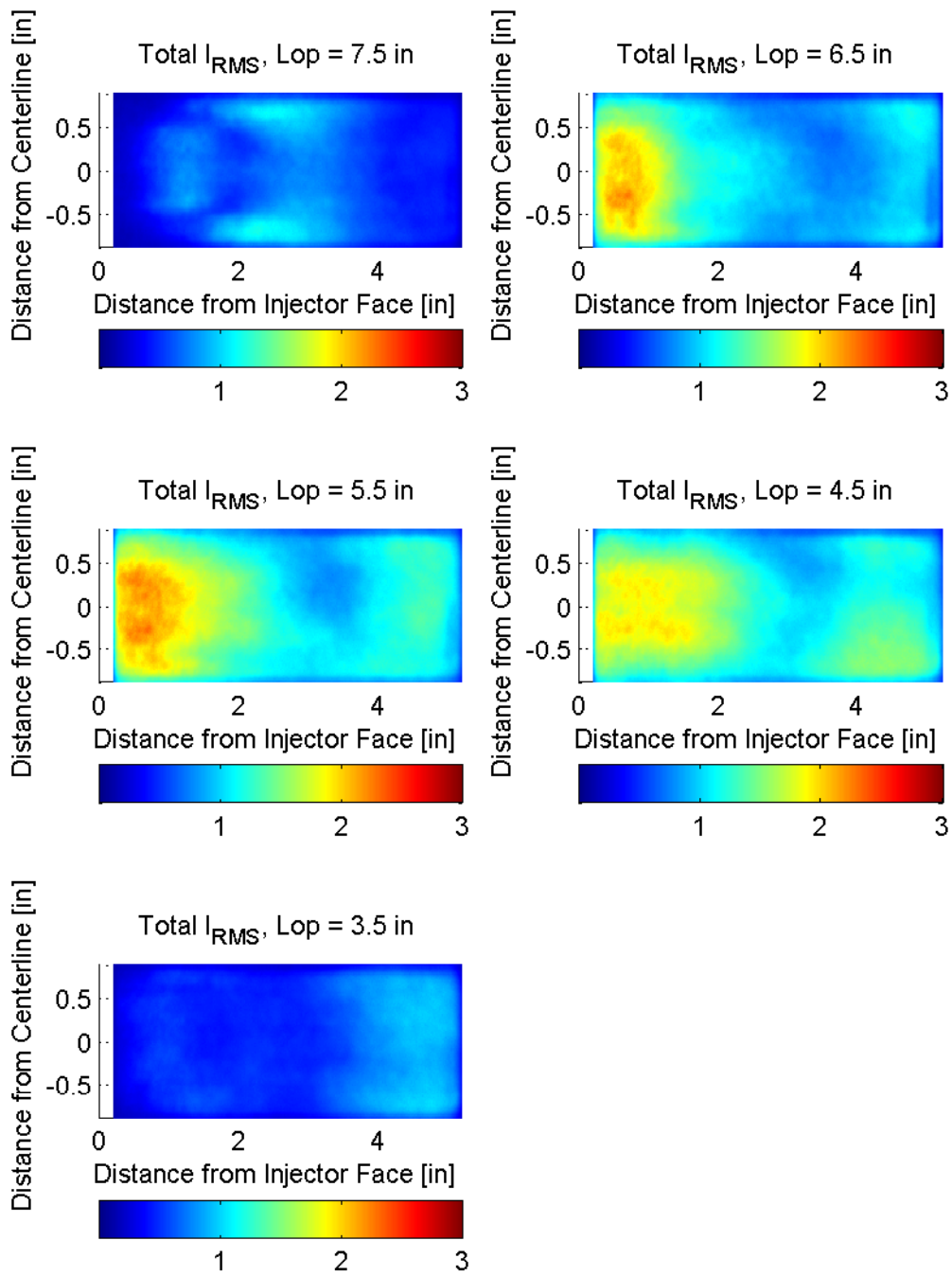
Figure 2.13. Test 1.2 Total RMS light intensity plots for various oxidizer post lengths. 0% hydrogen.
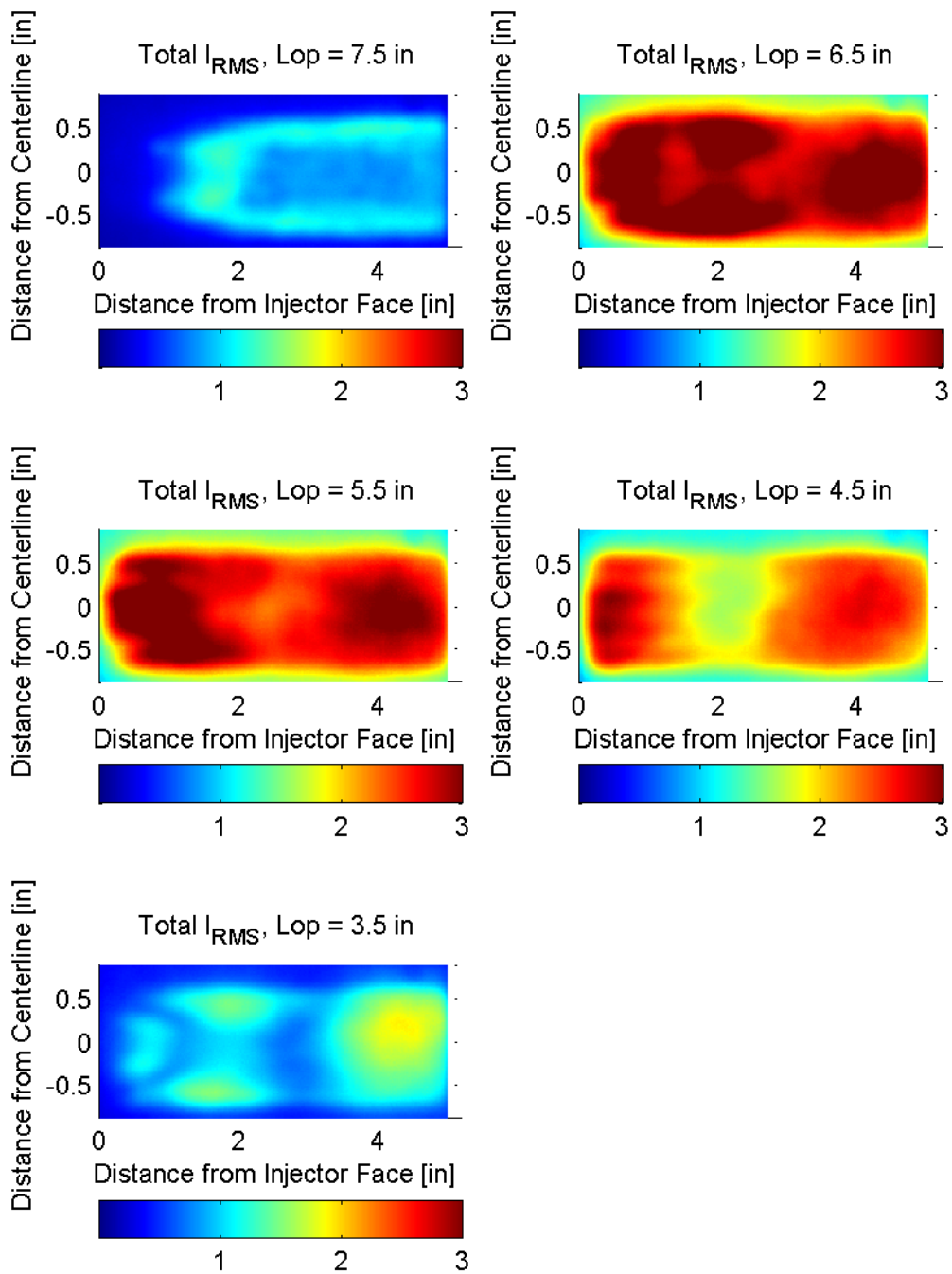
Figure 2.14. Test 2.2 Total RMS light intensity plots for various oxidizer post lengths. 80% hydrogen.
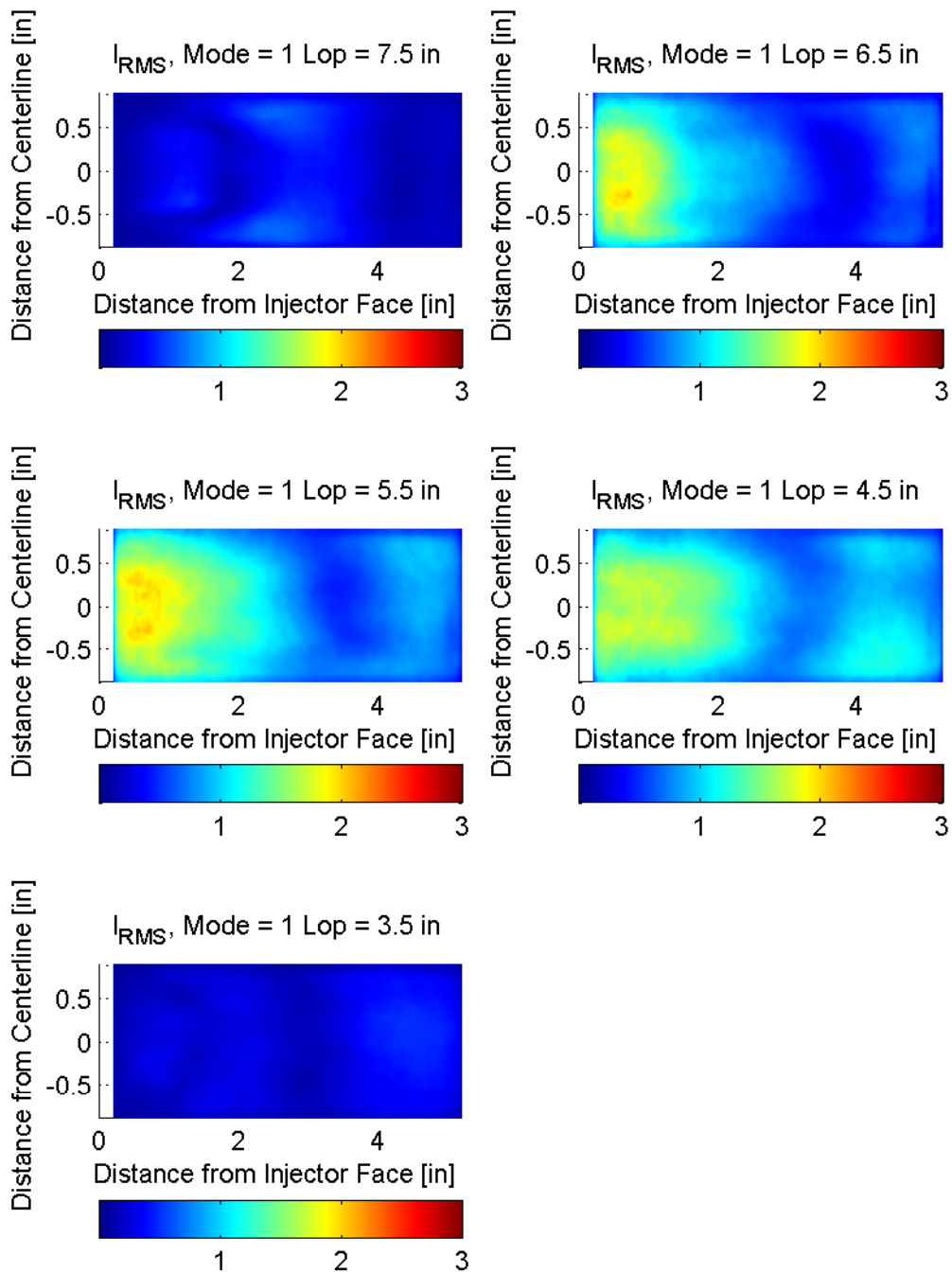
Figure 2.15. Test 1.2 1st mode band-pass filtered RMS light intensity plots for various oxidizer post lengths. 0% hydrogen

Figure 2.16. Test 2.2 1st mode band-pass filtered RMS light intensity plots for various oxidizer post lengths. 80% hydrogen
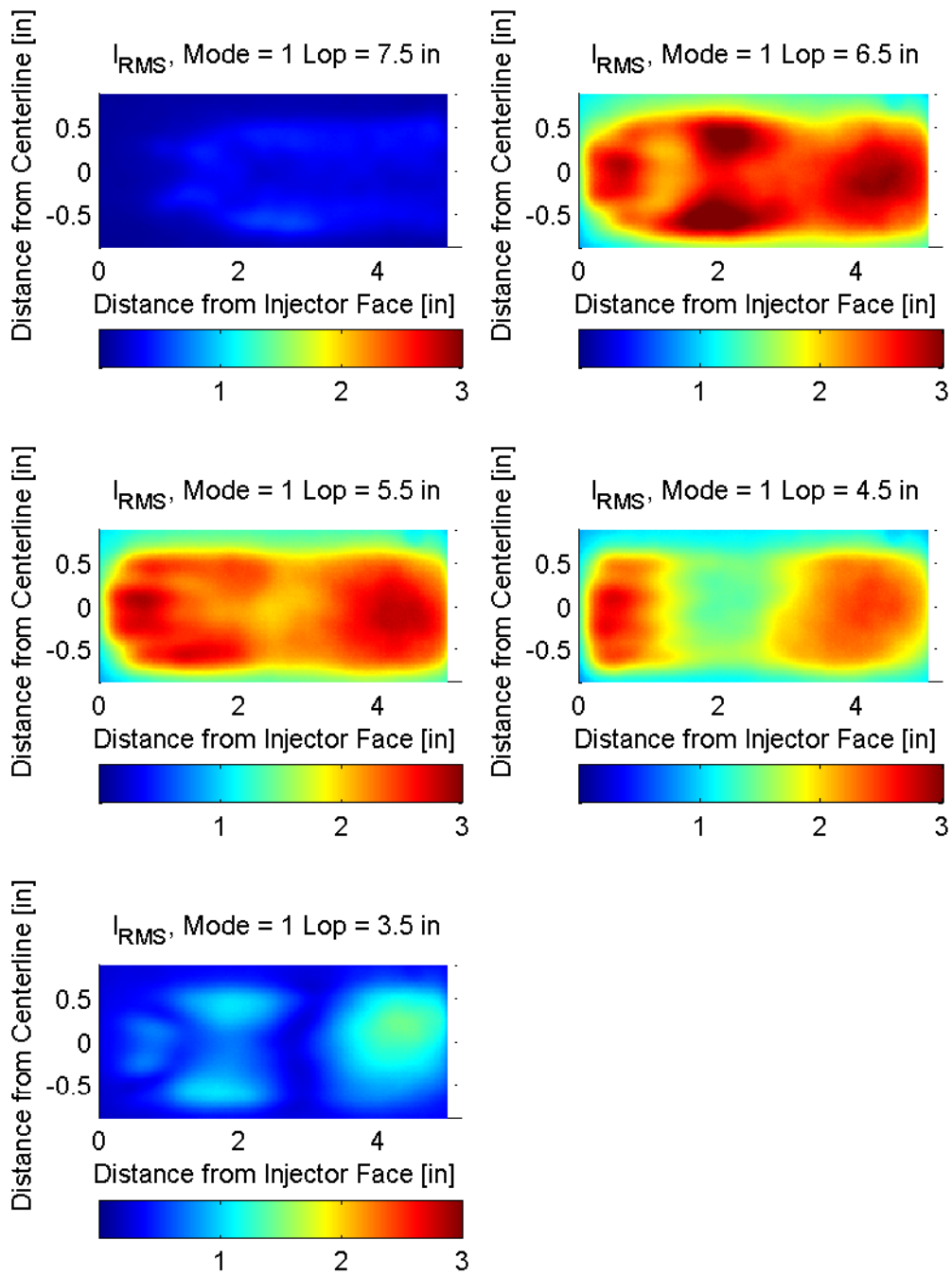

Figure 2.16. Test 2.2 1st mode band-pass filtered RMS light intensity plots for various oxidizer post lengths. 80% hydrogen

3. Particle Interactions

3.1 Introduction

Metal additives are used to enhance the energy of solid propellants and are also given consideration for loading in liquid slurries for the same reason. Historically, micron-sized particles have been used for this application, but the recent large-scale manufacture of nano-sized particles by numerous vendors changes the extent of complete burning of Aluminum particles, the overall number of existing particles, and their average spacing dramatically. For this reason, collision process that may have been neglected in the past could be of significant importance in these flows. In case of aluminum loaded solid propellants, Gany et al. [1] have experimentally investigate the Al/Al_2O_3 agglomerates forming on the propellant surface and observed large agglomerates, a mean of about 250 μm, consisting of thousands or millions of unburned aluminum particles when a propellant contains 6 μm aluminum particles. More recently, Najjar et al. [2] have referred to Sabnis et al. [3] and indicated that the typical values of the drop size distribution entering the combustion chamber are a mean of 150 μm for larger unburned Aluminum particle and 1.5 μm for smaller Aluminum Oxide particle, which is bimodal. Upon complete combustion of Aluminum particles in smaller motor, Cheung and Cohen [4] observed the particle from an order of hundred nanos to an order of microns depending on Aluminum particle loads in propellant. Thus, Nano-aluminum loaded solid propellants exhibit significantly different agglomeration near the surface and thus the size of agglomerates leaving the burning surface can be smaller than normal cases containing unburned large Aluminum particles. Much less is known about the potential for agglomeration of particle loaded liquid slurries/gels, but regions of high shear that are present due to mixing processes could presumable provide substantial opportunities for agglomeration to occur.

A simple analysis of the particle to particle distance in rocket chamber can show the substantial opportunities for agglomeration due to collision of particles. As Najjar et al. [2] have indicated that the burning of 20% aluminum loaded propellant of solid rocket booster results in approximately 10^{15} droplets of a mean diameter of 100 μm in a core volume of 63 m^3. Following Friedlander [5], the average center-to-center distance between two adjacent particles distributed randomly is given by $0.55396N_\infty^{-1/3}$ where N_∞ is a number density of particles. Given the number

density using the data of Najjar et al. (N_∞=number of droplets/contained volume), the average distance between two adjacent particles is approximately 22 μm. Considering the droplets of an order of microns, and that the overall distance traveled is of the order of 10's of meters, it is inevitable that collisions will occur.

Based on previous researches [4, 6, 7, and 52], the particle size variation in rocket chamber and nozzle can be idealized. The particles in combustion chamber grow by oxidation/condensation processes due to combustion process in combustion chamber. While the particles passing through the subsonic convergent section of nozzle, the particles experience the growth due to collision between particles. After the throat, particles experience significant velocity lags in accelerating flow field, they experience the reduction due to breakage due to aerodynamic force acting on particles. We have observed very similar results from our simulations with this idealized concept, and computation results are provided in the later section.

The past studies of two phase flow inside the rocket chamber have focused on the effects of the droplet on the gas flow by two-way coupling [2, 8, and 9] and the effects of the gas flow on the particle phase by one-way coupling [9]. However, none of these studies have been focusing on the effects of the collision and breakup of the droplets and consequent drop size change. Although Najjar et al. [2] have included the collision effects in assessing the drop mass variation, the collision efficiency in their model is simply set as a constant, 0.25. Other past studies considering particle size variation are limited by considering only collision process (no breakup effects) [7 and 52] or 1-D process [7, 11, and 52].

The flow in a large rocket chamber can experience highly shearing motion due to its mean velocity change and highly turbulent motion at the same time. The high Reynolds number and the complex geometry of solid rocket chamber leads to the locally complex flow motion and two adjacent particles can be easily intercepted by the turbulent motion of flow. In addition, the highly shearing motion of mean flow near boundary layer can result in collision/breakup. Thereby, stochastic collision and breakup events can be one of the governing mechanisms of the particle to particle interaction in a rocket chamber and collision and breakup due to mean flow motion can be another governing mechanism.

The coalescence and breakup process of drops [12 and 13] and bubbles [14] have been investigated in the chemistry and chemical engineering communities. The modeling of coalescence and breakup processes in an agitated vessel has been important topic in chemistry to

assess the mixing effects. Their interests are usually limited only by the turbulent viscous effect in a low turbulence case. Unlike the two immisicible liquids in an agitated vessel, the drops in a combustion chamber are exposed to a highly turbulent flow and consequent inertial effects of the drops induced by larger density of particles than the surrounding gas are important. These factors lead to difficulties in using coalescence and breakup models developed in chemistry but these models can be a good starting point in current modeling.

Thus, the stochastic collision and breakup are addressed here and the collision/breakup in laminar flow and combination of the mean flow effects and turbulent flow effects are discussed too. We divide the collision and breakup mechanisms into four regimes and each regime is modeled: laminar hydrodynamic collision/breakup, laminar aerodynamic collision/breakup, turbulent hydrodynamic collision/breakup, and turbulent aerodynamic collision/breakup. Here, the term, hydrodynamic, means the shearing motion of surrounding fluid is the main source for collision and breakup and the term, aerodynamic, means the velocity difference between the particle and the surrounding fluid is the main source for collision and breakup.

Along with the collision/breakup models, to assess the particle phase velocity field while holding the reasonable computational efficiency, an Eulerian-Fast (or Equilibrium) Eulerian two-phase methodology is chosen and the direct quadrature method moment (DQMOM) approximation is applied to the population balance equation (PBE) is used to model the coalescence and breakup.

The objective of the current study is to develop models for the collision and breakup processes applicable to a simulation of the two phase flow in a rocket nozzle and carry a test simulation in a typical rocket converging-diverging nozzle. For this purpose, MMD (Mass Mean Diameter) was predicted according to different droplet characteristics and pressure at nozzle inlet and the scales of nozzle. To validate the models, the predicted results were compared to experimental data at the nozzle exit plane. The results were reasonably agreed with the empirical correlation. The simulation was very sensitive with the initial droplet condition (i.e. mean diameter and standard deviation of number distribution), therefore, the initial conditions of droplets should be chosen very carefully.

3.2 Physical Modeling

3.2.1 Gas Flow field description – Navier-Stokes equation

The 2-D unsteady Navier-Stokes equations for the Newtonian viscous carrier fluid are applicable under the continuum condition. The flow field is described by mass, momentum and energy conservation laws complemented by an appropriate equation of state and additional constitutive relations. Two turbulence equation from the $k - \omega$ model of Wilcox [15] are added to the conservation form of the Navier-Stokes equations without any body forces and source terms induce by the particle phase. The gas phase governing equations is solved under the platform of Generalized Equation and Mesh Solver (GEMS) code [16], which uses contemporary numerical methods to solve coupled systems of partial differential equations.

3.2.2 Particle phase modeling – Population Balance Equation (PBE)

3.2.2.1 QMOM (Quadrature Methods of Moments)

The advection-diffusion equation for the number density field is given by

$$\frac{\partial n}{\partial t} + \nabla \cdot \left(\vec{U}_p n \right) = \nabla \cdot \left(D_s \nabla n \right) + S \tag{3.1}$$

where n is is the particle number density, D_s is the diffusion coefficient, and S is the source term corresponding to coagulation and breakup. In a high Reynolds number or shearing flow, the diffusion term can be ignored and the advection-diffusion equation becomes a form similar to Smoulchowski's equation [25] which is usually referred as the population balance equation.

Using a one-way coupling approach, no mass, momentum, and energy interchange is considered. The particle phase is also assumed to be in thermally equilibrium state. The equation constructing agglomeration/breakage models for the dispersed phase is the population balance equation for the particle number density which is as follows [17]:

$$
\begin{aligned}
\frac{\partial n(v,t)}{\partial t} &+ \nabla \cdot \left(\vec{U} n(v,t) \right) \\
&= \frac{1}{2} \int_0^n a_1(v - v^*, v^*) a_2(v - v^*, v^*) b(v - v^*, v^*) n(v - v^*, t) n(v^*, t) dv^* \\
&\quad - \int_0^\infty a_1(v, v^*) a_2(v, v^*) b(v, v^*) n(v, t) n(v^*, t) dv^* \\
&\quad + \int_n^\infty a(v, v^*) b(v^*) n(v^*, t) dv^* - a(v) n(v, t)
\end{aligned}
\tag{3.2}
$$

This equation assumes the same velocity of particle phase as the surrounding fluid. This equation expresses the fact that there is break-up and coalescence of droplets in the flow in the absence of interactions with walls. The term $n(v,t)$ is the number density function of the particle volume v and $\vec{u}$ is the velocity of the carrier fluid velocity due to Stokesian particle assumption. Here, α_1 is the collision efficiency between particles with volume v and v, α_2 is the coalescence efficiency, β is the volume based collsion kernel that describes the frequency that particles of volume v and v^* collide, a is the fragment distribution function, and b is the volume-based breakage kernel that is the frequency of breakage of a particle of volume v [17]. The first term on the right-hand side represents the formation of volume v by collision and the second term represents the loss of the volume v by collision. The third term represents the formation of volume v by break-up and the last term represents the loss of volume v by break-up.

Solving this equation directly will require large computational power due to the presence of a large number of classes of particles. In addition, the source terms in the equation represent that the equations for each phase are highly coupled by each other. Therefore, the simplification of the governing equations is highly required. This can be achieved by QMOM (Quadrature Method of Moments) developed by Mcgraw [6] which is a powerful technique to determine the evolution of the lower-order moments of the distribution by a quadrature-based approximation. Wang et al. [17] have successfully applied this approach in Taylor Coutte flow, and Marchisio et al. [19] have showed that this approach leads to very small error comparing to discretized population balance equation (DPB). Wang et al. [17]'s length based QMOM approximation process of PBE is summarized here. The QMOM starts from defining the moments and taking quadrature approximation. The volume based moments are given by

$$m_k = \int_0^\infty n(v,t)v^k dv \approx \sum_{i=1}^N w_i v_i^k \tag{3.3}$$

The length based moments are given by

$$m_z' = \int_0^\infty n'(l,t)l^z dl \approx \sum_{i=1}^N w_i' l_i^z \qquad \text{where } l^3 = v,\ z = 3k \tag{3.4}$$

The term N is the order of the quadrature formula and v is the particle volume. Accordingly, m_0 is the total particle number density and m_1 is the total particle volume concentration (same as particle volume fraction). Applying the length-based definition of moments to the transport equation of the particle density gives (superscript $'$ is omitted here):

$$\frac{\partial m_z}{\partial t} + \nabla \cdot \vec{U} m_z = \bar{S}_{m,k}$$

$$\text{where } \bar{S}_{m,k} = \frac{1}{2} \sum_i w_i \sum_j \alpha_{ij}^* \alpha_{ij}^{**} \beta_{ij} w_j \left[\left(l_i^3 + l_j^3 \right)^{z/3} - l_i^z - l_j^z \right] + \sum_i a_i b_i w_i - \sum_i b_i w_i l_i^z \tag{3.5}$$

The collision efficiency is $\alpha_{ij}^* = \alpha_1(l_i, l_j)$, the coalescence efficiency is $\alpha_{ij}^{**} = \alpha_2(l_i, l_j)$, the collision frequency of drops of length l_i and l_j is $\beta_{ij} = \beta(l_i, l_j)$, the breakage frequency of drops of length l_i is $b_i = b(l_i)$, and the daughter drop probability density function is given by

$$a_i = 2^{(3-z)/3} l_i^z \tag{3.6}$$

for binary fragmentation.

The weights, w_i and abscissas, l_i are found via using of the product-difference (PD) algorithm. and PD algorithm is explained in Appendix A.

3.2.2.2 DQMOM (Direct Quadrature Methods of Moments)

When the particles have significantly larger density than the gaseous phase, a distribution over particle velocities and the slip between particle phase and the carrier fluid are needed to be considered. As discussed in Marchisio and Fox [23], QMOM loses the simplicity and efficiency due to the non-linear term involved in PD algorithm [23]. At the same time, the dependency of $U_{p,i}$ on l leads to a complex formation of quadrature approximated PBE. In order to address these issues, Marchisio and Fox [23] formulated Direct QMOM which directly tracks weights and abscissas instead of tracking moments and it is summarized here. The DQMOM is summarized here and more details on DQMOM can be found in Marchisio and Fox [23] and Madsen [24].

A multivariate number distribution function n depends on l, $U_{p,i}$, x_i, t which can be denoted as $n(l, U_{p,i}, x_i, t)$. For simplification, the dependency of variables on x_i and t is omitted from now on. In this case, the transport equation is given by

$$\frac{\partial}{\partial t} n\left(l, U_{p,i}\right) + \frac{\partial}{\partial x_i} \left\{ U_{p,i} n\left(l, U_{p,i}\right) \right\} + \frac{\partial}{\partial U_{p,i}} \left\{ \frac{dU_{p,i}}{dt} n\left(l, U_{p,i}\right) \right\} = S\left(l, U_{p,i}\right) \tag{3.7}$$

which was proposed by Williams [22] for the LHS. Now, $U_{p,i}$ depends on l and it will be $U_{p,i} = U_{p,i}(l)$. The term $dU_{p,i}/dt$ represents the drag force acting on the droplet. To reduce the number of variables, the averaged number distribution function is given by

$$n(l) = \int_{-\infty}^{\infty} n\left(l, U_{p,i}\right) dU_{p,i} \tag{3.8}$$

The averaged drop phase velocities can be given as follows:

$$U_i(l) = \frac{\int_{-\infty}^{\infty} U_i n(l, U_{p,i}) dU_{p,i}}{n(l)} \tag{3.9}$$

Integrating the equation (3.7) over the velocity assuming a Dirac delta function of velocity distribution yields the following PBE:

$$\frac{\partial}{\partial t} n(l) + \frac{\partial}{\partial x_i} \left(U_{p,i}(l) n(l) \right) = S(l) \tag{3.10}$$

which is the same formula as the equation (3.1). Following Marchisio and Fox [23], the particle size distribution function can be treated as a sum of Dirac delta functions:

$$n(l) = \sum_{q=1}^{N} w_q \delta \left[l - l_q \right] \tag{3.11}$$

Substituting the equation (3.11) into the equation (3.10) and integrating the equation (3.10) after multiplying l_q over the particle size l gives the following the PBE approximated by DQMOM:

$$\frac{\partial}{\partial t} w_q + \frac{\partial}{\partial x_i} \left(U_{p,i} w_q \right) = S_{w,q} \qquad q = 1, \ldots, N$$

$$\frac{\partial}{\partial t} \xi_q + \frac{\partial}{\partial x_i} \left(U_{p,i} \xi_q \right) = S_{\xi,q} \qquad q = 1, \ldots, N \tag{3.12}$$

where ξ_q is the weighted abscissas defined by $\xi_q = w_q l_q$. The source terms can be obtained by solving the following equation.

$$(1-k) \sum_{q=1}^{N} l_q^k S_{w,q} + k \sum_{q=1}^{N} l_q^{k-1} S_{\xi,q} = \overline{S}_{m,k} \qquad k = 0, \ldots, 2N-1 \tag{3.13}$$

where $\overline{S}_{m,k}$ is the source term obtained in QMOM case and it is given in the equation (3.7). The source terms, $S_{w,q}$ and $S_{\xi,q}$, can be obtained from the linear system $Ax=b$ which each matrix is defined as follows:

$$A = \begin{pmatrix} 1 & \cdots & 1 & 0 & \cdots & 0 \\ 0 & \cdots & 0 & 1 & \cdots & 1 \\ -l_1^2 & \cdots & -l_1^2 & 2l_1 & \cdots & 2l_N \\ \vdots & \ddots & \vdots & \vdots & \ddots & \vdots \\ 2(1-N)l_1^{2N-1} & \cdots & 2(1-N)l_N^{2N-1} & (2N-1)l_1^{2N-2} & \cdots & (2N-1)l_N^{2N-2} \end{pmatrix}$$

$$x = \begin{pmatrix} S_{w,1} \\ \vdots \\ S_{w,N} \\ S_{\xi,1} \\ \vdots \\ S_{\xi,N} \end{pmatrix} \qquad b = \begin{pmatrix} \overline{S}_{m,0} \\ \vdots \\ \overline{S}_{m,2N-1} \end{pmatrix}$$

(3.14)

By using the averaged drop phase velocities given in the equation (3.9), the monovariate population balance equation is formulated and it is now applicable to the case holding a highly slip motion between particle and carrier fluid phases. Therefore, DQMOM is used for the current simulations.

3.2.2.3 Fast Eulerian approach

The number of drops in a rocket chamber is typically dense enough to treat the particle phase as continua. Therefore, the particle phase can be described via an Eulerian approach for smaller particles. For more simplicity and numerical efficiency, a fast (or equilibrium) Eulerian approach [1, 2] is used, such that mass and momentum conservation are automatically satisfied and they are no longer need to be sloved. In this approach, the particle phase velocity is handled as a field variable assuming the particle velocities are in a dilute limits. which is given by

$$\vec{U}_{p,i} = \vec{U} - (1-g)\, t_i \frac{D\vec{U}}{Dt}$$

$$\text{where } \quad g = \frac{3r}{2r_p + r} \qquad t_i = \frac{(2r_p + r)R_i^2}{9m}$$

(3.15)

where $\vec{U}_p$ and $\vec{U}$ are the particle phase and gaseous phase velocity vectors, respectively. The term τ is the relaxation time of the particle, D/Dt is the material derivative in the Eulerian view, and γ is the density ratio which can be assumed to be zero for gas-liquid two phase system.

According to Ferry and Balachandar [2], the application of a fast Eulerian method is limited by small but finite-size particles. The validity is only limited to the particles which hold the

relaxation time τ that is less than the fluid time scale which is defined by the inverse of the maximum of absolute compressive strain. Typically, in the current simulation, mass mean diameters over the entire domain do not exceed 10 µm for supersonic nozzles and then the relaxation time is in the limit of the fast Eulerian assumption almost over the entire domain. The errors maybe confined to the particle inside the boundary layer which does not affect the integrated particle size on a chosen face, i.e, nozzle exit. Najjar et al. [1] have applied this formula to simulate two-phase flow within a supersonic nozzle attached to a SRM chamber for 5 µm smoke particles.

3.2.3 Stochastic collision modeling

3.2.3.1 Spherical formulation of collision kernel

Saffman and Turner [26] have studied the collision frequency kernel and presented two formulations of the collision kernel which are spherical formulation and cylindrical formulation. Comparing these two formulations, the collision kernel in cylindrical formulation is the cylindrical volume passing through the effective collision circle per unit time (in other words, the fluid volume flux across the effective collision area) and the collision kernel in spherical formulation is the volume of fluid across the collision sphere surface (volume flux across the collision sphere surface). The cylindrical formulation is possible in the special case of uniform shear flow which is same case with Smoulchowski [25] and the more general way will be the spherical formulation because the relative velocity between particles depends on the orientation of the collision radius R_c as it is described in Wang et al. [27].

The Saffman and Turner [26]'s spherical formulation is described in Figure 3.1. Considering two particles of radii R_i and R_j, the moving particle is the particle of radius R_j supposing the particle of radius R_i as a fixed central particle. Assuming there is no distortion of flow field due to the existence of the particle, the particle R_j are moving along the streamlines. Defining the collision sphere as a sphere of radius $R_c = R_i + R_j$ centered on the fixed central particle, the collision frequency of the fixed central particle is the flux of the fluid having the velocity which is same as the relative velocity between two particles, multiplied by the number density of the moving particles. This flux should be induced by the relative velocity which is inwardly normal to the collision sphere because this directional component of velocity is only the component

causing the collision. Denoting the unit vector outwardly normal to the collision sphere (radial direction of the collision sphere) as $\vec{n}_r$ and the relative velocity inwardly normal to the collision sphere as $\vec{W}$, the flux J_l across the collision sphere is given by

$$J_l = -\oint \vec{W} \times \vec{n}_r \ dA \qquad (3.16)$$

The negative sign is given because the dot product between this velocity vector and outward normal vector is negative. Supposing that the particles are distributed in the flow, the collision frequency N_c which is the total number of collision between particles of the number densities n_1 and n_2 in unit volume and unit time is given by

$$N_c = -n_1 n_2 \oint \vec{W} \times \vec{n}_r \ dA \qquad (3.17)$$

Thus, the collision frequency function (or collision kernel) β_l for the laminar flow is given by

$$b_l = J_l = -\oint \vec{W} \times \vec{n}_r \ dA \qquad (3.18)$$

where dA is the area element on the surface of a sphere.
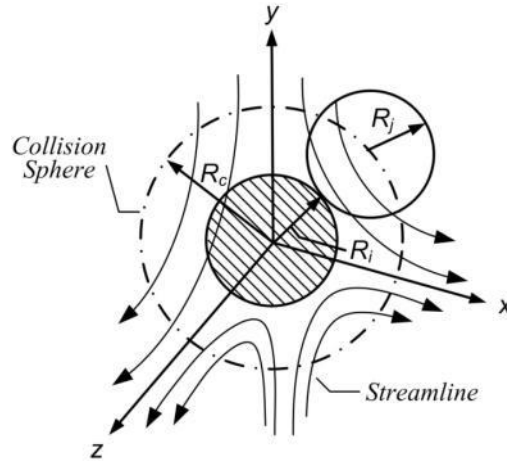
Figure 3.1 Schematic of collision of two droplets of radii R_i and R_j in Spherical formulation; the collision radius R_c is the sum of radii R_i and R_j, the relative motion follows the streamlines

Developing further for the turbulent flow, when the particles are randomly distributed and their fluctuating radial velocity component is w_r (sign of this component are not decided yet, the effect of its mean component $<W_r>$ is not considered), the mean flux J_t towards the collision sphere is given by

$$J_t = -\left\langle \oint_{w_r < 0} w_r \ dA \right\rangle \qquad (3.19)$$

Assuming the outward and inward fluxes across the collision sphere are equal, this assumption can be expressed by

$$- \oint_{w_r<0} w_r \, dA = \oint_{w_r>0} w_r \, dA \tag{3.20}$$

Thus, the mean flux J_t towards the collision sphere is given by

$$J_t = - \left\langle \oint_{w_r<0} w_r \, dA \right\rangle = \frac{1}{2} \oint \left\langle |w_r| \right\rangle \, dA \tag{3.21}$$

For isotropic turbulence, the collision kernel β_t is given by

$$b_t = 2\rho R_c^2 \left\langle |w_r| \right\rangle \tag{3.22}$$

which is the same form as Saffman and Turner [26]'s.

3.2.3.2 Collision frequency kernel in turbulent flow

Based on previous collision studies considering the classes of particle with energy cascade in turbulent flow, it is widely assumed that the particle which is much smaller than Kolmogorov's micro length scale has a well correlated velocity with the carrier fluid and the particle which is larger than the integral time scale has a less-correlated velocity with the carrier fluid. In these two limits, the widely used collision frequency results are given by Saffman and Turner [26] and Abrahmson [35], respectively. Supposing the widely distributed particles in turbulent flow, the particles corresponding to inertial subrange of turbulent flow may have a less correlated velocity than the particle in viscous subrange and more correlated velocity than the particle in energy containing eddy. Numerous authors [26,33,36, and 62] have assessed the collision mechanism in the inertial subrange and several models are available. The collision models from Williams and Crane [33] are employed here, which are considered as the first theory addressing the inertial collision on arbitrary particle sizes and added the shearing term from Saffman and Turner [26] to the total collision kernel.

The present study is focused on the collision (or coalescence) and breakup of two unequal spherical drops. Concerning the hydrodynamics between two drops, the assumption of two equal drops will make it easy to distinct which regime of turbulent flow can be applied on collision mechanism. Following Chesters [32], two unequal spherical drops can be characterized by two equal drops of equivalent radius, R_{eq}, which is given by

$$R_{eq} = \frac{2R_i R_j}{R_i + R_j} \qquad (3.23)$$

where R_i and R_j are radii of two unequal drops. When a drop of R_{eq} is smaller than Kolmogorov's length scale, the drop is considered as it is in the viscous subrange of turbulence and a drop larger than Kolmogorov's length scale is considered as it is in the inertial subrange. The Kolmogrov's length scale η is given by

$$\eta = \left(\frac{\nu^3}{\varepsilon}\right)^{1/4} \qquad (3.24)$$

where ν is the kinematic viscosity of the fluid.

3.2.3.2.1 Relative velocity between two drops

Before discussing the collision frequency function, it is convenient to consider the relative velocity between two colliding drops. In analogy with Williams and Crane [33], the relative velocity between two particles can be thought as it is induced by two major effects: the effect of velocity gradient of the carrier fluid between two particles and the effect of different inertial response of particles of different radius to the movement of carrier fluid. According to these considerations, the relative velocity between two particles can be constituted by the effects of velocity gradient and different inertial response. It is supposed that two droplets within the fluid have velocities $\vec{U}_{p,1}$ and $\vec{U}_{p,2}$ before they collide. The carrier fluid surrounding these drops have velocities $\vec{U}_1$ and $\vec{U}_2$. When the slip velocities between the particle and the carrier fluid are denoted by $\vec{Q}_1 = \vec{U}_{p,1} - \vec{U}_1$ and $\vec{Q}_2 = \vec{U}_{p,2} - \vec{U}_2$, the relative velocity vector $\vec{W} = \vec{U}_{p,2} - \vec{U}_{p,1}$ can be expressed:

$$\begin{aligned} \vec{W} &= \vec{W}_I + \vec{W}_S \\ &= \left(\vec{Q}_2 - \vec{Q}_1\right) + \left(\vec{U}_2 - \vec{U}_1\right) \end{aligned} \qquad (3.25)$$

The first term on RHS $\vec{W}_I$ represents the amount of velocity difference induced by inertial effects of large density particles and the second term $\vec{W}_S$ represents the velocity difference induced by the velocity gradient (or strain rate) of the carrier fluid.

Considering the collision of two particles of radius r_i and r_j, the responsible component of relative velocity to the collision is only the component in the direction of the centerline which

connects the center of two particles. Figure 3.2 illustrates which components of the relative velocity are related to the collision. Supposing the fixed central particle of radius r_j, the moving particle r_i has velocity $\vec{W}_I$ and $\vec{W}_S$ of which $\vec{W}_{I,r}$ and $\vec{W}_{S,r}$ makes two particles to approach each other whereas $\vec{W}_{I,t}$ and $\vec{W}_{S,t}$ cause movement away from the fixed central particle. Therefore, only the velocity components that induce approaching motion must be considered and the velocity components causing movement away must be neglected from the consideration.
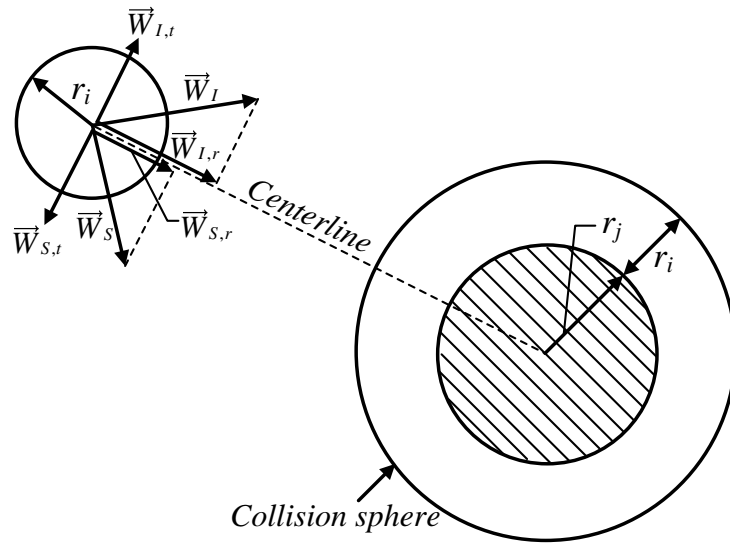

Figure 3.2 Schematic of components of relative velocity between two particles of radii r_i and r_j

Considering the turbulent flow, the mean square of the relative velocity is given by [26]

$$\left\langle \vec{w} \times \vec{w} \right\rangle = \left\langle \vec{w_I} \times \vec{w_I} \right\rangle + \left\langle \vec{w_S} \times \vec{w_S} \right\rangle \tag{3.26}$$

It is assumed that $\vec{w_S}$ is statistically independent of the slip velocities $\vec{q_1}$ and $\vec{q_2}$. Using the notation $\vec{w_S} = \left(w_{S,x}, w_{S,y}, w_{S,z} \right)$, the second term on the RHS is given by

$$\left\langle \vec{w_S} \times \vec{w_S} \right\rangle = \left\langle w_{S,x}^2 \right\rangle + \left\langle w_{S,y}^2 \right\rangle + \left\langle w_{S,z}^2 \right\rangle \tag{3.27}$$

Using the mean square of the velocity gradient in viscous subrange which is given by

$$\left\langle \left(\frac{\partial u}{\partial x} \right)^2 \right\rangle = \frac{1}{15} \frac{e}{v} \tag{3.28}$$

For isotropic turbulence, it has been shown that [63]

$$\left\langle u^2 \right\rangle = \left\langle u_x^2 \right\rangle = \left\langle u_y^2 \right\rangle = \left\langle u_z^2 \right\rangle$$
$$\left\langle \left(\frac{\partial u}{\partial x} \right)^2 \right\rangle = \frac{1}{2} \left\langle \left(\frac{\partial u}{\partial y} \right)^2 \right\rangle = \frac{1}{2} \left\langle \left(\frac{\partial u}{\partial z} \right)^2 \right\rangle \tag{3.29}$$

Thus,

$$\left\langle w_{S,x}^2 \right\rangle = R_c^2 \left\langle \left(\frac{\partial u}{\partial x} \right)^2 \right\rangle = \frac{R_c^2}{15} \frac{e}{v} \tag{3.30}$$

It follows that

$$\left\langle \vec{w_S} \times \vec{w_S} \right\rangle_{R_{eq} < h} = \frac{R_c^2}{3} \frac{e}{v} \tag{3.31}$$

This form is same as the velocity gradient term in the analysis of Saffman and Turner [26] considering the inertial effect together with the effect of velocity gradient term. For inertial subrange, the relative velocity between two colliding particles is given by [37]

$$\left\langle \vec{w_s} \times \vec{w_s} \right\rangle_{R_{eq} > h} = \left(1.37 \right)^2 \left(e R_c \right)^{2/3} \tag{3.32}$$

To evaluate the first inertial effect term $\left\langle \vec{w_I} \times \vec{w_I} \right\rangle$, it is assumed that the velocities of the carrier fluid near two adjacent particles are the same. This assumption is equivalent to the assumption of Saffman and Turner [26] which is used in evaluating the same term as the first inertial effect term of this paper. This assumption results in the assumption that the correlation

coefficient between $\vec{q}_1$ and $\vec{q}_2$ is unity where $\vec{q}_1$ and $\vec{q}_2$ are the fluctuating parts of the relative velocity between particle and its surrounding fluid of particle 1 and 2 respectively. Using the assumption, the first inertial effect term can be given by

$$\left\langle \vec{w}_I \times \vec{w}_I \right\rangle = \left\langle \left(\vec{u}_{p,2} - \vec{u}_{p,1} \right) \times \left(\vec{u}_{p,2} - \vec{u}_{p,1} \right) \right\rangle \tag{3.33}$$

Therefore, the i-direction mean square relative velocity between two particles, $\left\langle w_{I,i}^2 \right\rangle$ can be expressed:

$$\left\langle w_{I,i}^2 \right\rangle = \left\langle u_{p,1,i}^2 \right\rangle + \left\langle u_{p,2,i}^2 \right\rangle - 2\left\langle u_{p,1,i} u_{p,2,i} \right\rangle \tag{3.34}$$

This equation is the starting point of Williams and Crane [29]'s analysis of the fluctuating relative motion of two particles induced by slip motion between the particle and fluid. Saffman and Turner [26] also have derived the mean square of the relative velocity $\langle w \cdot w \rangle$ considering the effects of velocity gradient and the inertial effect in viscous subrange. However, in fundamental assumption of their approach, the relaxation time is smaller than the time scale of smallest eddy. So, the term for the inertial effect cannot be used in our case. Instead, Williams and Crane [29] have derived the term of inertial effect for the small drops which is not limited by the small relaxation time. In Williams and Crane [29]'s analysis, the particle motion is described by the simplified Tchen [34]'s force balance equation ignoring the added mass, Basset history, and gravitational acceleration terms:

$$\frac{du_{p,i}}{dt} + \frac{u_{p,i}}{\blacklozenge} = \frac{3r_g}{\left(2r_p + r_g\right)} \frac{du_i}{dt} + \frac{u_i}{\blacklozenge} \quad where \; \blacklozenge = \frac{\left(2r_p + r_g\right)r^2}{9m} \tag{3.35}$$

where u_i and $u_{p,i}$ are the fluctuating parts of the fluid and particle velocities in i-direction, ρ_g and ρ_p are the densities of the fluid and particle, and τ is the relaxation time of the particle of radius r. Stoke's drag law is applied here assuming the size of the particle is small enough. For $\rho_p \gg \rho_g$, the first term on RHS can be neglected. In analogy with Levins and Glastonbury [56], using a more accurate form of the wave-number spectrum which includes the influence of turbulence within the viscous subrange, the mean square of the particle velocity is obtained by Williams and Crane as follows:

$$\left\langle u_{p,i}^2 \right\rangle = \left\langle u_i^2 \right\rangle \frac{g}{g-1}\left[\frac{1}{1+q} - \frac{1}{\left(1+gq\right)g}\right]$$

$$\text{where} \quad q = \frac{t}{T_L} \qquad T_L = \frac{L_f}{\left\langle u^2 \right\rangle^{1/2}} \qquad g = 2\left(\frac{L_f}{\lambda}\right)^2 \qquad \lambda = \left\langle u^2 \right\rangle^{1/2}\left(\frac{15\nu}{\varepsilon}\right)^{1/2} \qquad \left\langle u_i^2 \right\rangle = \frac{2}{3}k \tag{3.36}$$

The mean square fluctuating velocity $\left\langle u^2 \right\rangle$ is given in terms of turbulent kinetic energy k assuming isotropic turbulence. The θ is the non-dimensional relaxation time of drop of radius r, τ is the particle relaxation time, and L_f is the longitudinal integral length scale which is approximated by $0.5L$ where L is the integral length scale of the largest energy-containing eddy approximated by $k^{1/2}/(B^*\omega)$ in $k-\omega$ model. Finally, λ is the Taylor's microscale length.

Starting from Panchev [64]'s integrated form of Tchen's equation of motion, Williams and Crane derived the covariance $\left\langle u_{p,1,i} u_{p,2,i} \right\rangle$ using the more accurate wavenumber spectrum for the small particles which satisfies the condition $\theta \ll 1$ (which imposes that the particle is in viscous subrange). Thus, using the mean square particle velocity and the covariance terms, the i-direction mean square relative velocity between two particles $\left\langle w_{I,i}^2 \right\rangle$ for viscous subrange can be expressed:

$$\left\langle w_{I,i}^2 \right\rangle_{R_{eq}<\eta} = \left\langle u_i^2 \right\rangle \frac{\gamma}{\gamma-1} \frac{(\theta_i - \theta_j)^2}{\theta_i + \theta_j} \left\{ \frac{1}{(1+\theta_i)(1+\theta_j)} - \frac{1}{(1+\gamma\theta_i)(1+\gamma\theta_j)} \right\} \tag{3.37}$$

For large particles which satisfy the condition $\theta \gg 1$ (which imposes the particle is in energy containing region), it was shown that:

$$\left\langle w_{I,i}^2 \right\rangle_{R_{eq}>L} = \left\langle u_i^2 \right\rangle \left[\frac{1}{(1+\theta_i)} + \frac{1}{(1+\theta_j)} - \frac{4}{\left\{\theta_i + \theta_j + \theta_i\theta_j\left(\frac{1}{(1+\theta_i)} + \frac{1}{(1+\theta_j)}\right)\right\}^{1/2}} \right] \tag{3.38}$$

They have successfully showed that the mean square relative velocity for viscous subrange goes to Saffman and Turner [26]'s inertial term at lower-limit of small relaxation time and the mean square relative velocity for energy containing region goes to Abrahamson [35]'s term at higher-limit of large particle size. They also derived the universal solution of the mean square relative velocity which can be used in inertial subrange, it is given by:

$$\left\langle w_{I,i}^2 \right\rangle_{\eta < R_{eq} < L} = \left\langle u_i^2 \right\rangle \frac{(\theta_i + \theta_j)^2 - 4\theta_i\theta_j \sqrt{\dfrac{1+\theta_i+\theta_j}{(1+\theta_i)(1+\theta_j)}}}{(\theta_i + \theta_j)(1+\theta_i)(1+\theta_j)} \tag{3.39}$$

The universal solution of Williams and Crane approaches Abrahamson [35]'s mean square relative velocity for energy-containing range at higher-limit. It should be noted here that their universal solution does not approach Saffman and Turner's inertial term as it is explained in Kuris and Kusters [36]. However, the divergence for very small particle is appreciable as it is shown by Williams and Crane [33].

Finally, the mean square relative velocity induced by different inertial response, $\left\langle \vec{w_I} \times \vec{w_I} \right\rangle$, can be calculated assuming the mean square relative velocities are same in an arbitrary direction which implies $\left\langle w_{I,x}^2 \right\rangle = \left\langle w_{I,y}^2 \right\rangle = \left\langle w_{I,z}^2 \right\rangle$. Saffman and Turner [26] have shown that only the small error is introduced in the collision frequency due to this anomaly. In isotropic turbulence, the mean square relative velocity for the viscous subrange is given by:

$$\left\langle \vec{w_I} \times \vec{w_I} \right\rangle_{R_{eq} < \eta} = 2k \frac{g}{g-1} \frac{(q_i - q_j)^2}{q_i + q_j} \left[\frac{1}{(1+q_i)(1+q_j)} - \frac{1}{(1+gq_i)(1+gq_j)} \right] \tag{3.40}$$

The mean square relative velocity for the inertial subrange is given by:

$$\left\langle \vec{w_I} \times \vec{w_I} \right\rangle_{R_{eq} > \eta} = 2k \frac{(q_i + q_j)^2 - 4q_iq_j \sqrt{\dfrac{1+q_i+q_j}{(1+q_i)(1+q_j)}}}{(q_i + q_j)(1+q_i)(1+q_j)} \tag{3.41}$$

Accordingly, the mean square relative velocity $\left\langle \vec{w} \times \vec{w} \right\rangle$ can be obtained using the equations given above for $\left\langle \vec{w_I} \times \vec{w_I} \right\rangle$ and $\left\langle \vec{w_s} \times \vec{w_s} \right\rangle$.

3.2.3.2.2 Collision frequency function

The collisions are likely to be dependent on the relative motion between two particles. The mechanisms considered for the collisions are the shear mechanism and the accelerating (inertia) mechanism. The shear mechanism is due to the relative motion induced by the viscous force inside the turbulent eddy. The accelerating mechanism is due to the relative motion induced by inertial effects between the drop and suspending fluid. The most widely used collision frequency model considering the shear mechanism only is the Saffman and Turner [26]'s model in viscous

subrange. Assuming that x-axis is aligned with radial direction ($\langle w_{S,r}^2 \rangle = \langle w_{S,x}^2 \rangle$) and $w_{S,r}$ is normally distributed ($\langle |w_{S,r}| \rangle = (2/\pi)^{1/2} \langle w_{S,r}^2 \rangle^{1/2}$), the shearing collision frequency function for turbulent flow in viscous subrange is given as follows using equations (3.22) and (3.30):

$$\beta_{t,S}^{v} = \left(\frac{8\pi}{15}\right)^{1/2} R_c^3 \left(\frac{\varepsilon}{\nu}\right)^{1/2} \tag{3.42}$$

This form is same as the collision frequency function in the analysis of Saffman and Turner [26].

For inertial subrange, the shearing collision frequency function for turbulent flow in inertial subrange is given by using equations (3.22) and (3.32):

$$\beta_{t,S}^{i} = 1.37 (8\pi)^{1/2} R_c^{7/3} (\varepsilon)^{1/3} \tag{3.43}$$

Saffman and Turner [26] have also derived the collision frequency including the accelerating mechanism. However, as explained in the previous section, it is assumed that the time scale of each drop is smaller than the Kolmogorov's time scale (time scale of the smallest eddy) fundamentally and this is not matched with the aluminum drops in the combustion chamber due to $\rho_p \gg \rho_g$. Instead, the collision kernel is modified to include Williams and Crane [33]'s result for small drops which is given in the previous chapter.

Using the equations (3.26), (3.40), and (3.42), the mean square relative velocity for viscous subrange is given as follows:

$$\langle \vec{w} \times \vec{w} \rangle_{R_{eq}<h} = \langle \vec{w_I} \times \vec{w_I} \rangle_{R_{eq}<h} + \langle \vec{w_S} \times \vec{w_S} \rangle_{R_{eq}<h}$$
$$= 2k \frac{g}{g-1} \frac{(q_i - q_j)^2}{q_i + q_j} \left[\frac{1}{(1+q_i)(1+q_j)} - \frac{1}{(1+gq_i)(1+gq_j)} \right] + \frac{R_c^2}{3} \frac{\varepsilon}{\nu} \tag{3.44}$$

The mean value of radial relative velocity $\langle |w_r| \rangle$ is independent of the orientation of radial direction in isotropic turbulence. In analogy with Saffman and Turner [26], it is assumed that w_r is aligned with the x-axis so that $\langle |w_r| \rangle = \langle |w_x| \rangle$. Assuming the mean square relative velocities are same in an arbitrary direction which implies $\langle w_x^2 \rangle = \langle w_y^2 \rangle = \langle w_z^2 \rangle$. Again, this anomaly leads to only small error as discussed in the previous chapter. Thus, multiplying the equation (3.44) by 1/3, the mean square relative velocity in radial direction is given by:

$$\langle w_r^2 \rangle_{R_{eq}<h} = \frac{2}{3} k \frac{g}{g-1} \frac{(q_i - q_j)^2}{q_i + q_j} \left[\frac{1}{(1+q_i)(1+q_j)} - \frac{1}{(1+gq_i)(1+gq_j)} \right] + \frac{R_c^2}{9} \frac{\varepsilon}{\nu} \tag{3.45}$$

In analogy with Williams and Crane [33], it is assumed that the relative velocity in radial direction spreads by a Gaussian distribution. Thus, the mean of absolute relative velocity is the first order moments of $|w_r|$ which is given by

$$\langle |w_r| \rangle = \int_{-\infty}^{\infty} |w_r| P(w_r) d(w_r)$$
$$= \left(\frac{2}{\pi}\right)^{1/2} \langle w_r^2 \rangle^{1/2}$$

(3.46)

Accordingly, using the equations (3.22), (3.45), and (3.46), the collision frequency function for the viscous subrange is given by:

$$\beta_{t,ij,R_{eq}<\eta}\left(R_i,R_j\right)$$
$$= (8\pi)^{1/2} R_c^2 \left[\frac{2}{3} k \frac{\gamma}{\gamma-1} \frac{(\theta_i - \theta_j)^2}{\theta_i + \theta_j} \left\{ \frac{1}{(1+\theta_i)(1+\theta_j)} - \frac{1}{(1+\gamma\theta_i)(1+\gamma\theta_j)} \right\} + \frac{1}{9} R_c^2 \frac{\varepsilon}{v} \right]^{1/2}$$

(3.47)

The same discrepancy as Saffman and Turner [26]'s two models is observed. When the drops are identical (inertial effects of two adjacent drops confined in the smallest eddy are same), the constant becomes 1.671 whereas the constant in the model concerned the shear mechanism only is 1.294. This discrepancy is caused by the different approximation in defining isotropy as explained by Saffman and Turner and the error is considered as small [26].

For inertial subrange, including the effect of velocity gradient in inertial subrange, the mean square relative velocity in radial direction and the collision frequency function for the inertial subrange are given as follows using the equations (3.22), (3.48), and (3.46):

$$\langle w_r^2 \rangle_{R_{eq}>\eta} = \frac{2}{3} k \frac{(\theta_i + \theta_j)^2 - 4\theta_i\theta_j \sqrt{\dfrac{1+\theta_i+\theta_j}{(1+\theta_i)(1+\theta_j)}}}{(\theta_i + \theta_j)(1+\theta_i)(1+\theta_j)} + 1.37^2 R_c^{2/3} \varepsilon^{2/3}$$

(3.48)

$$\beta_{t,ij,R_{eq}>\eta}\left(R_i,R_j\right) = (8\pi)^{1/2} R_c^2 \left[\frac{2}{3} k \frac{(\theta_i + \theta_j)^2 - 4\theta_i\theta_j \sqrt{\dfrac{1+\theta_i+\theta_j}{(1+\theta_i)(1+\theta_j)}}}{(\theta_i + \theta_j)(1+\theta_i)(1+\theta_j)} + 1.37^2 R_c^{2/3} \varepsilon^{2/3} \right]^{1/2}$$

(3.49)

3.2.3.3 Collision frequency kernel in Laminar flow

As the drops in a combustion chamber are accelerated in nozzles, large inertial forces are induced by larger density of particles and the surrounding gas. The high speed (high Reynolds

number) motion of the carrier fluid creates a significant deformation of fluid element. The resultant contraction and dilatation of fluid element due to compressible effects can affect collision rates. Accordingly, the previous shearing collision rate studies [25, 30, and 65] which are based on incompressible laminar flow are not appropriate to assess the collision mechanism in these high Reynolds number flows. Therefore, the hydrodynamic (shearing) and aerodynamic (inertial) collision frequency functions are derived for spherical particles with motivation to high-speed flows where compressibility effects are present. The results and comparisons with other collision mechanisms are presented in Appendix B.

3.2.4 Stochastic breakup modeling

The possible breakup mechanisms which occur in current simulation are shearing and inertial breakups. The shearing breakup mechanism is first considered by Taylor [41]. When a droplet is surrounded by viscous fluid having a strong velocity gradient around the droplet, the breakup is mainly driven by the shearing force exerting on the droplet surface by the velocity gradient. If the viscous force (shearing force) is large enough to overcome the interfacial surface tension, the splitting of the droplet is likely to occur. The inertial breakup mechanism is mainly governed by the relative motion between the particle and its surrounding gas causing non-uniform pressure on the surface. The external forces deform the shape of the droplet and then the droplet disintegrates if these external forces exceed the surface tension force acting on the droplet.

The hydrodynamic stress on a droplet surface due to the viscous force can be characterized by Capillary number, Ca, which is the ratio of the stress due to the continuous phase velocity gradient to the stress on the droplet surface. The Capillary number is usually used in the analysis of the viscous force acting on the drop without the inertial force. The breakup can be thought as it is occurred when the Capillary number exceeds the critical Capillary number Ca_{crit} [41]. The critical Capillary number depends on the flow type and the viscosity ratio between a drop and suspension flow μ_p/μ [43].

Similarly, the drag force acting on a droplet due to the slip between a particle and surrounding gas can be characterized by Weber number, We, which is the ratio of the fluid inertia to the surface tension. The aerodynamic breakup occurs when the droplet Weber number is larger than the critical Weber number. In other words, the slip between particle phase and the

carrier gas will result in the inertial forces on droplets that may lead to breakup. The definitions of Capillary and Weber number are given in later section.

3.2.4.1 Hydrodynamic (shearing) breakup frequency function in turbulent flow

The viscous shear forces in a turbulent suspension acts on the droplet surface and results in the velocity gradient. This velocity gradient leads to deform the droplet surface and the breakup of the drop may occur [42 and 48]. Considering the hydrodynamic stresses as a source of the breakup, Delichatsios and Probstein [49] have derived the breakup frequency in the inertial subrange. They have used the approximation of the probability density distribution of the velocity difference, $\Delta u_S(D_i) = |\vec{u}_1 - \vec{u}_2|$, which denotes the amount of velocity difference between point 1 and 2 across the drop of diameter D_i. The probability density is approximated to Gaussian distribution with the variance $\langle (\Delta u_S)^2 \rangle$ and cut-off velocity $\Delta u_{S,C}$. The breakup of a droplet occurs when the velocity difference exceeds its critical value $\Delta u_{S,crit}$. The breakup frequency function (breakup frequency kernel) $b_{t,S}(R_i)$ of the droplet of radius R_i and the distribution function are given by

$$b_{t,S,R_i>h}(R_i) = \frac{\langle (Du_S)^2 \rangle}{R_i} P(Du_{S,crit})$$

$$\text{where} \quad P(Du_S) = \frac{1}{\sqrt{2\rho s_v}} \left[\exp\left\{ -\frac{(Du_S)^2}{2s_v^2} \right\} - \exp\left\{ -\frac{(Du_{S,c})^2}{2s_v^2} \right\} \right]$$

(3.50)

respectively. In their model, the variance σ_v^2 and the cut-off velocity is given by

$$\sigma_v^2 = \langle (\Delta u_S)^2 \rangle = (1.37)^2 (2\varepsilon R_i)^{2/3}$$

(3.51)

$$\Delta u_{S,c} = 3\langle (\Delta u_S)^2 \rangle^{1/2} = 3\sigma_v$$

(3.52)

respectively. Regardless of the direction of velocity difference acting on a droplet, all of the velocity differences can be responsible for the breakup. Thus, the estimation of the velocity difference $Du_S(D_i) = |\vec{u}_1 - \vec{u}_2|$ is done in the way of finding the first order moment of $\Delta u_S(D_i)$ instead of using the root-mean-square of the velocity difference. Assuming that the relative velocity across the drop of diameter D_i, $(\vec{u}_1 - \vec{u}_2) \times \vec{n}$, spreads by the exact Gaussian distribution

(no term of the cut-off velocity, in analogy with Williams and Crane [33]), the velocity difference is given by

$$\Delta u_S = 1.37 \left(\frac{2}{\pi} \right)^{1/2} (2 \varepsilon R_i)^{1/3} \qquad (3.53)$$

Therefore, applying the above equation into the given distribution function, the breakup frequency for inertial subrange is expressed by

$$b_{t,S,R_i > \eta}(R_i) = 1.37(2)^{1/3} (2\pi)^{-1/2} \left(\frac{\varepsilon}{R_i^2} \right)^{1/3} \left[\exp\left\{ -\frac{1}{\pi} \left(\frac{\varepsilon_{crit}}{\varepsilon} \right)^{2/3} \right\} - \exp\left(-\frac{9}{2} \right) \right] \qquad (3.54)$$

It should be note that the probability distribution $P(\Delta u)$ is negative when $\varepsilon_{crit}/\varepsilon$ is smaller than 53.154 due to the existence of the term of the cut-off velocity. Thus, the breakup frequency is set to zero in this limit.

Kusters [55] have derived the breakup frequency by assuming that the velocity difference $\Delta u_S (D_i) = |\vec{u}_1 - \vec{u}_2|$ across the drop of diameter D_i follows the exact Gaussian distribution for the viscous and inertial subrange (in analogy with Saffman and Turner [26] and Williams and Crane [33]). His work has started from the same formula of the breakup frequency given by Delichatsios and Probstein [49] except the assumption of the probability distribution. Kusters [55]'s approach is used and the breakup frequency in viscous subrange is given by:

$$b_{t,S,R_i < h}(R_i) = \frac{\left\langle (Du_S)^2 \right\rangle}{R_i} \frac{1}{\sqrt{2 \rho} S_v} \exp\left[-\frac{(Du_{S,crit})^2}{2 S_v^2} \right] \qquad (3.55)$$

The variance σ_v^2 and the first order moment of Δu_S assuming Gaussian distribution of $\left(\vec{u}_1 - \vec{u}_2 \right) \times \vec{n}$ are given by

$$\sigma_v^2 = \left\langle (\Delta u_S)^2 \right\rangle = \frac{4}{3} \frac{\varepsilon}{v} R_i^2 \qquad (3.56)$$

$$\Delta u_S = \left(\frac{8}{3\pi} \right)^{1/2} \left(\frac{\varepsilon}{v} \right)^{1/2} R_i \qquad (3.57)$$

Therefore, the breakup frequency for viscous subrange is given by

$$b_{t,S,R_i < \eta}(R_i) = \left(\frac{2}{3\pi} \right)^{1/2} \left(\frac{\varepsilon}{\nu} \right)^{1/2} \exp\left(-\frac{1}{\pi} \frac{\varepsilon_{crit}}{\varepsilon} \right) \qquad (3.58)$$

The classical definition of the capillary number on a droplet radius R_i is given by $Ca = \mu G R_i / \sigma$ [42] where μ is the suspension flow viscosity, G is the velocity gradient, and σ is

the surface tension. According to the definition of the capillary number on a droplet radius R_i, the critical velocity gradient is given by

$$G_{crit} = \frac{\mu Ca_{crit} R_i}{\sigma} \quad (3.59)$$

The velocity gradients induced only by the viscous force, $G = \Delta u_S / 2R_i$, in viscous and inertial subrange are given by

$$G_{R_i < \eta} = \left(\frac{2}{3\pi} \frac{\varepsilon}{\nu} \right)^{1/2} \quad (3.60)$$

$$G_{R_i > \eta} = 1.37 \left(\frac{1}{2\pi} \right)^{1/2} \left(\frac{2\varepsilon}{R_i^2} \right)^{1/3} \quad (3.61)$$

Therefore, the critical energy dissipation rate corresponding to the critical Capillary number in viscous and inertial subrange is given by

$$\varepsilon_{crit, \, R_i < \eta} = \frac{3\pi}{2} \nu \left(\frac{\sigma Ca_{crit}}{\mu} \right)^2 R_i^{-2} \quad (3.62)$$

$$\varepsilon_{crit, \, R_i > \eta} = \frac{1}{2} \frac{(2\pi)^{3/2}}{1.37^3} \left(\frac{\sigma Ca_{crit}}{\mu} \right)^3 R_i^{-1} \quad (3.63)$$

Accordingly, the hydrodynamic breakup frequencies in viscous subrange using equations (3.58) and (3.62) and inertial subrange using equations (3.54) and (3.63) are given by

$$b_{t,S,R_i < \eta}(R_i) = \left(\frac{2}{3\pi} \right)^{1/2} \left(\frac{\varepsilon}{\nu} \right)^{1/2} \exp\left[-\frac{3}{2} \frac{\nu}{\varepsilon} \left(\frac{\sigma Ca_{crit}}{\mu} \right)^2 R_i^{-2} \right] \quad (3.64)$$

$$b_{t,S,R_i > \eta}(R_i) = 1.37(2)^{1/3} (2\pi)^{-1/2} \left(\frac{\varepsilon}{R_i^2} \right)^{1/3} \left[\exp\left\{ -\frac{2^{1/3}}{1.37^2} \frac{1}{\varepsilon^{2/3}} \left(\frac{\sigma Ca_{crit}}{\mu} \right)^2 R_i^{-2/3} \right\} - \exp\left(-\frac{9}{2} \right) \right] \quad (3.65)$$

Due to the lack of experimental data, the critical Capillary number is obtained from the results of immiscible fluids experiment in a simple shear flow. Cristini et al. [45]'s numerical result gives that the critical Capillary number is approximately 0.46 at the 1.3 viscosity ratio which approximates the condition inside the combustion chamber.

3.2.4.2 Aerodynamic (inertial) breakup frequency function in turbulent flow

The breakup mechanism of liquid drops in a gas suspension is usually characterized by the aerodynamic forces (or inertial forces) based on the relative velocity between the gas and droplet.

The non-dimensional parameters used in the breakup due to aerodynamic forces are the Weber number and Ohnesorge number given as follows:

$$We = \frac{\rho \Delta u_I^2 D_i}{\sigma} \tag{3.66}$$

$$Oh = \frac{\mu_p}{\sqrt{\rho_p D_i \sigma}} \tag{3.67}$$

which are the Weber number and Ohnesorge number for a droplet of diameter D_i. The term ρ is the gas density, $\Delta u_I = \left| \vec{u} - \vec{u}_{p,i} \right|$ is the velocity difference between the droplet i and its surrounding gas (slip velocity), and μ_p is the viscosity of the liquid droplet. The Ohnesorge number is the relative importance of the viscous forces to inertial and surface tension forces. The degree of deformation and breakup is determined by these parameters. According to Hsiang and Faeth [46], there is no breakup observed when the Ohnesorge number is larger than 4. Because this is not our case (the Ohnesorge number of Al/Al$_2$O$_3$ particles in a chamber is typically smaller than 4 under high temperature condition), the Weber number becomes the only parameter relating with breakup. Thus, the slip velocity, $\Delta u_I = \left| \vec{u} - \vec{u}_{p,i} \right|$, corresponding to the critical Weber number is given by

$$\Delta u_{I,crit} = \left(\frac{We_{crit}\, \sigma}{2\rho R_i} \right)^{1/2} \tag{3.68}$$

in terms of critical Weber number, We_{crit}. The appropriate critical Weber number for Al$_2$O$_3$ is found in Caveny and Gany [6] which is given as 28.

The aerodynamic breakup frequency for both of viscous and inertial subrange is assumed to be given by the following using the aerodynamic particle break time and the breakup efficiency corresponding to the critical velocity difference:

$$b_{t,I}\left(R_i\right) = C \left(\frac{\rho}{\rho_p} \right)^{1/2} \frac{\Delta u_I}{R_i} \exp \left(-\frac{\Delta u_{I,crit}}{\Delta u_I} \right) \tag{3.69}$$

where the constant C is obtained from the empirical correlation for the breakup time given by Hsiang and Faeth [46]. The constant C is given by

$$C = \frac{1}{5} \qquad \text{for} \quad Oh < 0.1$$

$$= \frac{1}{5}\left(1 - \frac{Oh}{7}\right) \qquad \text{for} \quad We < 10^3, \ 0.1 < Oh < 3.5 \tag{3.70}$$

Following Levins and Glastonbury [56] and Williams and Crane [33], the slip velocity Δu_I can be related to turbulence parameter of gas phase. Levins and Glastonbury have started from Tchen [34]'s force balance equation between a drop and surroundings and extended it to the random turbulent fluctuation motion of gas. In this case, the mean square slip velocity is given by [56]:

$$\left\langle \Delta u_I^2 \right\rangle = \frac{1}{2\pi} \int_0^\infty \frac{w^2}{\left(1/\tau^2 + w^2\right)} E_f(w) dw \tag{3.71}$$

where τ is the relaxation time of the particle and w is the angular frequency. The wave-number spectrum $E_f(w)$ can be obtained from Williams and Crane [33] and the more accurate form of the wave-number spectrum for particles in viscous subrange is given by [33]:

$$E_f(w) = 4\left\langle u_i^2 \right\rangle \frac{g}{g-1}\left[\frac{T_L}{1+T_L^2 w^2} - \frac{T_L}{g^2 + T_L^2 w^2}\right] \tag{3.72}$$

By putting the equation (3.72) into (3.71), the mean square slip velocity is obtained as follows:

$$\left\langle \Delta u_I^2 \right\rangle_{R_i < \eta} = \left\langle u_i^2 \right\rangle \frac{\gamma}{\gamma - 1}\left(\frac{\theta}{1+\theta} - \frac{\theta}{1+\gamma\theta}\right) \tag{3.73}$$

where the variables are same as the equation (3.36). Accordingly, assuming Gaussian distribution of $\left(\vec{u} - \vec{u}_{P,i}\right)\cdot\vec{n}$, the slip velocity is given by

$$\Delta u_{I,R_i < \eta} = \left[\frac{4}{3\pi}k\frac{\gamma}{\gamma - 1}\left(\frac{\theta}{1+\theta} - \frac{\theta}{1+\gamma\theta}\right)\right]^{1/2} \tag{3.74}$$

For particles in inertial subrange, the simple form of wave-number spectrum, which is more suitable for larger particle as described in Kruis and Kusters [36] and Williams and Crnae [33], is given by:

$$E_f\ w = 4\left\langle u_i^2 \right\rangle \frac{T_L}{1+T_L^2 w^2} \tag{3.75}$$

Putting the equation (3.75) into (3.71) and assuming Gaussian distribution, the slip velocity is obtained as follows:

$$\Delta u_{I,R_i > \eta} = \left[\frac{4}{3\pi} k \frac{\theta}{1+\theta} \right]^{1/2} \tag{3.76}$$

Accordingly, the aerodynamic breakup frequencies in viscous subrange using equations (3.69), (3.70), and (3.74) and inertial subrange using equations (3.69), (3.70), and (3.76) are given by

$$b_{t,I,R_i < \eta}(R_i) = C \left[\frac{4}{3\pi} \frac{\rho}{\rho_p} \frac{k}{R_i^2} \frac{\gamma}{\gamma - 1} \frac{(\gamma - 1)\theta^2}{(1+\theta)(1+\gamma\theta)} \right]^{1/2} \text{x}$$

$$\exp \left[-\left\{ \frac{3\pi}{8} \frac{We_{crit}\sigma}{\rho R_i} \frac{1}{k} \frac{\gamma - 1}{\gamma} \frac{(1+\theta)(1+\gamma\theta)}{(\gamma - 1)\theta^2} \right\}^{1/2} \right] \tag{3.77}$$

$$b_{t,I,R_i > \eta}(R_i) = C \left[\frac{4}{3\pi} \frac{\rho}{\rho_p} \frac{k}{R_i^2} \frac{\theta}{1+\theta} \right]^{1/2} \exp \left[-\left\{ \frac{3\pi}{8} \frac{We_{crit}\sigma}{\rho R_i} \frac{1}{k} \frac{1+\theta}{\theta} \right\}^{1/2} \right] \tag{3.78}$$

3.2.4.3 Hydrodynamic breakup frequency function in laminar flow

Following the same approach given in hydrodynamic collision frequency model in turbulent flow, the shearing breakup frequency due to mean flow is given by

$$b_{l,S} = \frac{\langle DU \rangle_S}{R_i} \exp \left(-\frac{\langle DU \rangle_{S,crit}}{\langle DU \rangle_S} \right) \tag{3.79}$$

where the term $\langle \Delta U \rangle_S / R_i$ is the breakup frequency and $\exp -\langle \Delta U \rangle_{S,crit} / \langle \Delta U \rangle_S$ is the exponentionally assumed breakup efficiency. This model imposes that the breakup occurs when velocity difference exceeds the critical velocity difference. The average mean velocity difference due to shearing motion of fluid across a droplet of radius R_i is given by Euclidean norm of rate of stress tensor and the critical velocity difference across the droplet $\langle \Delta U \rangle_{S,crit}$ can be obtained in terms of the critical Capillary number Ca_{crit} by the approximation of $G = \langle \Delta U \rangle_S / 2R_i$ as follows:

$$\langle \Delta U \rangle_S = R_i \sqrt{8 \ s_{11}^2 + 2s_{12}^2 + s_{22}^2} \tag{3.80}$$

$$\langle \Delta U \rangle_{S,crit} = 2 \frac{Ca_{crit}\sigma}{\mu} \tag{3.81}$$

Therefore, using equations (3.79), (3.80), and (3.81), the hydrodynamic breakup frequency function in laminar flow is given by

$$b_{l,S} = 2\sqrt{2\left(s_{11}^2 + 2s_{12}^2 + s_{22}^2\right)}\exp\left(-\frac{Ca_{crit}S}{m}\frac{1}{R_i}\frac{1}{\sqrt{2\left(s_{11}^2 + 2s_{12}^2 + s_{22}^2\right)}}\right) \qquad (3.82)$$

where s_{ij} is the rate of strain tensor which is given by

$$s_{ij} = \frac{1}{2}\left(\frac{\partial U_i}{\partial x_j} + \frac{\partial U_j}{\partial x_i}\right) \qquad (3.83)$$

3.2.4.4 Aerodynamic breakup frequency function in laminar flow

Using a fast (or equilibrium) Eulerian approach, the slip velocity between particle phase and carrier gas can be obtained again. In analogy with Saffman and Turner [26], assuming that the carrier fluid velocities near two adjacent particles are same, the velocity difference of the carrier fluid between two close point is neglected (this velocity difference is already considered in the previous section which explains the shearing collision in laminar flow) and then the relative slip velocity between two particles is given by

$$\left\langle \mathrm{D}U\right\rangle_I = t_i\left|\frac{D\left\langle\vec{U}\right\rangle}{Dt}\right| \qquad (3.84)$$

Once the slip velocity is obtained, the modeling of aerodynamic breakup in laminar flow can be obtained using the inertial breakup frequency function:

$$b_{l,I} = C\left(\frac{\rho}{\rho_p}\right)^{1/2}\frac{\left\langle\Delta U\right\rangle_I}{R_i}\exp\left(-\frac{\left\langle\Delta U\right\rangle_{I,crit}}{\left\langle\Delta U\right\rangle_I}\right) \qquad (3.85)$$

where the coefficient C is determined by the flow condition and given in equation (3.70).

The critical slip velocity is given by

$$\left\langle\Delta U\right\rangle_{I,crit} = \left(\frac{We_{crit}\sigma}{2\rho R_i}\right)^{1/2} \qquad (3.86)$$

in terms of critical Weber number, We_{crit}.

Therefore, using equations (3.84), (3.85), and (3.86), the aerodynamic breakup frequency function in laminar flow is given by

$$b_{l,I} = C \left(\frac{r}{r_p} \right)^{1/2} \frac{t_i}{R_i} \left| \frac{D\langle \vec{U} \rangle}{Dt} \right| \exp \left(- \left(\frac{We_{crit} \, S}{2 r R_i} \right)^{1/2} \frac{1}{t_i} \left| \frac{D\langle \vec{U} \rangle}{Dt} \right|^{-1} \right)$$

(3.87)

3.2.5 Coalescence efficiency

As Salita [38] explained, the assumption that all collisions result in coalescence has usually been used in the multiphase simulation of rocket combustion chamber. However, many prior studies (i.e., Ashgriz and Poo [39]) have shown experimentally that all collisions of two water drops does not result in coalescence. Four different types of collision outcomes were observed in the experiments as it is explained previously: bouncing, permanent coalescence, temporary coalescence followed by separation and temporary coalescence followed by a set of satellite drops. In bouncing mode, the drops are reflected in the reverse direction of their approaching velocity due to the effect of the fluid film between the drops. The permanent coalescence refers to the creation of stable drops after the drops are merged. The temporary coalescence with separation is when the merged drop is unstable and the merged drop is separated into two or more drops. The temporary coalescence with satellite drops is similar to separation mode but it is disintegrated into a set of very small satellite drops. Although the last three modes concern the phenomenon after the drops are contacted each other, the first bouncing mode concerns the drops before they are contacted.

Due to the absence of the coalescence model of metal droplets (Al or Al_2O_3 in the rocket propulsion), Salita [38] was motivated to perform a series of coalescence experiments using mercury drops, whose the density is 13.5 times and surface tension 6.5 times bigger than water drops at room temperature. By using the mercury drops, they can provide surface tension values near that of Al_2O_3. To compare the coalescence model with the experimental results, they have used the water drops coalescence model of Brazier-Smith et al. [40]. The model of Brazier-Smith et al. [40] postulates that the collision of drops always result in the unstable coalescence and then the merged drop will be separated into the same size of incident drops if the rotational energy of the merged drop exceeds the surface energy holding it together [38]. They concluded that the coalescence model of water drops accurately predicted that of mercury drops. The coalescence model of water drops is used here.

The processes of permanent coalescence and disintegration are described in Figure 3.3. Considering two particles of radii R_i and R_j, the moving particle is the particle of radius R_i supposing the particle of radius R_j as a fixed particle. A temporally formed agglomerate sphere due to the collision has a mass m_i+m_j and the corresponding radius $R_o = (R_i^3 + R_j^3)^{1/3}$. The

resulting rotational energy of the temporal agglomerate from the induced angular momentum by the impact of moving particle to the fixed particle is given by

$$E_R = \frac{5}{3} \rho r_p \overrightarrow{W}^2 \frac{x^2 R_i^6 R_j^6}{R_o^{11}}$$

(3.88)

Here the separation is assumed to occur in the way that only two product droplets which have the same size as the original two droplets because Brazier-Smith et al. [38]'s experimental results for water droplets have shown a good agreement with the modeling using this separation model. The energy required to separate the temporal agglomerate into droplets of radii $R_n^{'}$ is given by

$$E_S = 4\rho S \left[\sum_{n=1}^{N} \left(R_n^{'} \right)^2 - R_o^2 \right]$$

(3.89)

Thus, in case of separation into the two droplets which have the same size as the original two droplets is given by

$$E_{S,s} = 4\rho S \left(R_i^2 + R_j^2 - R_o^2 \right)$$

(3.90)

Therefore, the permanent coalescence occurs when $E_R < E_{S,s}$, and this condition gives that

$$x^2 < \frac{12}{5} \frac{S}{r_p \overrightarrow{W}^2} \frac{R_o^{11}}{\left(R_i R_j \right)^6} \left(R_i^2 + R_j^2 - R_o^2 \right)$$

(3.91)

Defining the coalescence efficiency as the ratio of collision cross section (πx^2) to the maximum available collision cross section πR_c^2, the coalescence efficiency is given by:

$$a_{ij}^{**} = \left(\frac{x}{R_c} \right)^2 = \frac{12}{5} \frac{S}{r_p \overrightarrow{W}^2} \frac{\left(R_i^2 + R_j^2 - R_o^2 \right)}{\left(R_i R_j \right)^6} \frac{R_o^{11}}{R_c^2}$$

(3.92)

where ρ_p is the density of the droplet, σ is the surface tension of droplet.

The mean velocity effect in turbulent flow on the collision process can be obtained by using decomposition of the relative velocity between two particles which is suggested by Saffman and Turner [26] as follows:

$$\left\langle \overrightarrow{W}^2 \right\rangle = \left\langle \left(\overrightarrow{U}_2 - \overrightarrow{U}_1 \right)^2 \right\rangle + \left\langle \left(\overrightarrow{Q}_2 - \overrightarrow{Q}_1 \right)^2 \right\rangle$$

(3.93)

Here, the square means the dot product. Using the Reynold's decomposition, the mean square relative velocity between particles becomes

$$\left\langle \overrightarrow{W}^2 \right\rangle = \left(\left\langle \overrightarrow{U}_2 \right\rangle - \left\langle \overrightarrow{U}_1 \right\rangle \right)^2 + \left(\left\langle \overrightarrow{Q}_2 \right\rangle - \left\langle \overrightarrow{Q}_1 \right\rangle \right)^2 + \left\langle \left(\vec{u}_2 - \vec{u}_1 \right)^2 \right\rangle + \left\langle \left(\vec{q}_2 - \vec{q}_1 \right)^2 \right\rangle \tag{3.94}$$

The lower cases q and u are fluctuating parts of the slip velocity and the surrounding fluid velocity. The first and second terms on the RHS are given by Eqs. (3.80) and hydrodynamic laminar collision frequency function, respectively (the average velocity difference across at a distance of R_c is obtained from Eq. (3.80) using Euclidean norm of rate of stress tensor). The sum of third and fourth terms is obtained from Eq. (3.44) for viscous subrange and Eq. (3.48) with $\left\langle w_x^2 \right\rangle = \left\langle w_y^2 \right\rangle = \left\langle w_z^2 \right\rangle$ for inertial subrange (the fourth term is neglected in inertial subrange). Therefore, the mean square relative velocity between colliding particles is given by

$$
\begin{aligned}
\left\langle \overrightarrow{W}^2 \right\rangle_{R_{eq}<h} = {}& 2R_c^2 \left(s_{11}^2 + 2s_{12}^2 + s_{22}^2 \right) + \left((t_1 - t_2) \frac{D\left\langle \overrightarrow{U} \right\rangle}{Dt} \right)^2 \\
& + \frac{R_c^2}{3} \frac{e}{v} + 2k \frac{g}{g-1} \frac{(q_i - q_j)^2}{q_i + q_j} \left[\frac{1}{(1+q_i)(1+q_j)^2} - \frac{1}{(1+gq_i)(1+gq_j)} \right]
\end{aligned}
\tag{3.95}
$$

$$
\begin{aligned}
\left\langle \overrightarrow{W}^2 \right\rangle_{R_{eq}>h} = {}& 2R_c^2 \left(s_{11}^2 + 2s_{12}^2 + s_{22}^2 \right) + \left((t_1 - t_2) \frac{D\left\langle \overrightarrow{U} \right\rangle}{Dt} \right)^2 \\
& + 1.37^2 (3) R_c^{2/3} e^{2/3} + 2k \frac{(q_i + q_j)^2 - 4q_i q_j \sqrt{\dfrac{1+q_i+q_j}{(1+q_i)(1+q_j)}}}{(q_i + q_j)(1+q_i)(1+q_j)}
\end{aligned}
\tag{3.96}
$$

Using equations (3.95) and (3.96) with (3.92), the coalescence efficiency is obtained.
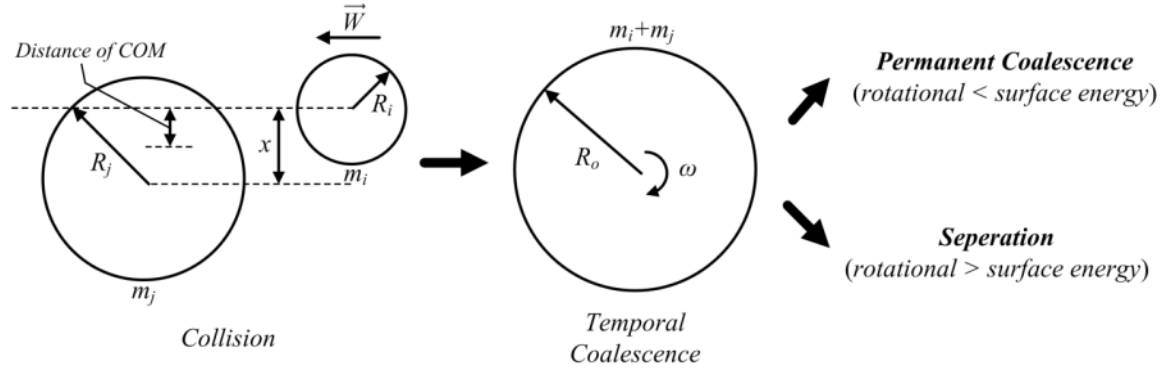
Figure 3.3 Schematic of coalescence and separation processes of collision between two droplets of radii R_i and R_j

3.2.6 Collision efficiency (Bouncing efficiency)

Following Coulaloglou and Tavlarides [12] and Tsouris and Tavlarides [13], the drop collision efficiency can be characterized by two terms; contact time and collision time. The contact time is the time of two drops staying together after they collided. The collision time is the time required for the drainage of liquid or gas films between two drops. If two drops are staying together after they collided for enough time for the film drainage, the collision of two drops occurs. Therefore, the collision occurs when the contact time is larger than the coalescence time. The function of the coalescence efficiency from Tsouris and Tavlarides [13] is given by

$$a^* = \exp\left(-\frac{\overline{T}}{\overline{t}}\right) \tag{3.97}$$

where $\overline{t}$ is the average contact time, $\overline{T}$ is the average coalescence time.

Considering the liquid droplets in gaseous fluid system, the deformation of the interface between two droplets is supposed to be significant unlikely to the solid particles in fluid. Thus, assuming the deformation of the interface is significant, the parallel-film approach can be used in this system. Figure 3.4 illustrates the idealized deformation of the interface in the parallel-film approach. Based on the classical lubrication theory, the film drainage process can be described by two equations given by [47]

$$\frac{\partial}{\partial t}(\rho hr) + \frac{\partial}{\partial r}(U_m \rho hr) = 0 \quad \text{(continuity equation)}$$

$$\frac{\partial P}{\partial r} + 12\mu \frac{U_m}{h^2} = 0 \quad \text{(r-momentum equation)} \tag{3.98}$$

where ρ is the gas density, μ is the dynamic viscosity, U_m is the gap-averaged radial velocity of draining flow, and P is the gap-averaged pressure. Considering incompressible gas flow (ρ is constant), two governing equations can be solved for the pressure in the gap between two spherical drops as follows:

$$P(r,t) = -3\mu r^2 \frac{\dot{h}}{h^3}$$ (3.99)

Neglecting Van der Waals attraction and electrostatic double-layer repulsive force, the balancing of inertial force by suspension flow and dynamic force exerted by the pressure inside the gap closes the system. The force balance equation is given by

$$F - \frac{3\rho\mu r_s^4}{2}\frac{\dot{h}}{h^3} = 0$$ (3.100)

where F is the compressive inertial force. Following Chesters [32], the amount of deformation is related to the compressive inertial force as follows:

$$F = \pi r_s^2 \left(\frac{2\sigma}{R_{eq}} \right)$$ (3.101)

Thus, eliminating the radius of the interfacial circle r_s from the force balance equation, the rate of film thickness change is expressed by

$$\frac{dh}{dt} = \frac{8}{3}\frac{\pi\sigma^2}{\mu R_{eq}^2 F}h^3$$ (3.102)

Consequently, assuming the constant force F, the calculation of the time required for film drainage when the drops deform is given by

$$\overline{T} = \frac{3}{16}\frac{\mu F}{\pi\sigma^2}\left(\frac{1}{h_f^2} - \frac{1}{h_0^2} \right)R_{eq}^2$$ (3.103)

where the h_f and h_0 is the final gap distance and initial gap distance between particles respectively. This collision time is also used in Coulaloglou and Tavlaride [12].

Here, F is the force acting on either ends of two adjacent drops. By assuming the force is propotional to the mean square velocity difference at either ends of the drops, Coulaloglou and Tavlarides [12] have used the following expression for turbulent flow:

$$F = \Gamma R_{eq}^2 \left\langle \overrightarrow{W}^2(2R_c) \right\rangle$$ (3.104)

where $\left\langle \overrightarrow{W}^2(2R_c) \right\rangle$ is the velocity difference across a distance of $2R_c$ in the turbulent flow. Using the same approach as above, the velocity difference across a distance of $2R_c$ can be obtained assuming the collision between the particles of radii $2R_i$ and $2R_j$. Therefore, F for viscous subrange and inertial subrange are given by

$$
\begin{aligned}
F_{R_{eq}<\eta} = 4\rho R_{eq}^2 \Bigg[& 2R_c^2\left(s_{11}^2 + 2s_{12}^2 + s_{22}^2\right) + \left(\left(\tau_1 - \tau_2\right)\frac{D\langle\vec{U}\rangle}{Dt}\right)^2 \\
& + \frac{1}{3}\frac{\varepsilon}{\nu}R_c^2 + 2k\frac{\gamma}{\gamma-1}\frac{(\theta_i-\theta_j)^2}{\theta_i+\theta_j}\left\{\frac{1}{(1+4\theta_i)(1+4\theta_j)} - \frac{1}{(1+4\gamma\theta_i)(1+4\gamma\theta_j)}\right\}\Bigg]
\end{aligned}
$$
(3.105)

$$
\begin{aligned}
F_{R_{eq}>\eta} = 4\rho R_{eq}^2 \Bigg[& 2R_c^2\left(s_{11}^2 + 2s_{12}^2 + s_{22}^2\right) + \left(\left(\tau_1 - \tau_2\right)\frac{D\langle\vec{U}\rangle}{Dt}\right)^2 \\
& + 1.37^2(3)R_c^{2/3}\varepsilon^{2/3} + 2k\frac{(\theta_i+\theta_j)^2 - 4\theta_i\theta_j\sqrt{\dfrac{1+4\theta_i+4\theta_j}{(1+4\theta_i)(1+4\theta_j)}}}{(\theta_i+\theta_j)(1+4\theta_i)(1+4\theta_j)} \Bigg]
\end{aligned}
$$
(3.106)

respectively. The final gap distance h_f between particles which is set as 300 armstrong meters which is the minimum of reasonable film thickness appearing in Coulaloglou and Tavlarides [12] and the initial gap distance h_0 is set as $0.1R_{eq}$ following Tsouris and Tavlarides [13]. The contact time due to the fluctuating parts for the viscous subrange and inertial subrange is set as Kolmogorov's time scale and Taylor's micro time scale, respectively. The contact time for the viscous subrange and inertial subrange are given by

$$
\bar{t}_{R_{eq}<\eta} = \left(\frac{\nu}{\varepsilon}\right)^{1/2}
$$
(3.107)

$$
\bar{t}_{R_{eq}>\eta} = \left(\frac{15\nu}{\varepsilon}\right)^{1/2}
$$
(3.108)

respectively. Following Chesters [32], the contact time for laminar flow is given as follows:

$$
\bar{t} = \left(\frac{4\rho_p}{3\rho+1}\frac{\rho R_{eq}^3}{2\sigma}\right)^{1/2}
$$
(3.109)

The contact time for turbulent flow is assumed as the sum of the contact times due to the fluctuating part and mean flow part.
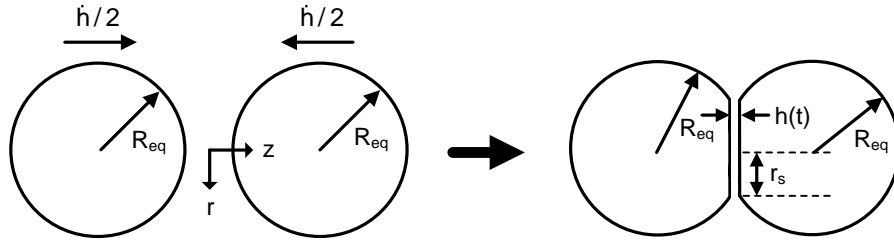
Figure 3.4 Schematic of idealized collision process between two deformable droplets of equal radius R_{eq}

3.2.7 Summary and implementation of the mean velocity effect in turbulent flow

The key parts of implementation of mean velocity effect in collision process are the calculation of collision and breakup frequency function. It is commonly assumed that the collision mechanisms due to Brownian motion, fluid shear, and differential sedimentation are independent from each other and the collision frequency functions are additive [28]. The collision induced by differential sedimentation is very similar to aerodynamic collision because the source of the collision is the velocity difference between two drops induced by different response of each drops to their surrounding fluid. It is further assumed here that the collisions induced by laminar and turbulent flow are independent. Details of this assumption are provided in next chapter. Thus, the sum of collision frequency functions of laminar hydrodynamic collision, laminar aerodynamic collision, and turbulent collision is used for the total collision frequency function.

In case of breakup frequency, the maximum value between laminar hydrodynamic breakup, laminar aerodynamic breakup, and turbulent breakup is used for the calculation. The summary of equations used for collision and coalescence efficiencies, and collision and breakup frequency function is provided in Table 3.1.

Table 3.2 Summary of equations used for collision/coalescence efficiencies and collision/breakup frequency functions

	Laminar		Turbulent		Turbulent with mean flow effects
Collision efficiency	Eq. 3.97 with Eqs. 3.80, 22 in Appendix B, 3.103, 3.104, and 3.109		Eq. 3.97		Eq. 3.97 with Eqs. 3.103, 3.105, 3.106, 3.107, 3.108, and 3.109 - the contact time is assumed as the sum of laminar and turbulent
			Viscous	Inertial	
			with Eqs. 3.44, 3.103, 3.104, and 3.107	with Eqs. 3.48, 3.103, 3.104, and 3.108	
Coalescence efficiency	Eq. 3.92 with Eqs. 3.80 and 22 in Appendix B		Eq. 3.92		Eq. 3.92 with Eqs. 3.95 and 3.96
			Viscous	Inertial	
			with Eq. 3.44	with Eq. 3.48	
Collision frequency function	Sum of Eqs. 15, 16, and 23 in Appendix B		Viscous	Inertial	Sum of Eqs. 15, 16, and 23 in Appendix B, 3.47, and 3.49
			Eq. 3.47	Eq. 3.49	
Breakup frequency function	Hydrodynamic	Aerodynamic	Hydrodynamic		Aerodynamic		Maximum between Eqs. 3.82, 3.87, (3.64 or 3.65), (3.77 or 3.78)
			Viscous	Inertial	viscous	inertial	
	Eq. 3.82	Eq. 3.87	Eq. 3.64	Eq. 3.65	Eq. 3.77	Eq. 3.78	

3.3 Validation studies

3.3.1 Geometry

Most applicable experimental data for the flowfields under consideration dates back to early development years for large solid rocket motors. The two-phase flow loss in the motor is a dominant loss mechanism for larger motors and this motivated a series of experiments aimed at identifying particle sizes exiting nozzles of various sizes. A series of simulation was performed to validate the code comparing the results to Crowe et al. [50] experimental results and Hermsen [10]'s correlation. The details of Hermsen's correlation will be given later. The UTC (United Technology Center) experiments of Crowe et al. [50] are performed with PBAN-based polymer type solid propellants containing 16% aluminum particles. Crowe et al.'s nozzle has a length of 5.2 cm and an inlet radius of 1.587 cm. The throat is located at 2.113 cm downstream from the inlet and its diameter is 1.27 cm. The corresponding area ratios of the throat to the inlet and the throat to the exit are 6.246. Figure 3.5 illustrates their nozzle geometry. In these experiments, measurement of particle size was accomplished by analyzing photo-micrographs collected from the receiver tank wall surface after firing the small solid rocket motor into the closed tank. Subsequent experiments [51] are also performed to obtain the particle distribution data at the nozzle inlet by firing the rocket motor without the nozzle attached to the receiver tank pressurized to the desired level.

A series of simulations was also performed to compare the results to the correlation under the nozzle configuration used by Shegal [53] for 150 psi chamber pressure. His experiments were performed with Polyurethane-type solid propellants containing 12% aluminum. The motor had a 5 inch outer diameter by 6 inch length with a circular port of 2 inch diameter. The conical convergent nozzle is attached to the motor and the chamber pressure was changed by adjusting the throat diameter. He obtained the particle size information at the nozzle exit (or nozzle throat) by firing motor into a tank. He reported the size data from the particles attached to tank wall.

Because Shegal did not provide detailed geometrical information, we estimated the nozzle throat diameter assuming isentropic flow. To account for the particle size variation in the diverging section and compare the particle size data at the nozzle exit, the conical diverging section with a 18 deg half angle is attached. In addition, the nozzle exit diameter is chosen

according to the perfect expansion assumption at the sea level and it gave the shock wave free condition inside the diverging section.

To avoid the limitation of the fast Eulerian assumption, the nozzle geometry for Shegal's 150 psi case is chosen and accordingly the relatively smaller particles exists in the nozzle. The large particle diameter gives the large relaxation time ($\tau = 2\rho_p + \rho_g \ r^2/9\mu$). Although the particle size falls in the applicable range for the fast Eulerian assumption, it can lead the relatively large errors in the particle phase velocity, $\vec{U}_p$, comparing to the case of smaller particle phase. According to Ferry and Balachandar [21], the particle phase velocity can be obtained from the fast Eulerian approach within the reasonable error bound when the relaxation time is less than the fluid time scale which is defined by the inverse of the maximum of absolute compressive strain. Typically, in the current simulation, mass mean diameters over the entire domain do not exceed 10 μm and then the relaxation time is in the limit of the fast Eulerian assumption or errors maybe confined in the small regions of boundary layer which does not affect the integrated particle size on a chosen face, i.e, nozzle exit.

However, the numerical difficulty specific to the fast Eulerian approach arises, which is that this approach can produce unphysical large amount of particle phase velocity. At the first cell from the wall or geometric boundary, a central scheme on the calculation of the gradient of velocity uses only information from two cells in perpendicular direction. This error leads to stiff source term and produces negative values of weights and non-physical large values of abscissas. In analogy to Najjar et al. [2], a clipping has been used to overcome this difficulty. With the aid of 2nd order boundary condition, the amount of clipping is set as a bound of 100±50% of gas stream velocity. The clipping only occurs at the very thin layer inside the boundary layer and it will not affect the overall results due to the small mass flow rate in the boundary layer. To minimize these errors while treating the particle velocity as a field variable, The modified fast Eulerian method by Ferry et al. [66] minimizing theses errors and treating the particle velocity as a field variable can be used but it is not considered currently. The details of modified fast Eulerian method is available in Chapter 7.

At the same time, numerical challenges specific to DQMOM method arise when the abscissas of the quadrature approximation goes to zero in a no particle existing zone. As it is indicated by Zucca et al. [57], the matrix A in a linear system of source term becomes nearly

singular and the solution of the system gives unphysical values of weights and abscissas. To overcome this difficulty, we set a bound of weights and abscissas. The lower and upper limits of abscissas are 0.1% and 100,000 % of the abscissas of initial distribution, respectively. The lower and upper limits of weights are 10^{-8} % and 1000 % of initial condition. Accordingly, when the abscissas or weights goes to null, the values will approach to lower limits of values. Avoiding this problem, a reconstruction of matrix A in a linear system by calculating of moments then applying a correction algorithm [67] may be used but it is not applied in current simulations.

Figure 3.6 highlights an axisymmetric mesh used in the computations for Shegal's geometry. The nozzle has a length of 15.4 cm and a inlet radius of 6.35 cm. The throat is located at 12.6 cm downstream from the inlet. The corresponding area ratio of the throat to the inlet is 30.57 and the ratio of the throat to the exit is 2.43. The inlet geometry is horizontally smoothed out to remove additional disturbances caused by sharp geometry. A simulation is performed in a typical axisymmetric unstructured mesh form. The physical time consumed during a typical steady case simulation is about seven days using 4 cpus and a time stepping by maximum CFL number in the message passing (MPI) environments.

The measurement of particle size is done by collecting the particles in the pressurized tank. The expansion of flow into the tank creates the shearing region in outer region of main stream and this shearing motion of flow will create high turbulent motion along with laminar shearing forces. As expected from the modeling of collision processes, the collision may significantly occur within this small confined region and result in larger particle size.
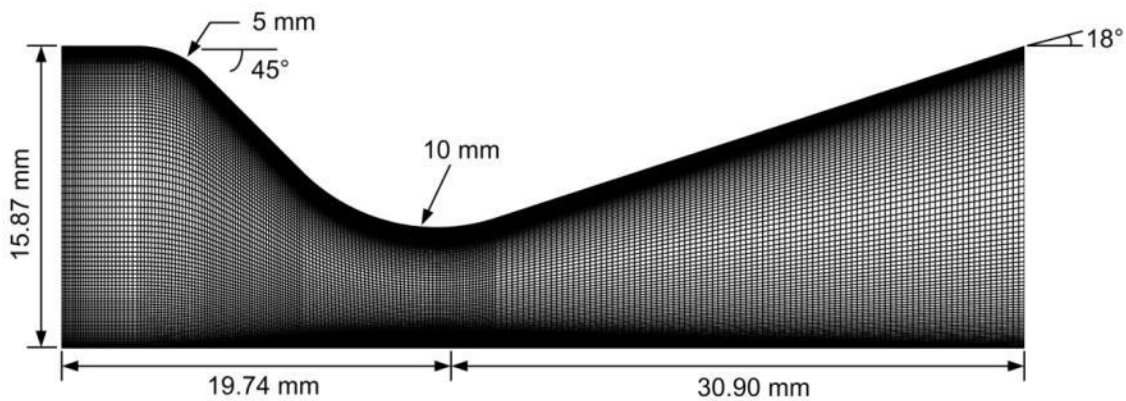

Figure 3.5 Schematic of the test nozzle geometry for Crowe et al.'s experiments (228x100 cell mesh)
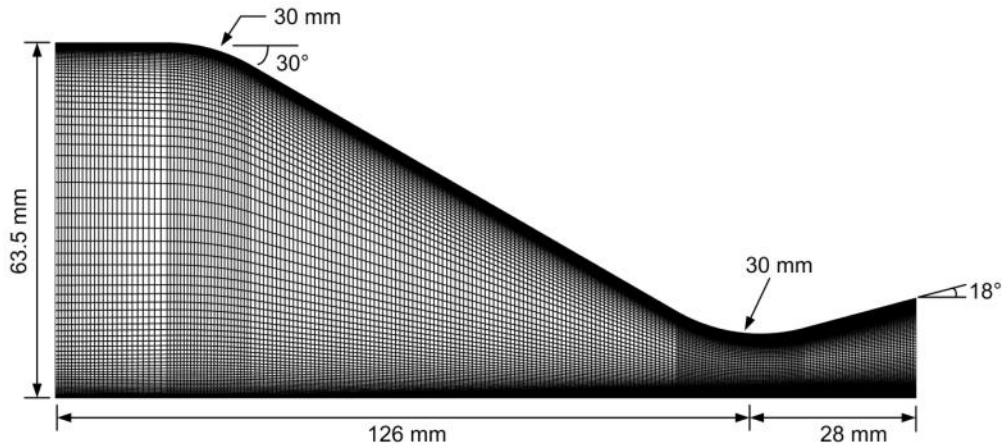
Figure 3.6 Schematic of the test nozzle geometry for Shegal's experiment (245x80 cell mesh)

3.3.2 Hatch-Choate formula

In our model and Crowe and Willoughby's model [52], it is required to provide the parameters for the inlet Al_2O_3 particle distribution. Crowe et al. [51] performed the experiments measuring the particle diameter at the chamber without the nozzle attached by pressurizing the collection chamber to a certain level. The combustion product collected from the motors containing 16% Aluminum particles had the MMD (mass median diameter) in a range of 0.74 to 1 µm and the standard deviation of 0.456 on pressure over 150 psi with only slight variation of values. As Crowe and Willoughby [52] used these parameters in their model as an inlet condition, we also applied this condition in our calculation.

The particle size information in the motor of Shegal can be obtained from Fein [54]. While holding the chamber pressure 150 and 500 psi by pressurizing the tank to the desired level, the motors without the nozzle are fired into the tank. The measured mass mean diameter of particles were 0.79 and 2.39 µm for 150 and 500 psi chamber pressures, respectively. At these chamber pressures, the measured mass mean diameters at the nozzle exit were 1.5 and 3.5 µm, respectively. As described in 3.1.1, the nozzle geometry for Shegal's 150 psi case is chosen as a baseline geometry to reduce the possible error due to the existence of too large particles in Fast Eulerian approach.

The parameters for dispersed phase tracked by QMOM and DQMOM are lower order moments and abscissas (or diameter) and weights (or number of particles), respectively.

Accordingly, count mean diameter (D_{10}), surface mean diameter (D_{20}), volume mean diameter (D_{30}), Sauter mean diameter (D_{32}), and mass mean diameter (D_{43}) can easily calculated using the following equation:

$$D_{ab} = \frac{m_a}{m_b} = \frac{\sum n_i D_i^a}{\sum n_i D_i^b} = \frac{\sum_{i=1}^{N} w_i l_i^a}{\sum_{i=1}^{N} w_i l_i^b} \tag{3.110}$$

Here, MMD (mass median diameter) represents the drop diameter that accounts for 50% of total particle mass in the distribution. If the drop size distribution is log-normal, the MMD can readily be related to other statistical drop size quantities using the Hatch-Choate formula [68]. For a given median diameter (or geometric mean diameter D_m) and standard deviation σ_s for log-normal distribution, any other representative drop size can be obtained by following formula:

$$D_x = D_m \exp\left[\left(q + \frac{p}{2}\right)\sigma_s^2\right] \tag{3.111}$$

where q and p depends on the types of D_x. The q and p values according to D_x are given in table 3.2. Therefore, the geometric mean diameter D_m is obtained by:

$$D_m = MMD / \exp\left(3\sigma_s^2\right) \tag{3.112}$$

The D_m and standard deviation σ_s of resultant particle phase are calculated using 2nd moment to 4th moment as follows:

$$D_m = \exp\left[3.5\ln\left(\frac{m_3}{m_2}\right) - 2.5\ln\left(\frac{m_4}{m_3}\right)\right]$$

$$\sigma_s = \left[\ln\left(\frac{m_4}{m_3}\right) - \ln\left(\frac{m_3}{m_2}\right)\right]^{1/2} \tag{3.113}$$

Table 3.2 The q and p values in Hatch-Choate formula

Representative particle size	q	p
D_{10}	0	1
D_{20}	0	2
D_{30}	0	3
D_{32}	2	1
D_{43}	3	1
MMD	3	0

3.3.3 Boundary conditions

3.3.3.1 Gas phase boundary conditions

A non-slip boundary condition is imposed at the nozzle wall and a pressure inlet and supersonic outlet condition is set as boundary conditions. The standard axisymmetric boundary condition is imposed along the centerline. The constant inlet kinetic energy k and specific dissipation rate ω are chosen. The inlet kinetic energy k for Crowe and Shegal is 864 m^2/s^2 and 21 m^2/s^2, respectively, which are approximately corresponding to the turbulent intensity I of 15% and 10% of centerline gas velocity, respectively. High turbulence intensity at the propellant surface due to the shearing motion is observed in Ciucci et al. [9] (approximately, 8 to 10%). Considering the shearing motion of flow detached from the propellant entering the combustion chamber at the end of SRM propellant, the high turbulent motion is expected but the distribution of turbulent parameters needs to be considered for more accurate calculation. The parametric studies on the inlet kinetic energy are also performed and the results are given in later section. The inlet specific dissipation rate ω for k-ω model is determined from the following relationship:

$$\omega = \frac{k^{1/2}}{0.09^{1/4} \ell} \tag{3.114}$$

where ℓ is the turbulence length scale and it is given by $\ell = 0.07 D_h$. The D_h is the hydraulic diameter at the nozzle inlet.

Table 3.3 Gas mixture properties and pressure boundary conditions

Quantity	Value
MW (kg/kmol)	27.76
C_p (J/kg · K)	2439.04
μ_{ref} (kg/m · s)	36.0e-05
$T_{inlet} = T_{ref}$ (K)	3279
S_{ref} (K)	120

The gas mixture properties are summarized in Table 3.3. These properties are obtained from the properties for solid propellant rocket simulations of Lupoglazoff and Vuillot [69] and Najjar et al [2]. The inlet temperature is obtained from Fein [54]. Sutherland's law is used for the viscosity rather than the constant viscosity assumption with the reference temperature T_{ref} and Sutherland's constant S_{ref} given in Table 3.3. The ambient pressure is used as outlet condition.

3.3.3.2 Dispersed phase boundary conditions

The density for the particle phase is obtained from Al_2O_3 density relationship given by Najjar et al. [2] as follows:

$$\rho_p = 5632 - 1.127T \quad (kg/m^3) \tag{3.115}$$

where T is in deg. K. A surface tension and dynamic viscosity of liquid Al_2O_3 are obtained from Hatch [60] for molten Aluminum instead of Aluminum Oxide. The surface tension and dynamic viscosity of molten Aluminum are given by

$$\sigma_p = 0.868 - 0.000152(T - T_m) \quad (N \cdot m^{-1})$$
$$\mu_p = 0.0001492 \exp(1984.5/T) \quad (N \cdot s/m^2) \tag{3.116}$$

where T_m is the melting temperature of Aluminum and it is given as 933.47 K.

The mass mean diameter (or Herdan's mean diameter) D_{43} can be obtained from the weights and abscissas which is calculated by

$$D_{43} = \frac{m_4}{m_3} = \frac{\sum_i n_i D_i^4}{\sum_i n_i D_i^3} = \frac{\sum_{i=1}^{N} w_i l_i^4}{\sum_{i=1}^{N} w_i l_i^3} \tag{3.117}$$

The volume fraction v_f and mass fraction α_f are given by

$$v_f = \frac{\pi}{6}\sum_{i=1}^{N} w_i l_i^3 \qquad\qquad \alpha_f = \frac{\rho_p}{\rho} v_f \qquad\qquad (3.118)$$

The mass averaged D_{43} over a face is calculated by

$$D_{43} = \frac{\oint_f \dot{m} \sum_{i=1}^{N} w_i l_i^4 \, ds}{\oint_f \dot{m} \sum_{i=1}^{N} w_i l_i^3 \, ds} \qquad\qquad (3.119)$$

The purpose of the current study is to simulate and investigate the coalescence/breakup processes in the typical converging/diverging nozzle. The coalescence/breakup processes are sensitive to the distribution of particles. The log-normal particle number distribution or exponential distribution can be used following Najjar et al. [2] and Fein [54], respectively. Najjar et al. have referred other researcher's finding of lognormal and bimodal size distribution of droplets entering the chamber from the solid propellant surface. Gany et al. [1]'s experimental results of the distribution of the droplets leaving the propellant surface is close to a lognormal distribution. The model proposed by Fein [54] is the exponential distribution rather than lognormal distribution. Fein compared his modeling with the experimental data performed by Shegal and the good agreement between the model and experiment is obtained.

Thus, the lognormal distribution is given by

$$f(D) = \frac{d\bar{n}}{dD} = \frac{1}{\sqrt{2\pi}D\sigma_s}\exp\left[-\frac{\left(\ln D - \ln D_m\right)^2}{2\sigma_s^2}\right] \qquad\qquad (3.120)$$

where $d\bar{n}$ is the number fraction of drops in a given range dD, σ_s is the standard deviation, and D_m is the geometric mean drop diameter. The transformed coordinate by $l^3=v$ (where v is the volume of a drop) can be expressed as $l=D$ via the DQMOM approach, and the distribution of l is also lognormal distribution. Therefore, the moments are given by

$$m_z = n_{total}\int_0^{\infty}\frac{d\bar{n}(l)}{dl}l^z dl \qquad\qquad (3.121)$$

The analytical expressions for the raw moments of lognormal distribution are given by

$$m_z = n_{total}\exp\left(z\ln D_m + z^2\sigma_s^2/2\right) \qquad\qquad z = 0......2N\text{-}1 \qquad\qquad (3.122)$$

The exponential distribution modeled by Fein [54] is particle volume distribution which is given by:

$$f(v) = \frac{2}{V_n^{1/3}(6v)^{2/3}}\exp\left[-\left(6v/V_n\right)^{1/3}\right]$$ (3.123)

where V_n is the number average particle volume. Therefore, the volume distribution needs to be converted to size distribution. Assuming the spherical droplet, the size distribution is obtained as follows:

$$f(l) = f(D) = 3\alpha_v D^2 f(v) = \lambda\exp[-\lambda D] \qquad \text{where } \lambda = \left(\pi/V_n\right)^{1/3}$$ (3.124)

where λ is the rate parameter and α_v is the shape factor for the sphere which is given by $\pi/6$. The analytical expressions for the raw moments of exponential distribution are given by

$$m_z = n_{total}\left(z!/\lambda^z\right) \qquad z = 0.......2N-1$$ (3.125)

The raw moments of inlet particle distribution are used to find weights (w_i) and abscissas (l_i) from the PD algorithm. To use these two distributions as an inlet condition, two and one variables should be known for lognormal and exponential distributions, respectively. As described above, we chose Shegal's nozzle configuration used for 150 psi chamber pressure. Thus, we used his experimental results for particles in the chamber as a nozzle inlet condition. According to Fein [54], while holding the chamber pressure 150 psi by pressurizing the tank, the motor without the nozzle gives that the rate parameter λ is 4858099.849 1/m and D_{43} is 0.79 μm. However, due to the slight variance of D_{43} occurring in PD algorithm approximating the distribution by three nodes and three weights, the calculated value of D_{43} using this rate parameter is 0.78 μm. To remove this undesirable effect from PD algorithm, the rate parameter is slightly adjusted and is set as 4804660.751 1/m. This adjustment will not deviate the results significantly.

To validate the modeling, we compared the predicted results to Crowe et al.'s experiments. In addition, the simulation is validated by comparing it with Hermsen's correlation [10] which is described in detail in the next section. We constructed one test matrix for Crowe et al.'s experiments and three different test matrices by varying the chamber pressure, particle concentration, and, nozzle scale for Shegal's cases. Tables 3.4-7 summarize the inlet conditions

for gas and particle phases and nozzle scales. In case of nozzle configuration of Crowe et al. [50], the chamber pressures are chosen to compensate pressure variation according to Hermsen [10].

Table 3.4 The particle phase inlet boundary conditions – for Crowe et al. [68]'s experiments

Case no.	C-1	C-2	C-3-1	C-3-2	C-3-3	C-4-1	C-4-2
D_t (in.)	0.5						
ξ_c	0.277						
P_c (psi)	110	470	650			980	
τ_c (ms)	15						
n_{total}	1.31e15	2.3e15	6.41e15	3.15e15	1.44e15	9.64e15	4.74e15
D_m (μm)	0.397	0.536	0.423	0.536	0.696	0.423	0.536
σ_s (μm)	0.456						

Table 3.5 The particle phase inlet boundary conditions – chamber pressure variation

Case no.	P-1	P-2	P-3	P-4	P-5	P-6	P-7	P-8	P-9
D_t (in.)	0.904								
ξ_c	0.240								
P_c (psi)	150	250	350	450	550	650	750	850	950
τ_c (ms)	4.15								
n_{total} (x 10^{15})	5.08	8.43	11.83	15.22	18.6	22.0	25.37	28.75	32.13
λ (1/m)	4804660.751								

Table 3.6 particle phase inlet boundary conditions – particle concentration variation

Case no.	M-1	M-2	M-3	M-4	M-5	M-6
D_t (in.)	0.904					
ξ_c	0.12	0.16	0.20	0.24	0.28	0.32
P_c (psi)	650					
τ_c (ms)	4.15					
n_{total}	10.99e15	14.65e15	18.31e15	22.0e15	25.65e15	19.31e15
λ (1/m)	4804660.751					

Table 3.7 The particle phase inlet boundary conditions – nozzle scale variation

Case no.	S-1	S-2	S-3	S-4	S-5	S-6
D_t (in.)	0.904	1.808	3.616	5.424	7.232	9.04
ξ_c	0.240					
P_c (psi)	650					
τ_c (ms)	4.15					
n_{total}	18.6e15					
λ (1/m)	4804660.751					

3.3.4 Hermsen's correlation

Although the current model has an ability to predict the drop size distribution inside the rocket chamber and nozzle, it is hard to validate the code due to the lack of experimental data of drop size inside the chamber. The high temperature and high velocity conditions in the rocket chamber and nozzle make it difficult to measure the particle size. Until now, the experiments are performed to measure the particle size at the exit plane of nozzle (i.e. Sambamurthi [61]) and lots of empirical correlations are developed to predict the particle size at the exit as it is described by Hermsen [10]. Thus, we decide to validate the predicted particle size data at the nozzle exit with the empirical correlation. The empirical correlation which is widely used in the solid rocket industry is Hermsen's model [10] for the aluminum oxide particle size:

$$D_{43} = 3.6304 D_t^{0.2932} \left(1 - \exp\left(-0.0008163 x_c P_c t_c\right)\right) \qquad \text{where } t_c = r_c V_c / \dot{m} \qquad (3.126)$$

where τ_c is the average chamber residence time (ms), D_{43} is the mass mean diameter (μm), D_t is the nozzle throat diameter (in.), ξ_c is the particle concentration in the chamber (gmol/100 g), P_c is the chamber pressure (psi), ρ_c is the gas density in chamber (kg/m^3), V_c is the volume in chamber (m^3), and $\dot{m}$ is the propellant mass flow rate (kg/s). Because the current DQMOM modeling uses the total number of particles, n_{total}, instead of the particle concentration, ξ_c, the total number of particles can be obtained using PD algorithm. After the weights (w_i) and abscissas (l_i) are obtained by PD algorithm for a certain n_{total}, a n_{total} corresponding to a given ξ_c is calculate by trial and error method on the following equation:

$$\sum_{i=1}^{N} w_i l_i^3 = \frac{6}{100\pi} \frac{\xi_c \rho_c M_{Al_2O_3}}{\rho_{Al_2O_3}}$$
(3.127)

where $M_{Al_2O_3}$ is the molar mass of Al$_2$O$_3$ (g/mole) which is given by 101.94 for the current study. According to Hermsen [10], the standard deviation of the correlation is 0.298 and it is corresponding to a deviation of D_{43} of about ±35% due to the data scatter obtained from various collection and measurement techniques.

3.3.5 Grid convergence study

The grid convergence study was performed on the geometry given in above section for Crowe et al. [50]'s 650 psi case (case no. C-3-2). The grid sizes used were 140x70 and 228x100. We also performed the simulation on 325x125 grids. This simulation required a long time to converge on 4 cpus, so the domain was parallelized on 8 cpus. The predicted mass mean diameter from 228x100 grids showed about 3% variance from the fine grid of 325x125. The slight differences were observed in the near regions of boundary layer. In intermediate and dense grids, the grid was stretched to match the value of dimensionless wall distance ($y+$) to unity as it is required in turbulent boundary layer calculation. In these two cases, all important parameters considered here in Table 3.8 showed the differences less than 3%. However, using a coarse grid of 140x170, the dimensionless wall distance ($y+$) is larger than unity mostly in divergent section, therefore, the discernable amount of differences at around boundary layer is observed. Thus, for accurate prediction, fine grid resolution may be the best grid, but we chose 228x100 grids due to computational efficiency.

Table 3.8 Averaged characteristics of gas and particle phase at nozzle exit for grid convergence studies

Quantity	140x70	228x100	325x125
Static Pressure (Pa)	0.135e+6	0.135e+6	0.134e+6
Mach number	0.267	0.268	0.269
Mass flow rate (kg/s)	0.055	0.056	0.056
D_{43} (μm)	1.986	2.006	2.011
v_f	0.305e-4	0.308e-4	0.305e-4
α_f	0.465	0.469	0.469

3.3.6 Validation studies

3.3.6.1 Comparisons to the experiments and correlation

A series of simulations was carried out to predict mass mean diameter at nozzle exit in the nozzle configuration given by Crowe et al. [50]. As described above, the small solid rocket motors are fired into the collection tank with the nozzle [50] and without nozzle [51] to assess the particle conditions obtained directly from the chamber. The chamber pressure was changed by varying the propellant burning area with a fixed nozzle attached. The experimental chamber pressures are approximately 130, 320, 570, 900, and 1000 psi. According to Crowe et al. [50], they observed the chamber pressure variation during tests, therefore, we chose the pressure values given by Hermsen [10] to account for the pressure variation. The chamber pressures of simulations are 110, 470, 650, and 980 psi and the corresponding case numbers are C-1-1, C-2, C-3-1 to 3, and, C-4-1 to 2, respectively. Hermsen [10] also reported the details of experimental data of Crowe et al. [50]. In this literature, the standard deviations of resultant log-normal distributions are reported based on $\log_{10}D$ which is not compatible with the current standard deviation based on $\ln D$. Therefore, the standard deviation based on 10 logarithm of D is converted to natural logarithm as follows:

$$\sigma_s = \ln(10)\sigma_{s,10} \tag{3.128}$$

Crowe et al. [50]'s experiments and Hermsen [10]'s correlation for current simulations and Crowe et al's experiments are compared in Figure 3.7. The horizontal lines associated with Crowe et al. [51]'s experimental results on nozzle inlet indicate the pressure variation during experiments. Crowe and Willoughby [52] stated that the directly collected mass median diameter

from the motor and chamber is approximately 1 µm but more detailed data is obtained from Crowe and Willoughby and they are plotted in Figure 3.7. The vertical bars represent 35% error bounds of Hermsen's correlation for each computational case. Hermsen also included Crowe et al. [50]'s measurement to obtain his correlation, thus, Hermsen's correlation and Crowe et al.'s measurement are very close to each other. The experimental data that the average chamber residence time is greater than 15 is not plotted because different chamber residence time values mean that SRM chamber dimension is different and possibly different particle phase condition should be given. The details of measurement and calculated value from Hermsen's correlation are given in Table 3.9.

The averaged mass mean diameter at nozzle exit plane is obtained from the simulation. At 110 psi, it is observed that the separation occurs in the divergent section, accordingly no particle zone is created and large agglomeration is observed in high shearing region of oblique shock detached from the wall. More details on this overexpanded nozzle will be given in next chapter. The predicted results are presented in Figure 3.7 and we observed that the overall particle sizes from the cases simulated for larger pressures than 470 psi are smaller than experimental data and correlation. The details are given in Table 3.9 and they are approximately 30% smaller than correlation. However, the predicted D_{43} is within the standard deviation of correlation, 0.298, which is approximately ±35%.

This difference between experiment (or correlation) and simulation can be highly related to the collection method. Crowe et al. [50] and Shegal [53] used pressurized tank collection method which measures particle size attached to the tank wall after the motor is fired into the tank. The collision of particles onto the wall possibly causes the creation of large agglomeration at the wall. Other methods reported in Hermsen [10], such as petri dishes, brass post collector, and wetted plate collector, also impose the collision of submicron particles onto the large collector which creates stagnation point in the flow and results in the large agglomeration induced by high shearing motion of flow. The recent measurement done by Sambamurthi [61] used a dart launched across the plume, and the measurement of particles on the dart surface may impose the same effects.

Table 3.9 Details of predicted and measured mass mean diameters (µm) at nozzle exit plane of Crowe et al.[50]'s configuration

Case no.	measured		Hermsen	Simulation				
	D_{43}	σ_s		D_{43}	D_{43} error % to Hermsen	D_m	σ_s	σ_s error % to measured data
C-1	0.93	0.60	0.92	0.88	4.35	0.39	0.48	20
C-2	2.20	0.67	2.36	1.74	26.27	0.49	0.60	10.45
C-3-1	2.69	0.88	2.64	1.52	42.42	0.37	0.64	27.27
C-3-2				2.00	24.24	0.55	0.61	30.68
C-3-3				2.01	23.86	1.04	0.44	50.00
C-4-1	2.99	0.76	2.86	2.01	29.72	0.48	0.64	15.79
C-4-2				2.07	27.6	0.82	0.51	32.89

The details of predicted values of particle phase are provided in Table 3.9. Interesting results are also observed with 650 and 980 psi cases. Almost same mass mean diameters are obtained using inlet D_{43} conditions of 1.09 and 1.41 µm at 650 psi and 0.79 and 1.09 µm at 980 psi. This trend is very similar to the correlation which shows reduced variation of D_{43} as chamber pressure increases. This is due to the fact that the breakup process tends to occur a lot with larger inlet mass mean diameters. At the same time, the increase of inlet particle size results in the increase of breakup rate of large particle, so, the prediction shows less variation of D_{43} as the inlet D_{43} changes from 1.09 to 1.41 µm at 650 psi and from 0.79 to 1.09 µm at 980 psi. However, the predicted D_m of log-normal distribution shows large differences. As inlet D_{43} increases, the resultant D_m also increases. Accordingly, when the inlet D_{43} is large, the resultant particle phase contains large particles but the amount of large particles decreases due to the breakup of large particles. The decrease of standard deviation of resultant particle phase shows an agreement with this explanation. More details of inlet particle variation effects will be provided in next chapter.

To summarize, considering the error bounds of correlation, the predicted mass mean diameter is in agreement with the mass mean diameter obtained by Hermsen's empirical correlation. More details on code validation are provided in later section with respect to chamber pressure variation, particle concentration variation, and nozzle scale variation by comparing the predicted results with the correlation.
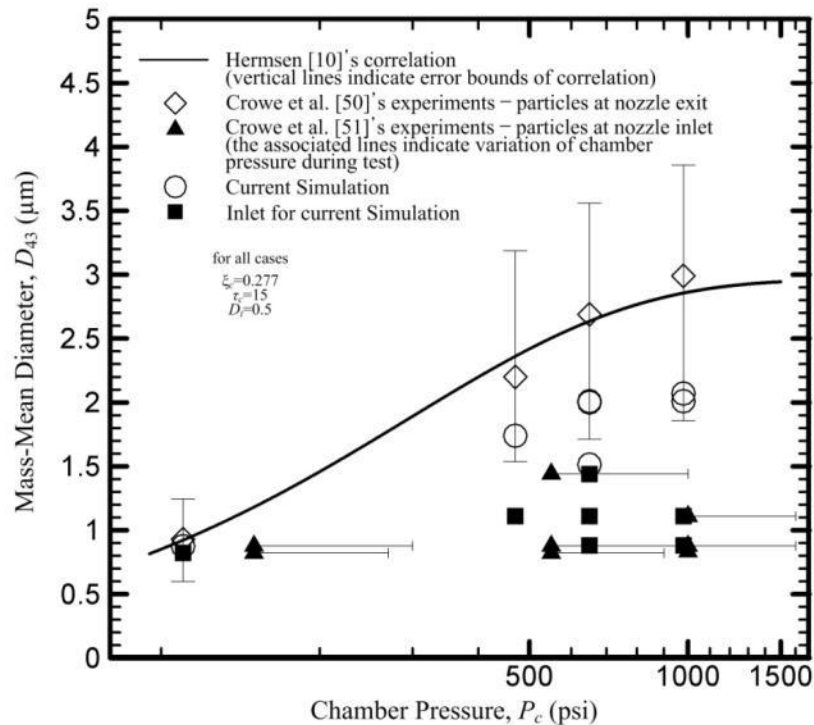
Figure 3.7 Comparisons of mass mean diameters at nozzle exit plane of Crowe et al.[68]'s configuration

3.3.6.2 Comparisons to the correlation for chamber pressure sensitivity

Since the gas density (and hence aerodynamic interactions between the droplets and the gas) is directly proportional to the chamber pressure, this variable is highly important when considering particle dynamics. The current modeling described previously was compared here to Hermsen's correlation and the dependence of mass mean diameter on the chamber pressure level was analyzed. A series of simulations was also performed to compare the results to the correlation under the nozzle configuration used by Shegal [53] for 150psi chamber pressure. The corresponding case numbers are from P-1 to 8 and the chamber pressures are varied from 150psi to 950psi.

The averaged value mass mean diameter at nozzle exit is compared with Shegal [53]'s experiments, Crowe and Willoughby [52]'s prediction, and Hermsen [10]'s correlation in Figure 3.8. The predicted results are mostly less than the measured results by Shegal. However, Dobbins and Strand [70] lately indicated that Shegal's experimental results did not agree with other measurements. Dobbins and Strand found that the particle size increases by a factor of 1.7 with a

ten-fold increase while Shegal's experimental results gave increases by a factor of 5 with a ten-fold increase, approximately. Therefore, it may not be meaningful to compare the prediction with Shegal's results.

Crowe and Willoughby's calculation which considered only the collision effect due to slip motion between a particle and surrounding gas and the momentum exchange from collision, also had lower values than Shegal's results. Crowe and Willoughby's calculation also included the effect of slip motion across the Mach disk as well as slip motion while the particles passing through the nozzle. Their assumption on the particle growth across a normal shock wave was as follows: the smaller particles decelerate rapidly while the larger particles decelerate more slowly, thus, the larger particles overtake the smaller particles and the collision results in the continuous particle growth [52]. However, they did not include the breakup of particles across the shock wave as the particles experience the strong aerodynamic forces while passing through the shock wave due to the acceleration or deceleration. The particle growth across the shock wave was studied in this study and the results given in next chapter shows both of growth and decay present across the shock wave at the same time. Even if the only collision effect was considered in Crowe and Willoughby's calculation, the predicted particle size was still smaller than Shegal's results.

The nozzle inlet conditions reported by Fein [54] for Shegal's 150 psi case was 0.240 of the particle concentration, 4.15 ms of the particle residence time, and 0.79 μm of the mass mean diameter. Using these initial conditions, the simulation was performed for various pressures and Hermsen's correlation was calculated. The results are shown in Figure 3.8. Over all chamber pressures considered, the variation trend is similar to Hermsen's correlation. The predicted results are larger than the results from Hermsen's correlation when the pressure is lower than 550 psi and vice versa. However, the predicted values are within the error bounds of Hermsen's correlation (35%) over 350 psi chamber pressure and the variation trends over 650psi is very close to Hermsen's correlation.

The details of predicted values of particle phase are provided in Table 3.10. When the considered chamber pressure is over 750 psi, the error percentage to the Hermsen's correlation is almost consistent and the value is approximately 14%. Interestingly, both of the predicted D_m and σ_s values increase with chamber pressure.

Table 3.10 Details of predicted and measured mass mean diameters (μm) at nozzle exit plane of Shegal [53]'s configuration according to the chamber pressure variation

Simulation case No.	Measured		Hermsen	Simulation			
	Pressure	D_{43}		D_{43}	D_{43} error % to Hermsen	D_m	σ_s
P-1	150	1.5	0.40	0.87	117.50	0.29	0.56
P-2	200	2.0	0.65	0.94	44.62	0.29	0.58
P-3	277	2.5	0.87	1.01	16.09	0.29	0.60
P-4	365	3.0	1.08	1.10	1.85	0.30	0.61
P-5	500	3.5	1.27	1.19	6.30	0.30	0.63
P-6	700	4.1	1.45	1.29	11.03	0.31	0.64
P-7	N/A	N/A	1.61	1.39	13.66	0.33	0.64
P-8	N/A	N/A	1.76	1.51	14.20	0.34	0.65
P-9	1000	4.75	1.90	1.63	14.21	0.37	0.65
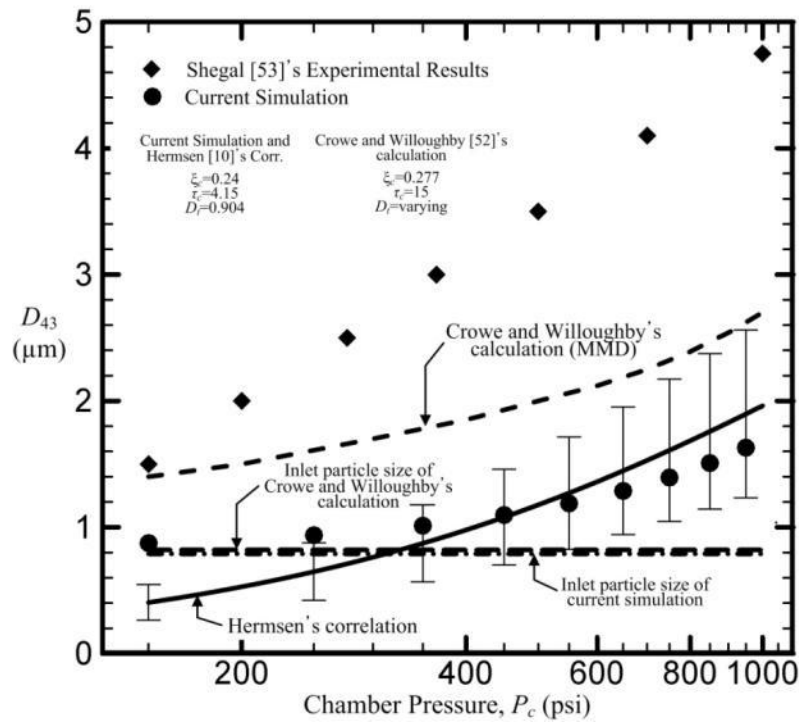
Figure 3.8 Predicted and measured mass mean diameter at nozzle exit plane of Shegal [53]'s experimental configuration according to the chamber pressure variation

3.3.6.3 Comparisons to the correlation for particle concentration sensitivity

Changes in particle concentration (via aluminum loading) have obvious implications for the collision rates within a given flowfield. The current modeling described previously was compared here to Hermsen's correlation and the dependence of the particle concentration in the chamber was analyzed. A series of simulations was performed to compare the results to the correlation under the nozzle configuration used by Shegal [53] for 150 psi chamber pressure. The corresponding case numbers are from M-1 to 6 and the particle concentrations in the chamber are changed from 0.12 to 0.32 gmol/100 g.

The predicted mass mean diameter at nozzle exit is compared with Hermsen's correlation in Figure 3.9. The variation trend is very similar to Hermsen's correlation over all particle concentrations used in simulations, but the predicted results are larger than the results from Hermsen's correlation when the particle concentration is below 0.16. When the particle concentration is 0.12, the predicted value is 22% below Hermsen's correlation. Overall, simulation results are within error bounds of Hermsen's correlation for all considered particle concentrations.

Crowe and Willoughby [52] also performed the similar studies and the results are also presented in Figure 3.9. In their calculation, they used the configuration given by Crowe et al. [50] and the chamber conditions were different from Shegal's configuration. The chamber pressure was 600 psi, the particle residence time was 15 ms, and the nozzle diameter was 0.5 inch. Due to the absence of the resultant standard deviation it was not able to calculate the mass mean diameter from mass median diameter, therefore, the mass median diameters are presented in Figure 3.9. Accordingly, their predicted values should be higher than the presented values in Figure 3.9 but it is expected that the amount of difference is small. Under the same chamber condition as Crowe and Willoughby, Hermsen's correlation is also presented. As shown in Figure 3.9, their predictions on the particle concentration of 0.28 and 0.35 are out of Hermsen's error bound. Details of Hermsen's correlation and predictions are presented in Table 3.11.

Even if it is considered that their prediction is mass median diameter, their results are significantly smaller than Hermsen's correlation. It should be noted here that Crowe and Willoughby predicted the particle size at two locations of nozzle exit and shock wave, whereas their predictions are located at shock wave in the previous section, the pressure sensitivity, their predictions here are located at nozzle exit. Basically, Hermsen's correlation does not impose the

particle growth across the shock wave of the under-expanded and perfect-expanded nozzles. Therefore, it is quite obvious that their prediction is small comparing to Hermsen's correlation. In the current simulation of Shegal's configuration, the nozzle is always under-expanded over all considered chamber conditions.

The details of current simulation are provided in Table 3.12. When the particle concentration is over 0.16, results are within 4-15% of Hermsen's correlation. Similarly to the sensitivity to pressure change, both of the predicted D_m and σ_s increases at the same time as the particle concentration increases.

Table 3.11 Comparisons of Crowe and Willoughby's calculation and Hermsen's correlation of Crowe et al. [68]'s configuration according to the particle concentration variation

Mole concentration (g-mole/100g)	Hermsen (D_{43})	MMD
0.087	1.40	1.30
0.173	2.13	1.46
0.277	2.58	1.60
0.346	2.73	1.70

Table 3.12 Details of predicted and measured mass mean diameters (µm) at nozzle exit plane of Shegal [71]'s configuration according to the particle concentration variation

| Simulation case no.	Her msen	D_{43}	D_{43} error % to Hermsen	D_m	σ_s
M-1	0.82	1.00	21.95	0.29	0.60
M-2	1.05	1.09	3.81	0.29	0.61
M-3	1.26	1.19	5.56	0.30	0.63
M-4	1.45	1.29	11.03	0.31	0.64
M-5	1.62	1.40	13.58	0.33	0.64
M-6	1.78	1.51	15.17	0.35	0.65
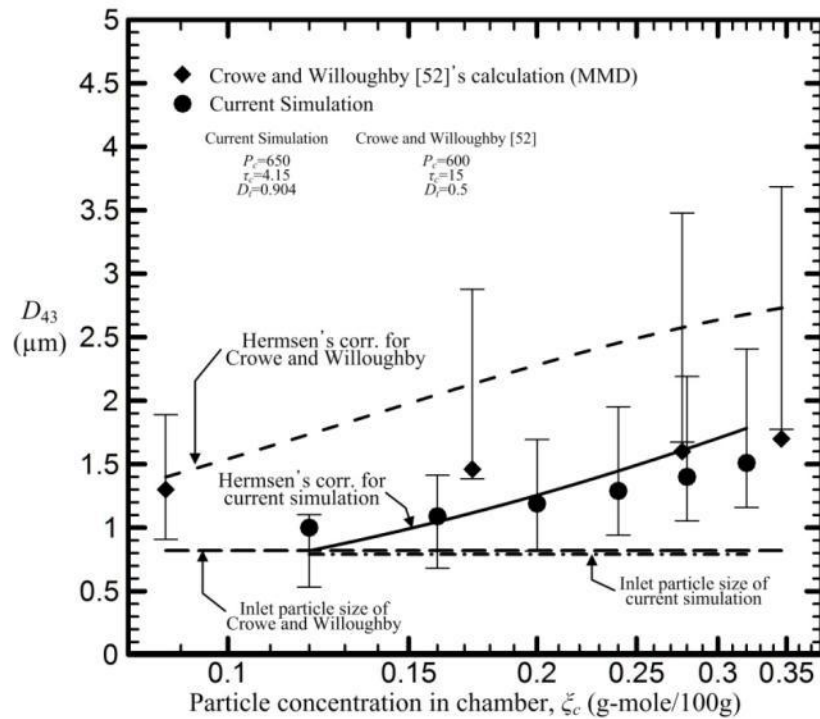
Figure 3.9 Predicted and measured mass mean diameter at nozzle exit plane of Shegal [53]'s experimental configuration according to the particle concentration variation

3.3.6.4 Comparisons to the correlation for nozzle scale sensitivity

A last series of simulations for the validation purpose were performed to assess the effect of nozzle scale on the mass mean diameter using the nozzle configuration used by Shegal [53] for 150 psi chamber pressure. As discussed in Crowe and Willoughby [52], an increase in nozzle scale gives longer particle residence time in the nozzle, which implies more opportunity for coalescence via particle collisions. The corresponding case numbers are from S-1 to 5.

The predicted mass mean diameter at nozzle exit is compared with Hermsen's correlation in Figure 3.10. The variation trend is very similar to Hermsen's correlation in small scale nozzles, as the mass mean diameter increases with an increase of nozzle scale. Over all nozzle scales, the results are in 35% error bounds of Hermsen's correlation. Within ten-fold increase of nozzle size, Hermsen's correlation increases by a factor of 1.96 and the current simulation increases by a factor of 1.75. As shown in Figure 3.10 and Table 3.13, Crowe and Willoughby [52]'s prediction shows smaller particle size than Hermsen's correlation as nozzle scale increases. When the considered nozzle throat diameter is over 3.616 in., the error percentage to the Hermsen's

correlation is very consistent and the value is approximately 20%. Interestingly, the predicted D_m increases continuously as nozzle scale increases but the predicted σ_s increases until the nozzle diameter of 3.616 in. and decreases as the nozzle scale increases above the diameter of 5.424 in. This means that the log-normal particle number distribution becomes narrow while the diameter of particles holding large numbers in the number distribution increases.

Table 3.13 Comparisons of Crowe and Willoughby's calculation and Hermsen's correlation of Crowe et al. [50]'s configuration according to the nozzle scale variation

Nozzle throat diameter (in)	Hermsen (D_{43})	MMD
0.25	2.10	1.48
0.5	2.57	1.60
1.0	3.16	1.88
3.0	4.36	2.1

Table 3.14 Details of predicted and measured mass mean diameters (μm) at nozzle exit plane of Shegal [53]'s configuration according to the nozzle scale variation

Simulation case no.	Hermsen	D_{43}	D_{43} error % to Hermsen	D_m	σ_s
S-1	1.45	1.29	11.03	0.31	0.64
S-2	1.77	1.46	17.51	0.33	0.65
S-3	2.17	1.73	20.27	0.37	0.66
S-4	2.44	1.94	20.49	0.44	0.65
S-5	2.66	2.11	20.67	0.50	0.64
S-6	2.84	2.26	20.42	0.56	0.63
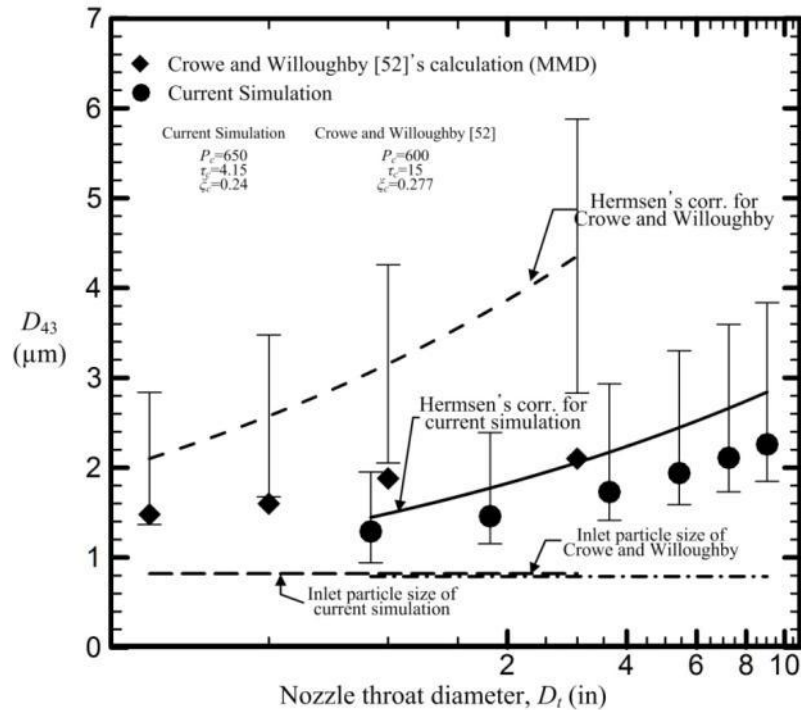
Figure 3.10 Predicted and measured mass mean diameter at nozzle exit plane of
Shegal [53]'s experimental configuration according to the nozzle scale variation

3.3.7 Summary and conclusions

A series of simulations was carried out to validate the numerical model against the experimental data and empirical correlation for typical supersonic rocket nozzles. The comparisons of predicted mass mean diameter with the experimental data showed a noticeable difference and the predicted value for overall considered cases tends to be smaller than the experimental data. However, it was noted that the collection methods in experiments generally caused the very high shearing motion of flow above the collection surface and it might result in the agglomeration and creation of larger particles. In addition, considering the error bounds of correlation, the predicted mass mean diameter was in agreement with the mass mean diameter obtained by empirical correlation. Further validations performed on the effects of chamber pressure, particle mass concentration, and nozzle scale showed a good agreement with empirical correlation and mass mean diameter variation trends were very similar to the behavior of the empirical correlation.

3.4 Parametric studies

3.4.1 Baseline case

3.4.1.1 Gas phase flow fields

Due to the assumed one-way coupling between the gas and particle phase, the flow field is undisturbed by the particle phase. The geometry and mesh presented in Figure 3.5 is employed. The steady solutions of gas phase density, Mach number, and, turbulent parameters of kinetic energy k and specific dissipation rate ω, are given in Fig. 3.11. As it is already shown by prior researchers for supersonic nozzle flow [71, 72], the turbulent kinetic energy has a peak in the throat region. The energy dissipation rate grows as the flow progress downstream from the inlet and is larger near wall. Thus, the small turbulent eddies are developed near the wall and the particles are more likely to be immersed in the inertial subrange of turbulence near wall as Kolmogorov micro length scale becomes small in this region due to high specific energy dissipation rate (η ranges from 5 to 15 μm in the divergent section). As explained in Section 3.2, the effect of local shear rate in this turbulent subrange can be significantly smaller than the effect of slip based on the large relaxation time induced by the larger density of metal drops comparing to the time scale of the small eddies. In contrast to the near wall region, the small energy dissipation rate and large kinetic energy near main stream imposes that the size of smallest eddies is large and the drops are in viscous subrange.

(a) Density ρ (kg/m^3)

(b) Mach number

(c) Turbulent Kinetic energy k (m^2/s^2)

(d) Specific energy dissipation ω (1/s)
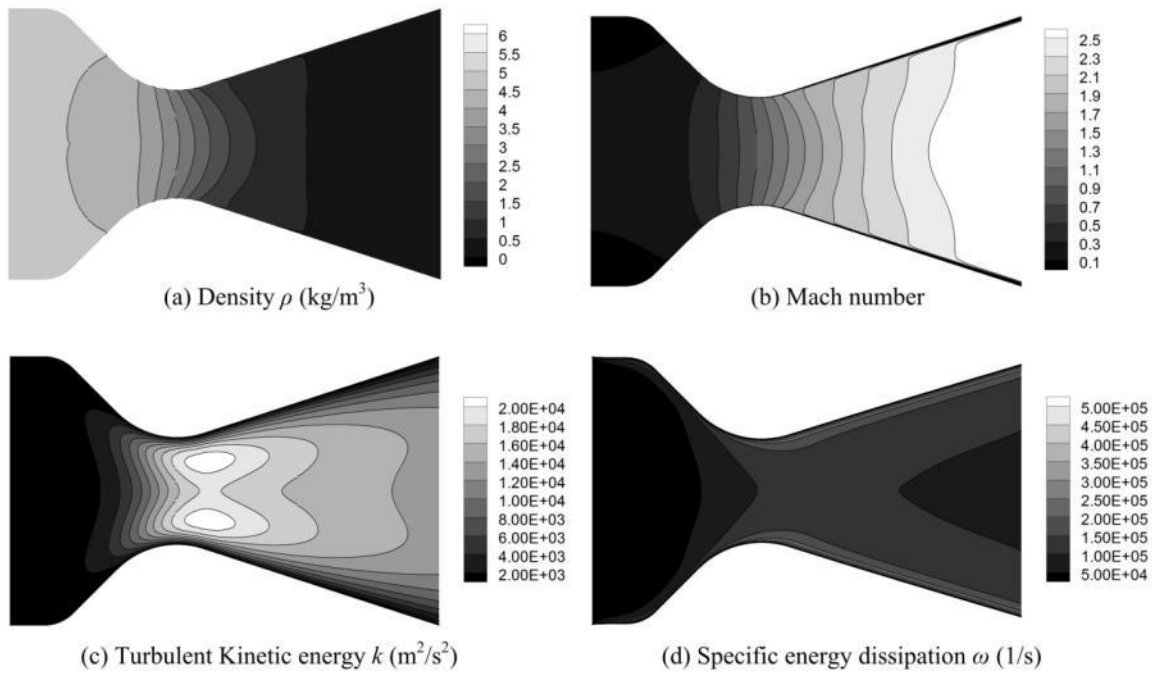
Figure 3.11 Gas phase flow variation in a rocket nozzle, case no. C-3-2; (a) density ρ (kg/m^3), (b) Mach number, (c) turbulent kinetic energy k (m^2/s^2), and (d) specific dissipation rate (1/s)

3.4.1.2 Statistics of the particle phase

Once the steady solution is obtained, the volume fraction, mass fraction, and mass mean diameter (D_{43}) contours over the entire computational domain are obtained for case no. C-3-2 and presented in Figure 3.12. The inlet boundary conditions are presented in Table 3.4. The D_{43} in (c) of Figure 3.12 shows that the growth of particles starts from the wall in converging section. The large agglomerates detached from the wall in converging section experience more growth while passing through the throat region. The large inertia of large particles passing the throat region inhibit influence by the gas phase and they tend to not react to curvature introduced in the nozzle profile. Accordingly, the maximum growth occurs downstream of the throat and far off the wall. The breakup mechanism due to slip velocity could be balanced with collision, then the mass mean diameter approaches becomes almost constant at far downstream. Accordingly, the balancing region between collision and breakup is the divergent section with more dominant effect of collision at the location near the throat.

Similar results were observed in 1-D calculations from Crowe and Willoughby [52] that considered only collision due to slip velocity and momentum exchange between particles and

Jenkins and Hoglund [7] that considered only collision due to slip velocity and turbulent acoustic field and growth due to condensation. Crowe and Willoughby [52]'s calculation showed that the growth starts in the nozzle convergence section, and the particle size keeps increasing to points far downstream. The largest growth occurs in the convergent section. Jenkins and Hoglund [7] showed that the growth starts from the slightly upstream from the throat and the largest growth occurs when the particle pass the throat region. Jenkins and Hoglund's calculation is much closer to the current prediction than Crowe et al..

In addition, Chang [73] showed a similar result of particle trajectory. In his 2-dimensional two-phase Eulerian simulation, 1 µm particles effectively turn around the nozzle throat whereas 20 µm particles do not turn around the throat corner and a distinctive particle-free zone appears near the wall [73]. Details of particle streamlines for current simulation are provided in Figure 3.13. The particle sizes in DQMOM can be characterized by three phases, l_1 , l_2, and l_3, when the order of DQMOM is 3 (N=3). The large and heavy particles which are l_3 phase in DQMOM calculation are detached earlier than other phases and the detachment point is located in the middle of convergent section. Whereas the l_2 phase which holds medium size and weight is detached at slightly upstream from the throat, it looks like the smallest particle phase l_1 follows the gas phase streamline. This explains why the particle size becomes smaller near the wall downstream than the center region as it is shown in (a) of Figure 3.12. At the same time, it is obvious that the divergence of velocity increases fast along the axis, the particle growth occurs slowly and smaller particles can pass the throat in this region.

The computed mass and volume fractions of particle are presented in (b) and (a) of Figure 3.12. As the gas phase significantly expanded at the divergent section and the density of the gas decreased along the axis, the volume fraction keeps decreasing at the downstream. At the region of particle detachment, particles are collapsed in a small region due to the detachment, accordingly, it is observed that large volume and mass fractions. The mass fraction keeps increasing axially at the downstream due to the decrease of gas density. The small amount of particle mass and volume exists within the wall boundary layer at downstream because the large and heavy particles are not transported to this region.

(a) volume fraction
(V_p/V_g)

	1.40E-03
	1.29E-03
	1.18E-03
	1.07E-03
	9.60E-04
	8.50E-04
	7.40E-04
	6.30E-04
	5.20E-04
	4.10E-04
	3.00E-04
	1.90E-04
	8.00E-05

(b) mass fraction
(M_p/M_g)

	0.70
	0.65
	0.60
	0.55
	0.50
	0.45
	0.40
	0.35
	0.30
	0.25
	0.20
	0.15
	0.10

(c) D43
(µm)

	3.00
	2.85
	2.69
	2.54
	2.38
	2.23
	2.08
	1.92
	1.77
	1.62
	1.46
	1.31
	1.15
	1.00
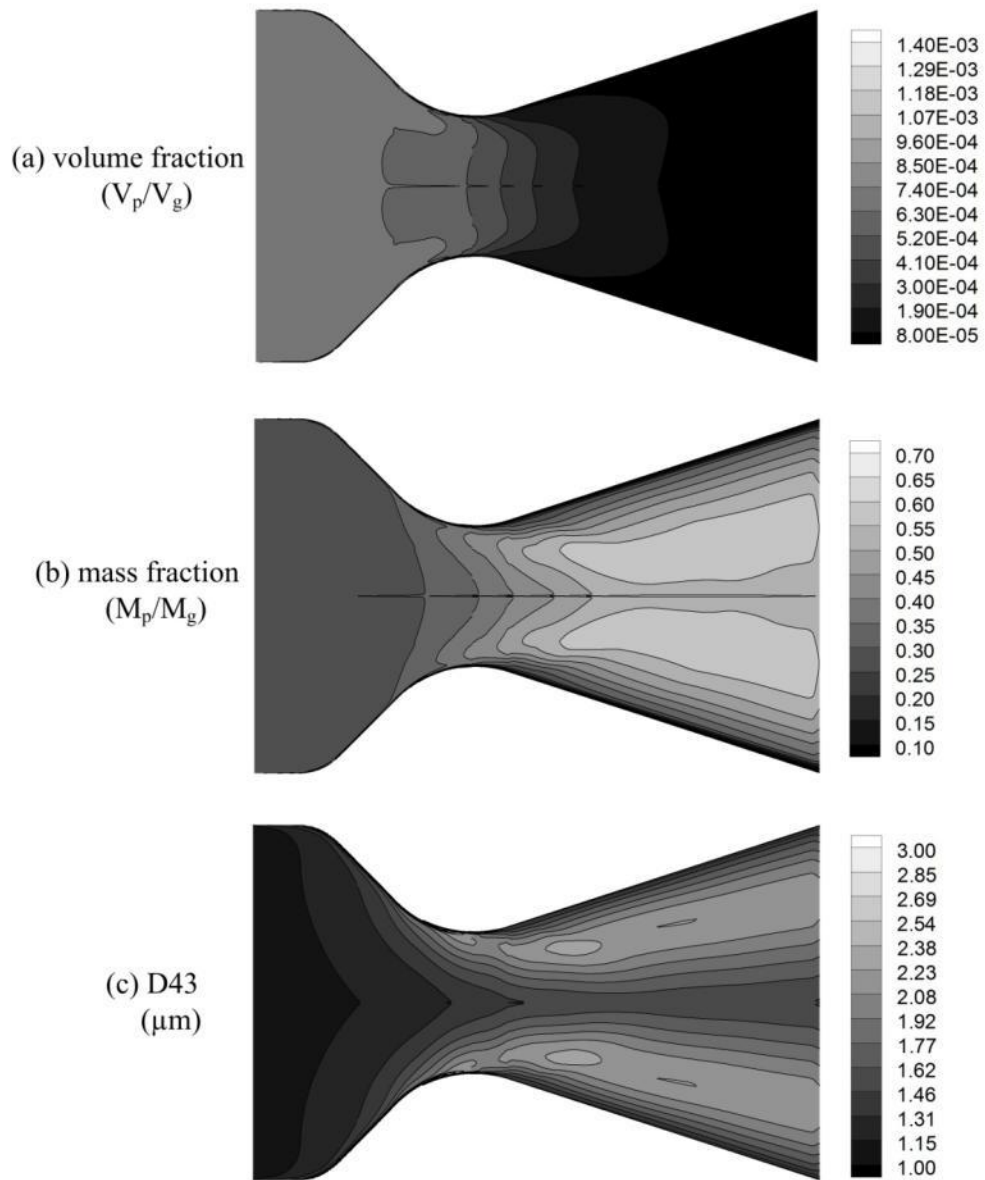
Figure 3.12 Predicted (a) volume fraction, (b) mass fraction, and, (c) mass mean diameter (D_{43}) for case no. C-3-2

(a) particle l_1 streamline
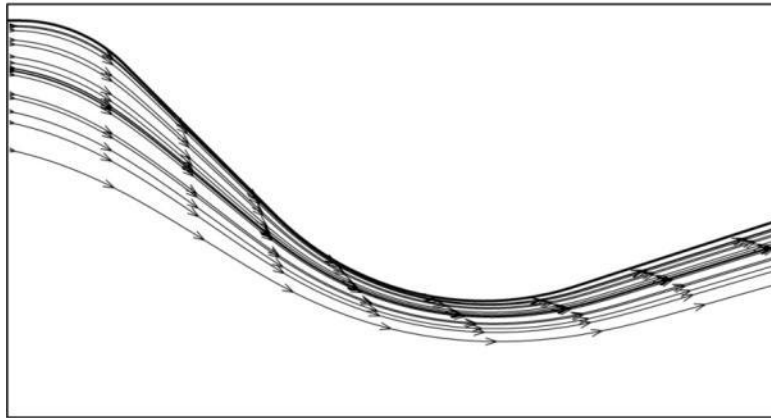
(b) particle l_2 streamline

Detachment point
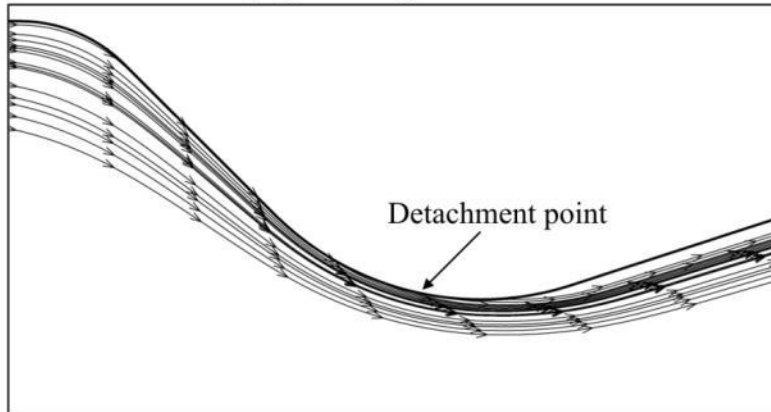
(c) particle l_3 streamline

Detachment point
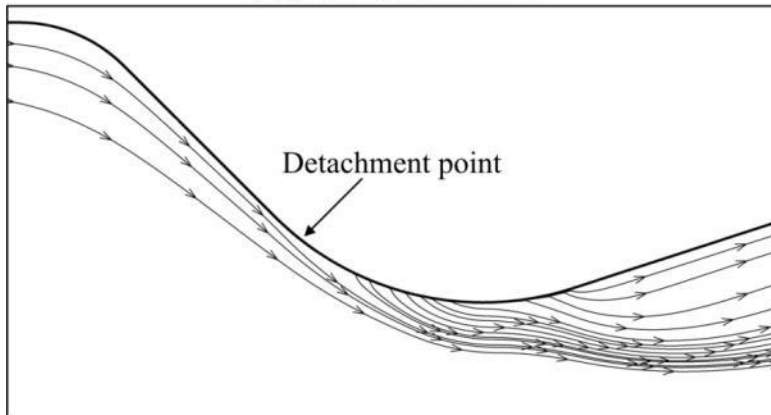
Figure 3.13 Predicted particle phase streamlines for case no. C-3-2 and *N*=3 DQMOM calculation

The variation of the D_{43} at the wall can be an important observation point considering the nozzle wall erosion due to the existence of the particle phase. Figure 3.14 shows the D_{43} variation along the centerline (a) and wall (b). Parts (a) and (b) of Figure 3.15 show the radial variation of mass fraction and D_{43} at various axial locations. In (b) of Figure 3.14, it is clearly observed where the larger particles started to be detached from the wall (vertical line near x=0 in Fig. 3.14b). However the remaining smaller particles continue undergoing collisions up to the throat. At the throat, all of particles are completely detached from the wall and no particle zone right above the downstream wall is created. In (a) of Figure 3.14, it is clearly identified where the most of particle growth occurs along the centerline. In analogy with Crowe et al., the most of growth occurs in the convergent section and slight amount of growth after the throat is observed. However, as described above, the current 2-D simulation shows that the maximum growth occurs at the location of downstream from the throat and off the wall. Details of radial variation of particles presented in Figure 3.15 verify the above explanations.
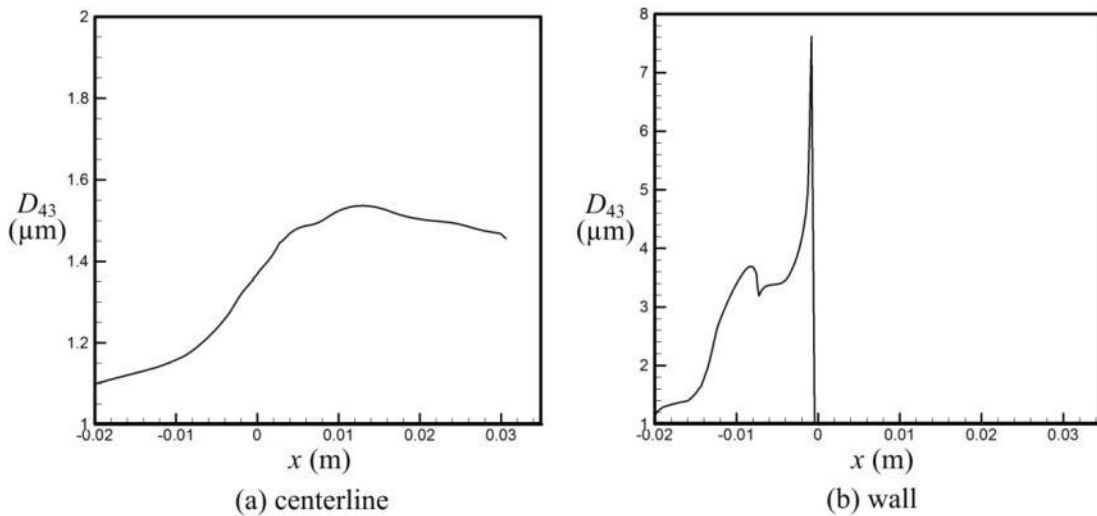
(a) centerline   (b) wall

Figure 3.14 Predicted mass mean diameters (D_{43}) along (a) centerline and (b) wall for case no. C-3-2
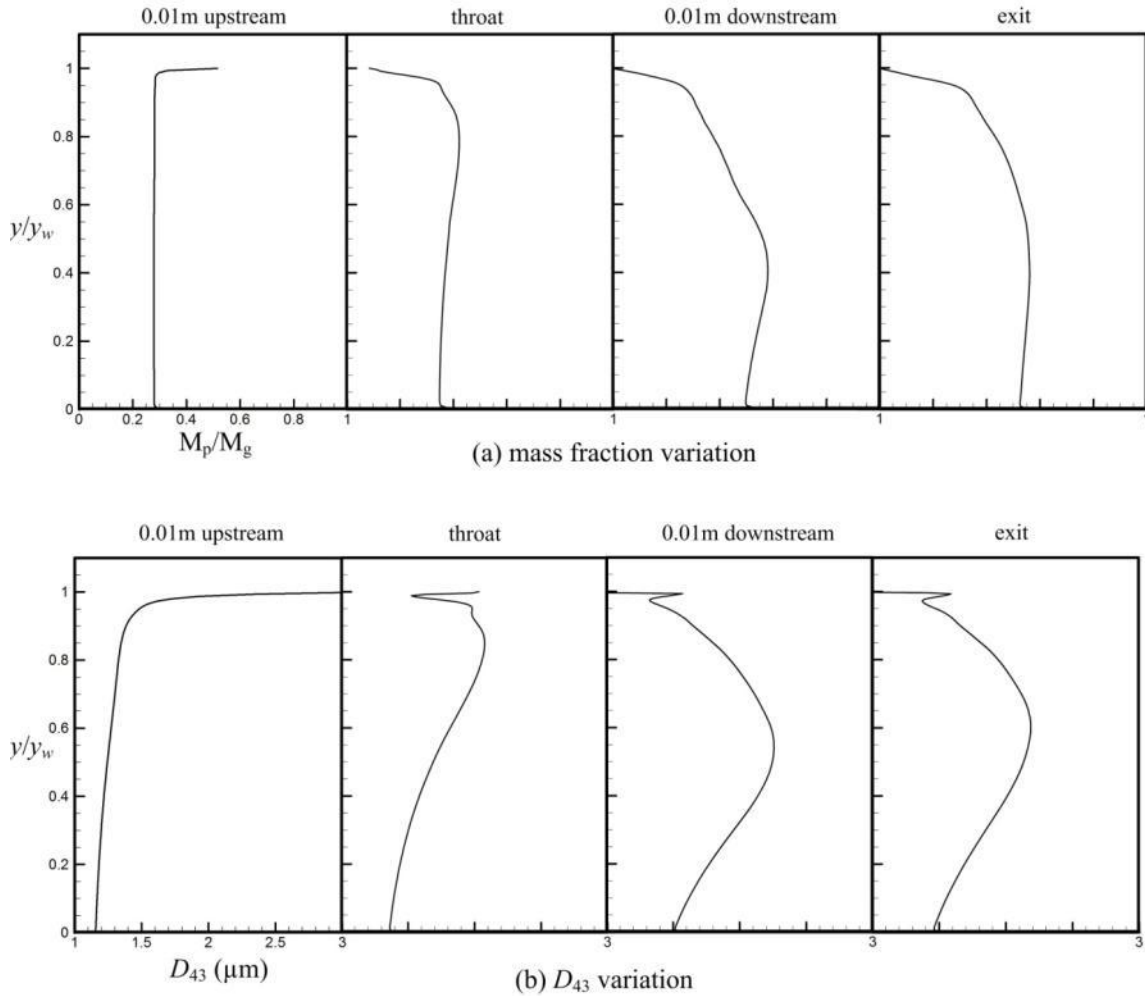
Figure 3.15 Predicted radial variation of (a) mass fraction and (b) mass mean diameters (D_{43}) at various locations for case no. C-3-2

3.4.1.3 Relative velocities

To assess the detailed influence of the various agglomeration mechanisms, we compare the relative velocities that lead to collisions. Particle-to-particle relative velocities ($\langle W_{S,r} \rangle$ and $w_{S,r}$ due to shearing motion, $\langle W_{I,r} \rangle$ and $w_{I,r}$ due to inertial motion) and velocity differences across a droplet (ΔU_S and Δu_S due to shearing motion, ΔU_I and Δu_I due to inertial motion) which are responsible for collision and breakup. The comparisons are presented in Figures 3.16 and 3.17.

Because the collision and breakup of particles are highly stochastic, are subject to the conditions in surrounding gases, and are dependent on the particle concentration, the direct comparison of above velocities does not explain which collision and breakup mechanisms are

dominant and responsible to the resultant particle size. However, by comparing above velocities, it may further increase the understanding of particle dynamics in a rocket nozzle.

As expected, no discernible variation of shearing relative velocities is observed in the main flow region which is far above the boundary layer. Thus, we plotted above relative velocities in the near regions of boundary layer at 0.01 m upstream from the throat, throat and 0.01 m downstream from the throat, and exit for the baseline case in Figure 3.16. The relative velocities between particles are for l_2 and l_3 in the current simulation of $N=3$ in DQMOM approximation and the velocity difference across a droplet and the velocity difference between a particle and surrounding gas are for l_3 particles. The largest shearing relative velocity is $w_{S,r}$ for converging (part (a)) , throat (part (b)), downstream (part (c)) regions, and nozzle exit (part (d)). Most of shearing occurs in the divergent section where the core stream velocity is higher. The shearing motion accounting for the compressible effect in laminar flow incurred by accelerating flow motion in the convergent section does not show a significant contribution to the shearing relative velocities as shown in (a) and (b). At the very near the wall in the divergent section, the shearing relative velocities radially decrease as the amount of l_3 particle phase becomes small.

The inertial relative velocities, shown in Figure 3.17, also radially decrease within boundary layer. The inertial relative velocity in turbulent motion $w_{I,r}$ shows a larger amount than $\langle W_{I,r} \rangle$ and the inertial relative velocity in laminar flow $\langle \Delta U_I \rangle$ is larger than $\Delta u_{I,r}$ almost over the entire domain. So, it can be expected that the dominant collision mechanism is turbulent inertial collision and the dominant breakup mechanism is laminar inertial breakup.

Moreover, the inertial relative velocities are also widely distributed over the entire domain, so the contours are presented in Figures 3.18 and 19. Figure 3.18 shows the collisional relative velocities between l_2 and l_3 particles and Figure 3.19 shows the relative velocities between l_3 particle and gas phase which is responsible for the breakup. Whereas the shearing collisional relative velocity in laminar motion $\langle W_{S,r} \rangle$ shows the large amount in convergent section in (a) of Figure 3.18, the maximum points of other collisional relative velocities are located in the slightly downstream from the throat. The maximum locations of all slip velocities are also in the divergent section slightly after the throat as shown in Figure 3.19. The slip velocities are widely distributed in divergent section but they are also developed in the convergent section starting

from the slightly upstream from the throat. Therefore, it can be identified that the region of most active collision/breakup processes in the nozzle is the slight downstream from the throat where the nozzle wall starts to diverge.
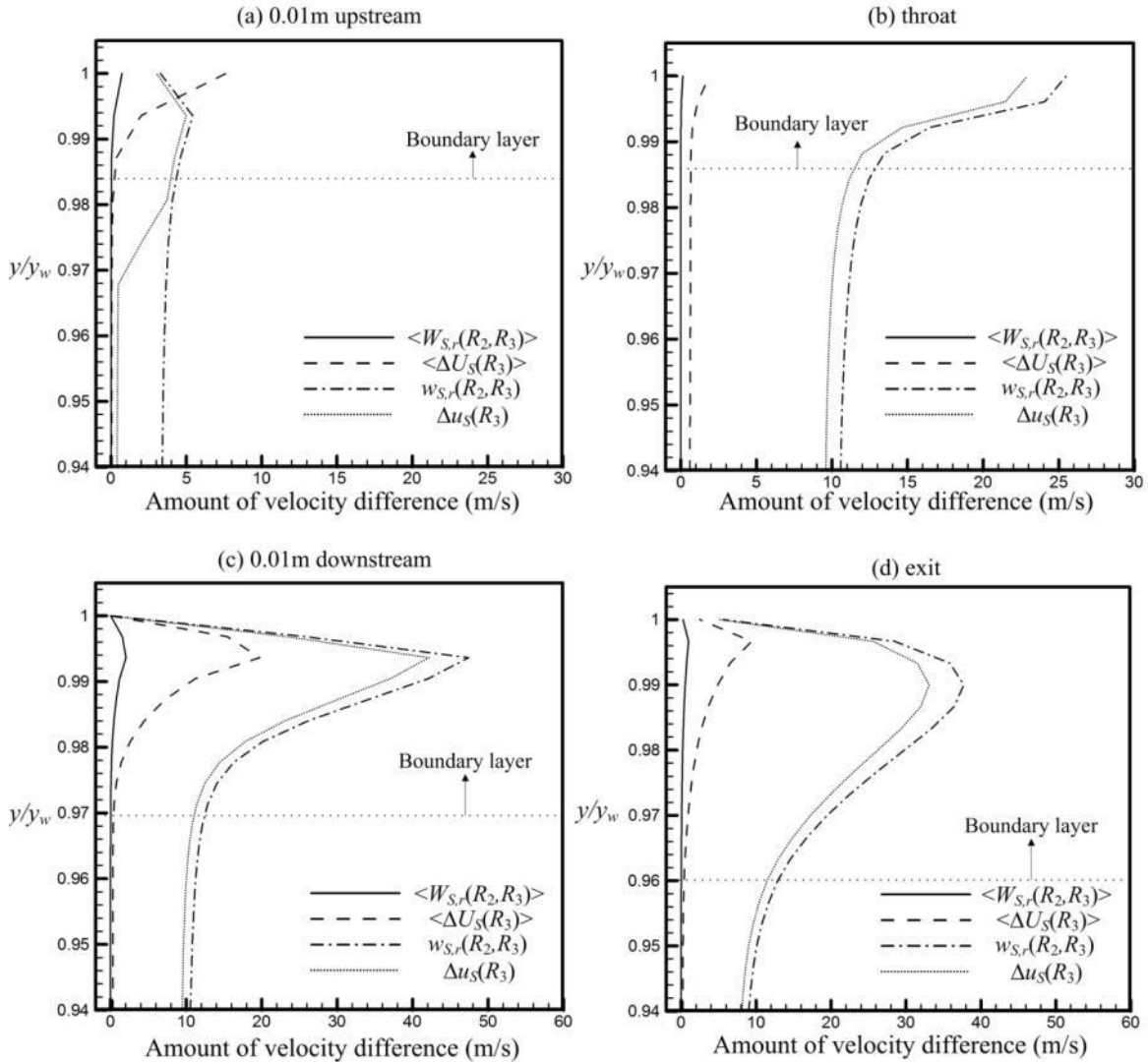

Figure 3.16 Computed shearing relative velocities in mean and turbulent flows at various locations for case no. C-3-2
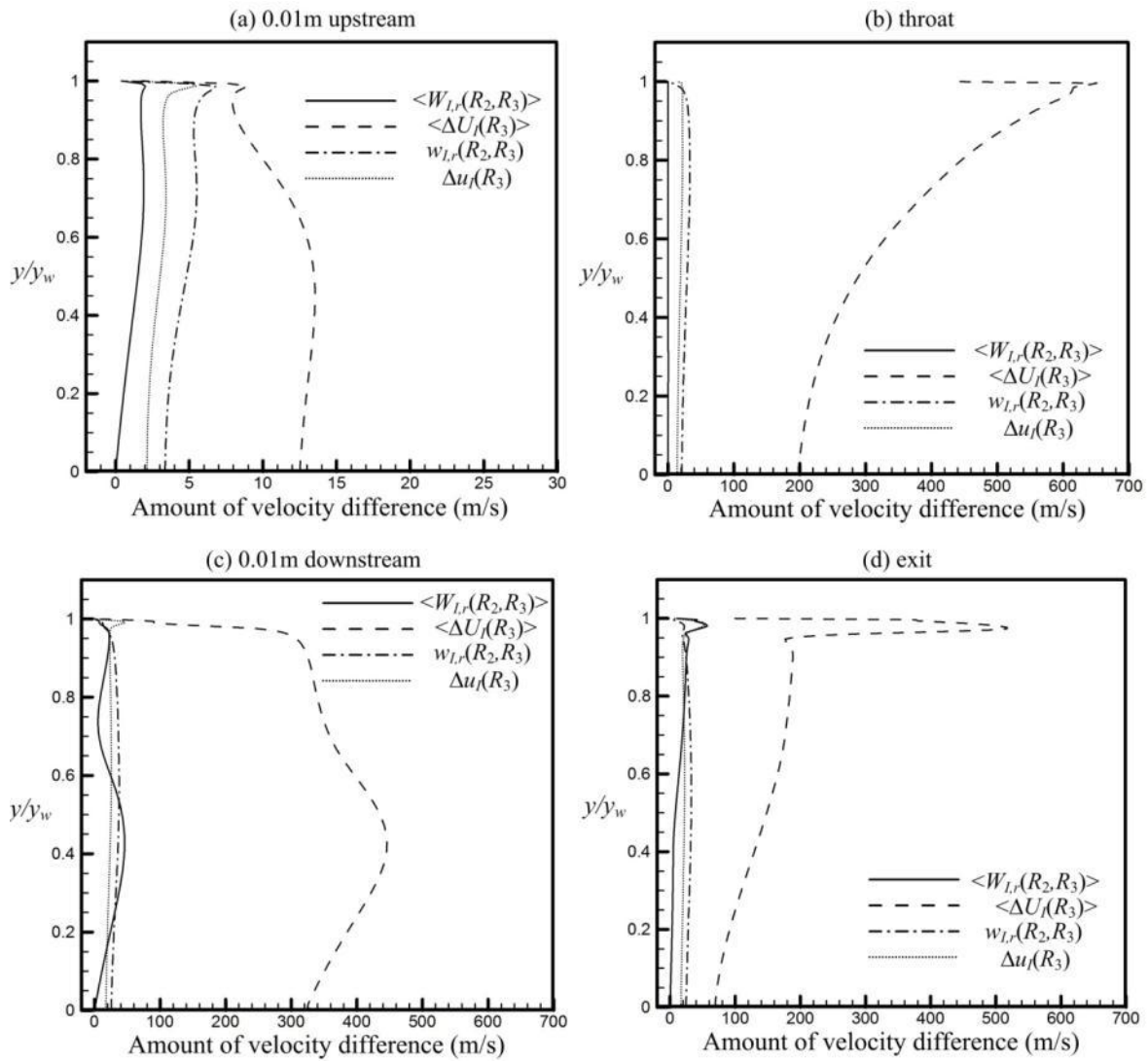
Figure 3.17 Predicted inertial relative velocities in mean and turbulent flows at various locations for case no. C-3-2
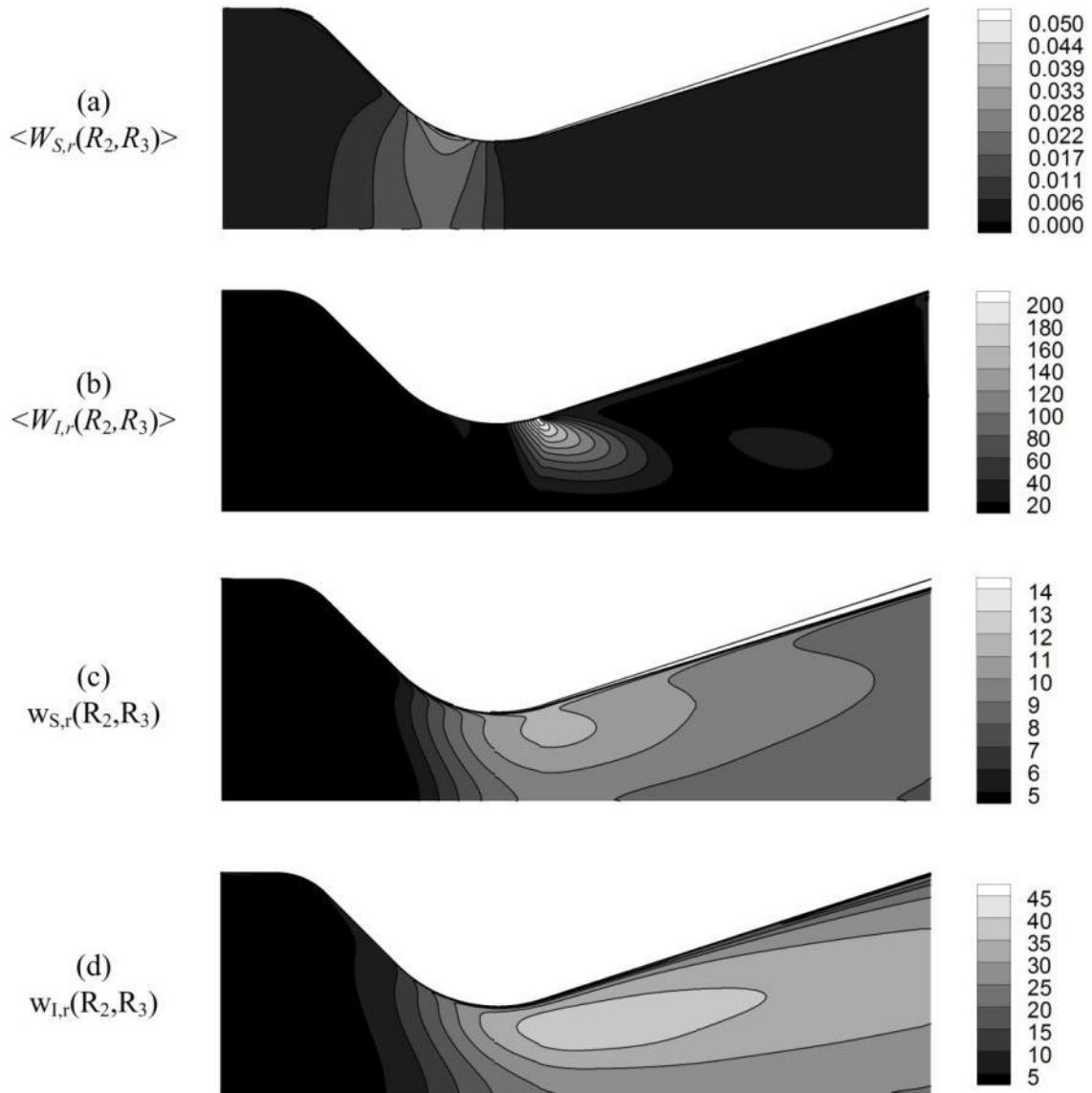
Figure 3.18 Predicted collisional relative velocities in mean and turbulent flows over entire domain for case no. C-3-2 (units: m/s)
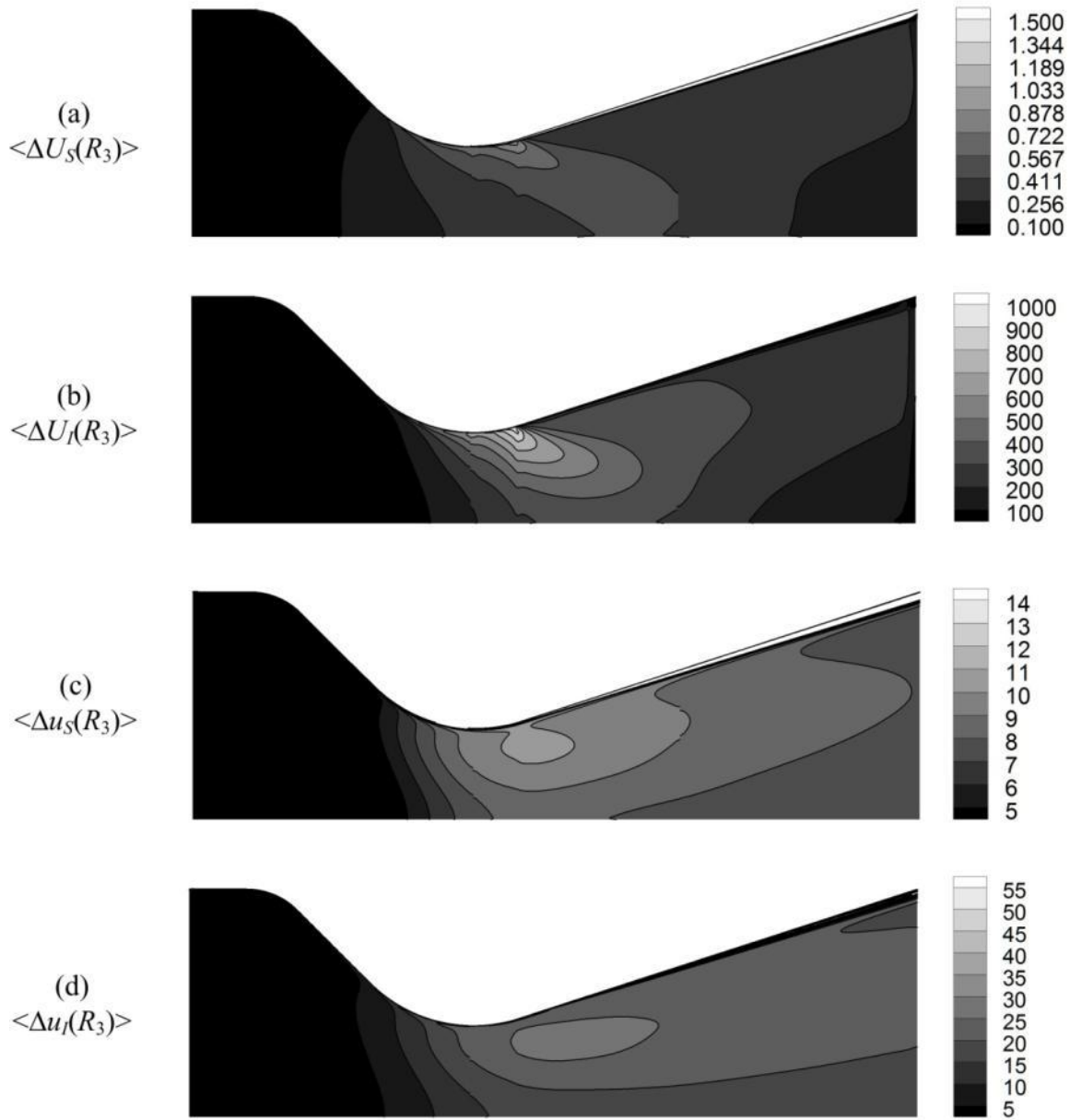
Figure 3.19 Predicted slipping relative velocities in mean and turbulent flows over entire domain for case no. C-3-2 (units: m/s)

3.4.1.4 Mean flow and turbulent flow effects

Results from the baseline simulation can be assessed to identify which collision or breakup mechanisms are dominant in the nozzle. The mass mean diameter contours considering only mean flow collision/breakup effect and only turbulent collision/breakup effect are provided in (a) and (b) of Figure 3.20. Collisions due to mean flow effects occur significantly in the divergent section after the throat, while collisions due to turbulent flow effects occur mostly in the throat region. Therefore, the maximum D_{43} in turbulent case is located at far upstream as compared to the mean flow case. Details of predicted D_{43} are provided in Table 3.15. The D_{43} values at the nozzle exit plane from both cases are significantly smaller than the case considering both effects at the same time. The errors with respect to Hermsen's correlation are 45, 42, and 24% for the cases with only mean flow effect, only turbulent effect, and both effects, respectively. Accordingly, it can be concluded that both of mean and turbulent effect on the collision/breakup processes in a high Reynolds number flow are important.

Another interesting difference between mean flow and turbulent flow cases is the D_{43} behavior near the centerline. Whereas the D_{43} contours show a cusped shape near the centerline in mean flow case, a smoother behavior is noted in the turbulent flow case. Because of the assumption that only two directional components of slip velocity are responsible for the inertial collision in an axisymmetric mean flow, the velocity component in r-direction acts on a plane surface instead of curvature surface of cylindrical fluid element. Due to this assumption, the collision frequency is underpredicted along the centerline in an axisymmetric simulation. However, as negligible mass is present in this very small region, global results are still meaningful. This issue may be easily resolved in 3-D simulation.

More details on the variation of mass mean diameter in a radial direction are provided in Figures 3.21-23 to assess how collision/breakup mechanisms are distributed. Figure 3.21 illustrates the variation of D_{43} at the 0.01 m upstream from the throat. As explained above, this location is in a region where wall impingement occurs, and thus the particle size keeps increasing to the wall within boundary layer. Comparing the results from mean flow and turbulent flow with the case considering total effects, it can be concluded that this increase is due to the turbulent effects. The collision and breakup due to mean flow effect is very small in this region. Moreover, this increase is mainly due to both of shearing and inertial collision as shown in Figures 3.16 and 3.17. At the throat, in Figure 3.22, we observed 4 zones in a radial direction. In the first zone, the

variation of mass mean diameter is very small and the collision and breakup are balanced well in a radial direction. In the second zone, the inertial collision due to turbulent flow has an influence until a certain location above the boundary layer. Then, the inertial breakup due to mean flow effects is dominant than other collision mechanisms in the third zone, accordingly the decrease of particle size is observed. In the fourth zone within boundary layer, shearing collision due to turbulence is dominant and the particle size increases.

At the 0.01 m location downstream from the throat in Figure 3.23, inertial collisions due to mean flow effects and inertial breakup due to mean flow and turbulent flow are prominent in the main stream. The turbulent shearing collision due to turbulence takes place within the boundary layer.

(a) D_{43} with mean flow effect   (b) D_{43} with turbulent flow effect

| 1 | 1.08 | 1.16 | 1.24 | 1.32 | 1.4 | 1.48 | 1.56 |
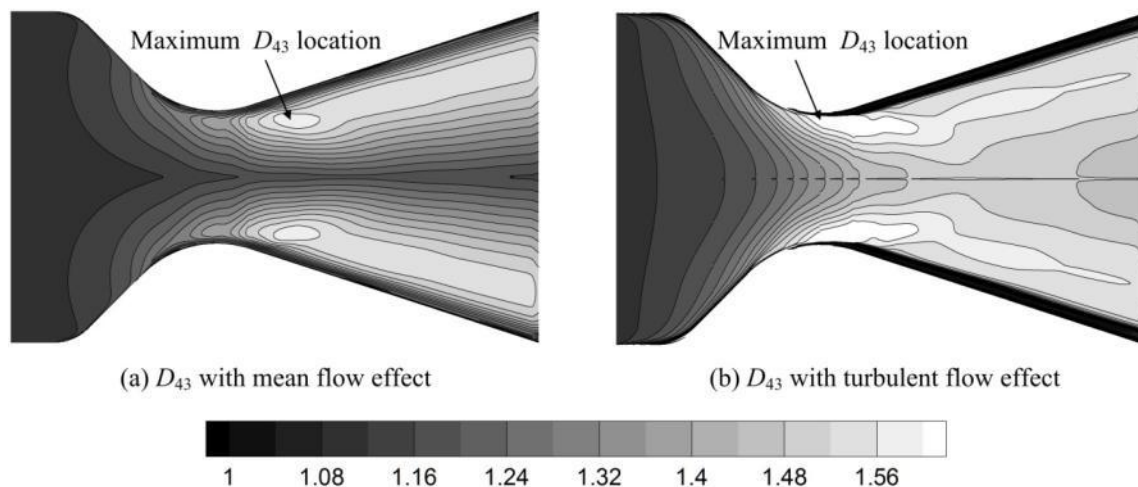
Figure 3.20 Predicted volume mean diameters (D_{43}) only with (a) mean flow collision/breakup effect and (b) turbulent collision/breakup effect for case no. C-3-2

Table 3.15 Comparisons of predicted mass mean diameters (µm) at nozzle exit plane between mean flow and turbulent effect for case no. C-3-2

Simulation case	D_{43}	D_{43} error % to Hermsen	D_m	σ_s
Mean flow effect	1.45	45.07	0.49	0.56
Turbulent effect	1.52	42.42	0.51	0.56
Mean and turbulent effect	2.00	24.24	0.55	0.61
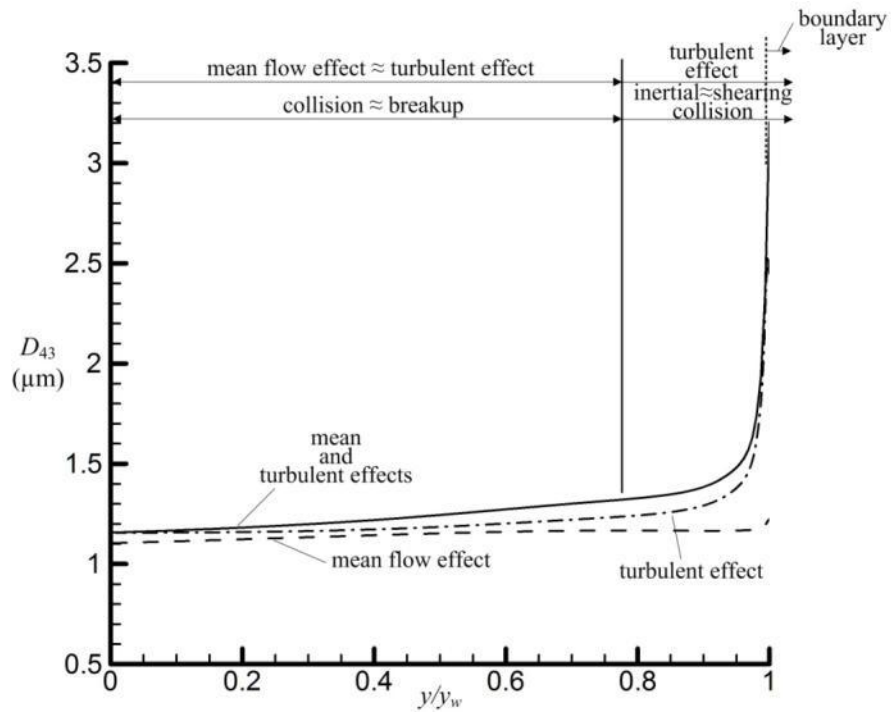
Figure 3.21 Predicted radial variation of D_{43} at 0.01 m upstream from the throat for case no. C-3-2
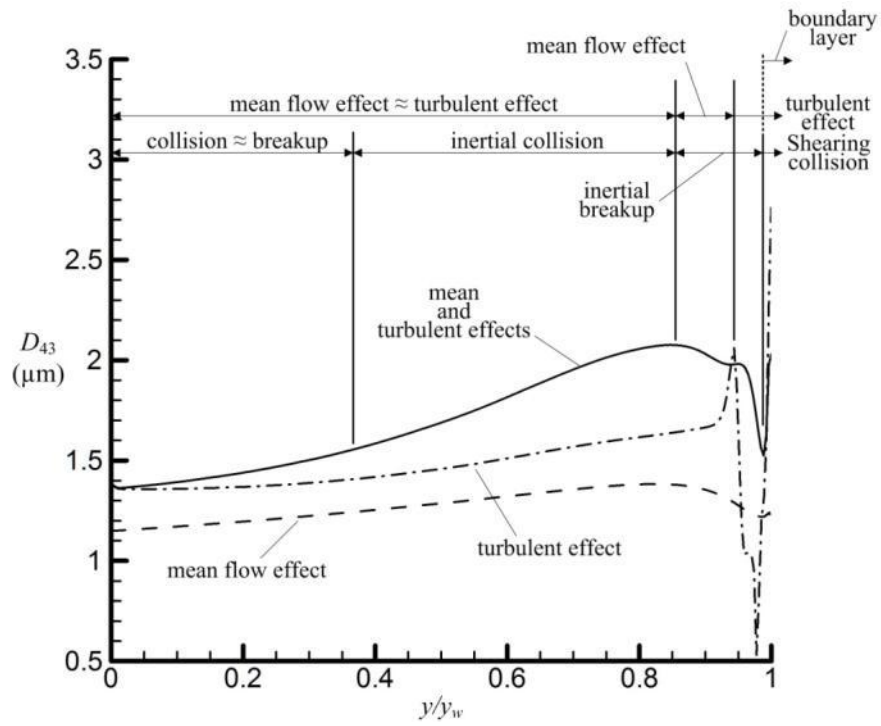
Figure 3.22 Predicted radial variation of D_{43} at throat for case no. C-3-2
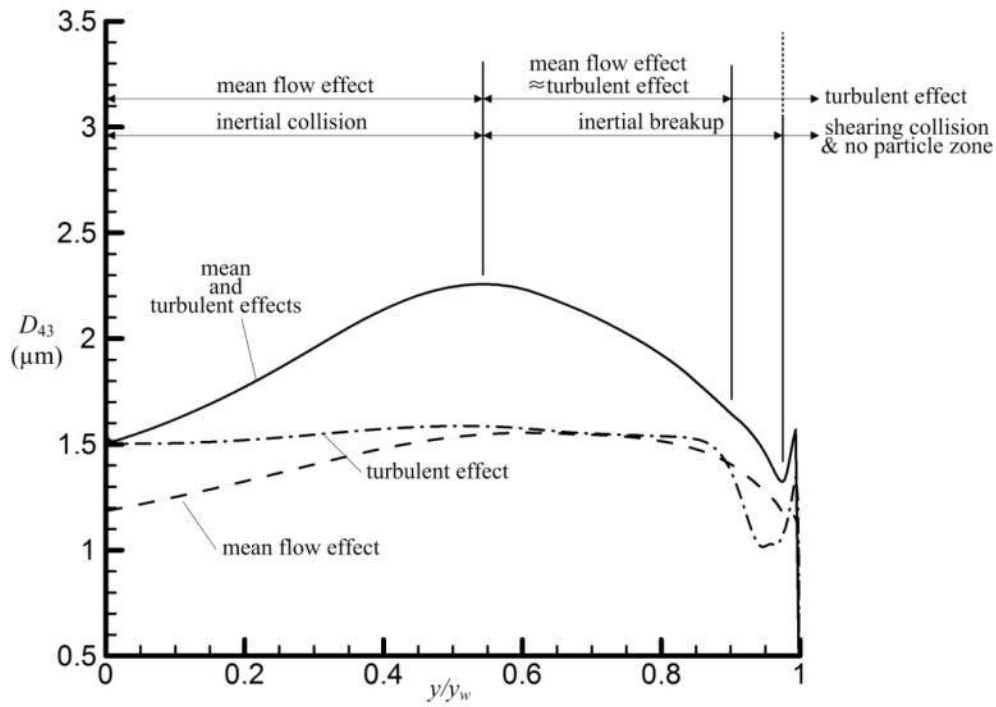
Figure 3.23 Predicted radial variation of D_{43} at 0.01 m downstream from the throat for Baseline case.

3.4.2 Parametric studies

3.4.2.1 Particle agglomeration and breakup in an Over-expanded nozzle

Simulation of an over-expanded nozzle flow condition is considered in this section. Predicted Mach number, mass mean diameter, mass fraction, and volume fraction on case no. C-1 are illustrated in Figure 3.24. The inlet boundary conditions for C-1 are presented in Table 3.4. When the nozzle flow is over-expanded, the recirculated flow interacts with main stream, and steady simulation fails due to the unsteadiness in the shear layer region. Therefore, after running the code in steady mode for a while, the code is switched to unsteady mode using $\Delta t = 5e-8$ s.

Flow separation is noted in (a) of Figure 3.24. Downstream of the separation point, a large recirculation zone is created and accordingly a large particle-free zone is created as shown in (b) of Figure 3.24. The oblique shock emanating from the separation point leads to a large number of collisions due to shear created by the shock as noted in Figure 3.24(b).

In this overexpanded case, the Mach disk is located outside of the nozzle exit and it is invisible in Figure 3.24. In this front region of Mach disk, a significant amount of breakup occurs and results in the smaller particle size at the nozzle exit. More details on the particle agglomeration/breakup response to shock waves will be presented later in this chapter based on the unsteady supersonic rocket plume simulation.

The corresponding mass and volume fraction shows sharp gradients in mass and volume of particles along the oblique shock as illustrated in (c) and (d) of Figure 3.24. These regions are located inside the main stream, slightly above the oblique shock wave. Therefore, the particles inside these layers have smaller size than the particles across oblique shock wave. It is interesting to note that the contour of mass fraction resembles the contour Mach number. At the region of maximum Mach number where the pressure and density of gas are lowest across the entire domain, large mass fractions are present.
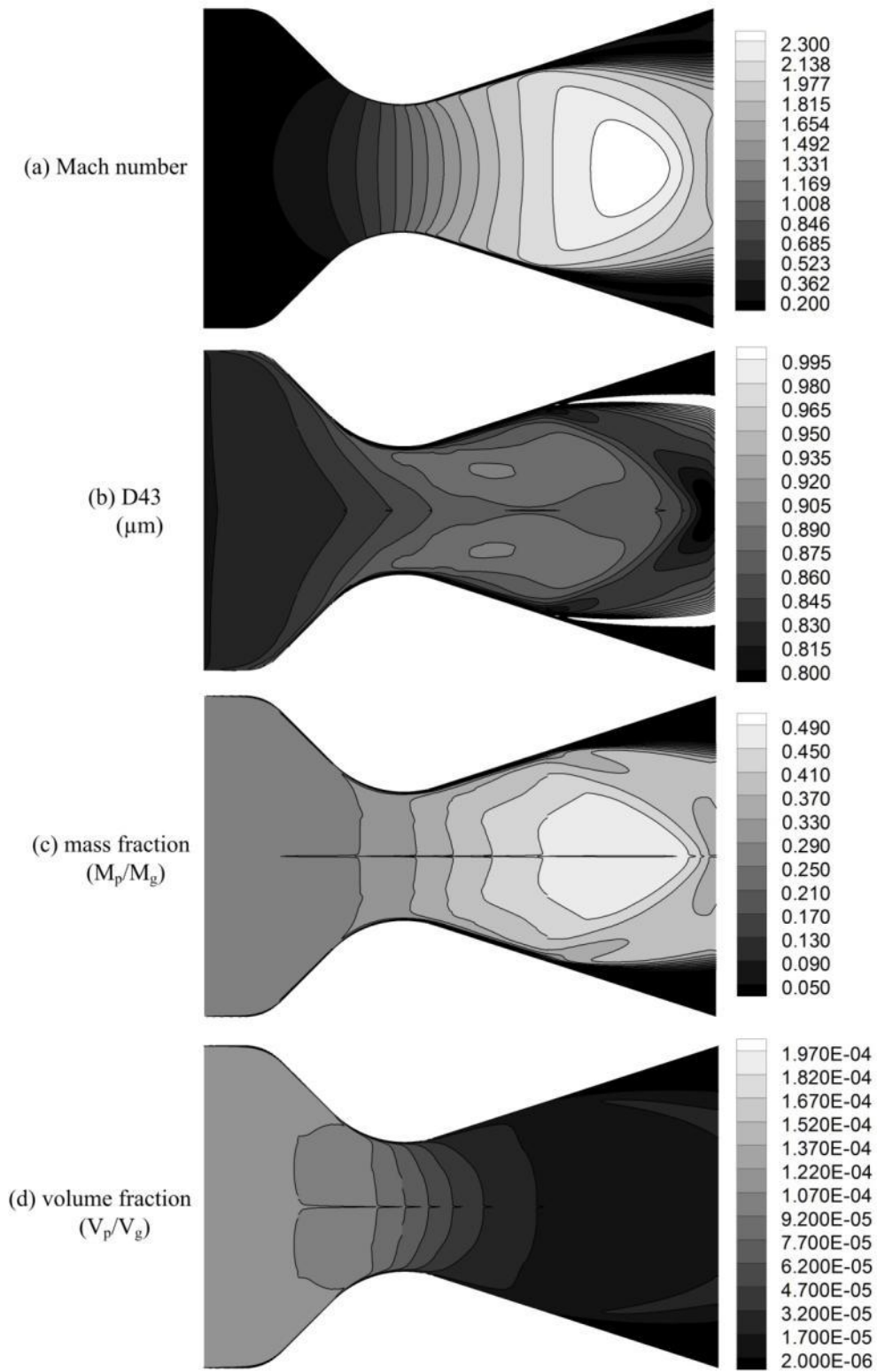
Figure 3.24 Predicted (a) Mach number, (b) mass mean diameter (D_{43}), (c) mass fraction, and (d) volume fraction for case no. C-1

3.4.2.2 The effect of turbulent kinetic energy

The effect of inlet turbulent kinetic on mass diameter distribution over the domain is assessed by comparing the cases for inflow turbulent intensity for 5% to 20% on Crowe et al. [50]'s configuration. The baseline case designated assumed an inflow turbulent intensity of 15%. The effect of turbulent kinetic energy is assessed by varying only this parameter. Details of inlet conditions are provided in Table 3.16.

Figure 3.25 illustrates the mass mean diameter distributions for these cases. The change of distribution shape is barely discernible. As illustrated clearly in (c) and (d) of Figure 3.25, the maximum of D_{43} is located downstream of the throat and far off the wall. As noted in Section 3.4.1.3, this location corresponds to the location of maximum growth of particles due to mean flow effect and it is unaffected by kinetic energy variation.

When the inlet kinetic energy is small, the particle growth at the throat wall is decreased and the resultant D_{43} at the nozzle exit is also decreased. As the inlet turbulent kinetic energy increases, the agglomeration rate increases and D_{43} at the nozzle exit increases too. The D_{43} error % to Hermsen's correlation is a maximum at the 5% level and the error decreases as the turbulent intensity increases. Considering complex flow motion leaving the propellant surface, the turbulent intensity range at nozzle inlet could be 5~15%. [74, 75] Accordingly, the current modeling is well fit in the error bounds. For more accurate calculation, the radially distributed turbulent kinetic energy and specific dissipation rate entering the nozzle can be used after obtaining them from experiments or simulations.

Table 3.16 Inlet boundary conditions for turbulent kinetic energy sensitivity tests

Case no.	K-1	K-2	K-3	K-4
D_t (in.)	0.5			
ξ_c	0.277			
P_c (psi)	650			
τ_c (ms)	15			
n_{total}	3.15e15			
D_m (μm)	0.536			
σ_s (μm)	0.456			
I	5%	10%	15%	20%

Table 3.17 Details of predicted particle phase characteristics at nozzle exit for turbulent kinetic energy sensitivity tests

Simulation case no.	D_{43}	D_{43} error % to Hermsen	D_m	σ_s
K-1	1.83	30.68	0.51	0.60
K-2	1.91	27.65	0.52	0.61
K-3	2.00	24.24	0.55	0.61
K-4	2.09	20.84	0.59	0.60

(a) $I=5\%$

(b) $I=10\%$

(c) $I=15\%$

(d) $I=20\%$

1.00 1.15 1.30 1.45 1.60 1.75 1.90 2.05 2.20 2.35 2.50 2.65 2.80 2.95
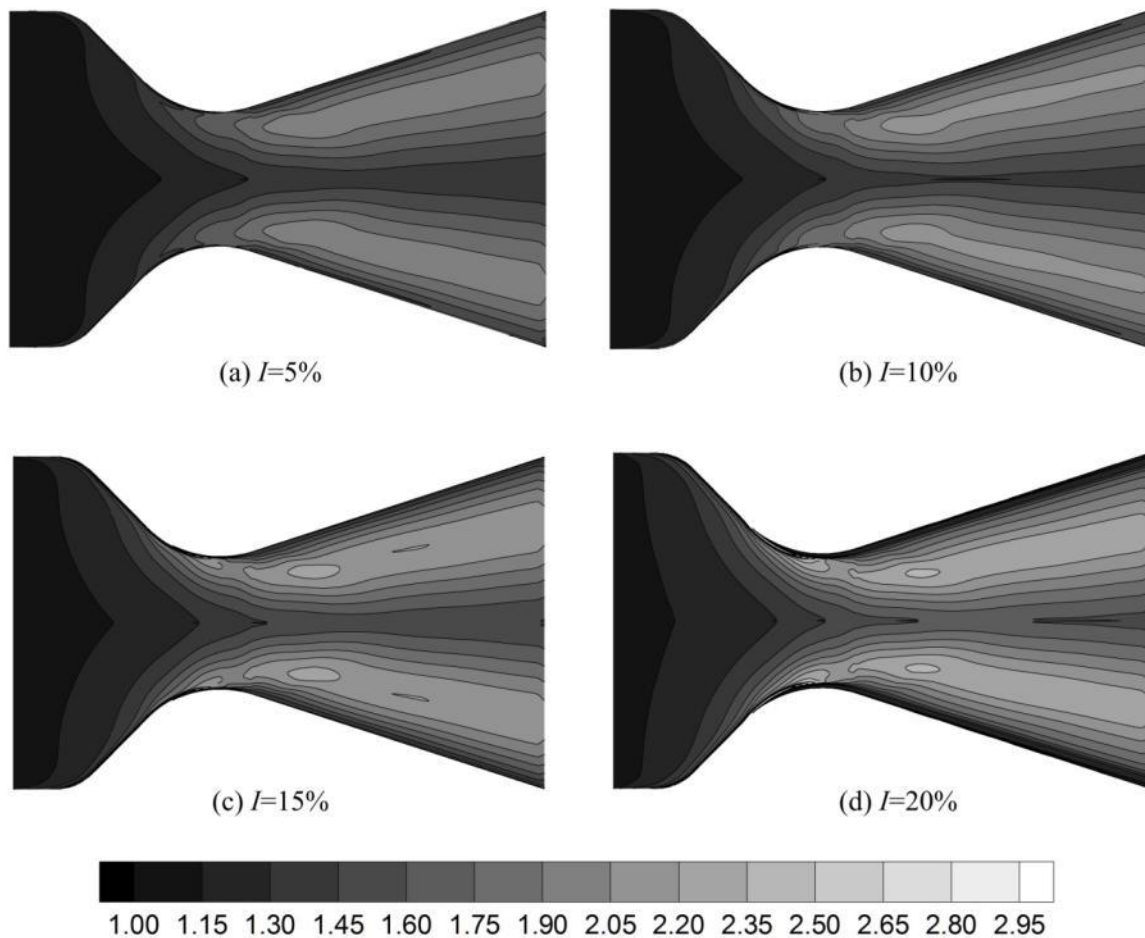
Figure 3.25 Predicted D_{43} contours of turbulent intensities from 5 to 20% for cases k-1 to 4

3.4.2.3 The effect of inlet particle size

The effect of inlet particle size is assessed by varying the geometric mean diameter (D_m) of log-normal distribution at nozzle inlet. Table 3.18 provides details of inlet condition. The geometric mean diameter, D_m, varies from 0.361 to 0.696 microns with the same other inlet conditions as the baseline case. By varying D_m retaining the same standard deviation, the log-normal distribution will be shifted to the right holding the same shape of distribution.

Figure 3.26 illustrates the mass mean diameter distributions over the entire domain. Comparing the (a), (b), and (c), no discernible changes of distribution shape are observed. In these cases, even the l_3 particle size of DQMOM can effectively follow the streamlines, and then particle can exist in the very close region to boundary layer. Accordingly, D_{43} keeps increasing as approaching to the wall from the centerline. Definitely, Figure 3.26(c) shows the largest D_{43} in the divergent section.

When D_m has larger values, in cases of (d), (e), and (f), the l_3 particle size of DQMOM cannot effectively follow the streamlines. Accordingly, most of particles holding the l_3 particle size of DQMOM exist at far above the wall. This results in the collision of large particles in a wide region close to the centerline and larger particle size in this region. The corresponding mass mean diameters at the nozzle exit are given in Table 3.19. The predicted D_{43} increases continuously as D_m at inlet increases. However, in D-1 to 3, the predicted standard deviations are almost constant. From D-3 to 6, the predicted standard deviation keeps decreasing. This means that the log-normal particle number distribution at nozzle exit becomes narrow while the diameter of particles holding large numbers in the number distribution increases. In addition, becoming narrow means that there are no extremely large particles. The large l_3 particle phase of DQMOM are much susceptible to breakup, accordingly, the amount of D_{43} increase due to l_3 particles is small and the standard deviation becomes smaller.

Figures 3.27 and 3.28 show the radial variation of mass fraction and D_{43} at various locations. At 0.01m upstream from throat, the large particles exist within the boundary and a larger D_{43} is observed with a larger D_m on overall range. When the geometric mean diameters are large, in cases of 0.536, 0.634, and 0.696, the detachment of large particles is occurred before they reach the throat and only small particles exist within the throat boundary. When the geometric mean diameters are from 0.361 to 0.436, the particles keep growing from the convergent section to the throat, the detachment occurs after the throat. As shown in (b) of Figure 3.27 and (a) and (b) of

Figure 3.28, the maximum D_{43} location in a radial direction which is the peak location of D_{43} moves from the outside (wall) to the inside (centerline) when the D_m becomes large because the inertial force of large particle is large and it significantly deviates the trajectory of large particles.

Table 3.18 Inlet boundary conditions to assess the effect of geometric mean diameter of log-normal distribution

Case no.	D-1	D-2	D-3	D-4	D-5	D-6
D_t (in.)	0.5					
ξ_c	0.277					
P_c (psi)	650					
τ_c (ms)	15					
n_{total}	10.57e15	8.80e15	5.94e15	3.15e15	1.98e15	1.44e15
D_m (μm)	0.361	0.385	0.436	0.536	0.634	0.696
σ_s (μm)	0.456					
D_{43}(μm)	0.74	0.79	0.89	1.10	1.30	1.43

Table 3.19 Details of predicted particle phase characteristics at nozzle exit for various geometric mean diameter of log-normal distribution

| Simulation case no.	D_{43}	D_m	σ_s
D-1	1.23	0.31	0.63
D-2	1.35	0.33	0.64
D-3	1.60	0.39	0.64
D-4	2.00	0.55	0.61
D-5	2.00	0.84	0.51
D-6	2.01	1.04	0.44
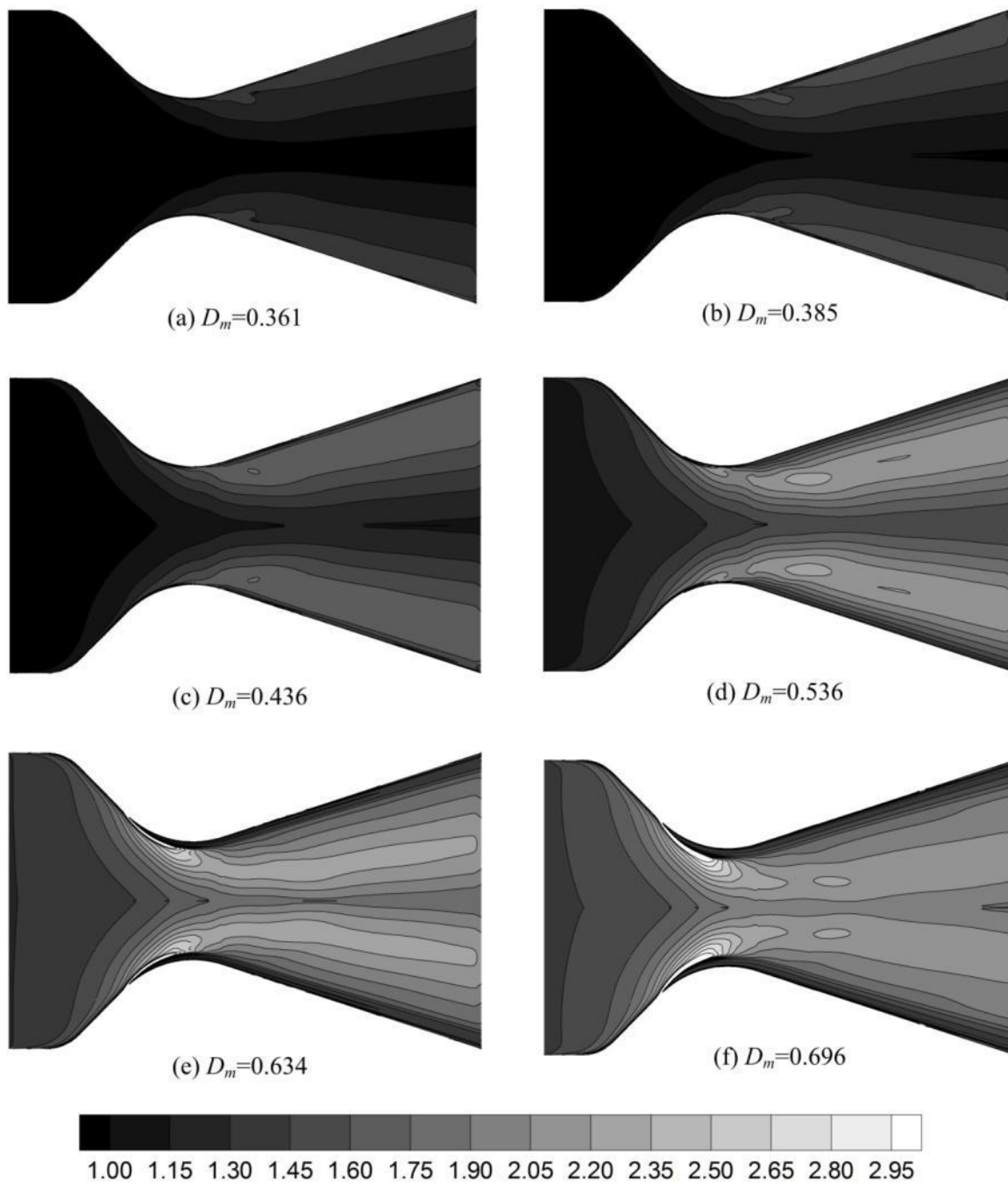
Figure 3.26 Predicted D_{43} contours of the geometric mean diameters from 0.361 to 0.696 μm for D-1 to 6
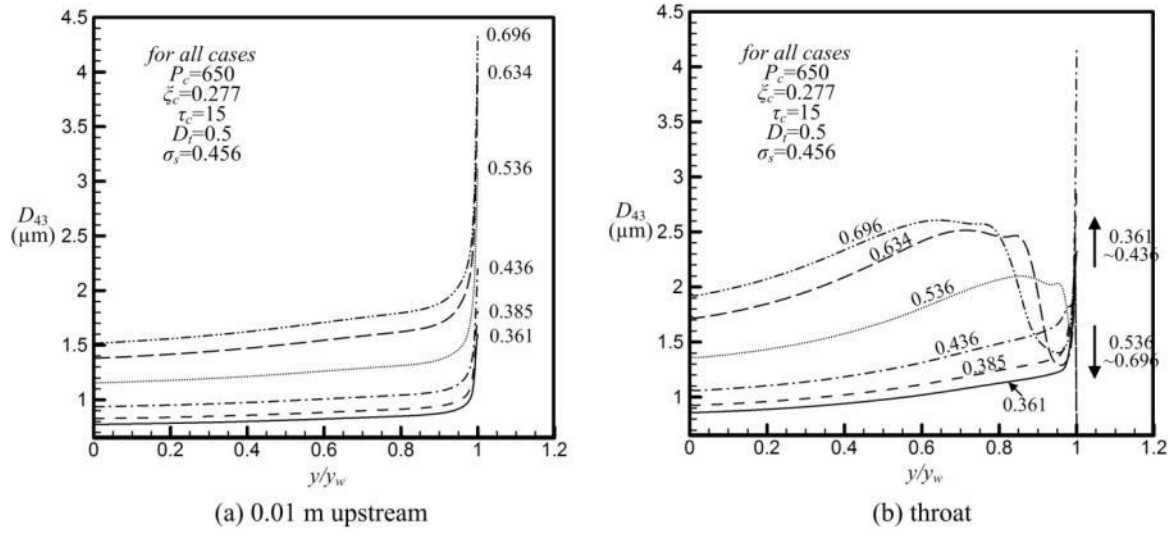
Figure 3.27 Predicted mass mean diameters at (a) 0.01 m upstream from throat and (b) throat for inlet geometric mean diameters of 0.361 (D-1) to 0.696 μm (D-6)
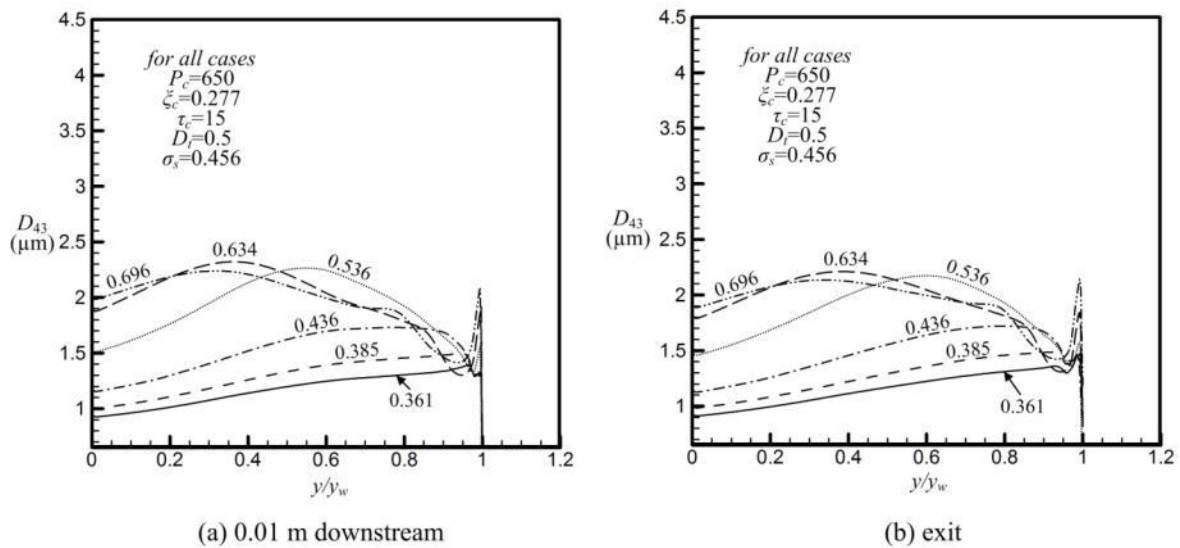

Figure 3.28 Predicted mass mean diameters at (a) 0.01 m downstream from throat and (b) exit for inlet geometric mean diameters of 0.361 (D-1) to 0.696 μm (D-6)

3.4.2.4 The effect of width of the particle distribution

The effect of the width of the inlet particle size distribution is assessed by varying the standard deviation assuming a log-normal distribution as in the other cases. Table 3.20 provides details of inlet condition. The geometric mean diameter D_m of 0.536 is used for all cases. The standard deviation varies from 0.156 to 0.520 μm with the same other inlet conditions as the baseline case. As σ_s is increased, the bin sizes corresponding to the various particle classes considere are correspondingly effected. In addition, the inlet D_{43} also becomes larger when a large σ_s is used. Table 3.20 provides details of inlet conditions.

Figure 3.29 illustrates D_{43} distributions over the entire domain. As observed in previous sections, smaller particles can follow gas phase streamlines well and particles of l_3 particle size in DQMOM can exist in the very close region to boundary layer at throat and in the divergent section. In (a) and (b) of Figure 3.29, the maximum D_{43} location in a radial direction is very close to the wall in the divergent section as the 3rd particle size can exist in this region.

When σ_s is large, as shown in (c) and (d) of Figure 3.29, the l_3 particle size of DQMOM cannot effectively follow the streamlines at around the throat and the maximum D_{43} location is created at around this region. As the inlet σ_s increases, the resultant D_{43} at nozzle exit also increases. The resultant particle sizes at the nozzle exit are given in Table 3.21. They show a very similar behavior to the variation of geometric mean diameter. From SD-1 to 3, the predicted D_{43} and σ_s increase continuously as inlet σ_s increases. Comparing SD-3 and 4, the predicted mass mean diameters are same whereas D_m increases and σ_s decreases as inlet σ_s increases. The same explanation as D_m variation cases can be made. The extremely large particles cannot be created because they are much susceptible to breakup. Accordingly, the distribution becomes very narrow.

An interesting observation can be drawn by the comparison of D-1 and SD-2. The inlet mass mean diameters for those cases are almost same. The inlet D_{43}s of D-1 and SD-2 are 0.74 and 0.73 μm, respectively. The distribution parameters D_m and σ_s for D-1 are 0.316 and 0.456 μm. The D_m and σ_s for SD-2 are 0.536 and 0.3 μm. The difference of resultant D_{43} at exit for those cases are quite noticeable and the values are 1.23 and 1.04 μm for D-1 and SD-2, respectively. The reason is that the wide distribution creates more opportunities for collision due to increased collisions based on large particles .

Figures 3.30 and 3.31 show the radial variation of mass fraction and D_{43} at various locations. Trends are similar to the effect of mean particle size. At 0.01m upstream from throat, the large particles exist within the boundary and a larger D_{43} is observed with a larger D_m except the case of SD-4. When the standard deviation is large in SD-4, the detachment of very large particles is occurred before they reach the throat and only small particles exist within the boundary. At throat wall, the large particles of SD-1 and 2 keep growing but the large particles of SD-3 and 4 are detached from the wall. As shown in Figure 3.30(b) and Figure 3.31(a,b), the maximum D_{43} location in a radial direction which is the peak location of D_{43} moves from the outside (wall) to the inside (centerline) due to the large inertial force of large particles.

Table 3.20 Inlet boundary conditions to assess the effect of standard deviation of log-normal distribution

Case no.	SD-1	SD-2	SD-3	SD-4
D_t (in.)	0.5			
ξ_c	0.277			
P_c (psi)	650			
τ_c (ms)	15			
n_{total}	7.23e15	5.38e15	3.15e15	2.42e15
D_m (μm)	0.536			
σ_s (μm)	0.156	0.300	0.456	0.520
D_{43}(μm)	0.58	0.73	1.10	1.37

Table 3.21 Details of predicted particle phase characteristics at nozzle exit for various standard deviation of log-normal distribution

Simulation case no.	D_{43}	D_m	σ_s
SD-1	0.69	0.52	0.28
SD-2	1.04	0.49	0.46
SD-3	2.00	0.55	0.61
SD-4	2.00	0.79	0.52

(a) σ_s=0.156

(b) σ_s=0.300

0.60 0.65 0.70 0.75 0.80 0.85 0.90 0.95 1.00 1.05 1.10 1.15 1.20

(c) σ_s=0.456

(d) σ_s=0.520

1.00 1.15 1.30 1.45 1.60 1.75 1.90 2.05 2.20 2.35 2.50 2.65 2.80 2.95
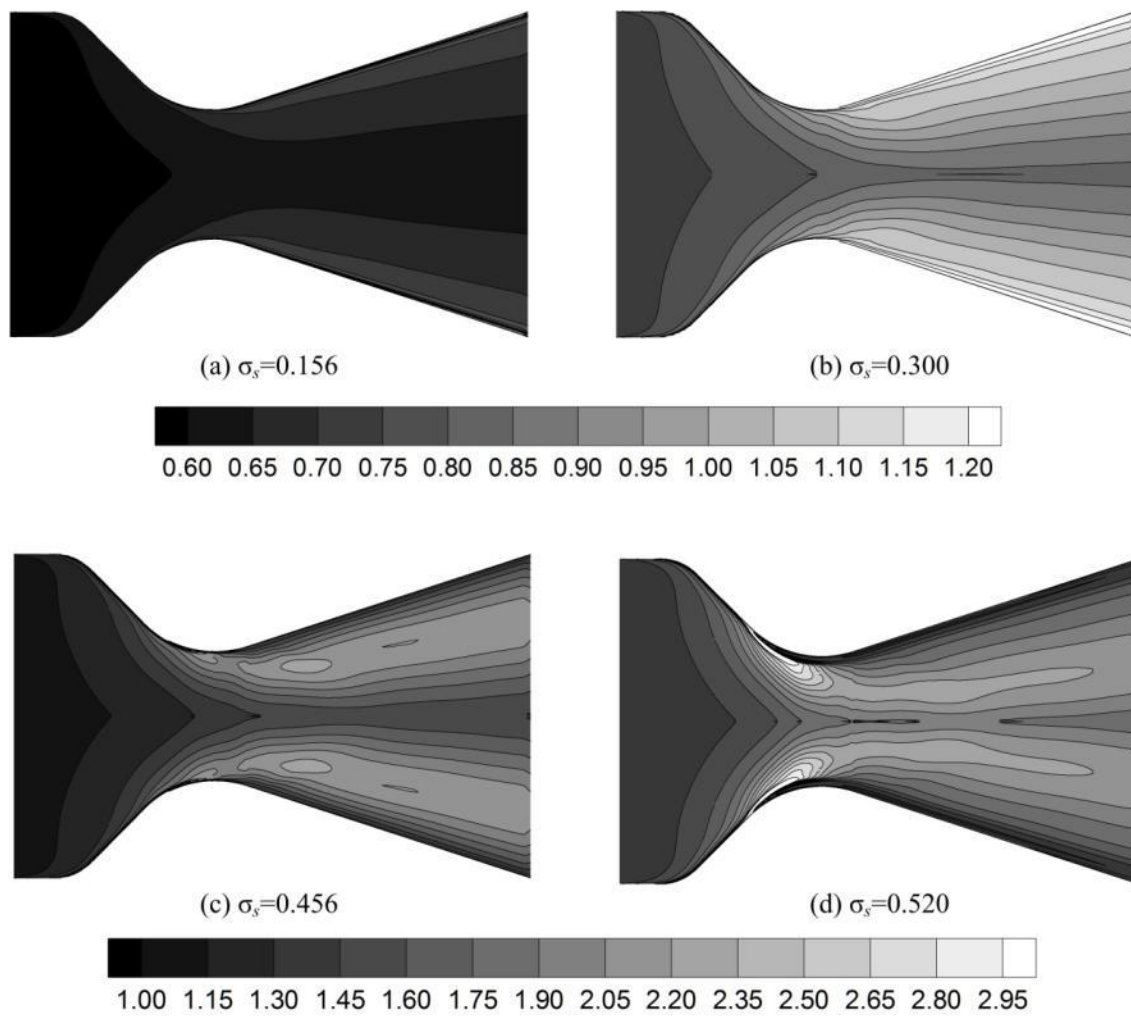
Figure 3.29 Predicted D_{43} contours of the standard deviations from 0.156 to 0.520 μm for SD-1 to 4
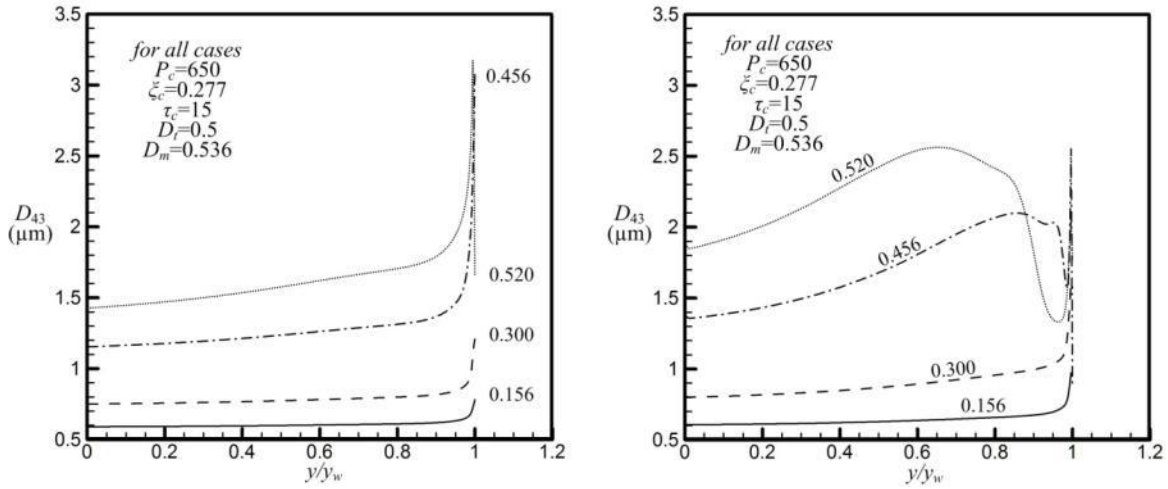
Figure 3.30 Predicted mass mean diameters at (a) 0.01 m upstream from throat and (b) throat for inlet standard deviations of 0.156 (SD-1) to 0.520 µm (SD-4)
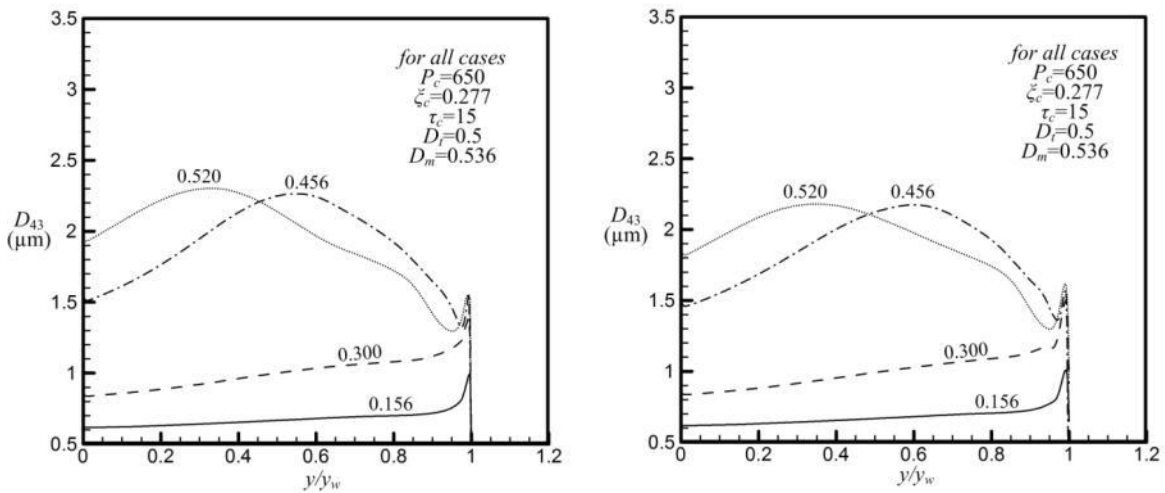
Figure 3.31 Predicted mass mean diameters at (a) 0.01 m downstream from throat and (b) exit for inlet standard deviations of 0.156 (SD-1) to 0.520 µm (SD-4)

3.4.2.5 The effect of contraction angle

The effect of nozzle inlet contraction angle on is assessed for contraction angles of 35 to 65 deg. with 10 deg. differences on Crowe et al. [50]'s configuration. The details of nozzle profile and inlet conditions are given in Figure 3.32 and Table 3.22, respectively. The baseline case has a contraction angle of 35 deg. The same inlet conditions as C-3-2 except the value of D_m are used. The D_m for C-3-2 is 0.536. Currently, the D_m of 0.361 is chosen and the particle distribution under this condition will show less detachment of l_3 in DQMOM. Accordingly, the variation of distribution can be easily identified if detachment is fortified due to the variation of contraction angle. Comparing (b) in Figure 3.33 and (c) in Figure 3.12 shows that I-2 has less detachment than C-3-2.

Figure 3.33 illustrates the mass mean diameter distributions of computed cases. The change of distribution shape is very discernible. As illustrated clearly in (a) and (b) of Figure 3.33, the l_3 particle size of DQMOM can effectively follow the streamlines, and then particle can exist in the very close region to boundary layer in divergent section. Accordingly, D_{43} keeps increasing as approaching to the wall from the centerline. When the contraction angle is large, the l_3 particle phase of DQMOM is detached from the wall at the convergent section and this phase does not exist at the region close to wall in divergent section as shown in (c) and (d) of Figure 3.33. As clearly shown in Figure 3.33, (b) of Figure 3.34, and (a) and (b) of Figure 3.35, as the contraction angle increases, the particles are detached earlier in the convergent section and the smaller particle region close to the wall in the divergent section becomes larger.

The mass mean diameters at the nozzle exit are given in Table 3.23. Interestingly, the predicted D_{43} increases continuously as the contraction angle increases. As shown in (b) of Figure 3.34 and (a) and (b) of Figure 3.35, a large increase is observed at the region close to wall from the throat to divergent section where there is a slip between 3rd particle phase and other phases. The amount of difference of D_{43} at around the centerline is small for various contraction angle as shown in Figure 3.33-35. Therefore, it can be concluded that the contraction angle can significantly alter the collision process in the nozzle and the resultant D_{43} at nozzle exit increases as the contraction angle increases.
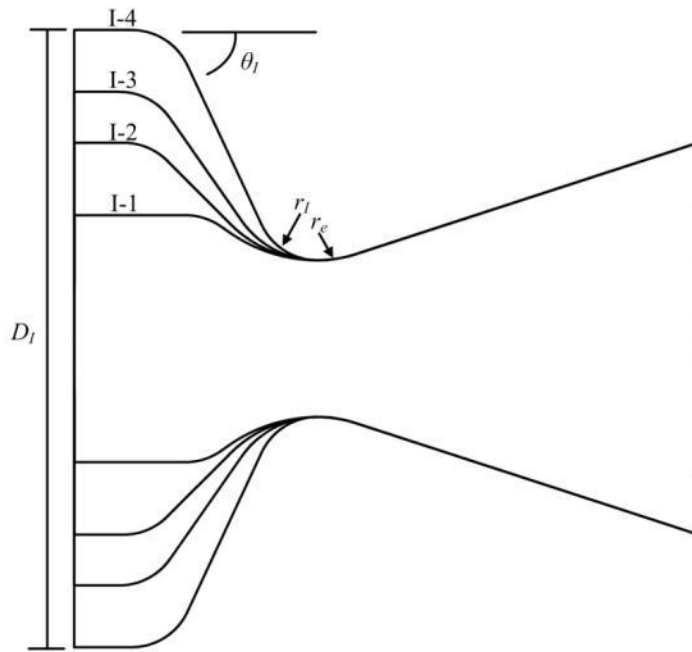
Figure 3.32 Schematic of the test nozzle geometries for contraction angle variation

Table 3.22 Inlet boundary conditions to assess the effect of contraction angle

Case no.	I-1	I-2	I-3	I-4
D_t (in.)	0.5			
ξ_c	0.277			
P_c (psi)	650			
τ_c (ms)	15			
n_{total}	10.57e15			
D_m (μm)	0.361			
σ_s (μm)	0.456			
D_I (in.)	0.394	0.625	0.787	0.984
θ_I	35	45	55	65
r_I	0.492	0.394	0.295	0.197
r_e	0.394			

Table 3.23 Details of predicted particle phase characteristics at nozzle exit for various contraction angle

Simulation case no.	D_{43}	D_m	σ_s
I-1	1.05	0.31	0.59
I-2	1.23	0.31	0.63
I-3	1.40	0.31	0.66
I-4	1.71	0.34	0.68

(a) $\theta_i = 35$

(b) $\theta_i = 45$

(c) $\theta_i = 55$

(d) $\theta_i = 65$

0.74 0.84 0.94 1.04 1.14 1.24 1.34 1.44 1.54 1.64 1.74 1.84 1.94
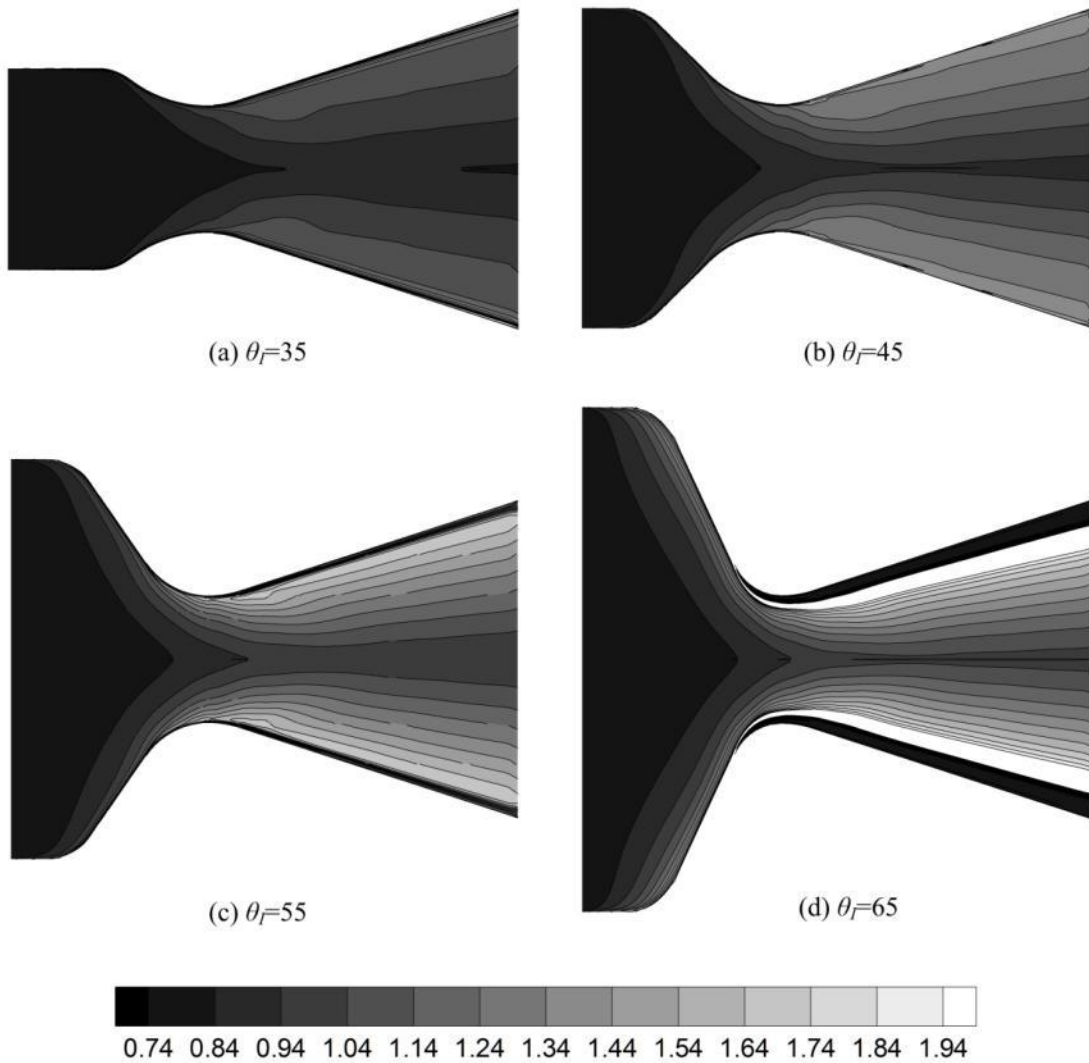
Figure 3.33 Predicted D_{43} contours of the contraction angles from 35 to 65 deg. for I-1 to 4
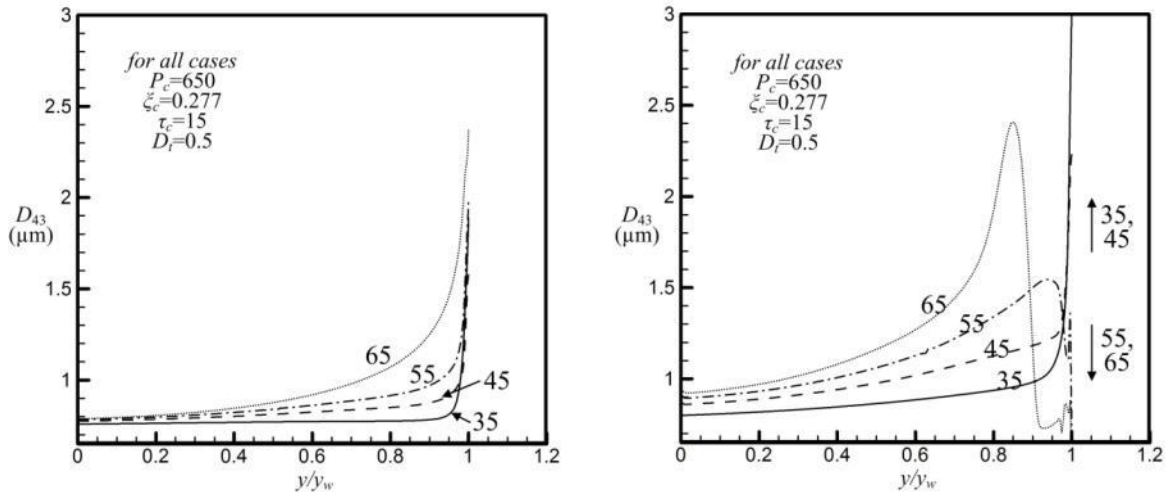
Figure 3.34 Predicted mass mean diameters at (a) 0.01 m upstream from throat and (b) throat for contraction angles of 35 (I-1) to 65 deg. (I-4)
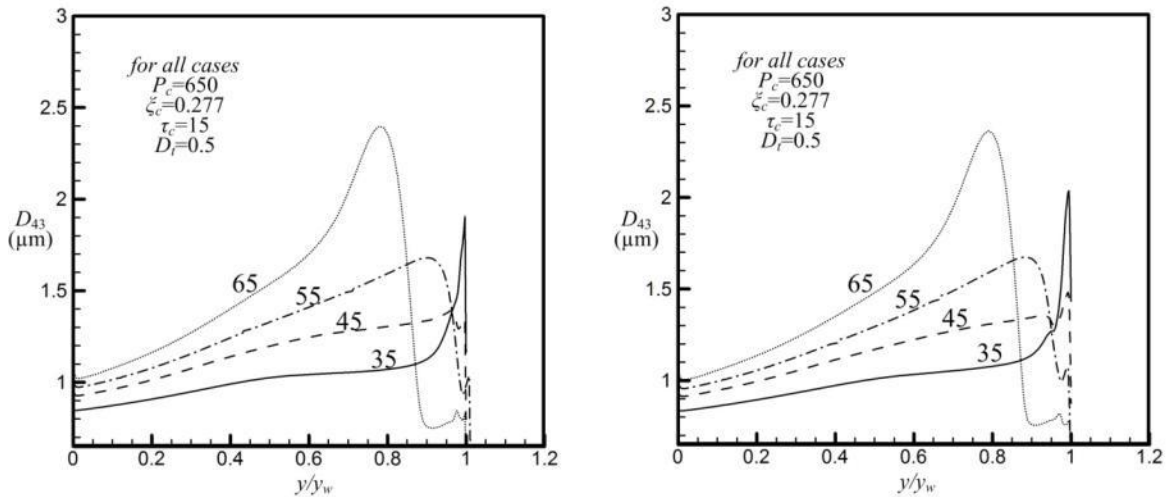
Figure 3.35 Predicted mass mean diameters at (a) 0.01 m downstream from throat and (b) exit for contraction angles of 35 (I-1) to 65 deg. (I-4)

3.4.2.6 The effect of divergence angle

The effect of divergence angle on mass diameter distribution over the domain is assessed by comparing the cases for divergence angles of 13 to 30 deg. on Crowe et al. [50]'s configuration. The details of nozzle profile are given in Figure 3.36. As shown in this figure, all cases have the same outlet area to ensure the same gas phase condition at outlet. Details of inlet boundary conditions and geometry to assess the effect of divergence angle are given in Table 3.24. The baseline case already introduced in previous sections has a divergence angle of 18 deg. The same inlet conditions as the baseline case are used.

Figure 3.37 illustrates the mass mean diameter distributions of computed cases. The change of distribution shape is discernible. In Figure 3.37, the l_3 particle size of DQMOM can effectively follow the streamlines in convergent section. However, when the divergence angle is large, the l_3 particle phase of DQMOM is detached from the wall after the throat and this phase does not exist at the region close to wall in divergent section as shown in (c) of Figure 3.37. As clearly shown in Figure 3.38, as the divergence angle increases, the smaller particle region close to the wall in the divergent section becomes larger.

The mass mean diameters at the nozzle exit are given in Table 3.25. Similar to contraction angle variation cases, the predicted D_{43} increases continuously as the divergence angle increases but the amount of difference is quite small. As shown in (c) of Figure 3.37 and Figure 3.38, a large increase is observed at the region close to wall from the throat to divergent section where there is a slip between l_3 particle phase and other phases for O-3.
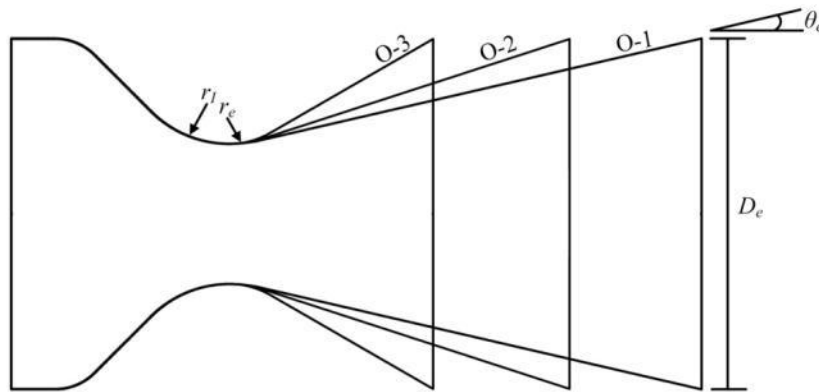

Figure 3.36 Schematic of the test nozzle geometries for divergence angle variation

Table 3.24 Inlet boundary conditions and details of geometry to assess the effect of divergence angle

Case no.	O-1	O-2	O-3
D_t (in.)	0.5		
ξ_c	0.277		
P_c (psi)	650		
τ_c (ms)	15		
n_{total}	10.57e15		
D_m (μm)	0.361		
σ_s (μm)	0.456		
D_e (in.)	0.625		
θ_e	13	18	30
r_e	0.492	0.394	0.295
r_I	0.625		

Table 3.25 Details of predicted particle phase characteristics at nozzle exit for various divergence angle

Simulation case no.	D_{43}	D_m	σ_s
O-1	1.19	0.31	0.62
O-2	1.23	0.31	0.63
O-3	1.30	0.31	0.64

(a) $\theta_e = 13$

(b) $\theta_e = 18$

(c) $\theta_e = 30$

0.74 0.84 0.94 1.04 1.14 1.24 1.34 1.44 1.54 1.64 1.74 1.84 1.94
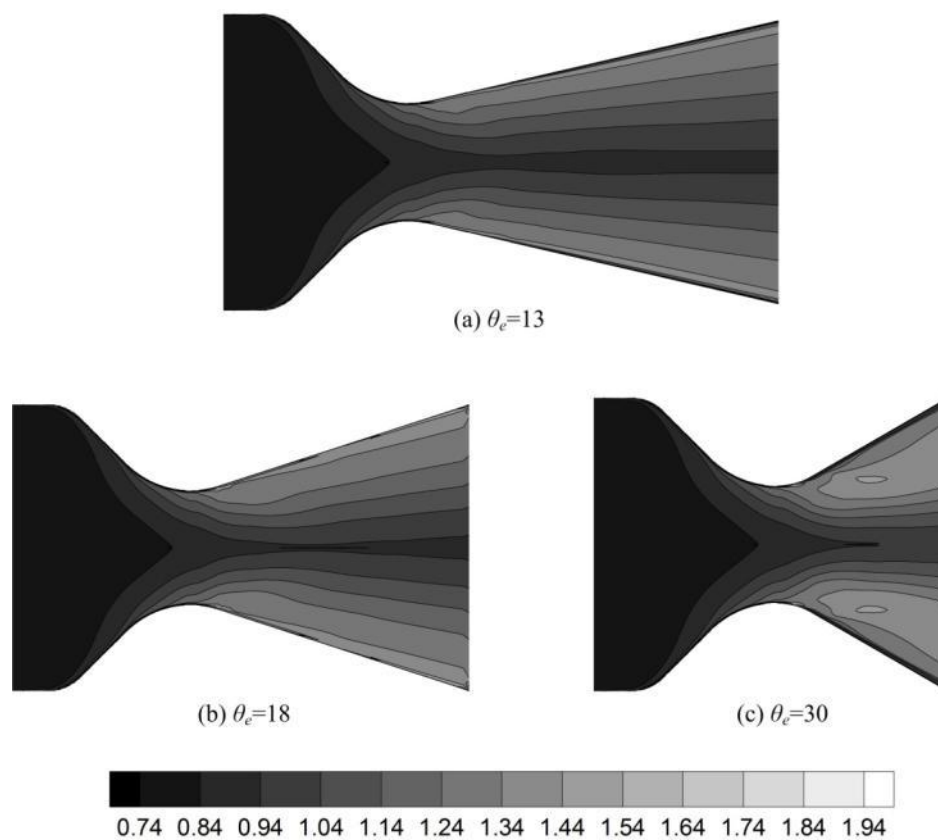
Figure 3.37 Predicted D_{43} contours of the divergence angles from 13 to 45 deg. for O-1 to 3
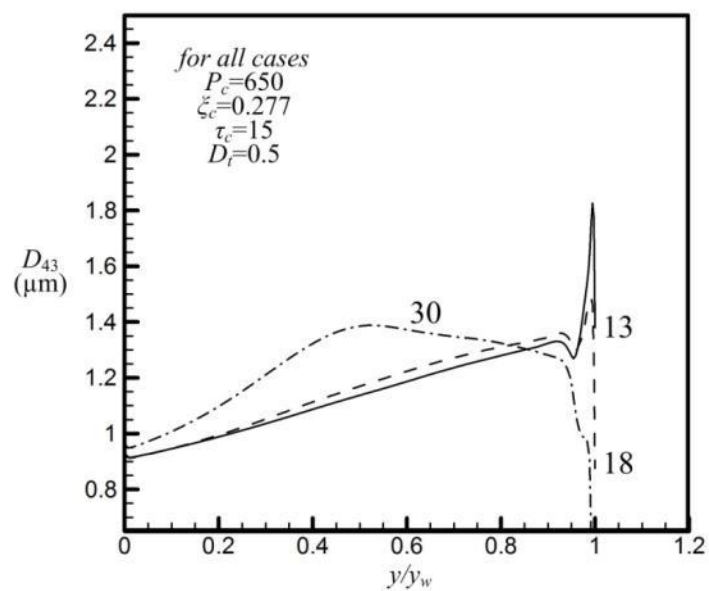
Figure 3.38 Predicted mass mean diameters at exit fort divergence angles of 13 (O-1) to 30 deg. (O-4)

3.4.2.7 The effect of chamber pressure

The effect of chamber pressure on particle distribution is assessed using the results obtained from the validation simulations of Shegal [53]'s configuration presented in the previous chapter. The corresponding case numbers are from P-1 to 8 and the chamber pressures are varied from 150 psi to 950 psi. Details of inlet boundary conditions and resultant particle characteristics at exit are provided in Tables 3.5 and 3.10.

Figure 3.39 shows the effect of the chamber pressure on the mass mean diameter along the axis and wall, and at throat and nozzle exit plane. Figure 3.39(a) shows that the largest growth rate occurs in the convergent section, especially, in the short region upstream of the nozzle throat. The mass mean diameter after passing the throat shows little growth in divergent section at low chamber pressure but the mass mean diameter after the throat shows significant growth in divergent section at high chamber pressure. The breakup mechanism due to slip between a particle and gas might be balanced with collision in far downstream from the throat, then the mass mean diameter approaches a certain value in this region.

Figure 3.39(b) shows the variation of mass mean diameter in the boundary layer and it shows more complicated variation than centerline case. Three peaks are observed for almost all cases. The first peak corresponds to the recirculation region which leads to significant shearing motion of flow then shearing collision of particles and it is observed at all considered pressures. The second peak corresponds to the maximum mass mean diameter in the entire domain for lower pressure cases and this peak diminishes as the chamber pressure increases. Accordingly, the second peak is very small when the pressures are high. The second peak comes from the wall impingement region in convergent section of nozzle. The third peak is the location where the breakup process becomes dominant. Particles experience growth when they approach the throat, and then the breakup process becomes dominant at a certain point and results in the third peak. The growth rate for particles passing through the throat increases with chamber pressure. It is interesting the third peak is located far downstream from the throat with low chamber pressure and located almost at the throat with high chamber pressure. Therefore, it can be concluded that the variation of chamber pressure can change the location where the breakup process becomes dominant in the wall boundary. Unlike to the simulations on Crowe et al.'s nozzle configuration, the complete detachment of l_3 particle phase of DQMOM in the divergent section is not observed.

Figure 3.40 shows radial profiles of mass mean diameter at the throat and nozzle exit planes.
It is clearly observed that the large amount of growth occurs within boundary layer due to flow
shearing and it occurs more in higher pressure cases than lower pressure case.
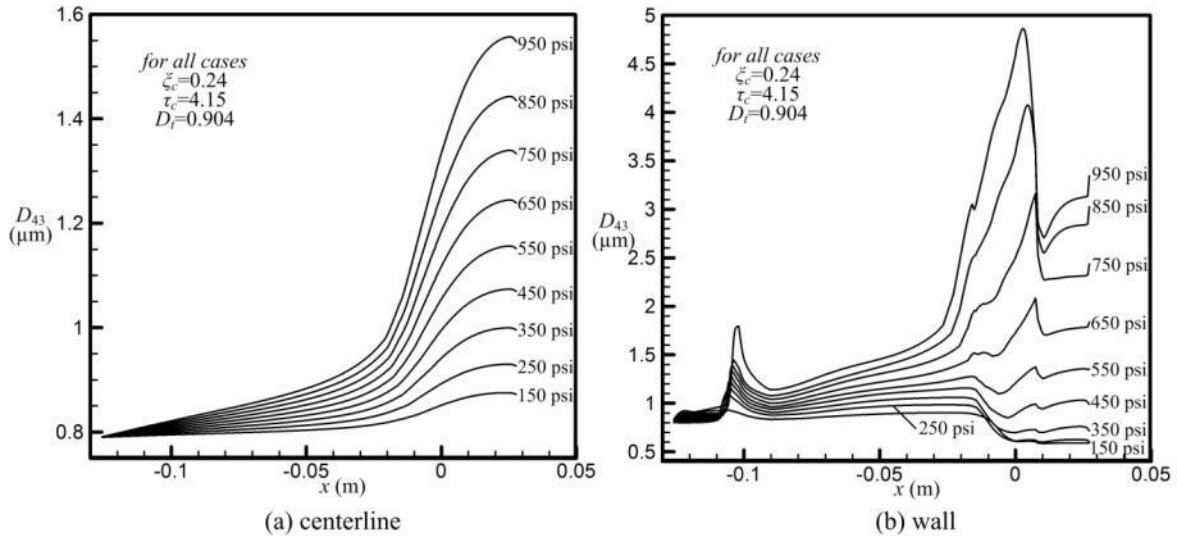
Figure 3.39 Axial variation of the predicted volume mean diameter along the centerline and
wall according to chamber pressure variation
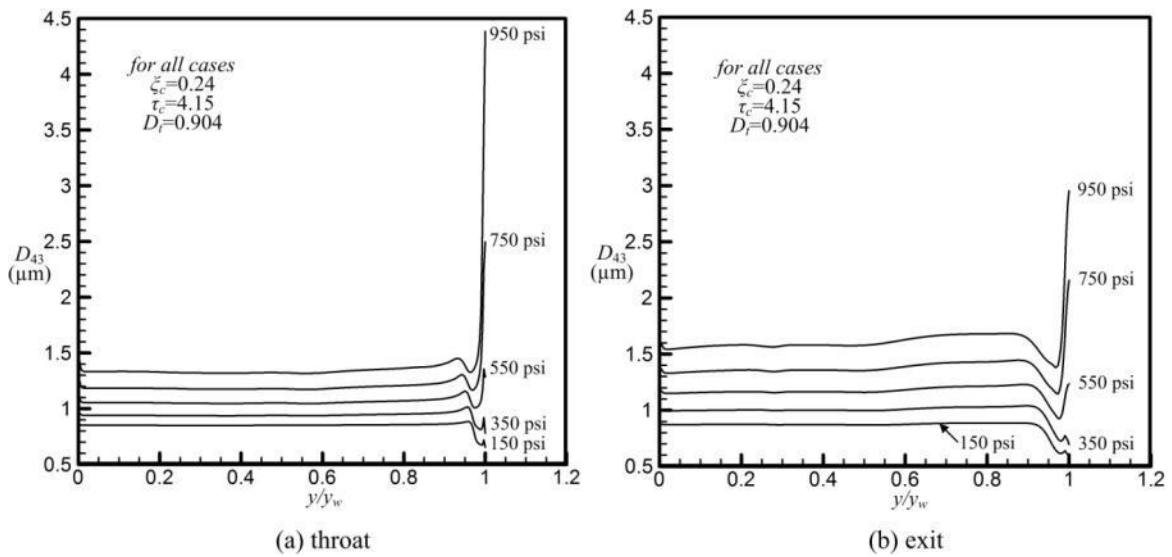
Figure 3.40 Radial variation of the predicted volume mean diameter at throat and nozzle exit
plane according to chamber pressure variation

3.4.2.8 The effect of particle concentration

The effect of particle concentration on particle distribution is assessed using the results obtained from the validation simulations of Shegal [53]'s configuration presented in the previous chapter. The corresponding case numbers are from M-1 to 6 and the particle concentrations in a chamber are varied from 0.12 to 0.32 gmol/100g . Details of inlet boundary conditions and resultant particle characteristics at exit are provided in Tables 3.6 and 3.12.

Figures 3.41-42 show the effect of the particle concentration on the mass mean diameter along the axis and wall, and at throat and nozzle exit plane. All of figures show the same trends obtained in the chamber pressure variation cases. Three peaks along the wall are observed for the concentrations of 0.12 and 0.16 and four peaks are observed for other considered concentrations. The second and third peaks are located at almost same place. All of last peaks are located at slightly downstream of the throat. The locations of the maximum growth rate along the centerline are all same as shown in Figure 3.41. Accordingly, the variation of particle concentration does not change the location where the breakup is dominant. Due to the detachment of larger particles started at the convergent section, the smaller particle zone near the wall at the throat and downstream is observed but the complete detachment of larger particle in the divergent section is not observed.
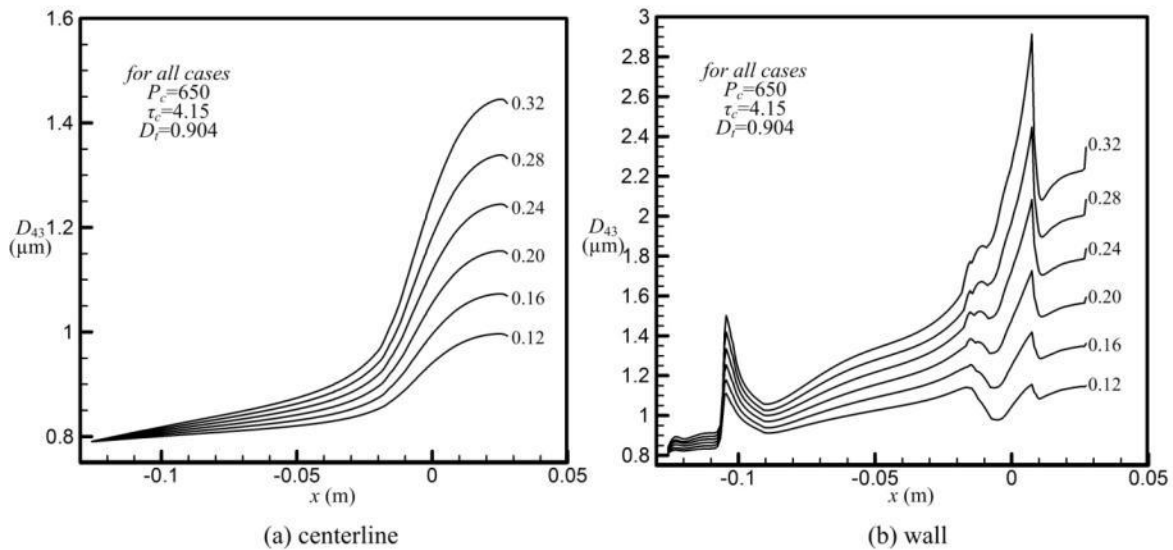

(a) centerline (b) wall

Figure 3.41 Axial variation of the predicted volume mean diameter along the centerline and wall according to particle concentration variation in chamber
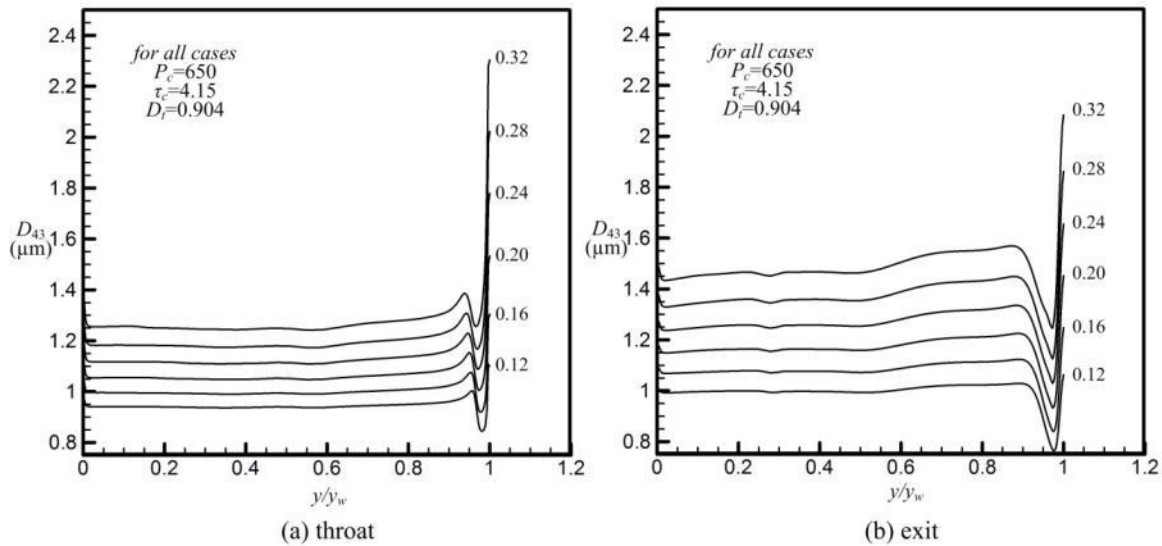
Figure 3.42 Radial variation of the predicted volume mean diameter at throat and nozzle exit plane according to particle concentration variation in chamber

3.4.2.9 The effect of nozzle scale

Figures 3.43 and 3.44 show the effect of the nozzle scale on the mass mean diameter along the axis and wall, and at throat and nozzle exit plane. The effect of nozzle scale on particle distribution is assessed using the results obtained from the validation simulations of Shegal's [53] configuration presented in the previous chapter. The corresponding case numbers are from S-1 to 6 and the throat diameter are varied from 0.904 to 9.040 inches. Details of inlet boundary conditions and resultant particle characteristics at exit are provided in Tables 3.7 and 3.14.

The results show the similar trends obtained in the chamber pressure variation cases at smaller scales as it is shown in Figure 3.43(a). In Figure 3.44(b) the last peak where the breakup process becomes dominant at wall boundary takes place before the throat when the nozzle diameter is larger than 5.424 inches. At lower throat diameter cases, the collision occurring within the recirculation zone of nozzle inlet corner is quite noticeable but it is not noticeable when the nozzle throat diameter is larger than 5.424 inches.

When the nozzle throat diameter is larger than 5.424 inches, the detachment of larger particles does not occur in the convergent section and the smaller particle zone near the wall at the throat is not observed in these cases. As shown in Figure 3.44(b), the smaller particle zone exists in the divergent section and the complete detachment of larger particles does not occurs.

(a) centerline

(b) wall
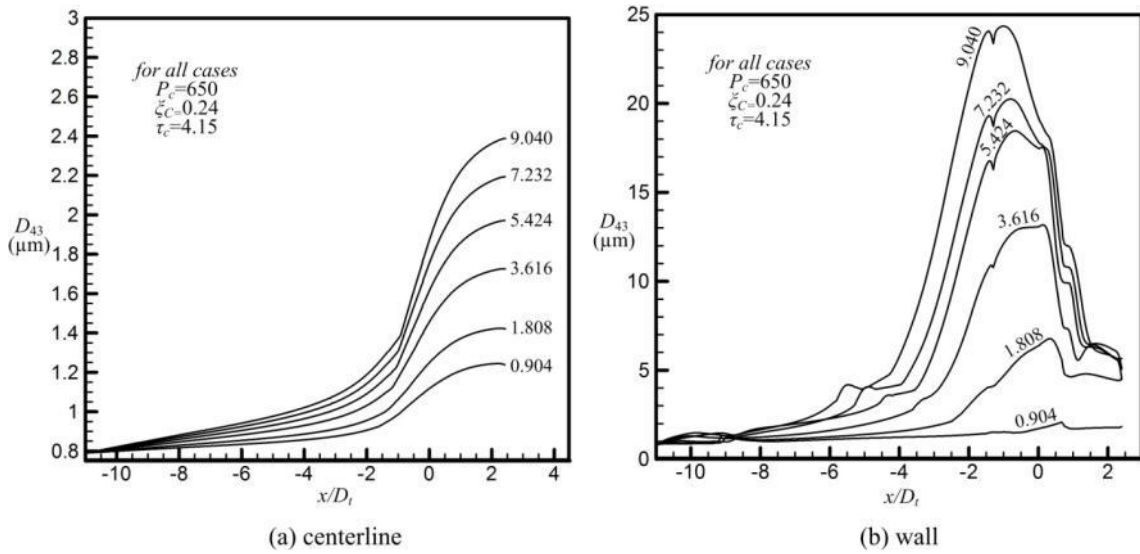
Figure 3.43 Axial variation of the predicted volume mean diameter along the centerline and wall according to nozzle scale


(a) throat

(b) exit
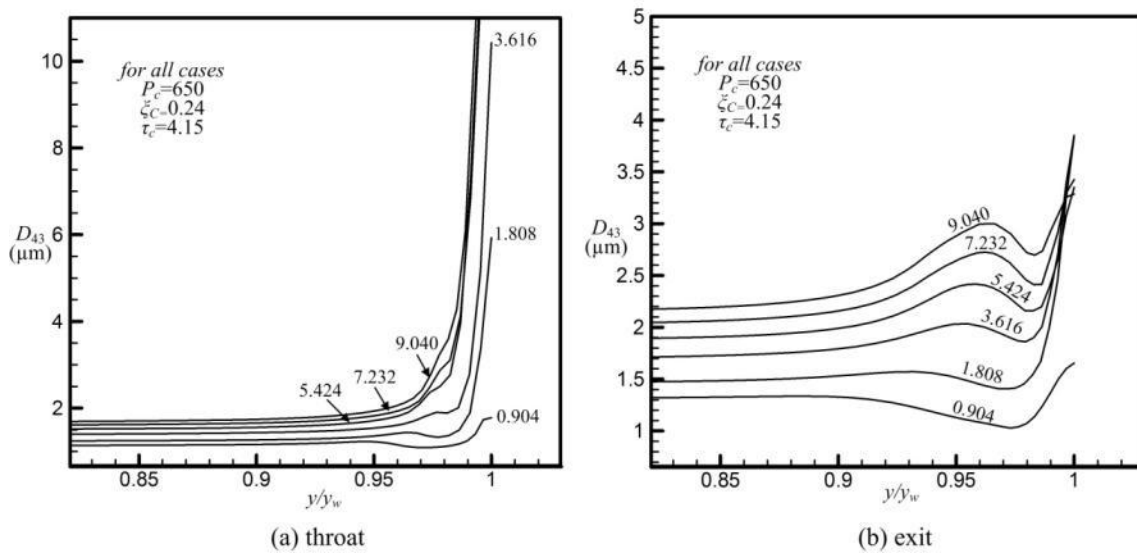
Figure 3.44 Close up view of radial variation of the predicted volume mean diameter at throat and nozzle exit plane according to nozzle scale

3.4.2.10 Agglomeration/breakup response to shock diamonds

The details on the particle agglomeration/breakup response to shock waves are presented here based on the unsteady supersonic rocket plume simulation. The corresponding case numbers are C-1 and C-3-2 and details of inlet boundary conditions are provided in Table 3.4. To facilitate the convergence of code, the code is switched to unsteady mode using Δt=5e-7 s after running the code in steady mode for a while.

As explained in the previous chapter, particle size measurement is sometimes done by collecting the particles in the pressurized tank. The expansion of flow into the tank creates the shearing region in outer region of main stream and this shearing motion of flow will create high turbulent motion along with laminar shearing forces. As expected from the modeling of collision processes, the collision may significantly occur within this small confined region and result in larger particle size. To take into account this effect, an axisymmetric mesh with farfield boundary conditions is created and unsteady simulation is performed on Crowe et al. [50]'s configuration. Figure 3.45 highlights an axisymmetric mesh used in the computations for Crowe's geometry with farfield boundary conditions. Two simulations on C-1 and C-3-2 was performed on this mesh and the results also showed the variation of particle size across the shock wave under the over-expanded and under-expanded nozzle conditions.
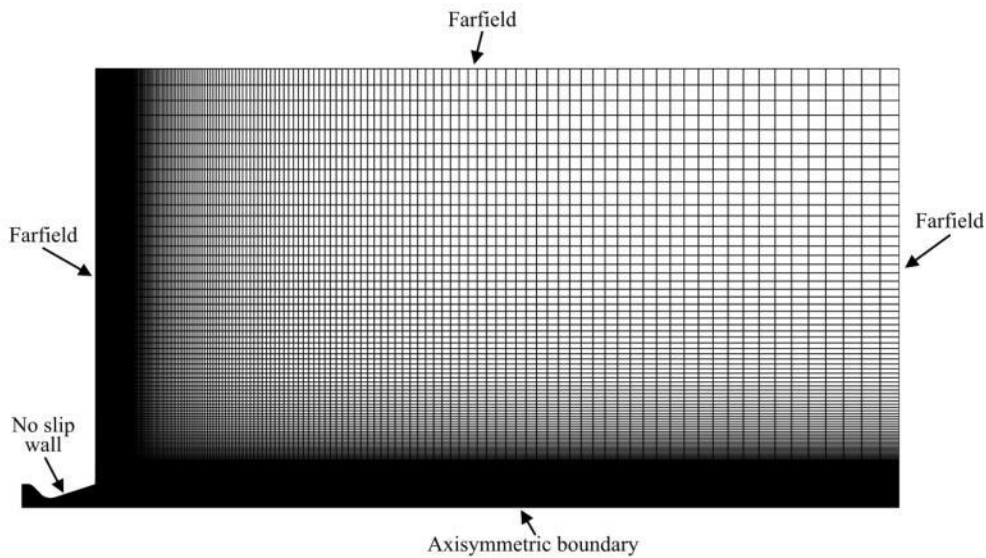

Figure 3.45 Schematic of the test nozzle geometry using farfield boundary conditions for Crowe's experiment (total 46240 cells)

The results of simulation of over-expanded nozzle are given in Figure 3.45 and the predicted static pressure, Mach number, mass fraction, and mass mean diameter on case no. C-1 are illustrated. The shock diamonds are notable in Figure 3.46(a) and (b). As explained in above section, the flow separation in the divergent section take place and large recirculation zone is created in this region. The first Mach disk is located just outside of the exit. Therefore, the significant decelerating of flow takes place across the normal shock wave. In addition, the pattern of subsequent processes of accelerating-decelerating are observed. At far downstream, this patter is dissipated and the patter is hardly observed.

As explained above, between the main flow stream and separation region, the oblique shock wave exists and it leads the large amount of collision due to shearing motion of flow and creates large particles following the oblique shock as indicated in Figure 3.46(d). This process are repeated at the regions of subsequent expansion and compression waves where the flow shearing is maximized . Accordingly, it is observed that large agglomerates are trailing at around the outer perimeter. At these regions, the mass fraction shows small values comparing to the main stream because large amount of particles exists within the main stream.

When the flow is accelerated and decelerated across the shocks, the particles can experience collision or breakup via inertial forces. In shock regions, the gas decelerates faster than particles and as a result the particles are moving faster than the gas in these regions. Larger particles have more inertia and exhibit larger slip velocities as a result.This slip motion causes significant breakup of particles as shown in Figure 3.47.

The opposite effect occurs in regions where gas accelerates downstream of shocks and particle inertia leads to locally lower velocities in the condensed phase in this region. These breakup-collision processes are repeated like the alternating motion of shock diamonds leading to the pattern observed in Figure 3.47. The minimum particle size is exactly located at the Mach disk.

A similar process occurs in the under-expanded flow of C-3-2 as shown in Figures 3.48 and 49. The sequence of breakup-collision processes is identical to the over-expanded flow described in Figures 3.46 and 47. The only difference is that the first breakup zone in front of the Mach disk is very small comparing to the over-expanded flow due to the suppression of the first shock wave in under-expanded flow.
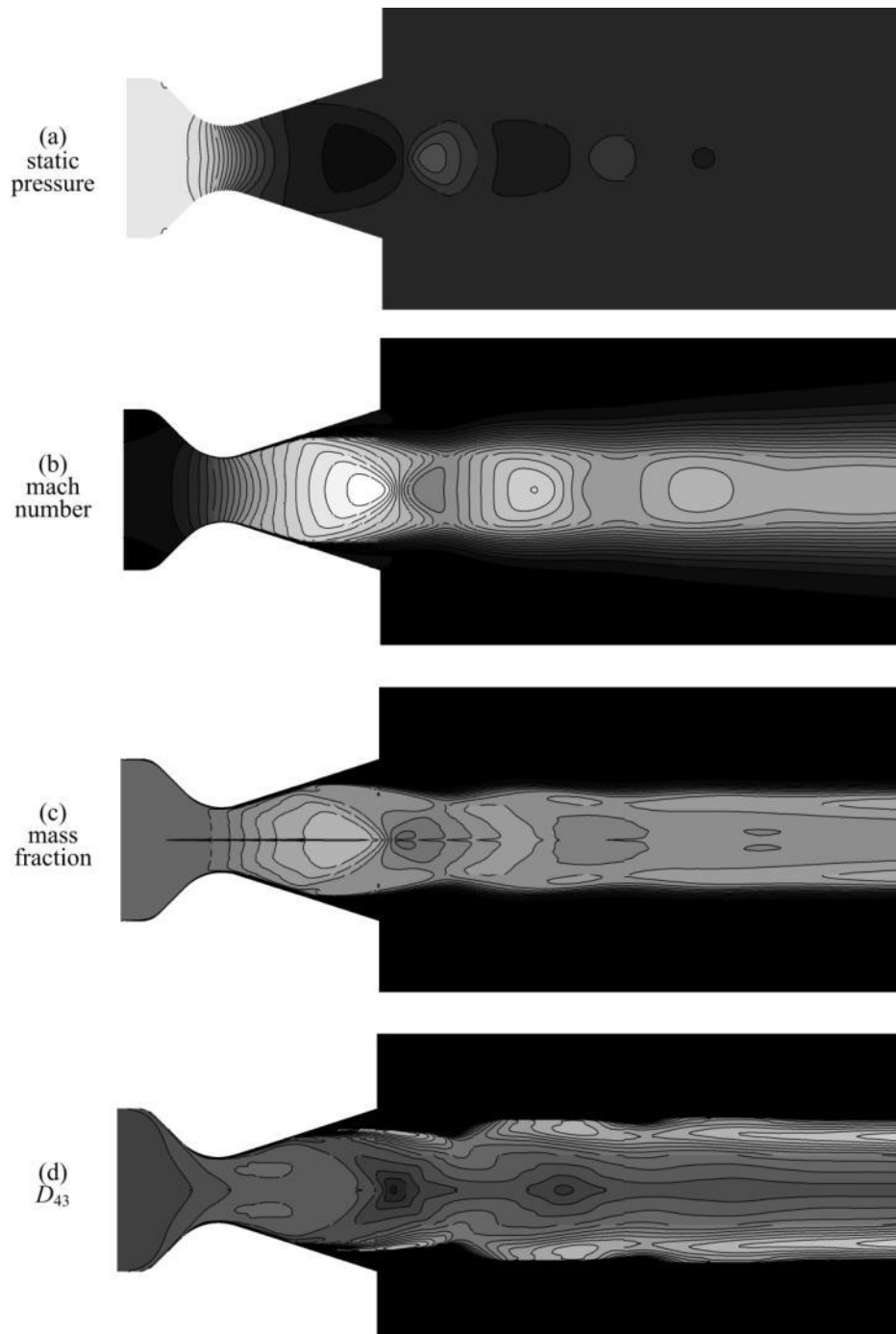
Figure 3.46 Zoomed view of predicted (a) static pressure, (b) Mach number, (c) mass fraction, and (d) mass mean diameter (D_{43}) for case no. C-1 (over-expanded)
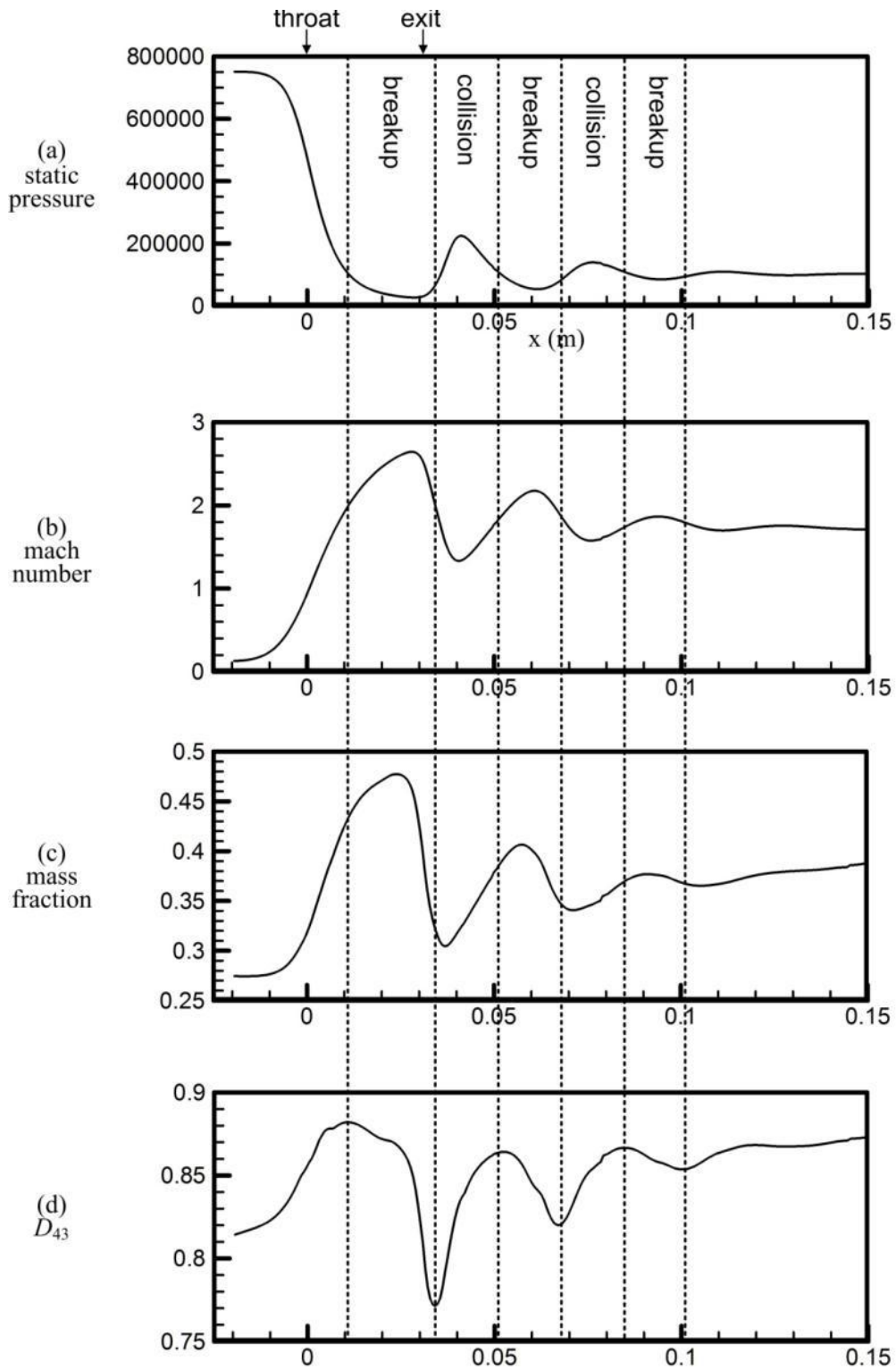
Figure 3.47 Zoomed view of predicted (a) static pressure, (b) Mach number, (c) mass fraction, and (d) mass mean diameter (D_{43}) on the centerline for case no. C-1 (over-expanded)
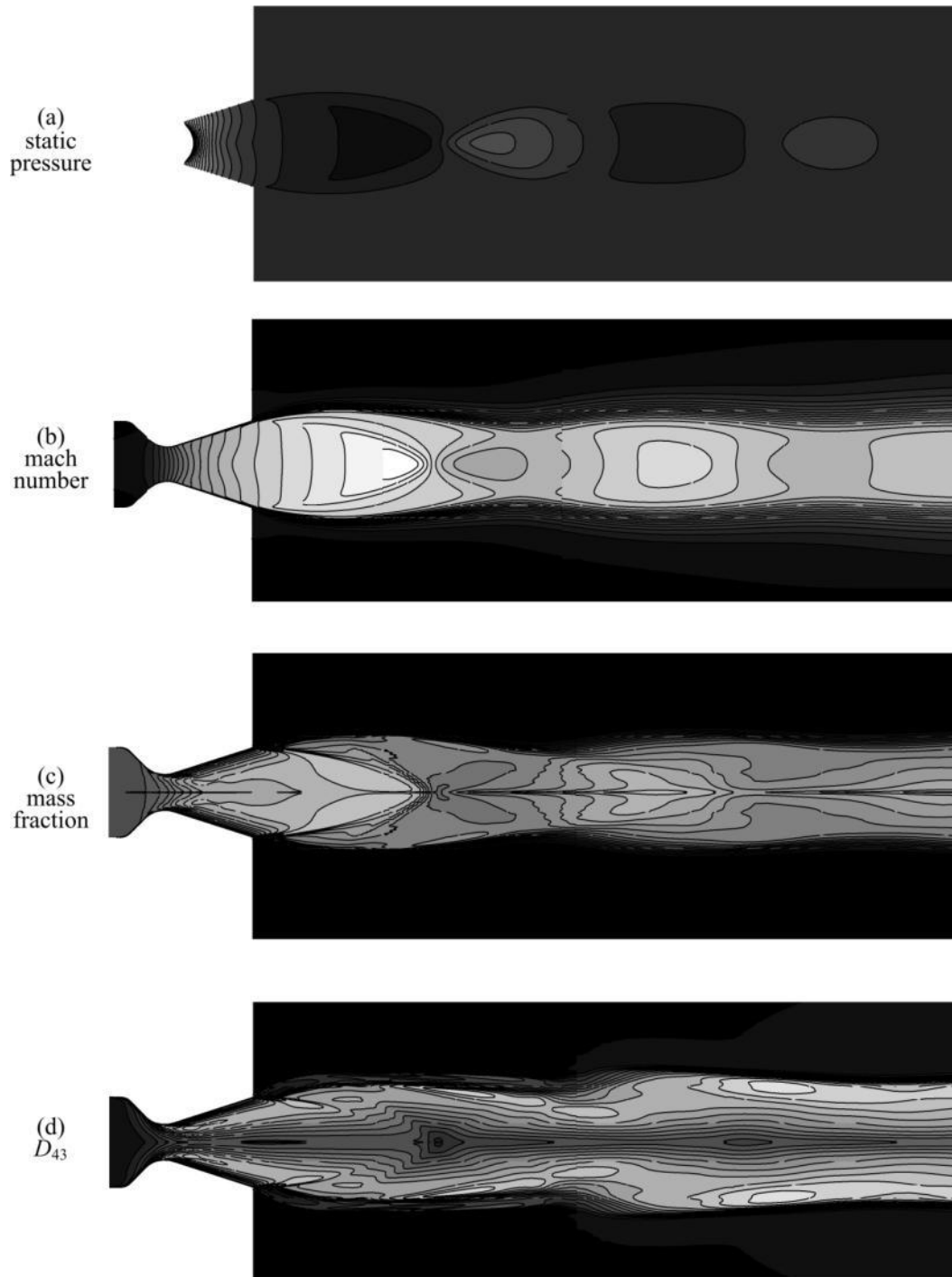
Figure 3.48 Zoomed view of predicted (a) static pressure, (b) Mach number, (c) mass fraction, and (d) mass mean diameter (D_{43}) for case no. C-3-2 (under-expanded)
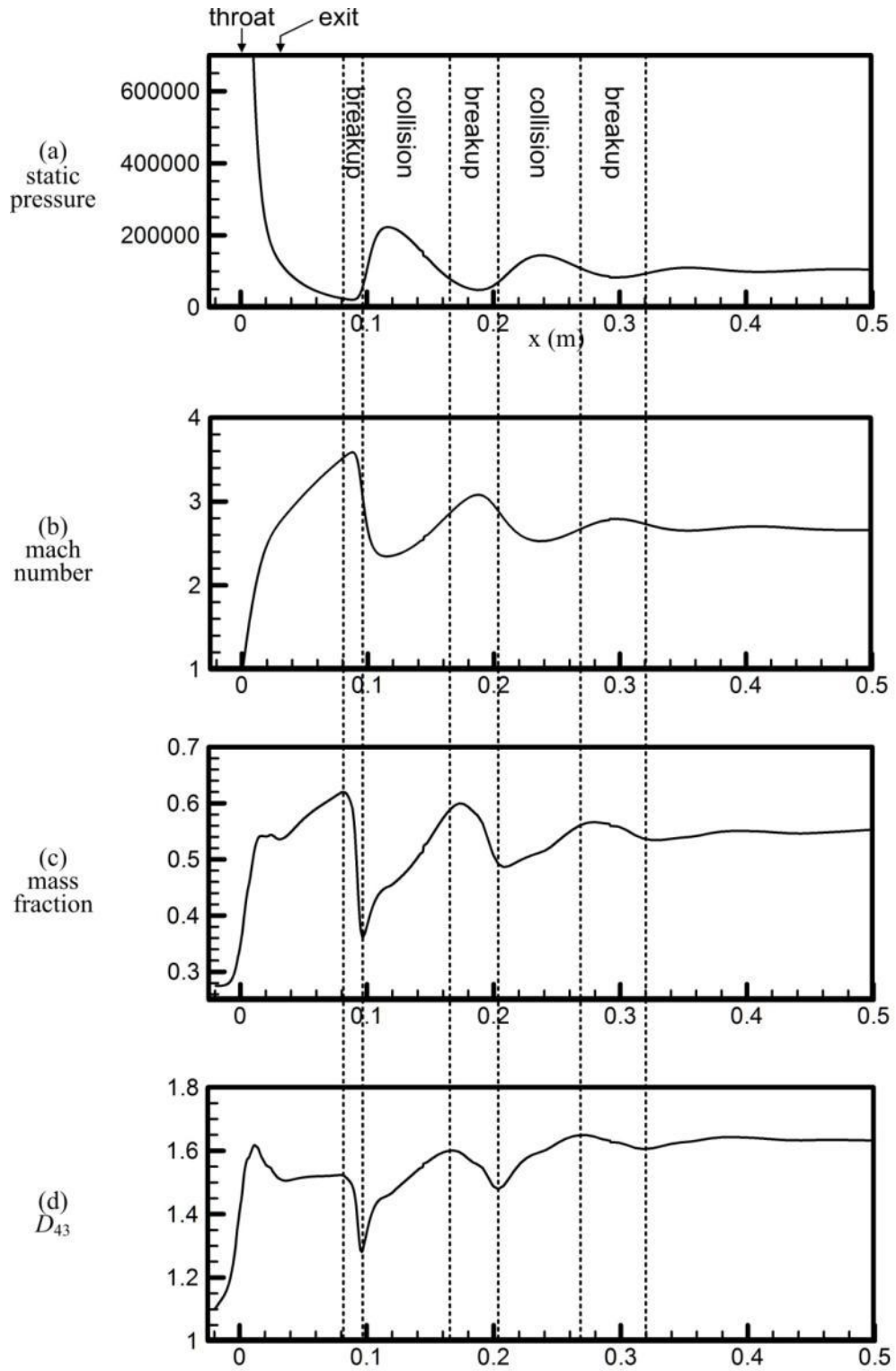
Figure 3.49 Zoomed view of predicted (a) static pressure, (b) Mach number, (c) mass fraction, and (d) mass mean diameter (D_{43}) on the centerline for case no. C-3-2 (under-expanded)

3.4.3 Summary and conclusions

Some of important conclusions can be made from data analysis on the entire domain as follows:

- Coalescence is shown to occur in the convergent section leading to the throat, while breakup processes tend to become important in the throat region and exit cone.

- In the main stream, inertial coalescence/breakup mechanisms are dominant while most of shearing growth due to turbulence is observed within boundary layer.

- In a supersonic rocket nozzle, both mean and turbulent effects on the coalescence/breakup processes are important.

- In overexpanded nozzle, a significant particle breakup due to velocity lag is observed at the front region of Mach disk in divergent section.

- In overexpanded nozzle, a significant particle collision occurs across the oblique shock region.

- With larger inlet particles, larger amount of growth occurs in the convergent section than other inlet particle size, but the width of particle distribution does not change much because larger particles are more susceptible to breakup.

- While holding the same throat to exit area ratio, the increase of converging and diverging angles of a nozzle results in the significant increase of mass mean diameter.

- Within the shock diamonds trail, particles experience the breakup-coalescence trails in an axial direction.

The restriction of current model is the necessity of the accurate information on the particle characteristics in the chamber. Therefore, the analytical techniques accurately addressing the particle size and concentration in chamber should be obtained for more accurate predictions.

3.5 Radial slot flows in SRM

The particle agglomeration/breakup studies in a solid rocket motor with radial slot were performed. The radial slot is often created to control the motor flow or make it easy to create the desired propellant geometry. The strong cross flow in the region near radial slot can result in the strong shearing motion or turbulence. The effect of this cross flow on the particle agglomeration was assessed and presented in Appendix C. Parametric studies were performed on various radial slot geometries with inhibitors based on the space shuttle booster radial slot. The effect of cross flow was assessed with respect to Mach number (or pressure difference), mass flow ratio between main and slot flows, step height behind the slot, and mass fraction of the dispersed phase.

3.6 Conclusions

An integrated and generalized numerical model has been developed to assess coalescence/breakup processes in rocket combustion applications. The model extends the capability of current low-Reynolds number models to high-Reynolds number flow with the ability to simulate coalescence/breakup processes in both laminar and turbulent flow regimes. The dominant collision mechanism within the forced convective flow, the orthokinetic collision, is responsible for most collision processes in rocket applications and it was modeled using shearing and inertial collision frequency functions.

Due to the absence of applicable models for high Reynolds numbers, new laminar collision frequency kernels were derived for application to high speed flows. The influence of multidimensional and mean flow (inertial collision) behavior permits application to flows in which shear layers are present and extension to compressible flow permits solution in a variety of high-speed flow applications such as rocket nozzles. The new models agreed well with prior incompressible formulations in this limit. Compressibility introduces a significant new effects on the collision kernel due to the contraction and dilatation effects of a fluid element. In addition, the total collision kernel employing the newly derived laminar collision frequency kernels showed more smooth behavior than prior studies when colliding particles are nearly the same size.

A series of simulations were carried out to validate the numerical model against the experimental data and empirical correlation for typical supersonic rocket nozzles. The comparisons of predicted mass mean diameter with the experimental data showed a noticeable difference and the predicted value for overall considered cases tends to be smaller than the experimental data. However, it was noted that the collection methods in experiments generally created very high shear near the collection surface which may lead to agglomeration and creation of larger particles. Considering the error bounds of correlation, the computed mass mean diameter of particles was in agreement with the mass mean diameter obtained by empirical correlation. Further validations performed on the effects of chamber pressure, particle mass concentration, and nozzle scale showed a good agreement with empirical correlation and mass mean diameter variation trends were very similar to the behavior of the empirical correlation.

Parametric studies were performed to assess particle agglomeration/breakup processes in rocket nozzles. Most importantly, comparisons between mean and turbulent flow effects showed that both mean and turbulent flow contribute to coalescence/breakup processes in a high-Reynolds number flow. The investigation of coalescence/breakup processes inside the shock diamonds trail showed breakup-coalescence trails in an axial direction and a high agglomerating zone across the oblique shock. These processes are induced because large particles experience breakup due to the existence of shock in front of Mach disk. After Mach disk, small particles accelerate quickly and they collide with large particles accelerating slowly. Evaluating the effects of chamber pressure, particle concentration, nozzle scale, geometric mean diameter and standard deviation of log-normal inlet particle number distribution, and the converging and diverging angles of nozzle wall were performed, and, as a result, their role on the coalescence/breakup processes was determined.

Furthermore, a series of numerical simulations was performed to study the gas flow and particle agglomeration in a solid rocket motor with a radial slot which produce a strong cross-flow into the main stream. A bound vortex and vena contracta are formed near the exit of the radial slot. It was found that the vortex is created when slot flows is high and the core mach number is small while at higher core mach number, lower slot flows can still create the structure. Simulations showed the strong agglomeration of particles at the vena contracta region. The particles entrained in the vena contracta region experience the strong shearing motion between the reversed axial flow and normal axial flow and result in the formation of large agglomerates.

The maximum averaged D_{43} at slot outlet and just after the vena contracta was obtained at mid mass flow ratio with a constant core Mach number. Accordingly, at a given Mach number, the low and high mass flow ratios resulted in the reduction of agglomeration at slot outlet and vena contracta region. In the vena contracta region, the maximum D_{43} over the wide range of mass flow ratios increased as Mach number increased. The additional investigation of the effect of step height and particle concentration along with Mach number and mass flow ratio showed their role on the coalescence/breakup processes in a solid rocket motor with a radial slot.

3.7 References

[1] Gany, A., Caveny, L. H., and Summerfield, M., Aluminized Solid Propellants Burning in a Rocket Motor Flowfield, *AIAA Journal*, Vol. 16, No. 7, 1978, pp. 736-739.

[2] Najjar, F. M., Ferry, J. P., Haselbacher, A., and Balachandar, S., Simulations of Solid-Propellant Rockets: Effects of Aluminum Droplet Size Distribution, *Journal of Spacecraft and Rockets*, Vol. 43, No. 6, 2006, pp. 1258-1270.

[3] Sabnis, J. S., deJong, F. J., and Gibeling, H. J., A Two-Phase Restricted Equilibrium Model for Combustion of Metalized Solid Propellant, *AIAA* Paper 92-3509, July 1992.

[4] Cheung, H., and Cohen, N. S., Performance of Solid Propellants Containing Metal Additives, AIAA Journal, Vol. 3, No. 2, 1965, pp. 250-257

[5] Friedlander, S. K., *Smoke, Dust, and Haze*, 2nd Ed., Oxford Univ. Press, New York, 2000, pp. 9.

[6] Caveny, L. H. and Gany, A., Breakup of Al/Al_2O_3 Agglomerates in Accelerating Flowfields., *AIAA Journal*, Vol. 17, No. 12, 1979, pp.1368-1371.

[7] R. M. Jenkins and R. F. Hoglund, A Unified Theory of Particle Growth in Rocket Chambers and Nozzles, AIAA No. 69-541, 1969

[8] Daniel, E., Eulerian Approach for Unsteady Two-Phase Solid Rocket Flows with Aluminum Particles, *Journal of Propulsion and Power*, Vol. 16, No. 2, 2000, pp. 309-317.

[9] Ciucci, A., Iaccarino, G., Amato, M., Numerical Investigation of 3D Two-Phase Turbulent Flows in Solid Rocket Motors, *AIAA* Paper 98-3966, July 1998.

[10] Hermsen, R. W., Aluminum Oxide Particle Size for Solid Rocket Motor Performance Prediction, *Journal of Spacecraft and Rockets*, Vol. 18, No. 6, 1981, pp. 483-490.

[11] Salita, M., Implementation and Validation of the One-Dimensional Gas/Particle Nozzle Flow Code OD3P, CPIA 529 (Vol. II), 26th JANNAF Combustion Meeting, Oct. 1989, pp. 69-82

[12] Coulaloglou, C. A., and Tavlarides, L. L., Description of Interaction Processes in Agitated Liquid-Liquid Dispersions, *Chemical Engineering Science*, 1977, Vol. 32, pp. 1289-1297.

[13] Tsouris, C., and Tavlarides, L. L., Breakage and Coalescence Models for Drops in Turbulent Dispersions, *AlChE Journal*, 1994, Vol. 40, No. 3, pp. 395-406.

[14] Prince, M. J., and Blanch, H. W., Bubble Coalescence and Break-up in Air-Sparged Bubble Columns, *AlChE Journal*, Vol. 36, No. 10, 1990, pp. 1485-1499.

[15] Wilcox, D. C., *Turbulence Modeling for CFD*, 2nd Ed., DCW Industries, La Canada, CA, 1998.

[16] Li, D., Venkateswaran, S., Fakhari, K., and Merkle, C. L., Convergence Assessment of General Fluid Equation on Unstructured Hybrid Grids, *AIAA* Paper 2001-2557, June 2001.

[17] Wang, L., Marchisio, D. L., Vigil. R. D., and Fox. R. O., CFD Simulation of Aggregation and Breakage Processes in Laminar Taylor-Couette Flow, *Journal of Colloid and Interface Science*, Vol. 282, 2005, pp. 380-396.

[18] McGraw, R., Description of Atmospheric *Aerosol* Dynamics by the Quadrature Moment of Methods, *Aerosol Sci. Tech.*, Vol. 27, 1997, pp. 255-265.

[19] Marchisio, D. L., Pikturna, J. T., Fox, R. O., and Vigil, R. D., Quadrature Method of Moments for Population-Balance Equations, *AlChE Journal*, Vol. 49, No. 5, 2003, pp. 1266-1276.

[20] Press, W. H., Teukolsky, S. A., Vetterling, W. T., and Flannery, B. P., *Numerical Recipes*: *The Art of Scientific Computing*, 3rd Ed., Cambridge University Press, 2007.

[21] Ferry, J., and Balachandar, S., A fast Eulerian method for disperse tow-phase flow, *International Journal of Multiphase Flow,* Vol. 27, 2001, pp. 1199-1225.

[22] Williams, F. A., Spray Combustion and Atomization, The physics of fluids, Vol. 1. No. 6, 1958, pp.541-545

[23] Marchisio, D. L., and Fox, R. O., Solution of Population Balance Equations using the Direct Quadrature Method of Moments, *Aerosol Science*, Vol. 36, 2005, pp. 43-73

[24] Madsen, J., *Computational and Experimental Study of Sprays from the Breakup of Water Sheets,* PhD thesis, Aalborg University, 2006.

[25] Smoluchowski, M. v., Versuch einer Mathematischen Theorie der Koagulationskinetik Kolloider Losungen, *Zeitschrift fur Physikalische Chemie*, Vol. 92, 1917, pp. 129-168.

[26] Saffman, P. G., and Turner, J. S., On the Collision of Drops in Turbulent Clouds, *Journal of Fluid Mechanics*, Vol.1, 1956, pp. 16-30.

[27] Wang, L., Wexler, A. S., and Zhou, Y., Statistical Mechanical Descriptions of Turbulent Coagulation, *Physics of Fluids*, Vol. 10, No. 10, 1998, pp. 2647-2651.

[28] Han, M., and Lawler, D. F., The (Relative) Insignificance of G in Flocculation, Journal American Water Works Association, 1992, Vol. 84, Issue 10, pp. 79-91.

[29] Williams, J. J. E., and Crane, R. I., Particle Collision Rate in Turbulent Flow, *International Journal of Multiphase Flow*, Vol. 9, No. 4, pp. 421-435.

 [30] Kramer, T. A. and Clark, M. M., Influence of Strain-Rate on Coagulation Kinetics, *Journal of Environmental Engineering*, Vol. 123, No. 5, 1997, pp. 444-452.

[31] Clark, M. M., Critique of Camp and Stein's RMS velocity-gradient., *J. Envir. Engrg. Div., ASCE*, Vol. 111, No. 3, 1985, pp.741-754.

[32] Chesters, A. K., The Modeling of Coalescence Processes in Fluid Liquid Dispersions – A Review of Current Understanding, *Chem. Eng. Res. Des.*, Vol. 69, 1991, pp. 259-270.

[33] Williams, J. J. E., and Crane, R. I., Particle Collision Rate in Turbulent Flow, *International Journal of Multiphase Flow*, Vol. 9, No. 4, pp. 421-435.

[34] Tchen, C., *Mean Value and Correlation Problems Connected with the Motion of Small Particles Suspended in a Turbulent Fluid*, PhD thesis, Delft Univ. of Technology, 1947.

[35] Abrahamson, J., Collision Rates of Small Particles in a Vigorously Turbulent Flow, *Chem. Eng. Sci.*, Vol. 30, 1975, pp. 1371-1379.

[36] Kruis, F. E., and Kusters, K. A., The Collision Rate of Particles in Turbulent Flow, *Chem. Eng. Comm.*, Vol. 158, 1997, pp.201-230.

[37] Rotta, J. C., *Turbulente Stromungen*, B. G. Teubner, Stuttgart, 1972, pp. 96.

[38] Salita, M., Use of Water and Mercury Droplets to Simulate Al_2O_3 Collision/Coalescence in Rocket Motors, *Journal of Propulsion and Power*, Vol. 7, No. 4, 1991, pp. 505-512.

[39] Ashgriz, N., and Poo, J. Y., Coalescence and Seperation in Binary Collisions of Liquid Drops, *Journal of Fluid Mechanics*, Vol. 221, 1990, pp. 183-204.

[40] Brazier-Smith, P. R., Jennings, S. G., and Latham, J., The Interaction of Falling Water Drops: Coalescence, *Proceedings of the Royal Society of London, Series A*, Vol. 326, 1972, pp. 393-408.

[41] Taylor, G. I., The Formation of Emulsion in Definable Field of Flow, *Proceedings of the Royal Society (London)*, *Series A*, Vol. 146, 1934, pp.501.

[42] Sevik, M., and Park, S. H., The Splitting of Drops and Bubbles by Turbulent Fluid Flow, *ASME Journal of Fluids Engineering*, Vol. 95, 1973, pp. 53-60.

[43] Somasundaran, P., *Encyclopedia of Surface and Colloid Science*, 2nd Ed., *Taylor and Francis*, 2006.

[44] Grace, H. P., Dispersion Phenomena in High Viscosity Immiscible Fluid Systems and Application of Static Mixers as Dispersion Devices in such Systems, *Chem. Eng. Commun.,* Vol. 14, 1982, pp.225-277.

[45] Cristini, V., Guido, S., Alfani, A., Blawzdziewicz, J., and Loewenberg, M., Drop Breakup and Fragment Size Distribution in Shear Flow, *J. Rheol.*, Vol. 47, No. 5, 2003, pp.1283-1298.

[46] Hsiang, L. –P., and Faeth, G. M., Near-Limit Drop Deformation and Secondary Breakup, *International Journal of Multiphase Flow*, Vol. 18, No. 5, 1992, pp. 635-652.

[47] Kytomaa, H. K. and Schmid, P. J., On the Collision of Rigid Spheres in a Weakly Compressible Fluid, *Phys. Fluids*, Vol. 4, No. 12, 1992, pp. 2683-2689.

[48] Liao, Y., and Lucas, D., A Literature Review of Theoretical Models for Drop and Bubble Breakup in Turbulent Dispersions, *Chemical Engineering Science*, Vol. 64, 2009, 3389-3406.

[49] Delichatsios, M. A., and Probstein, R. F., The Effect of Coalescence on the Average Drop Size in Liquid-Liquid Dispersions, *Ind. Eng. Chem. Fundam.*, Vol. 15, No. 2, 1976, pp. 134-138.

[50] Crowe, C. T. et al., Dynamics of Two-Phase Flow in Rocket Nozzles, *United Technology Center*, UTC 2102-FR, Final Report, Contract N0w264-0506-C, Sept. 1963.

[51] Crowe, C. T. et al., Investigation of Particle Growth and Ballistic Effects on Solid Propellant Rockets, *United Technology Center*, UTC 2128-FR, Final Report, Contract N0265-0222-f, June 1966.

[52] Crowe, C. T. and Willoughby, P. G., A study of Particle Growth in a Rocket Nozzle, *AIAA Journal*, Vol. 5, No. 7, 1967, pp. 1300-1304

[53] Shegal, R., An experimental investigation of a gas-particle system, *Jet Propulsion Lab.*, TR 32-238, March 1962.

[54] Fein, H. L., A Theoretical Model for Predicting Aluminum Oxide Particle Size Distributions in Rocket Exhausts, *AIAA paper*, No. 65-10, 1965.

[55] Kusters, K. A., *The Influence of Turbulence on Aggregation of Small Particles in Agitated Vessels*, PhD thesis, Eindhoven Univ. of Technology, Eindhoven, The Netherlands, 1991.

[56] Levins, D. M., and Glastonbury, J. R., Particle-Liquid Hydrodynamics and Mass Transfer in a Stirred Vessel Part I – Particle-Liquid Motion, *Trans. IChemE*, Vol. 50, 1972, pp. 32-41.

[57] Zucca, D. L. Marchisio, A. A. Barresi, and, R. O. Fox, "Implementation of the population balance equation in CFD codes for modeling soot formation in turbulent flames", Chemical engineering Science, Vol. 61, 2006, pp. 87-95.

[58] Lupoglazoff, N., and Vuillot, F., Numerical Simulation of Vortex Shedding Phenomenon in 2D Test Case Solid Rocket Motors, *AIAA Paper*, No. 92-0776, July 1992.

[60] Hatch., J. E., *Aluminum: Properties and Physical Metallurgy*, Volume 1, *ASM International*, 1984

[61] Sambamurthi, J. K., Al_2O_3 Collection and Sizing from Solid Rocket Motor Plumes, *Journal of Propulsion and Power*, Vol. 12, No. 3, pp. 598-604, 1996.

[62] L. Pan and P. PADOAN, Relative Velocity of Inertial Particles in Turbulent Flows, *Journal of Fluid Mechanics*, Vol. 661, 2010, pp. 73-107.

[63] Batchelor, G. K., *The Theory of Homogeneous Turbulence*, Cambridge University Press., 1953, p. 110.

[64] Panchev, S., *Random Fluctuations and Turbulence*. Pergamon, Oxford, 1971.

[65] Pedocchi, F. and Piedra-Cueva, I., Camp and Stein's Velocity Gradient Formalization, *Journal of Environmental Engineering*, Vol. 131, No. 10, 2005, pp. 1369-1376.

[66] Ferry, J., and Rani, S. L., and Balachandar, S., A Locally Implicit Improvement of the Equilibrium Eulerian Method, *International Journal of Multiphase Flow*, Vol. 29, 2003, pp. 869-891.

[67] Petitti, M., Nasuti, A., Marchisio, D. L., Vanni, M., Baldi, G., Mancini, N., and Podenzani, F., Bubble size distribution modeling in stirred gas-liquid reactors with QMOM augmented by a new correction algorithm, *AlChE Journal*, Vol. 56, No. 1, 2010, pp. 36-53.

[68] Hatch, T., and CHOATE, S. P., Statistical Description of the Size Properties of Non-uniform Particulate Substances, *J. Franklin Inst.*, Vol.207, 1929, pp.369-387.

[69] Lupoglazoff, N., and Vuillot, F., Numerical Simulation of Vortex Shedding Phenomenon in 2D Test Case Solid Rocket Motors, *AIAA Paper*, No. 92-0776, 1992.

[70] Dobbins, R.A., and Strand, L.D., A Comparison of Two Methods of Measuring Particle Size of Al_2O_3, Produced by a Small Rocket Motor, *AIAA Journal,* Vol. 8, No. 9, 1970, pp. 1544-1550.

[71] Jacobs, C., Qin, Z., and Bremhorst, K., Comparison of RANS Modeling with DNS and Experimental Data for a Converging-diverging Nozzle and a Rotating Cylinder Electrode, *Fifth International Conference on CFD in the Process Industries*, CSIRO, Melbourne, Australia, 13-15 December 2006.

[72] Pandey, K. M. and Singh A. P., CFD Analysis of Conical Nozzle for Mach 3 at Various Angles of Divergence with Fluent Software, *International Journal of chemical Engineering and Applications*, Vol. 1, No. 2, 2010, pp. 179-185.

[73] Chang, I-S., One- and Two-Phase Nozzle Flows, *AIAA Journal*, Vol. 18, No. 12, 1980, pp. 1455-1461.

[74] Sabnis, J., Madabhushi, R., and Gibeling, H., On the Use of k-e Turbulence Model for Computation of Solid Rocket Internal Flows, *AIAA paper*, No. 89-2558, 1989.

[75] Ciucci, A., Iaccarino, G., Moser, R., Najjar, F., and Durbin, P., Simulation of rocket motor internal flows with turbulent mass injection, Center for Turbulence Research, *Proceedings of the Summer Program*, 1998, pp. 245-265.

Appendix A - PD (Product Difference) algorithm

The product difference (PD) algorithm, which is used to find weights (w_i) and abscissas (l_i) from the moments (m_z) while solving PBE, is given by Mcgraw [18] and Wang et al. [17] and it is summarized here.

The first step is to obtain a matrix **P** as follows:

$$P_{i,1} = \delta_{i1} \qquad\qquad \text{for} \quad i=1,......,2N+1$$
$$P_{i,2} = (-1)^{i-1} m_{i-1}' \qquad\qquad \text{for} \quad i=1,......,2N \qquad\qquad (A.1)$$
$$P_{i,j} = P_{1,j-1}P_{i+1,j-2} - P_{1,j-2}P_{i+1,j-1} \quad \text{for} \quad i=1,......,2N+2-j \text{ and } j=3,......,2N+1$$

From the obtained matrix **P**, the coefficients (α_i) are given as follows:

$$\alpha_1 = 0$$
$$\alpha_i = P_{1,i+1}/(P_{1,i}P_{1,i-1}) \qquad \text{for} \quad i=2,......,2N \qquad\qquad (A.2)$$

Then, a symmetric tridiagonal matrix **S** is obtained with the following diagonal ($s_{d,i}$) and co-diagonal ($s_{cd,i}$) components:

$$s_{d,i} = \alpha_{2i} + \alpha_{2i-1} \qquad \text{for} \quad i=1,......,N$$
$$s_{cd,i} = -\sqrt{\alpha_{2i}\alpha_{2i+1}} \qquad \text{for} \quad i=1,......,N-1 \qquad\qquad (A.3)$$

After the symmetric tridiagonal matrix is obtained, the weights and abscissas are obtained by finding its eigenvalues and eigenvectors. The eigenvalues of the matrix **S** are the abscissas and the weights are given by

$$w_i' = m_0' \nu_{i1}^2 \qquad \text{for} \quad i=1,......,N \qquad\qquad (A.4)$$

where ν_{i1} is the first component of eigenvector ν_i . The eigenvalues and eigenvectors are found by *QL* algorithm.

Effects of Ammonia Borane on the Combustion of an Ethanol Droplet at Atmospheric Pressure

M. A. Pfeil[a], L. J. Groven[b], R. P. Lucht[b], and S. F. Son[b]

[a]*School of Aeronautics and Astronautics, Purdue University, West Lafayette, IN 47907, USA*
[b]*School of Mechanical Engineering, Purdue University, West Lafayette, IN 47907, USA*

Abstract

Adding compounds rich in hydrogen to liquid fuels has the potential to change the combustion behavior of the fuel, possibly enhancing performance. One potential additive is ammonia borane (AB), which contains 19.6 wt.% hydrogen and can be dissolved in anhydrous ethanol (up to 6.5 wt.%). Single droplet combustion experiments are performed with AB concentrations in ethanol varying from 0 to 6 wt.%. Measurements performed using high speed (5 kHz) planar laser-induced fluorescence (PLIF) indicate that hydrogen gas addition from the decomposition of AB continues throughout the droplet burning process. The hydrogen addition leads to an increase in the D^2 law rate constant of up to 16%. While AB participates throughout the combustion process, it dramatically impacts the combustion behavior at the end of the droplet lifetime. The rate of energy release increases significantly near the end of the burning process as the droplet shatters, causing fine atomization and rapid combustion of the remaining fuel. Boron is also oxidized in this short period of time, increasing the energy released. In combustors, droplet shattering could enhance mixing and increase combustion efficiency. Thus adding compounds rich in hydrogen is a promising method to introduce H_2 gas to practical combustion systems, while enhancing performance.

1. Introduction

Recently, several efforts have been made to change the combustion behavior of fuels by adding hydrogen (H_2) gas to combustion systems [1]-[3]. Hydrogen is typically added in gaseous or liquid state in or upstream of the combustor producing varying results. Guo *et al.* [4] reduced combustor emission levels while increasing the combustion efficiency of a fuel through the addition of H_2. Hydrogen also lowered the flammability limits of fuels, allowing the combustors to operate fuel lean; this in turn promoted lower emissions [5]-[7]. Gaseous hydrogen has shown potential in stabilizing a normally unstable rocket combustor [1] suggesting that hydrogen addition to other fuels could produce the same effects. In fact, Rosen *et al.* [2] showed that as little as 5 wt.% addition of gaseous hydrogen to gaseous methane could change the stability characteristics of a system.

The current method of introducing H_2 into a combustor is to store it separately from the fuel and inject it into the fuel line or combustor. While acceptable for research purposes, this method is impractical for many applications due to the large volumes required to store gaseous H_2, or the cryogenic requirements of using liquid H_2. One possible solution that has yet to receive significant attention involves introducing H_2 into the fuel through additives high in hydrogen content such as metal hydrides or boranes. These materials would not only be a practical pathway of introducing H_2 but also have the potential of increasing energy density and overall fuel performance.

However, adding hydrogen to a fuel through additives restricts the control of when and where the hydrogen is added to the combustion process which is controlled by the proximity of the fuel boiling point to the decomposition temperatures of the hydrogen containing additive. High boiling points and low decomposition temperatures will allow hydrogen to be introduced to the

combustion process early and thus allow it to influence the combustion behavior of the system. The opposite trend will inhibit the influence of hydrogen, making it an ineffective additive. Therefore, the determination of when and how hydrogen is released from the fuel becomes important when evaluating an additive and its potential effects on the combustion process of a system.

This paper examines one possible fuel and additive combination of ethanol and ammonia borane (AB). These two fuel components are selected due to the high concentration of hydrogen that AB contains (19.6 wt.%) and the close proximity of the boiling point and decomposition temperature of the two. We attempt to determine how this additive, specifically the H_2, influences the combustion process of the fuel. Questions addressed are first, when will the hydrogen be released from the liquid fuel, second, how the addition of hydrogen will influence the combustion behavior of the fuel, and third, how will the other decomposition products of AB influence the combustion process. These questions are investigated through a series of fundamental, single droplet experiments while implementing high speed cinematography and high speed OH planar laser-induced fluorescence measurements. These experiments provide general insight into combustion changes and allow for dynamic observations of the effect of AB addition on the combustion of ethanol.

2. Experimental Setup

2.1. Fuel

The fuels selected in this investigation consisted of ethanol and AB. Ammonia borane (NH_3BH_3), consists of 19.6 wt.% hydrogen, and can be dissolved into fuels ranging from alcohols to ethers. In addition to hydrogen, AB also contains boron that adds energy to a system.

In ethanol, ammonia borane can be dissolved up to 6.5 wt.% allowing 1.3 wt.% of the fuel to be hydrogen.

The two types of AB used for these experiments included AB from Sigma Aldrich, 97% pure, and AB produced at Purdue University through a process developed by Ramachandran *et al.* [8], 98% pure. The AB was dissolved into 200 proof ethanol resulting in an unstable fuel mixture that produced ammonia gas over several months, thus the fuel was used within several days of preparation. The decomposition of AB was probably caused by water adsorbed by the ethanol from the surrounding air.

2.2. **Droplet Combustion**

Droplets were suspended on quartz rods with beads formed at the end, a method previously used by other researchers [9],[10]. Quartz was chosen due to its relatively low thermal conductivity, resulting in minimal heat transfer to the droplet. Quartz rod diameters right above the bead ranged from 62 to 192 μm while bead sizes ranged from 217 to 376 μm. Several droplets of neat ethanol were burned on each rod before burning a droplet containing AB. The rods were cleaned between droplet burns using a butane flame. The rod was exchanged after the combustion of two droplets containing AB to avoid buildup of AB combustion products.

The quartz rods were suspended in a clear acrylic box with an aluminum bottom and an open top. This configuration was used to minimize forced convection effects on the droplet while allowing it to combust in atmospheric air. A coiled 30 gauge Nichrome wire was inserted through the side of the acrylic box and positioned near the droplet. A voltage was applied across the wire causing it to heat and ignite the droplet. After ignition, the Nichrome wire was removed in order to avoid interaction with the combustion zone. Backlighting, produced by a halogen lamp placed behind an Interfit translucent light reflector, provided a contrasting, white

background. A Vision Research Phantom V. 7.3 black and white high speed camera was operated at a frame rate of 5000 fps, a pixel resolution of 320x240, and a 14 bit image depth. A schematic diagram of this experimental system is shown in Figure 16. The videos taken using the high speed camera were analyzed using MATLAB software [11] to determine the equivalent diameter of the droplet cross-sectional area as a function of time.
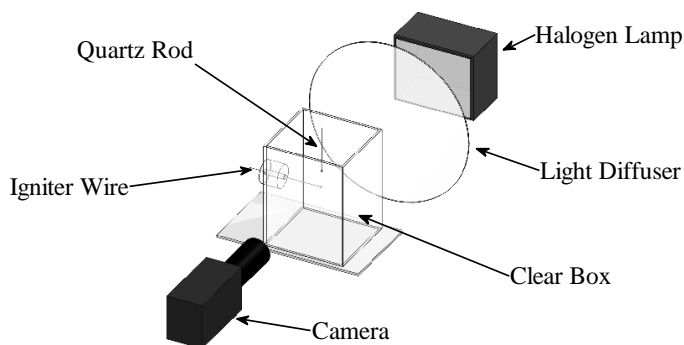

Figure 16 Schematic diagram of the droplet combustion experiment.

The high speed camera implemented two lens configurations to observe various combustion behaviors. The first configuration consisted of an Infinity Photo-Optical Company K2 Long Distance Microscope lens and was used to make general observations of the combustion behavior. The second configuration incorporated the use of a Thorlabs laser line filter with the Infinity K2 lens. The filter had a transmission of 70%, a center wavelength of 543.5 nm ±2, and a full width half max of 10 nm ±2. A lens with this particular wavelength was used as various researchers have reported strong bands of emission for either boron or boron compounds burning between 536 and 548 nm [12], thus allowing for a reliable measurements of where and when boron combustion was occurring. A Vision Research Phantom V. 7.3 color high speed camera, with the same Infinity K2 lens, was also used to record general combustion behavior, primarily to observe flame color during combustion.

2.3. **High Speed Planar Laser-Induced Fluorescence (PLIF) System**

A brief description of the high speed PLIF system is given here. For further details about the system, the reader is referred to the work done by Hedman *et al.* [13]. A Sirah Credo (CREDO-DYE) dye laser was pumped at a repetition rate of 5 kHz by an Edgewave Nd:YAG (IS811-DZ) solid state laser. The pulse energy of the frequency-doubled 283.23 nm beam from the dye laser was measured to be 0.15 mJ/pulse.

The beam was expanded vertically and horizontally using a negative spherical lens ($f = $ -75 mm, Clear Aperture (C.A) = 21.3 mm) and expanded further horizontally using another negative cylinder lens (f= 50 mm, C.A = 21.3 mm). The beam was then focused using a positive spherical lens ($f = $ 500 mm, C.A = 50.0 mm) resulting in a well collimated beam having a large circular cross section of approximately 5 cm. A thin sheet was then produced after the light was focused through a square cylindrical lens ($f = $ 250 mm, C.A = 43.2 mm * 43.2 mm). The distance between these lenses was adjusted to change the sheet height and width. The width of the beam was smaller than the droplet initial diameters and was tall enough to capture the diffusion flame around the droplet.

The laser wavelength was set to 283.2 nm to excite the Q1(7) OH line. Experiments were also performed at a laser wavelength of 283.1 nm that did not excite the OH radical, thus allowing us to distinguish between broadband fluorescence and the OH radical. Experiments performed using the wavelength of 283.1 nm will be referred to as "detuned" throughout this paper.

The OH signal was recorded using a UV intensifier, high speed camera assembly. A Video Scope International high speed image intensifier (VS4-1845HS), capable of operating at 100 kHz with a gain of up to 80,000, was attached to the Vision Research Phantom V. 7.3 camera. A UV-

grade lens (UKA Optics - UV1054B 105mm F/4.0 Quartz Lens) was attached to the UV intensifier. A Semrock interference filter (FF01-320/40-25) that had a transmission of 74% at 310 nm was used to transmit OH fluorescence and block broadband flame emission and scattered laser light. This camera assembly was placed perpendicular to the laser plane as shown in the schematic diagram in Figure 17.

Images acquired using this setup were post processed with MATLAB software [11]. Droplet diameter and OH intensity distributions were recorded. The laser caused the droplet itself to fluoresce thus allowing the droplet diameter to be determined from the edge of this fluorescence. The light emission immediately around the droplet was removed in MATLAB before finding the droplet size to provide a more accurate measurement. Quartz rods similar to those used in Sec. 2.2 were placed within the laser sheet and a drop was deposited on the bead. The diameter of these quartz rods just above the bead ranged from 103 to 198 μm while bead sizes varied from 313 to 516 μm. Bead sizes were generally larger to allow for larger droplets of fuel. This was done so that a relatively large droplet of fuel was still present when ignition occurred as the energy from the laser increased the evaporation rate of the fuel before ignition. The amount of time the droplet was exposed to the laser before ignition was minimized as well to reduce the amount of evaporation prior to ignition.
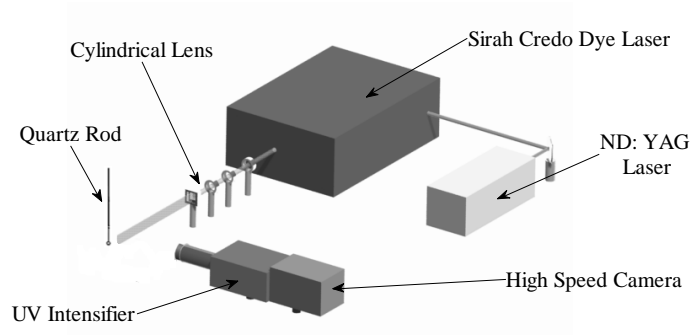
Figure 17 Schematic diagram of the high speed OH PLIF experiment.

2.4. **Droplet Combustion Modeling**

There were two models used in this study to help interpret results. They included a classical droplet combustion model and a finite rate computational program known as COSILAB [14]. The classical droplet combustion model, discussed in detail by Law *et al.* [15], was used to investigate the effects of AB addition on the burning rate of the droplet. According to this model, the D^2 law rate constant for ideal combustion, k_0, of a droplet is dependent on the thermal properties of the fuel and oxidizer and is given by,

where λ_1 is a combination of the thermal conductivities of the fuel and oxidizer in the space between the flame and the droplet, c_1 is the specific heat of the fuel vapor in the same region, ρ_f is the density of the fuel at its boiling point, and B is the transfer number. The D^2 law rate constant for ideal combustion was based solely on these parameters, and effects such as finite-rate chemistry and buoyancy were neglected. B is given by,

where $Y_{O\infty}$ is the oxygen mass fraction, T_∞ is the temperature of the oxidizing medium, T_b is the boiling point of the fuel, q is the heat of combustion of the fuel at T_∞, i is the stoichiometric oxygen to fuel mass ratio, and   is the latent heat of vaporization of the fuel at T_b.

Several assumptions were made to incorporate the addition of AB to the fuel droplet. The first assumption was that H_2 gas was the only decomposition product of AB to join ethanol in the fuel vapor and react with the oxygen. The other decomposition products were assumed to remain within the liquid droplet. This was deemed to be a valid assumption due to 1) the proximity of the boiling temperature of ethanol (351 K) and the temperature at which the first stage of AB decomposition occurs for high heating rates (385 K) [16], which produces mainly H_2 gas, 2) the findings of others indicating that the decomposition temperature of AB can decrease when in solution [17]-[19], and 3) AB decomposition has been noted to begin at lower temperatures of 343 K when low heating rates are used [20]. Other decomposition products are formed at temperatures above 400 K, but it was assumed that this temperature was not reached within or at the droplet surface during the quasi-steady burning process until the ethanol was nearly consumed. Quasi-steady burning refers to the portion of the droplet lifetime where the regression rate is fairly constant, neglecting the ignition and extinction transients. It was thus assumed that 1.1 mole of H_2 was produced for every mole AB, at temperatures less than 400 K as has been observed [21]. This resulted in 7.2 wt.% of the AB being converted into H_2 gas during the combustion of ethanol. This produced a fuel vapor composed of 0.5 wt.% of H_2 and 99.5 wt.% of ethanol when 6 wt.% of AB is added to ethanol.

The H_2 gas addition to the fuel vapor affected the thermal conductivity, specific heat, heat of combustion, flame temperature, latent heat of vaporization, and the stoichiometric oxygen to fuel ratio of the fuel vapor while the addition of AB affected only the density of the liquid fuel. With

the exception of density and thermal conductivity, each parameter was weighted depending on the mass fraction of H_2 in the fuel vapor (e.g. having a mass fraction of 0.1 of H_2 gas gave a specific heat that is 10% of the specific heat of H_2 and 90% of the specific heat of ethanol). The thermal conductivity of the fuel vapor was calculated using the Wassiljewa equation and implementing the Mason and Saxena modification [22] that has been shown to calculate the thermal conductivity of two gas mixtures within a few percent. Data for each parameter were taken from several sources [23]-[26] while flame temperatures were obtained from NASA's CEA2 code [27]. The data were fitted as a function of temperature giving the desired value at the required temperature. Extrapolation was used when data were not available in the specific temperature range. The density of the ethanol-AB solution was measured at room temperature and compared to the density of ethanol. The percent change in density at room temperature between ethanol and ethanol with 6 wt.% AB was calculated and used to determine the density of the ethanol-AB solution at the boiling point of ethanol. Values used in these calculations are shown in 3.

3 Parameters Used in Droplet Combustion Model

| Liquid Fuel Density, g/cm³ | Hydrogen Wt.% | Fuel Vapor Parameters | | | | | |
		Thermal Conductivity, W/mK	Specific Heat, J/gK	Heat of Combustion, J/g	Flame Temperature, K	Latent Heat of Vaporization, J/g	Stoichiometric O/F Ratio
			Ethanol				
0.7379	0	0.3038	4.2857	2.9668×10^4	2240	837.00	8.9424
			Ethanol with 6 wt.% AB				
	0	0.3038	4.2857	2.9668×10^4	2240	837.00	8.9424
	0.2298	0.3092	4.3132	2.9925×10^4	2241	836.10	9.0001
0.6938	0.4839	0.3149	4.3433	3.0210×10^4	2242	835.11	9.0640
	0.7663	0.3215	4.3781	3.0527×10^4	2244	834.01	9.1349
	1.0821	0.3281	4.4153	3.0881×10^4	2245	832.77	9.2142
	1.4377	0.3356	4.4583	3.1280×10^4	2247	831.38	9.3035

Law *et al.* [15] considered the effects of natural convection and finite-rate chemistry on the burning rate of the droplet. These correction factors incorporate constants that were determined

by empirical calibration. As such, the constants can be found for the neat ethanol fuel, but because of transients during burning, this model was inadequate to compare how AB and H_2 gas addition will influence the effects of natural convection and finite rate chemistry. Nevertheless, these two effects can play an important role in the burning rate of the fuel and will be discussed later.

The other model used proceeds from the program COSILAB, using 1-D spherical geometry diffusion flame and implementing detailed finite-rate chemistry. The fuel side consisted of H_2 gas added to ethanol at 351 K (the boiling point of ethanol), and the oxidizer side consisted of air initially at 300 K. A hot spot was placed between the fuel and oxidizer to start the reaction which proceeded until a steady state solution was found given the boundary conditions. The fuel boundary was given a specific, fixed radius equal to the desired droplet size. Reaction rates, mechanisms, thermodynamic properties, and transport properties used in the detailed chemistry were compiled by Marinov [28]. The spherical and diffusive flame similarities between the experiment and model allow for trend comparisons as H_2 gas is added to the fuel vapor.

3. Results and Discussion

Neat ethanol fuel is used as a baseline for comparison. During combustion, a droplet of this fuel is surrounded by a light blue flame and exhibits a smooth regression rate except during ignition and extinction transients. The regression rate changes when the size of the droplet becomes comparable to the bead size. Typical images taken using the high speed camera and with the high speed PLIF system for ethanol are shown in Figure 18. Due to backlighting, the light blue flame cannot be distinguished.
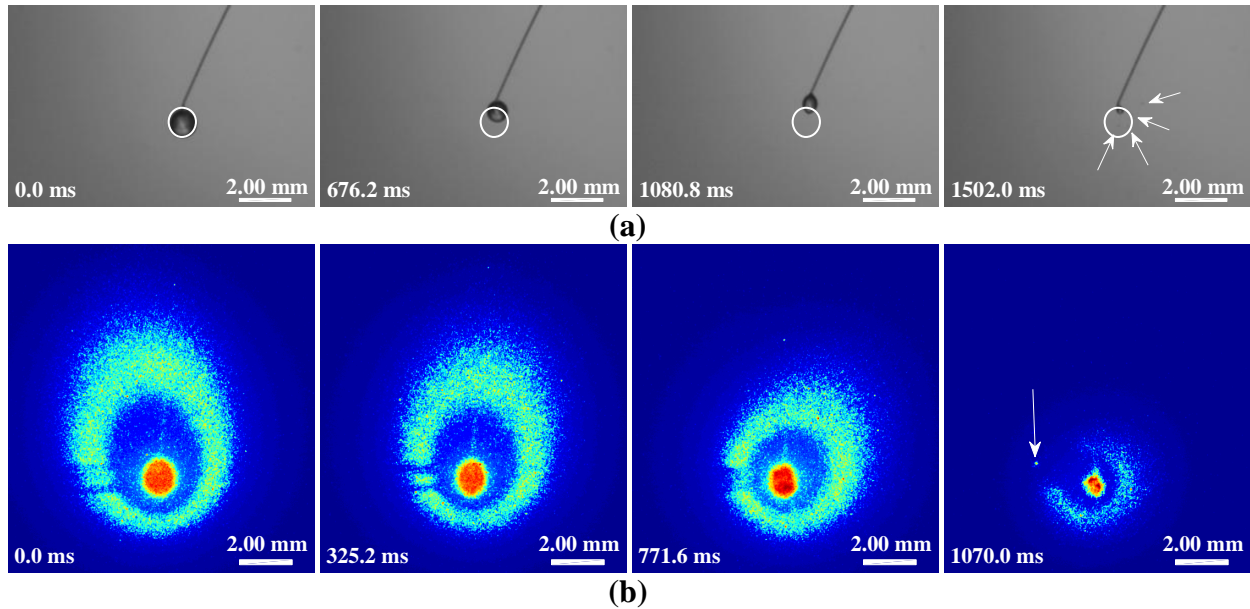
Figure 18 Combustion behavior for an ethanol droplet. (a) Backlit visual images of droplet that have been brightened. Arrows indicate liquid that has been ejected from main droplet and ellipse is given as a reference of the droplet initial shape and location. (b) PLIF measurements of separate droplet with false coloring.

When the majority of the fuel has been consumed, small bubble formation can occur, causing liquid to be expelled from the droplet surface as the bubble ruptures. The droplet then extinguishes itself or breaks apart, as seen in the fourth frame of Figure 18. Similar behavior is observed in the PLIF measurements as seen in the fourth frame of Figure 18(b). In the PLIF images, the OH signal is the circular band around the droplet and is asymmetric due to natural convection. The OH band is present throughout the burn and is only disturbed near the end of the droplet lifetime when small amounts of expelled fuel break the ring; however, it is always discontinuous to the left of the droplet because the energy from the laser is either absorbed or reflected by the droplet.

Droplets containing AB combust very differently. These drops are surrounded by a blue flame throughout the majority of the burn that becomes green near the end of the droplet lifetime. Figure 19 shows typical observations for a droplet of ethanol containing 6 wt.% AB. Unlike neat ethanol, gas generation leading to bubble formation within the droplet is common throughout the

duration of the burn. Clearly the AB is decomposing inside of the droplet causing bubbles to
form, coalesce, and grow, eventually reaching the surface of the droplet. Once at the surface, the
bubbles rupture, and gas and small liquid droplets are expelled from the main droplet. This
behavior influences the local droplet regression behavior causing it to be non-steady; however,
the overall regression rate still follows the typical D^2 law behavior. Droplets also experience a
change in the apparent regression rate when the droplet size becomes comparable to the bead
size.

(a)

(b)
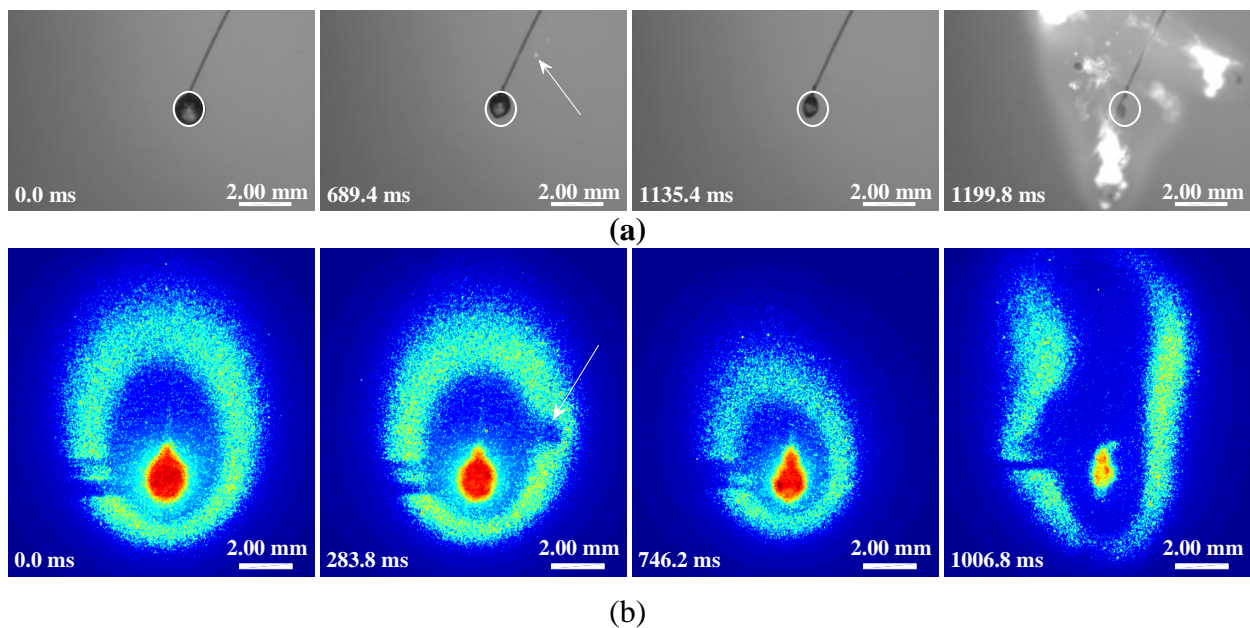
Figure 19 Combustion behavior for an ethanol droplet with 6 wt.% AB. (a) Backlit visual
images of droplet that have been brightened. Arrows indicate liquid that has been ejected from
main droplet and ellipse is given as a reference of the droplet initial shape and location. (b) PLIF
measurements of separate droplet with false coloring.

As the droplet approaches the end of its lifetime, the liquid becomes more viscous. Such
behavior allows for larger bubbles to form within the droplet. The rupture of these large bubbles
often causes the droplet to shatter leading to atomization of the remaining fuel into small droplets
that burn very quickly. The flame also changes from blue to green when this occurs. The result
of such an event is shown in the fourth frames of Figure 19(a) and Figure 19(b).

3.1. **Effects of Ammonia Borane on Flame Structure**

The addition of AB to ethanol causes the OH band around the droplet (indicative of the reaction zone) to elongate as if the droplet was placed into a forced convective environment becoming more pronounced as AB concentration increases. This behavior can be seen in Figure 20 which are PLIF images of droplets with equivalent diameters, ~1.37 mm. The plots in Figure 21 provide a more quantitative depiction of the shift in the reaction zone with the addition of AB. The data for these figures are produced by removing "slices" from the plots in Figure 20, indicated by the white lines, and indicate the intensity of the fluorescence signal as a function of distance from the droplet centroid measured in droplet radii. The intensity of the droplet fluorescence is removed from these plots and replaced with zero to indicate where the droplet is located, while data is only shown on one side of the droplet since the signal on the other side of the droplet is obscured. The addition of 3 wt.% AB causes the reaction zone to move farther away from the droplet, while the reaction zone 6 wt.% has relatively the same distance as neat ethanol. The reaction zone below the droplet has no noticeable change with the addition of AB, Figure 21(b), but moves farther away from the droplet as the concentration of AB increases.
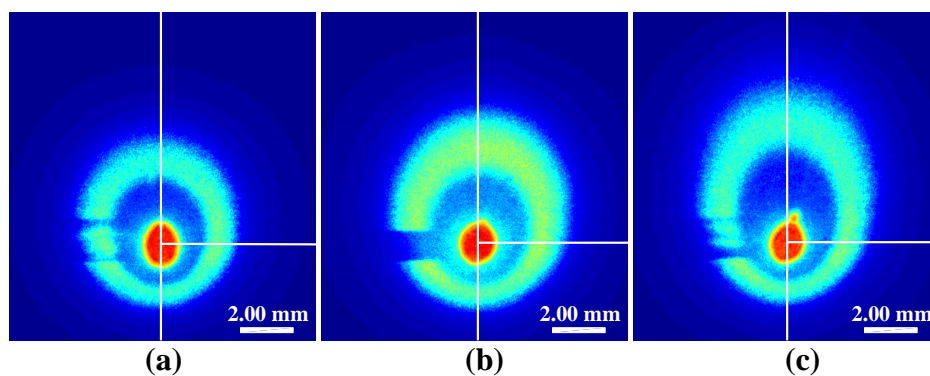

Figure 20 False colored PLIF measurements of droplets burning with laser operating at the OH excitation frequency of 283.23 nm and averaged over 4.2 ms. (a) Neat ethanol. (b) Ethanol with 3 wt.% AB. (c) Ethanol with 6 wt.% AB.

The peaks of these reaction zones, indicated by the o, $+$, and x markers, show the same behavior just noted. Next to the droplet, the distance of the peak of the reaction zone from the droplet centroid increases from 3.02 radii to 3.39 radii with the addition of 3 wt.% AB and drops

to 3.29 for 6 wt.%. Above the droplet, the peak moves from 4.40 radii to 4.86 radii and 7.15

radii for 3 and 6 wt.% AB respectively. These relative trends continue throughout the quasi-

steady combustion process as shown in Figure 22 which is a plot of the distance from the peak of

the reaction zone to the droplet centroid as these droplets burn. The data presented are from the

droplets depicted in Figure 20 while the lines are linear fits of the data from all droplets for each

particular fuel. The linear fits for the data of the reaction zone next to the droplet indicate no

significant deviation by adding AB to the fuel, Figure 22(a); however, above the droplet, the

increasing AB concentration moves the reaction zone from roughly 4.5 radii, neat ethanol, to 5.5

and 6.5 radii for 3 and 6 wt.% AB respectively, Figure 22(b). The difference of 2 radii between

neat ethanol and ethanol with 6 wt.% AB is consistent through the burn, while it appears that the

fuel containing 3 wt.% AB initially has the same distance as the fuel containing 6 wt.% AB and

then decreases until the reaction zone has almost the same distance as the neat fuel. The linear

fits and data also indicate that the relative distance between the droplet and reaction zone

increases as the droplet becomes smaller, except for the reaction zone above the droplet for the

fuel with 3 wt.% AB. This is consistent with the observations made by Yozgatligil *et al.* [29]

who found that the distance between the droplet and flame sheet increased as the droplet

diameter decreased for neat ethanol droplets.

**(a)**   **(b)**
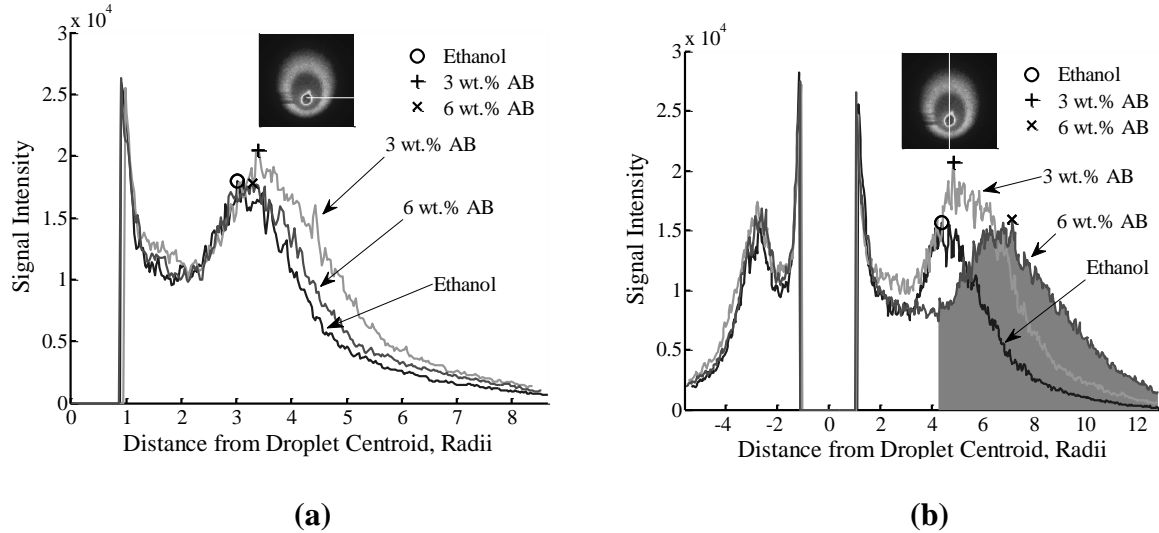
Figure 21 Horizontal, (a), and vertical, (b), slices taken from images in Figure 20 showing the OH PLIF signal as a function of droplet radius. The signal from the droplet itself is removed from the figures by giving it a value of zero. The *o*, +, and *x* markers correspond to the peaks in the OH reaction zone.

The most plausible explanation for the apparent increased convective flow around the droplet causing the reaction zone to elongate is the decomposition of AB during combustion leading to the release of H_2 gas into the fuel vapor. Hydrogen gas is a very low density (8.99×10^{-5} g/cm^3) gas that rises quickly in the presence of gravity and other gases. Its high diffusive rates allow it to move quickly away from the surface of the droplet producing the larger void between the droplet and the flame above the droplet in Figure 20. The rate of H_2 gas being produced remains constant for the droplet containing 6 wt.% AB; however, this does not appear to be the case for the droplet containing 3 wt.% AB. Initially the rates of H_2 generation is the same for the droplets containing 3 and 6 wt.% AB, but the rate for the 3 wt.% decreases eventually producing similar flame structures to the neat fuel. This could be brought about by the depletion of H from the AB within the droplet or possibly other heavier decomposition products such as ammonia (NH_3) are being produced in place of hydrogen.
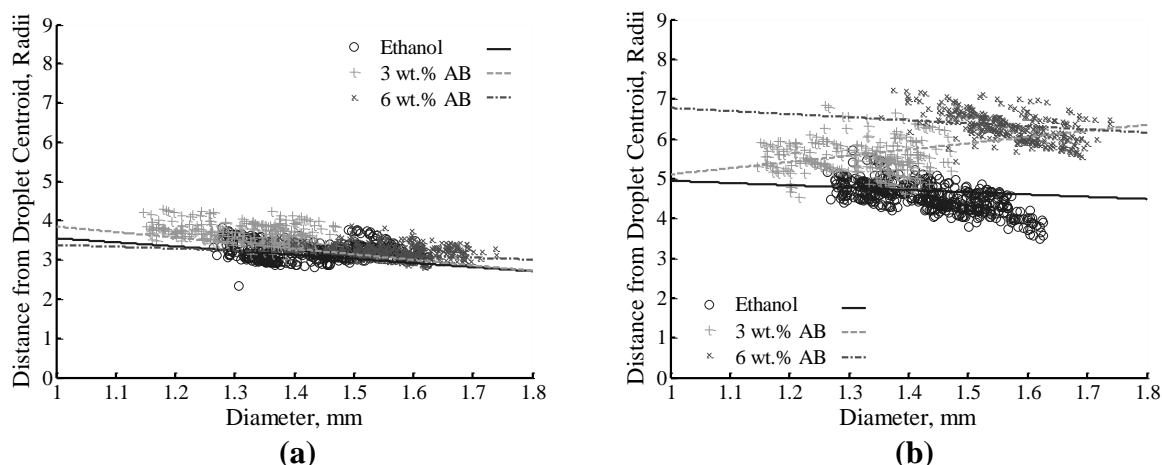
Figure 22 Distance of peak in OH band from droplet centroid as a function of droplet diameter at various locations around the droplet. Data shown is from single droplet experiments while lines are linear fits of data from all droplets of each particular fuel type. (a) Right of droplet. (b) Above droplet.

A change in the quantity of OH present in the reaction zone occurs as AB is added to the fuel. The amount of OH, along the same axis in Figure 21, is found by finding the minimum in the signal intensity between the droplet and the OH reaction zone. Everything between this minimum and the droplet is assumed not to be OH while everything outside of this minimum is assumed to be OH. This assumption is reasonable since the signal emission immediately around the droplet is not OH as was determined by repeating these experiments with the laser detuned. The area under the curve, shaded region in Figure 21, is then found through integration and determined to be the amount of OH present in that portion of the flame. Representative data obtained from this method is shown in Figure 23. Initially, the amount of OH to the right of the droplet is the same for all of the fuels but changes as the droplets burn, Figure 23(a). The amount of OH remains the same for both the neat fuel and fuel containing 6 wt.% AB, while the fuel with 3 wt.% AB increases as the droplet burns. The amount of OH above the droplet is notably higher for the droplets containing AB when compared to the neat fuel, a consistent trend throughout the burn, Figure 23(b).
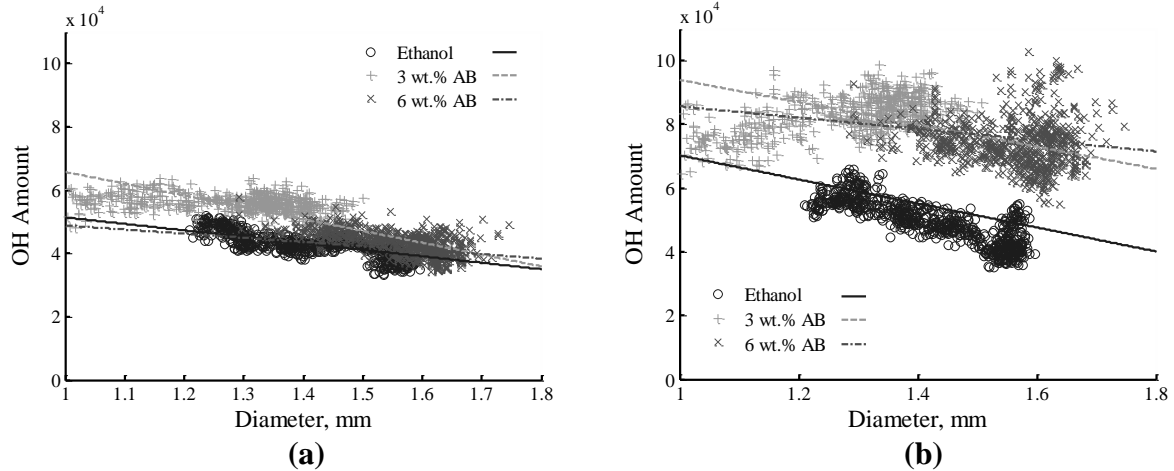
Figure 23 OH signal concentration intensity as a function of droplet diameter in various locations in the flame. Data shown is from single droplet experiments while lines are linear fits of data from all droplets of each particular fuel type. (a) Right of droplet. (b) Above droplet.

Calculations performed in COSILAB [14] indicate that the addition of H_2 gas to the fuel vapor, 1.1 wt.%, will increase the OH mass fraction in the reaction zone by 5%. Hydrogen gas addition to the fuel vapor is thus attributed as the cause for the increase in OH around the droplet when AB is added to the fuel providing another indication of continuous decomposition of AB during combustion. The light molecules of H_2 probably move quickly upwards causing the OH concentration next to the droplet to be unaffected by H_2 production. The increase in the amount of OH to the right of the droplet for the fuel containing 3 wt.% AB is again probably caused by a shift from H_2 generation to heavier NH_3 or other gaseous decomposition products containing H atoms. The heavier decomposition products would not rise so quickly, thus causing increased OH generation on the side of the droplet.

3.2. **Effects of Hydrogen on Combustion Behavior of the Droplet**

Ammonia borane has a noticeable effect on the regression rate of ethanol. Figure 24(a) shows typical droplet regression rate behaviors for both neat ethanol and ethanol with 6 wt.% AB droplets during quasi-steady combustion. The D^2 law rate constants are found from the slopes of these lines before the quartz bead influences the regression rate. The measured rate constant for

neat ethanol is 0.80 mm^2/s with a standard deviation of ±0.05 mm^2/s, similar to the findings of

Godsave (0.82 mm^2/s) [9] and Kumagai *et al.* (0.75 mm^2/s) [10] when ethanol is burned in

similar buoyant, atmospheric conditions in air. Adding 6 wt.% AB increases the D^2 law rate

constant to 0.93 mm^2/s with a standard deviation of ±0.08 mm^2/s. This represents a 16%

increase in the D^2 law rate constant. Results obtained using the simplified model of Law *et al.*

[15] produced similar increasing trends in the D^2 law rate constant with the addition of AB.

Calculations indicate that neat ethanol has a D^2 law rate constant of 0.67 mm^2/s, which is in good

agreement with experiments performed by Yozgatligil *et al.* [29] in a buoyant free environment

(microgravity) for droplets with an initial diameter of ~1 mm. The addition of AB to the fuel

increases the D^2 law rate constant by 8% when assuming 0.5 wt.% of the fuel vapor is hydrogen,

see Sec. 2.4. This is only half of the measured increase found in the experiments.
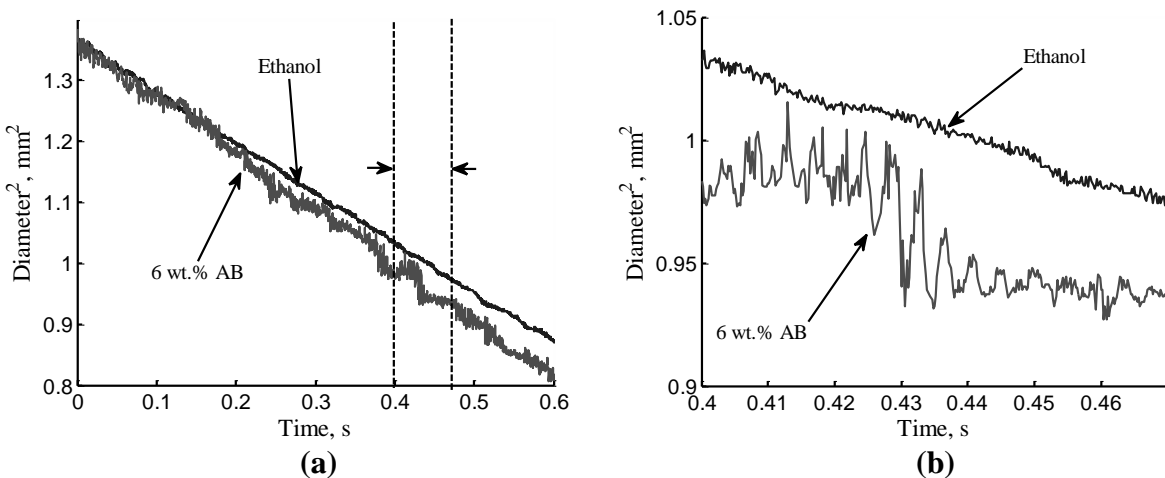

Figure 24 Droplet diameter time history of neat ethanol and ethanol with 6 wt.% AB. The overall general behavior is shown in (a) as well as a close up (taken from between the dashed lines) of the local oscillatory behavior of ethanol with 6 wt.% AB (see b.).

The remaining increase in the D^2 law regression rate constant is caused by the non-ideal

conditions of the experiment. Natural convection is present, as noted earlier, which can have a

significant impact on the regression rate. Kumagai *et al.* [10] showed by controlling the gravity

to which their experiment was subjected that they could change in the effects of natural

convection and were able to increase the burning rate of ethanol by up to 50%. It is therefore likely that increased natural convective environment around the droplet, caused by the presence of H_2 gas in the fuel vapor, resulted in an increase in the regression rate.

It is probable that the variations in combustion dynamics from neat ethanol to ethanol with AB also influenced the regression rate. Hydrogen gas generation and subsequent bubble formation are causes of the dynamic combustion behavior observed for fuels containing AB. As the bubbles grow within the droplet, the droplet swells thus increasing the surface area of the droplet. This leads to an increase in the mass evaporation rate of the fuel at the droplet surface and in the rate of heat transfer back into the droplet. These effects continue even after the bubble bursts as ripples travel throughout the droplet causing the diameter to oscillate as seen in Figure 24(b). Because of these constant perturbations to the droplet diameter, it will always have a greater surface area than the ethanol droplets for the same amount of fuel leading to faster regression rates. The rupture of the bubbles at the droplet surface also causes small quantities of fuel to leave the droplet further increasing the regression rate of the fuel.

One factor that hinders the burning rate of the droplet is the finite-rate reaction mechanism between the fuel and oxidizer that leads to incomplete combustion. Finite rate chemical kinetics result in lower flame temperatures and oxygen diffusing through the flame front towards the droplet, both of which contribute to slower burning rates. Hydrogen gas can help reduce these effects as H_2 has fast reaction kinetics and high diffusion rates that promote better mixing, leading to more complete combustion. Both of these benefits of H_2 gas will reduce the effects of finite-rate chemistry mechanisms, allowing for faster droplet regression rates.

3.3. **Effects of AB Solid Decomposition Products on Combustion Behavior of the Droplet**

The solid decomposition products of AB play a large role towards the end of the droplet lifetime. As the liquid fuel is consumed, the ratio of AB decomposition products to liquid fuel increases, causing the remaining fuel to become notably more viscous resulting in combustion behavior typical of gelled fuels [30]. An example of the change in combustion behavior is shown in Figure 25. Droplet swelling is depicted in Figure 25(c)-Figure 25(e). Pressure builds within the droplet causing it to swell and eventually resulting in the fuel vapor breaking through the surface and jetting outwards. This behavior continues until the swelling becomes so significant and the pressure within the droplet so high that the droplet shatters expelling fuel droplets in many directions, Figure 25(f). The gelled droplet combustion behavior is also exhibited by the fuel fragments that leave the main droplet. This causes the remaining fuel to be consumed quickly, producing the large reaction zone around the original main droplet, Figure 25(g). At this point, the boron reacts with the surrounding air producing a bright, green diffusion flame. Images taken using the 543.5 nm filter confirm that the green flame is caused by boron combustion.

The viscous droplet combustion process occurs very quickly when compared to the combustion process of the quasi-steady burning portion of the droplet lifetime. The amount of fuel consumed between Figure 25(b) and Figure 25(c) is significantly less than the amount of fuel consumed between Figure 25(c) and Figure 25(h); however, the time for the two instances is the same, illustrating the dramatic increase in fuel consumption.
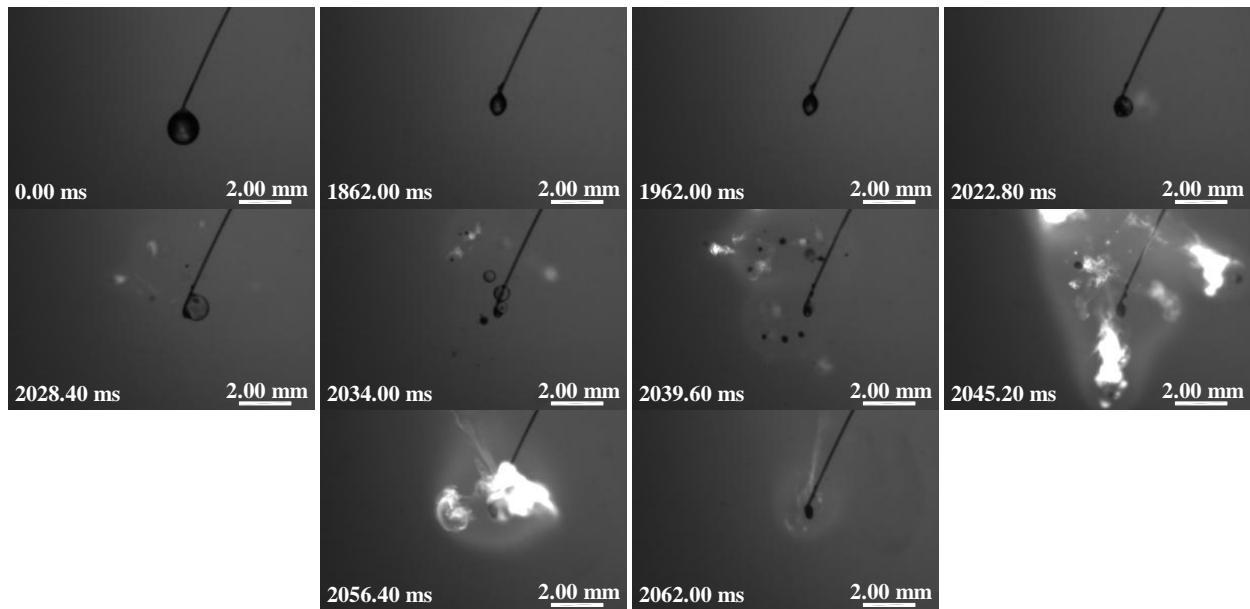
Figure 25 Fragmentation of 6 wt.% AB in ethanol droplet with subsequent combustion of fragments in 100 ms at ambient conditions. The time between the second and third frames and the third and tenth frames is 100 ms.

The jets of gas that escape the surface of the droplet can produce enough force to move the quartz rod. They also distort the diffusion flame around the droplet, and at times cause local extinction as the jet passes through the reaction zone as seen in Figure 26. In this instance, the flame can reignite locally as it propagates along the edge of the jet of gas until connecting back together far from the droplet. After the flame closes around the fuel jet, a diffusion flame forms and the OH concentration increases as gas continues to be expelled from the droplet in the same direction as the jet. Occasionally this local extinction of the flame results in extinction of the droplet as the flame cannot propagate back to around the droplet. This violent burning could result in significant effects in a combustor.
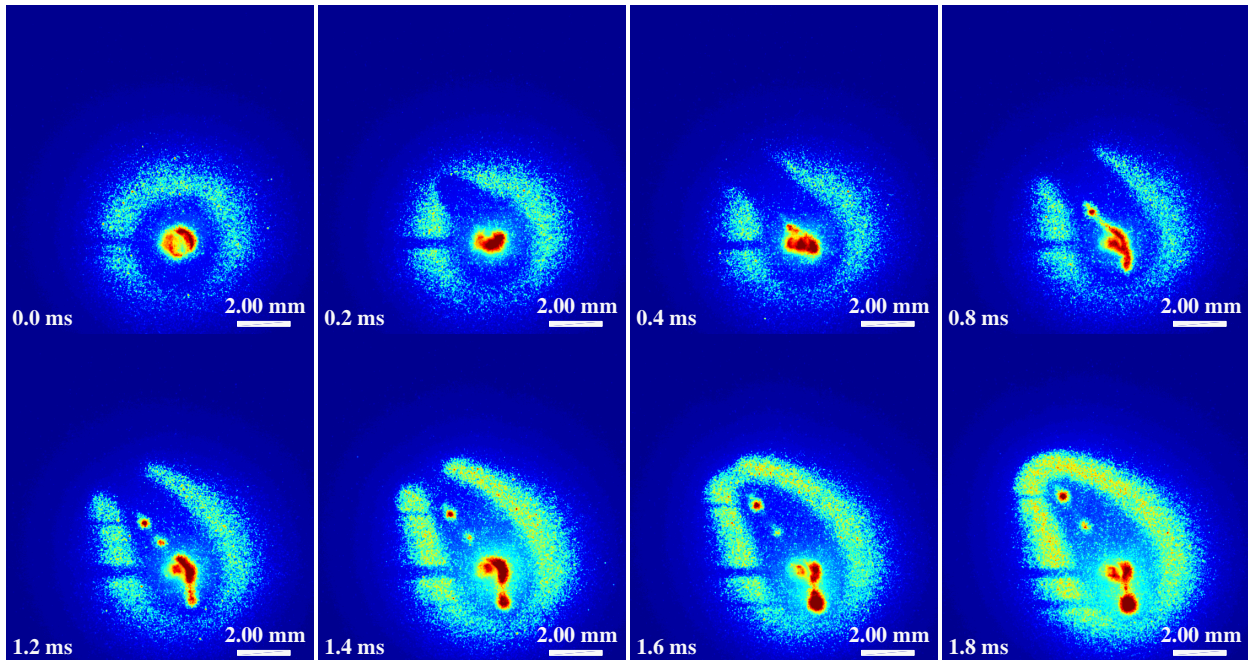
Figure 26 Local flame extinction and then subsequent re-ignition for a droplet burn containing 3 wt.% AB.

4. Conclusions

Evidence of hydrogen generation and addition to the reaction zone was seen throughout the life time of the droplet during combustion. This result means that systems operating with similar conditions will have hydrogen introduced to the combustion process continually throughout the combustion zone. This should allow the hydrogen to produce the same benefits observed in systems where hydrogen gas is introduced to the fuel upstream of the reaction zone. Thus, this fuel could see better flame stability allowing for more fuel lean operation of the system leading to reduced emissions.

The addition of hydrogen to the reaction zone also increased the regression rate of the fuel notably. This is a desirable characteristic for systems that have small geometry constraints such as reaction control systems. For other systems, faster reaction rates should lead to better combustion efficiency; however, the faster reaction can reduce the energy release distribution as well which can lead to hot spots within the system.

The other important observation made was the change of the combustion behavior of the fuel from liquid droplet to gelled droplet combustion towards the end of the droplet lifetime. This change leads to shattering of the droplet increasing the reaction zone quite significantly. Such behavior is advantageous for combustion systems as this will promote better mixing of the fuel and oxidizer leading to better combustion efficiency. It was also observed that boron combustion was very pronounced during this time. Coupling this with the shattering of the droplet and rapid consumption of the fuel can lead to high energy release in a concentrated area within the system. This can have negative consequences as pollutants can be formed in such regions.

The observed trends are for atmospheric conditions. It is suspected that the combustion behavior will change at higher pressures since the boiling point of ethanol increases while the decomposition temperature of AB remains relatively the same. This will result in hydrogen being released before ethanol combusts possibly causing the droplet to shatter earlier if hydrogen generation is very rapid. This will provide for a different combustion dynamic than what is observed at atmospheric conditions. It also provides a method of tailoring the combustion process by changing the operating pressures till the desired conditions are met.

5. Acknowledgements

6   References

[1] Y. C. Yu, S. M. Koeglmeier, J. C. Sisco, W. E. Anderson, Combustion Instability of Gaseous Fuels in a Continuously Variable Resonance Chamber (CVRC), AIAA/ASME/SAE/ASEE 44th Joint Propulsion Conference & Exhibit, Hartford, CT, AIAA 2008-4657, 2008.

[2] S. C. Rosen, M. A. Pfeil, Y. Y. Matsutomi, W. E. Anderson, Effects of Hydrogen Addition on the Combustion Stability of an Unstable Methane Rocket Combustor, 49th AIAA Aerospace Sciences Meeting including the New Horizons Forum and Aerospace Exposition, Orlando, FL, AIAA 2011-328, 2011.

[3] G. McTaggart-Cowan, S. N. Rogak, S. R. Munshi, P. G. Hill, W. K. Bushe, Int.l J. of Engine Research 10 (1) (2009) 1-1-13.

[4] H. Guo, G. J. Smallwood, F. Liu, Y. Ju, Ömer L. Gülder, Proc. Combust. Inst. 30 (2005) 303 - 311.

[5] R. Sankaran, H. G. Im, Combust. Sci. and Tech. 178 (2006) 1585-1611.

[6] R. W. Schefer, D. M. Wicksall, A. K. Agrawal, Proc. Combust. Inst. 29 (2002) 843 - 851.

[7] R. W. Schefer, Int. J. of Hydrogen Energ. 28 (2003) 1131-1141.

[8] P. Ramachandran, P. Gagare, Inorganic Chem. 46 (19) (2007) 7810-7817.

[9] G. A. E. Godsave, Proc. Combust. Inst. 4 (1953) 818-830.

[10] S. Kumagai, H. Isoda, Proc. Combust. Inst. 6 (1957) 726-731.

[11] MATLAB, version 7.11.0 (R2010b), The MathWorks Inc., Natick, Massachusetts, 2010.

[12] R. W. B. Pearse, A. G. Gaydon, The Identification of Molecular Spectra, Chapman and Hall, New York, NY, 1976.

[13] T. Hedman, K. Cho, A. Satija, L. Groven, R. Lucht, S. Son, Combust. and Flame 159 (2012) 427-437.

[14] Rotexo GmbH & Co. KG, COSILAB version 3.0.2, Bochum, Germany, 2009.

[15] C. K. Law, F. A. Williams, Combust. and Flame 19 (1972) 393-405.

[16] G. Wolf, J. Baumann, F. Baitalow, F. P. Hoffmann, Thermochimica Acta 343 (2000) 19-25.

[17] J. S. Wang, R. A. Geanangel, Inorgan. Chimica Acta 148 (1987) 185-190.

[18] S. Basu, Y. Zheng, J. P. Gore, J. of Power Sources 196 (2011) 734-740.

[19] M. E. Bluhm, M. G. Bradley, R. B. III, U. Kusari, L. G. Sneddon, J. of the American Chem. Soc. 128 (2006) 7748-7749.

[20] M. Bowden, T. Autrey, I. Brown, M. Ryan, Current Applied Physics 8 (2008) 498-500.

[21] F. Baitalow, G.Wolf, J. Baumann, K. Jaenicke-Rößler, G. Leitner, Thermochimica Acta 391 (2002) 159-168.

[22] R. C. Reid, J. M. Prausnitz, T. K. Sherwood, The Properties of Gases and Liquids, The McGraw-Hill Book Company, 1977.

[23] S. R. Turns, An Introduction to Combustion Concepts and Applications, The McGraw-Hill Companies, Inc., 2000.

[24] W. M. Haynes, CRC Handbook of Chemistry and Physics, CRC Press, 91st edn., 2010.

[25] N. B. Vargaftik, Tables on the Thermophysical Properties of Liquids and Gases in Normal and Dissociated States, Hemisphere Publishing Corporation, Washington, D.C., 1975.

[26] J. Hilsenrath, C. W. Beckett, W. S. Benedict, L. Fano, H. J. Hoge, J. F. Masi, R. L. Nuttall, Y. S. Touloukian, H. W.Woolley, Tables of Thermal Properties of Gases, National Bureau of Standards, Washington, D.C., 1955.

[27] Lewis Research Center, Chemical Equilibrium with Applications version 2, National Aeronautics and Space Administration, Cleveland, Ohio, 2002.

[28] N. M. Marinov, Int.l J. of Chem. Kinetics 31 (1999) 183{220, Lawrence Livermore National Laboratory, Livermore, CA, UCRL-JC-131657.

[29] A. Yozgatligil, S. Park, M. Y. Choi, A. Kazakov, F. L. Dryerl, Combust. Sci. and Tech. 176 (2004) 1985-1999.

[30] Y. Solomon, B. Natan, Y. Cohen, Combust. and Flame 156 (1) (2009) 261 - 268.

The Influence of Ammonia Borane on the Combustion Stability of a Liquid Rocket Combustor

Mark A. Pfeil,[1] Steven F. Son,[2] and William E. Anderson[3]
Purdue University, West Lafayette, IN, 47907

I.   Introduction

THE use of additives to tailor the combustion behavior of a system is a potential method of suppressing combustion instabilities in liquid rocket combustors. Traditionally, modifications to geometric features and operating conditions of a system have been used to influence combustion behavior, resulting in the suppression of combustion instabilities [1],[2]. Such modifications are unique for each specific engine and propellant combination, resulting in large initial costs to design new combustors; however, using additives to control stability characteristics presumably would not incur such costs if combustion behavior could be modified to fit the system.

As of yet, the use of additives (including solid additives) to modify the combustion stability of a system has not been investigated in liquid rocket combustors. Research has shown however that additives can modify different aspects of the combustion behaviors of liquid fuels. Changes observed include lower ignition temperatures [3][4], reduced ignition delay [5], increased burning rate [6], and increased system energy [7],[8]. Such changes can lead to modifications of the overall combustion behavior of a fuel resulting in suppression of combustion instabilities.

One potential additive is ammonia borane (AB), NH_3BH_3. At temperatures above 343 K, which is below the normal boiling point of ethanol (351 K), AB can dissociate into NH_2BH_2 and H_2. More H_2 is released at higher temperatures. Experiments by Pfeil et al. [10] showed that the burning behavior of ethanol drops doped with AB differs from neat ethanol in two major ways. First, the droplet burning rate increased notably with the addition of AB, presumably as a result of hydrogen being added to the combustion process. The addition of hydrogen could potentially prove advantageous in suppressing combustion instabilities as it has been shown to increase the flammability limits of a fuel [11]-[13]. Also, it is common knowledge that hydrogen-fueled rocket combustors tend to less prone to combustion instability than their kerosene-fueled counterparts. The second different behavior was droplet shattering, observed later in the life of the droplet. This behavior is seen typically with multi-component droplets [14][15]. As the addition of AB had a notable impact on the combustion behavior of droplets, we anticipated a change in the behavior of a model rocket combustor with a well-documented behavior of self-excited instability using kerosene and gaseous methane fuels [16],[17].

The main objective of this work was to determine if the changes in combustion behavior observed in the droplet experiments would result in measurably different stability behavior in the model combustor. The different stability behavior could then presumably be related to the behaviors observed in the droplet combustion experiments. Experiments were performed in the model rocket combustor with neat ethanol and the ethanol/AB mixture. Stability characteristics in terms of pressure oscillation amplitudes as a function of combustor geometry and unsteady heat release profile were determined for the two fuel types and compared. It was found that AB addition to the fuel produced a bimodal temporal and spatial heat release, which is not present for neat ethanol, leading to a wider range of unstable geometries. In the remainder of the paper, a brief description of the experiment is provided, followed by a results section that describes the different stability behavior. Finally a brief discussion on the differences is provided.

II.   Experimental Setup

D. Fuel Description and Preparation

---

[1] Graduate Student, School of Aeronautics and Astronautics, 500 Allison Rd., W. Lafayette, IN 47907, AIAA Student Member.

[2] Professor, School of Mechanical Engineering, 500 Allison Rd., W. Lafayette, IN 47907, Associate AIAA Member.

[3] Professor, School of Aeronautics and Astronautics, 701 W. Stadium Ave., West Lafayette, IN 47907, AIAA Associate Fellow.

The neat ethanol used in these experiments was obtained from Koptec, and the AB was obtained from Sigma Aldrich. The fuel was prepared by adding 6 wt. % AB, the same concentration previously used by Pfeil et al. [10], to the ethanol and allowing the AB to dissolve. Experiments were performed within 12 hours of mixing the fuel and at the conditions denoted in Table 1.

Table 1 Experimental conditions

Fuel	Additive	Mean Pressure, kPa	O/F
Ethanol	None	1480	6.88
Ethanol	6 wt. % AB	1480	7.00

E. Experimental Configuration

The oxidizer used in this experiment was 90 wt. % hydrogen peroxide and 10 wt. % water, which was fed through a gas generator, shown in Fig. 1. The hydrogen peroxide is decomposed into warm oxygen and water and then fed through the oxidizer manifold into a choked inlet that forms the upstream boundary of the combustor. The unique aspect of this experiment is the ability to translate the choked inlet during an experiment to change the combustor system resonance. The inlet tube resonance could be changed between a quarter-wave and a half-wave resonator, with respect to the combustor length. In addition to changing the system resonance, varying the resonance of the tube changes the flow dynamics in the tube and gives rise to different stability behavior as a function of tube length.

Once past the choked inlet, the oxidizer traveled down the oxidizer post and encountered the fuel that was introduced to the system through a co-axial swirl configuration. A step expansion occurred immediately after the fuel injector as the fuel and oxidizer entered the combustion chamber. The 1st third of the combustion chamber consisted of a quartz tube surrounded by an acrylic housing to provide structural support. This optical chamber allowed for visual measurements of the combustion process. The combustion products then traveled down the steel combustion chamber and out a short expansion nozzle.

Various low frequency (Druck PMP 1260 and PMP 1265 8-30 Vdc sampling at 500 Hz) and high frequency (Kulite WCT-312M sampling at 100 kHz) pressure transducers were placed in various locations throughout the combustor. These pressure measurements allowed for analysis of mean pressures as well as high frequency pressure variations. Further details of this setup can be found in References [16],[17].
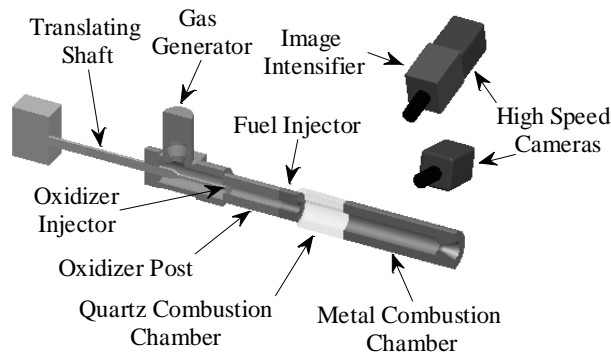

Fig. 27 Unsteady rocket combustor experimental setup.

F. Measurement Techniques

Two high speed camera setups were used to make visual measurements of the combustion process. The first setup used a Vision Research Phantom sampling at 10 kHz and fitted with a Nikon 28-105 mm lens connected to a Thorlabs laser line filter with a 70% transmission, a center wavelength of 543.5 nm ±2, and a full width half max of 10 nm ±2. This filter was employed to single out light emission produced by boron oxidation as researchers have

reported that boron or boron compounds produce strong bands of emission between 536 and 548 nm during combustion [18].

The other high speed camera setup employed a Video Scope International high speed image intensifier (VS4-1845Hs) attached to another Vision Research Phantom sampling at 10 kHz. A Sigma 24-70 mm F2.8 lens with a Semrock interference filter (FF01-434/17-25) with a transmission 90% transmission at 431 nm was attached to the camera assembly. The filter allowed for the recording of light emission associated with the radical CH* which is an indicator of heat release.

III.   Results

The effects of adding AB on the stability of the system can be seen in Fig. 28 which displays the pressure-based stability behavior of the 1st acoustic mode of the system. During the experiment, the choked inlet translates and changes the length of the oxidizer post length. Fig. 28, (a) shows the peak value of the 1st mode taken from a power spectral density analysis as a function of oxidizer post length while Fig. 28, (b) shows the corresponding frequency. Both fuel types produce unstable combustion behavior for oxidizer post lengths between 10.1 and 16.6 cm at relatively the same magnitude; however, the fuel containing AB exhibits unstable combustion behavior for both longer and shorter oxidizer post lengths than the neat ethanol fuel. The frequency of the 1st acoustic mode also has a measureable increase with the addition of AB.

(a)   (b)
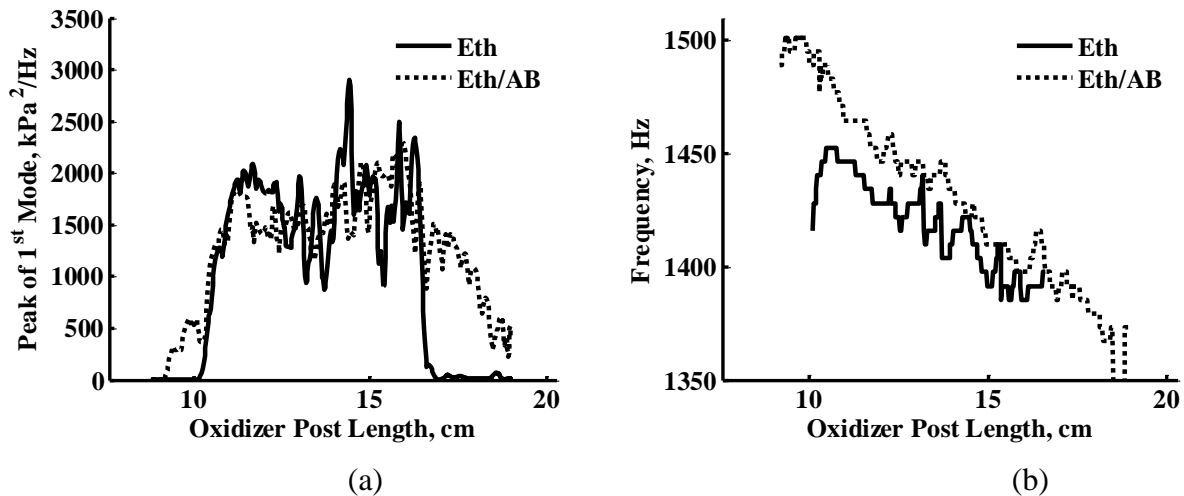
Fig. 28 Power spectral density analysis summary of the 1st acoustical mode of the system. (a) Peak magnitude as a function of oxidizer post length. (b) Corresponding frequency of peak magnitude.

The addition of AB also influences the location of unsteady heat release within the combustor as shown in Fig. 29 which shows the location of unsteady heat release for selected oxidizer post lengths spanning the tested spectra of geometries. The data used to produce the plots in Fig. 29 were obtained by applying a power spectral density analysis to the light fluctuations from the centerline of the optical chamber. Peaks of the strongest mode, the 1st mode, were obtained and then plotted as a function of distance from the injector. The data were then normalized by the maximum peak of each fuel from all the geometries studied. Ethanol combustion results in unsteady heat addition occurring towards the middle of the quartz combustion chamber while the addition of AB causes the unsteady heat addition to occur near the injector and towards the aft end producing a bimodal spatial unsteady heat release.
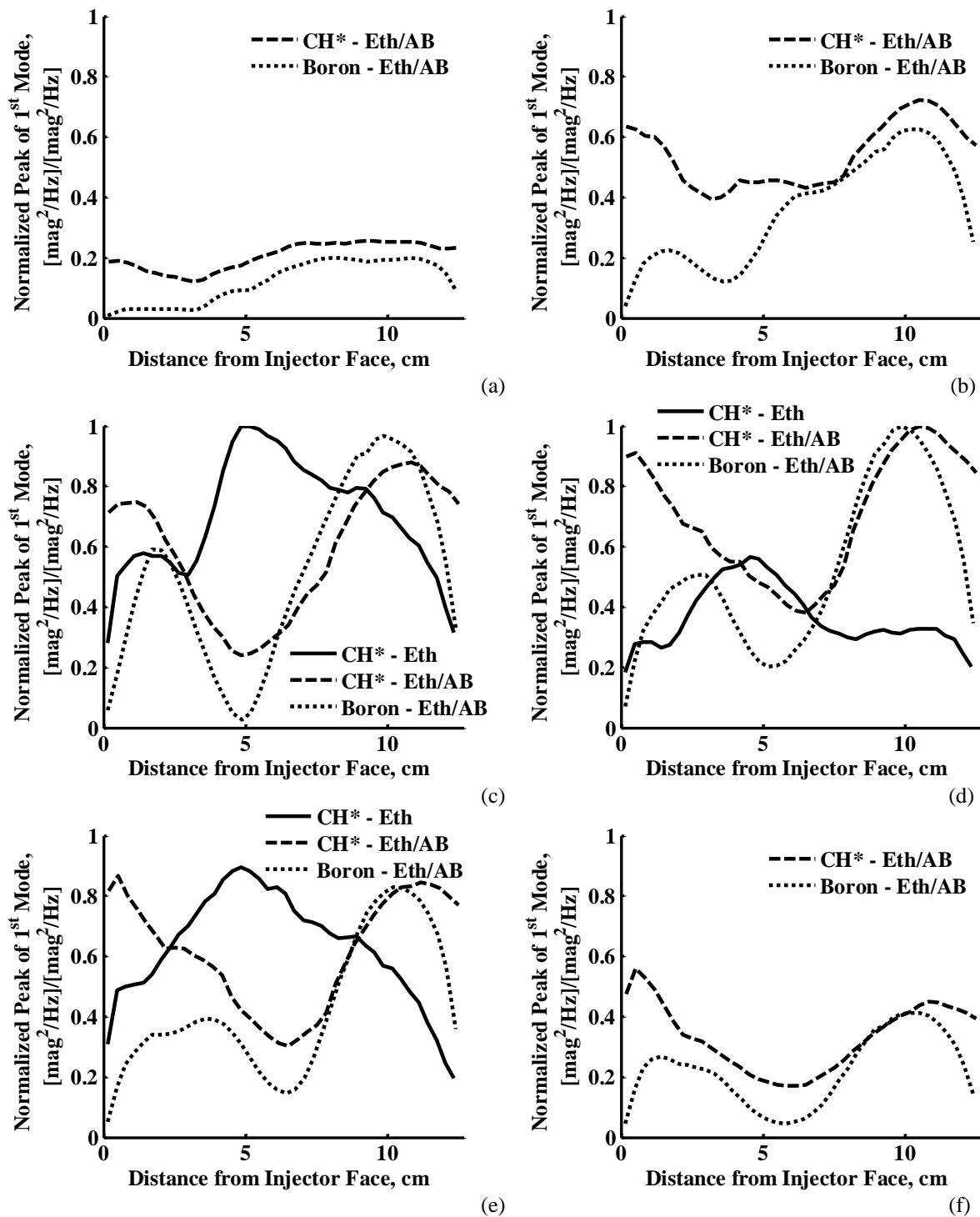
Fig. 29 Peaks of the 1st mode taken from a power spectral density analysis of light fluctuations in the first 12.7 cm of the combustion chamber. Peaks are normalized by the highest peak of all of the oxidizer post lengths investigated, data are taken from the centerline of the combustion chamber, and data are only displayed for fuels that exhibited unstable combustion at that oxidizer post length. Oxidizer post lengths: (a) 19.1 cm, (b) 17.8 cm, (c) 16.5 cm, (d) 14.0 cm, (e) 11.4 cm, and (f) 10.2 cm.

The emission signal from the boron oxidation is similar to the CH* chemiluminescence near the front and aft end of the quartz chamber. However, the magnitude of unsteady boron oxidation near the aft end of the chamber is notably higher than the unsteady boron combustion near the injector. This could be a result of the ethanol combusting before boron, as in the droplet combustion experiments [10], causing the majority of the boron to burn towards the aft end of the quartz chamber. This behavior is consistent for all oxidizer post lengths investigated.

The final significant change to note is the effects of the additive on the temporal unsteady heat release which are shown in Fig. 30. These plots show the relative phase of the unsteady heat addition with respect to the local maximum of unsteady pressure oscillation which was determined by assuming 180 degrees phase difference with the aft chamber pressure measurement and then correcting for convective flow effects. A positive phase angle indicates unsteady heat release occurs prior to the compression wave. A phase angle within +/- 90 deg indicates an amplification of the compression wave according to the Rayleigh Criterion.
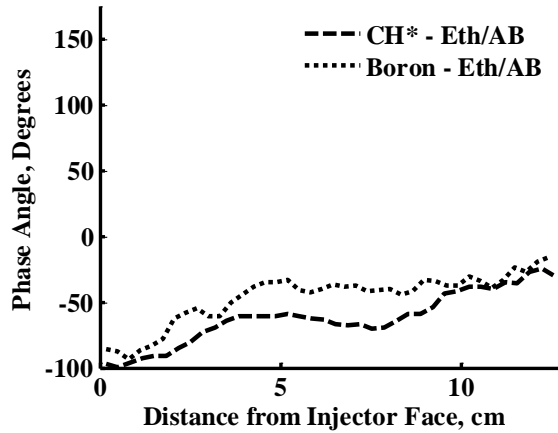
(a)
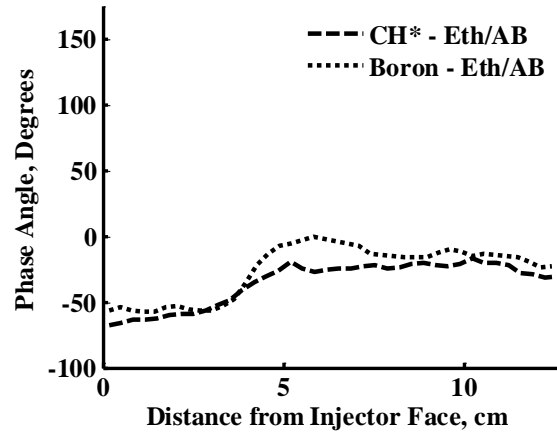
(b)
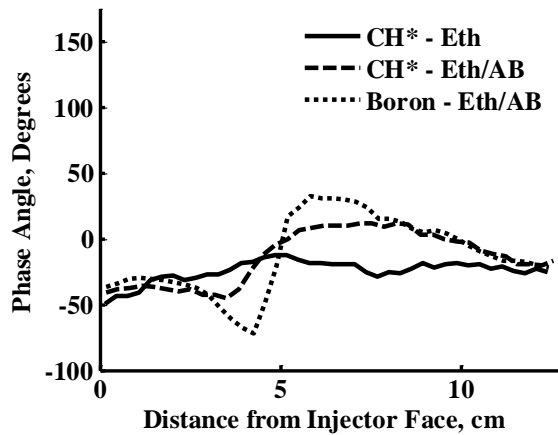
(c)
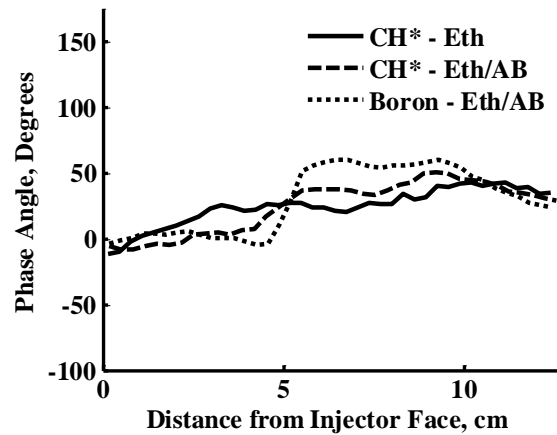
(d)
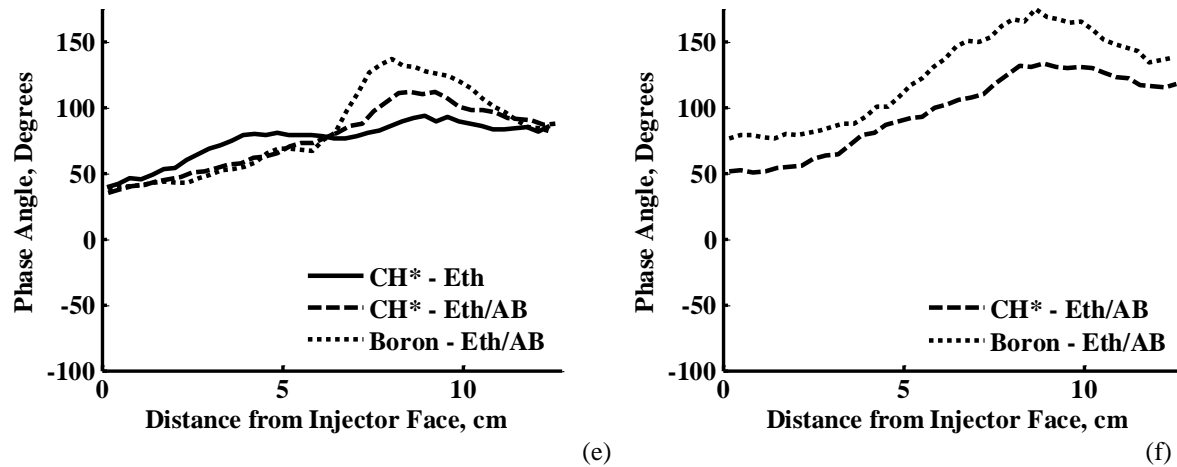
Fig. 30 Temporal phase angle of light oscillations with respect to pressure oscillations. Data are only displayed for fuels that exhibited unstable combustion at that oxidizer post length. Oxidizer post lengths: (a) 19.1 cm, (b) 17.8 cm, (c) 16.5 cm, (d) 14.0 cm, (e) 11.4 cm, and (f) 10.2 cm.

Neat ethanol exhibits a phase angle that is fairly constant for each specific oxidizer post length with the phase angle at the aft end of the quartz chamber being a little higher than the front end. The addition of AB to the fuel results in two phase angles for each oxidizer post length; the first third of the quartz chamber always having a lesser phase angle than the aft two thirds of the chamber resulting in a bimodal temporal energy release. Interestingly, these two phase angles correspond to the two spatial regions of unsteady heat release shown in Fig. 29. Unsteady boron combustion exhibits the same bimodal phase angle as well.

IV.   Conclusions

The observed bimodal spatial and temporal unsteady heat releases, due to the addition of AB, are speculated to be the cause of the wider geometric range for which the system is unstable. The system is unstable for the ethanol/AB fuel for oxidizer post lengths between 16.6 and 19.1 cm because the unsteady heat release towards the aft end of the quartz chamber is close enough in phase with the pressure oscillations to drive instabilities. Neat ethanol remains stable in this range as the unsteady heat release is too far out of phase. For the shorter oxidizer post lengths between 9.1 and 10.1 cm, the system is unstable for the ethanol/AB fuel as well because the unsteady heat release towards the front end of the chamber is in phase with the pressure oscillations.

Both fuels show similar magnitudes in instability for the middle oxidizer post lengths because all the unsteady heat release for both fuels is occurring enough in phase with the acoustics of the system to drive the unstable behavior. Theoretical calculations performed using the NASA CEA thermochemical code [19] indicate a temperature increase of only a few degrees Kelvin with the addition of 6 wt. % AB to the fuel; thus, we should not observe an increase in the magnitude of the instability with the addition of AB to the fuel. The increase in the frequency of the instability probably results from the bimodal spatial unsteady heat release producing more regions of elevated temperatures allowing the pressure oscillations to travel faster in the chamber.

It appears that the two rates of energy release observed in droplet experiments did yield two modes of energy release in the combustor. As with the droplets, ethanol appears to react first leaving a mixture of ethanol and AB decomposition products, including boron, to react later. This yields different rates of energy release and more opportunities for the acoustics of the system and the unsteady heat release to be in phase. It is thus recommended that additives implemented in liquid combustors to influence combustion instabilities need to result in a uniform energy release and either decrease or increase the regression rate. Adding more energy to the system through additives can also positively influence the stability of the system as long as the additive produces a uniform energy increase.

Acknowledgments

References

[1] Natanzon, M. S., *Combustion Instability*, Progress in Astronautics and Aeronautics, AIAA, Reston, VA, 1999.

[2] Yang, V., and Anderson, W. E., *Liquid Rocket Engine Combustion Instability*, Progress in Astronautics and Aeronautics, AIAA, Washington, DC, 1995.

[3] Tyagi, H., Phelan, P. E., Prasher, R., Peck, R., Lee, T., Pacheco, J. R., and Arentzen, P., "Increased Hot-Plate Ignition Probability for Nanoparticle-Laden Diesel Fuel," *Nano Letters*, Vol. 8, No. 5, 2008, pp. 1410-1416.

[4] Wickham, D. T., Cook, R., De Voss, S., Engel, J. R., and Nabity, J., "Soluble Nano-Catalysts for High Performance Fuels," *Journal of Russian Laser Research*, Vol. 27, 2006, pp. 552-561.

[5] Allen, C., Mittal, G., Sung, C., Toulson, E., and Lee, T., "An Aerosol Rapid Compression Machine for Studying Energetic-Nanoparticle-Enhanced Combustion of Liquid Fuels," *Proceedings of the Combustion Institute*, Vol. 33, 2011, pp. 3367-3374.

[6] Sabourin, J. L., Yetter, R. A., Asay, B. W., Lloyd, J. M., Sanders, V. E., Risha, G. A., and Son, S. F., "Effect of Nano-Aluminum and Fumed Silica Particles on Deflagration and Detonation of Nitromethane," *Propellants, Explosives, Pyrotechnics*, Vol. 34, 2009, pp. 385-393.

[7] Pang, K., Yu, K. H., and Young, G., "Characterization of Nano- and Micron-Sized Aluminum Particles Burning in Dump Combustor," *47th AIAA Aerospace Sciences Meeting Including The New Horizons Forum and Aerospace Exposition*, Orlando, FL, January 2009, AIAA 2009-228.

[8] Young, G., Balar, R., Krasel, M., and Yu, K., "Effect of Nanoparticle Additives in Airbreathing Combustion," *14th AIAA/AHI Space Planes and Hypersonic Systems and Technologies Conference*, Canberra, Australia, November 2006, AIAA 2006-7593.

[9] Bowden, M., Autrey, T., Brown, I., and Ryan, M., "The Thermal Decomposition of Ammonia Borane: A Potential Hydrogen Storage Material," *Current Applied Physics*, Vol. 8, 2008, pp. 498-500.

[10] Reference forthcoming.

[11] Sankaran, R., and Im, H. G., "Effects of Hydrogen Addition on the Markstein Length and Flamability Limit of Stretched Methane/Air Premixed Flames," *Combustion Science and Technology*, Vol. 178, 2006, pp. 1585-1611.

[12] Schefer, R. W., Wicksall, D. M., and Agrawal, A. K., "Combustion of Hydrogen Enriched Methane in a Lean Premixed Swirl-Stabilized Burner," *Proceedings of the Combustion Institute*, Vol. 29, No. 1, 2002, pp. 843-851.

[13] Schefer, R. W., "Hydrogen Enrichment for Improved Lean Flame Stability," *International Journal of Hydrogen Energy*, Vol. 28, 2003, pp. 1131-1141.

[14] Wang, C. H., Liu, X. Q., and Law, C. K., "Combustion and Microexplosion of Freely Falling Multicomponent Droplets," *Combustion and Flame*, Vol. 56, 1984, pp. 175-197.

[15] Solomon, Y., and Natan, B., "Experimental Investigation of the Combustion of Organic-Gellant-Based Gel Fuel Droplets," *Combustion Science and Technology*, Vol. 178, Issue 6, 2006, pp. 1185-1199.

[16] Sisco, J., Yu, Y., Sankaran, V., and Anderson, W., "Examination of Mode Shapes in an Unstable Model Rocket Combustor," *Journal of Sound and Vibration*, Vol. 330, Issue 1, 3 January, 2011, pp. 61-74.

[17] Yu JPP, accepted by JPP.

[18] Pearse, R. W. B., and Gaydon, A. G., *The Identification of Molecular Spectra*, Chapman and Hall, New York, NY, 1976.

[19] NASA CEA, Chemical Equilibrium with Applications, Ver. 2, Lewis Research Center, Cleveland, OH, 2002.

MODELING PARTICLE COLLISION PROCESSES IN HIGH REYNOLDS NUMBER FLOW

Ki Sun Park[4] and Stephen D. Heister[5]

School of Aeronautics and Astronautics, Purdue University
701 W. Stadium Avenue, West Lafayette, IN 47907-2045, USA

Hydrodynamic and aerodynamic collision frequency functions are derived for spherical particles with motivation to high-speed flows where compressibility effects are present. Orthokinetic collision is considered under laminar flow where the radial component of relative velocity between two colliding particles is a source of collision. For a general laminar movement of flow, contraction and dilatation effects in compressible flow on hydrodynamic collision are assessed. The newly derived hydrodynamic collision frequency function is consists of compressible and incompressible parts and it is obtained from first principles using the local strain-rate tensor. It is shown that the contraction and dilatation of a fluid element significantly effects hydrodynamic collisions. The new hydrodynamic collision frequency function is compared with aerodynamic collision frequency under laminar flow and the laminar total collision frequency is compared with the total collision frequency function for turbulent flow.

INTRODUCTION

The study on the coalescence and breakup process of drops [1, 2] and bubbles [3] have been investigated for many years in diverse applications in aerosols, chemistry, and chemical engineering communities. The modeling of the coalescence and breakup processes in atmospheric flows or agitated vessels has been important topics in these industries. These applications typically focus on turbulent viscous effects at low and modest Reynolds numbers. A wealth of existing literature exists in the area stemming from the pioneering works of Smoulochowski [4], to the classic text of Saffman and Turner [9] and Williams and Crane [12]. They are usually limited only by the turbulent viscous effect in a low turbulence case.

The present application was motivated by particulate flows in aerospace combustors including solid rocket motors, liquid rocket engines, and ramjet engines. Metal particles have been considered or utilized for these applications and the dynamics of metal oxide combustion

---

[4] E-mail: sunnypark@purdue.edu
[5] Corresponding author, Tel: 1-765-494-5126, Fax: 1-765-494-0307, E-mail: heister@purdue.edu

products is of practical importance in these devices. Historically, micron-sized powders have been employed in solid propellants or liquid propellant slurries, but the recent advent of nano-sized powders has vast implications on volumetric number densities and serves as a prime motivation for the current study.

As the drops in a combustion chamber are accelerated in nozzles, large inertial forces are induced by larger density of particles and the surrounding gas. The high speed (high Reynolds number) motion of the carrier fluid creates a significant deformation of fluid element. The resultant contraction and dilatation of fluid element due to compressible effects can affect collision rates. Accordingly, the previous shearing collision rate studies [4, 5, and 6] which are based on incompressible laminar flow are not appropriate to assess the collision mechanism in these high Reynolds number flows.

The equation tracking the change of number density field of dispersed phase is derived by Smoluchowski considered a simple 1-d laminar shearing collision [4]. To assess the effect of more complex motion of fluid, the general aggregation-breakage equation is derived after Smoluchowski [7] and this equation is known as Population Balance Equation (PBE). Solving this equation directly will require large computational power due to the presence of a large number of classes of particles. In addition, the particles have larger density than the gaseous phase, the slip velocity is needed to be considered. Recently suggested method by Marchisio and Fox [8], Direct Quadrature Method of Moments (DQMOM), can effectively solve this problem and their result is given by:

$$\frac{\partial}{\partial t} w_q + \frac{\partial}{\partial x_i}\left(\langle U_{q,i}\rangle w_q\right) = S_{w,q} \qquad q = 1,.....,N$$

$$\frac{\partial}{\partial t} \xi_q + \frac{\partial}{\partial x_i}\left(\langle U_{q,i}\rangle \xi_q\right) = S_{\xi,q} \qquad q = 1,.....,N$$

(1)

where ξ_q is the weighted abscissas defined by $\xi_q = w_q l_q$. The source terms can be obtained by solving the following linear system of equations:

$$\left(1-k\right)\sum_{q=1}^{N} l_q^k S_{w,q} + k\sum_{q=1}^{N} l_q^{k-1} S_{\xi,q} = S_{m,k} \qquad k = 0,.....,2N-1$$

$$\text{where} \quad S_{m,k} = \frac{1}{2}\sum_{i}^{N}\sum_{j}^{N} \alpha_{ij}\beta_{ij} w_i w_j \left[\left(l_i^3 + l_j^3\right)^{z/3} - l_i^k - l_j^k\right] + \sum_{i}^{N} a_i b_i w_i - \sum_{i}^{N} b_i w_i l_i^k$$

(2)

The term N is the order of the quadrature formula and l is the particle length which is the diameter. The coalescence efficiency is $\alpha_{ij} = \alpha(l_i, l_j)$, the collision frequency of drops of length l_i and l_j is $\beta_{ij} = \beta(l_i, l_j)$, the breakage frequency of drops of length l_i is $b_i = b(l_i)$, and the daughter drop probability density function for the binary fragmentation is $a_i = 2^{(3-z)/3} l_i^z$. The key components of modeling the coagulation/breakup are proper parameters for the collision and breakup processes. The required parameters for collision process are collision frequency function (or collision kernel), collision efficiency, and coalescence efficiency. The required parameter for the breakup process is breakup frequency function (or breakup kernel). The current study has focused on assessing the proper collision frequency function and other related parameters are set aside for future studies.

In this paper, a general framework is derived in order to assess disperse phase collision mechanisms in high Reynolds number flow with particle inertia and carrier fluid compressibility effects. A new shearing collision frequency function, consisting of compressible and incompressible parts, is obtained from first principles using local strain rates. Collision kernels for the various scenarios are derived in the following section and comparisons are made to highlight compressibility and particle inertia effects. Mean flow and turbulent flow effects are also considered separately in order to assess overall importance for various particulate loading and flow regimes. Conclusions from the effort are summarized in the final section of the paper.

SPHERICAL FORMULATION OF COLLISION KERNEL

Saffman and Turner [9] have studied the collision frequency kernel for particles in turbulent flow and presented two formulations based on spherical and cylindrical topologies. In each case, the collision kernel is represented as the volumetric flux through the respective cylindrical/spherical surface. The cylindrical formulation is applicable to a planar shear flow, as investigated by Smoulchowski [4] and the spherical formulation provides a more general approach because the relative velocity between particles depends on the orientation of the collision radius, R_c, which can be oriented in any direction [10].

Consider a stationary particle of radius R_i and a moving particle of radius R_j. Assuming there is no distortion of the flow field due to the presence of the particle, the particle "j" moves along

streamlines as illustrated in Figure 1. Defining the collision sphere as a sphere of radius $R_c = R_i + R_j$ centered on the fixed central particle "i", the collision frequency of particle i is the flux of the fluid having the velocity which is same as the relative velocity between two particles, multiplied by the number density of the moving particles. This flux should be induced by the relative velocity which is inwardly normal to the collision sphere because this component of velocity is only the component causing the collision. Denoting the unit vector outwardly normal to the collision sphere (radial direction of the collision sphere) as $\vec{n}_r$ and the relative velocity inwardly normal to the collision sphere as $\vec{W}_r$, the flux, which is the collision frequency function β_l for the mean flow, across the collision sphere is given by:

$$\beta_l = - \int_{W_r<0} W_r \, dA \qquad \text{where } W_r = \vec{W}_r \cdot \vec{n}_r \qquad (3)$$

where dA is the area element on the surface of the collision sphere. The negative sign is given because the dot product between this velocity vector and outward normal vector is negative.
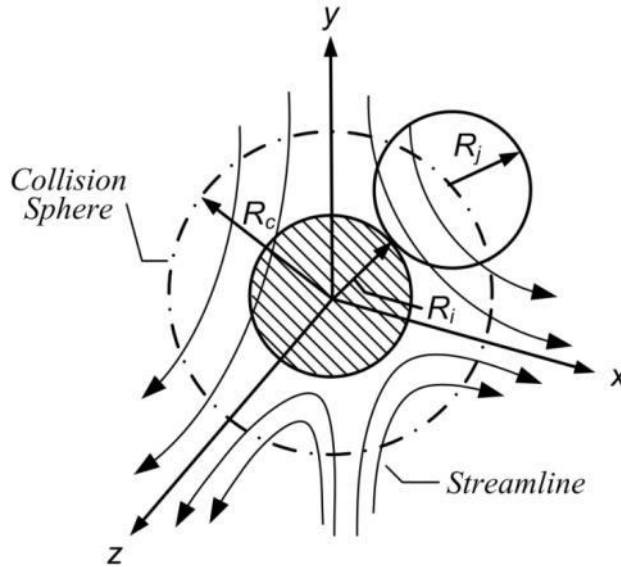

Fig. 1 Schematic of streamlines of two colliding particles

Developing further for a turbulent flow, when the particles are randomly distributed in a fluid with fluctuating radial velocity component, w_r, the total mean flux β_{total} toward the collision sphere is:

$$\beta_{total} = -\left\langle \int_{W_{r,t}<0} W_{r,total}\ dA \right\rangle \qquad \text{where}\ \ W_{r,total} = \left\langle \overrightarrow{W}_r \right\rangle + \overrightarrow{w}_r \cdot \overrightarrow{n}_r \qquad (4)$$

Assuming collision mechanisms due to mean flow and turbulence are independent, as it is noted by Han and Lawler [11] for orthokinetic coagulation and differential sedimentation, the mean flux is given by:

$$\beta_{total} = -\int_{\langle W_r\rangle<0} \langle W_r\rangle\ dA - \left\langle \int_{w_r<0} w_r\ dA \right\rangle \qquad \text{where}\ \ \langle W_r\rangle = \left\langle \overrightarrow{W}_r \right\rangle \cdot \overrightarrow{n}_r,\ \ w_r = \overrightarrow{w}_r \cdot \overrightarrow{n}_r \qquad (5)$$

Following Saffman and Turner, the outward and inward fluxes across the collision sphere are equal, and then the mean flux due to fluctuating parts towards the collision sphere is given by:

$$\beta_t = -\left\langle \int_{w_r<0} w_r\ dA \right\rangle = \frac{1}{2}\int \langle |w_r| \rangle\ dA \qquad (6)$$

Finally, for isotropic turbulence, the total collision kernel β_{total} is given by

$$\beta_{total} = \beta_l + \beta_t \qquad \text{where}\ \ \beta_t = 2\pi R_c^2 \langle |w_r| \rangle \qquad (7)$$

The first term on RHS of equation (7) is the collision kernel induced by mean flow and the second term is the same form as Saffman and Turner [9] for turbulent flow.

SHEARING COLLISION KERNEL OF MEAN FLOW

Before discussing the collision frequency function, it is convenient to consider the relative velocity between two colliding drops. In analogy with Williams and Crane [13], the relative velocity between two particles is influenced by two major effects: the effect of velocity gradient of the carrier fluid between two particles and the effect of different inertial response of particles of different radii to the movement of the carrier fluid. Therefore, the relative velocity between two particles can be described by the effects of velocity gradient and differing inertial response. It is supposed that two droplets within the fluid have velocities $\overrightarrow{U}_{p,i}$ and $\overrightarrow{U}_{p,j}$ before they collide.

The carrier fluid surrounding these drops have velocities $\vec{U}_i$ and $\vec{U}_j$. When the slip velocities between the particle and the carrier fluid are denoted by $\vec{Q}_i = \vec{U}_{p,i} - \vec{U}_i$ and $\vec{Q}_j = \vec{U}_{p,j} - \vec{U}_j$, the relative velocity vector $\vec{W} = \vec{U}_{p,j} - \vec{U}_{p,i}$ can be expressed:

$$\vec{W} = \vec{W}_S + \vec{W}_I = \vec{U}_j - \vec{U}_i + \vec{Q}_j - \vec{Q}_i \qquad (8)$$

Assuming two collision mechanisms are independent, the collision frequency function β_l for the mean flow is:

$$\beta_l = \beta_{l,S} + \beta_{l,I} = -\int_{W_{r,S}<0} W_{S,r}\ dA - \int_{W_{r,I}<0} W_{I,r}\ dA$$

$$\text{where} \quad W_{S,r} = \vec{W}_{S,r} \cdot \vec{n}_r, \ W_{I,r} = \vec{W}_{I,r} \cdot \vec{n}_r \qquad (9)$$

where dA is the area element on the surface of a sphere. The first term $\beta_{l,S}$ represents the flux obtained from the velocity difference induced by the velocity gradient (or strain rate) of the carrier fluid and the second term $\beta_{l,I}$ represents flux from the velocity difference induced by inertial effects of large density particles.

Recently, Kramer and Clark [5] considered the spherical formulation to obtain the orthokinetic collision frequency for the laminar incompressible flow considering the strain rates acting within the fluid. Although their approach can be considered as more comprehensive than Smoulchowski's analysis, it is still limited because the strain rates which cause departure of a moving particle from a fixed central particle are simply eliminated from the collision process. More precisely, the positive strain rate can contribute to the amount of flux flowing towards the surface of the collision sphere because the negative and positive strain rate can be applied at the same time. Thus, the positive strain rate will result in decrease of the total flux and it should not be ignored. In addition, more practically, the compressible effect can deform the fluid element and thus contribute to the particle collision because the contraction of element occurs ($\partial U_i / \partial x_i < 0$) leading to enhanced collisions when compared to the incompressible case ($\partial U_i / \partial x_i = 0$). This effect can be significant in case of high Reynolds number flow.

One can envision the fluid element responding linearly to deformation rate (or velocity gradient, deformation rate tensor is $e_{ij} = \partial U_i / \partial x_j$) when the fluid element is small. In addition, the values of deformation rate acting on the fluid element can be considered as constants as long as the fluid element is sufficiently small. When two adjacent particles are assumed to exist in a

fluid element, the motion of the particles is determined by the deformation of the element. An infinitesimal element will undergo a linear deformation for imposed shear and volume change can occur in the case of compressibility. In addition, rotation and angular deformation may also change the shape of the fluid element. The deformation rate tensor, e_{ij}, can be represented by a linear combination of two 2nd rank tensors as follows:

$$e_{ij} = \frac{\partial U_i}{\partial x_j} = \Omega_{ij} + s_{ij} = \frac{1}{2}\left(\frac{\partial U_i}{\partial x_j} - \frac{\partial U_j}{\partial x_i}\right) + \frac{1}{2}\left(\frac{\partial U_i}{\partial x_j} + \frac{\partial U_j}{\partial x_i}\right) \tag{10}$$

The first term Ω_{ij} in RHS is antisymmetric part of the deformation rate tensor which is called as the rate of rotation tensor and the second term s_{ij} is symmetric part called as the rate of strain tensor. Pure rotation does not induce the collision [5] so it is the rate of strain tensor which yields linear and angular deformations that can be thought of as collision sources [5] including compressibility.

   Following Kramer and Clark [5] and Clark [13], the rate of strain tensor can be diagonalized without loss of information by the rotation of the coordinate system to principal coordinate because the rate of strain tensor is symmetrical:

$$\begin{bmatrix} s_{11} & s_{12} & s_{13} \\ s_{21} & s_{22} & s_{23} \\ s_{31} & s_{23} & s_{33} \end{bmatrix} \rightarrow \begin{bmatrix} s_{11}' & 0 & 0 \\ 0 & s_{22}' & 0 \\ 0 & 0 & s_{33}' \end{bmatrix} \tag{11}$$

(a) Linear deformation   (b) Contraction   (c) Dilatation
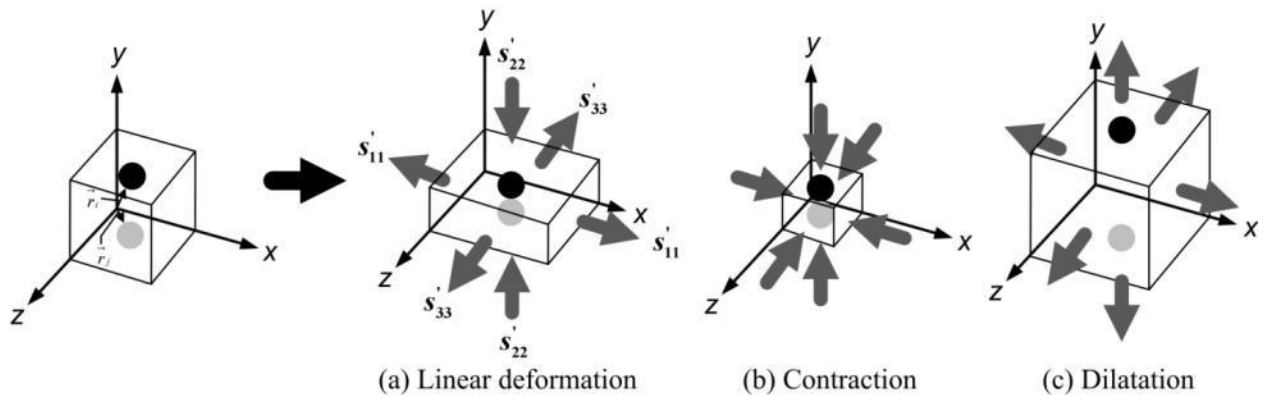
Fig. 2 Schematic of particle collision in fluid element in response to the principal rate of strain tensor; linear deformation and compression result in collision and extension result in no collision

Due to symmetry of the rate of strain tensor, the principal rate of strain tensor can be easily obtained as follows:

$$s'_{11} = \max(\lambda_1, \lambda_2, \lambda_3)$$
$$s'_{22} = \min(\lambda_1, \lambda_2, \lambda_3) \tag{12}$$
$$s'_{33} = s_{11} + s_{22} + s_{33} - s'_{11} - s'_{22}$$

where λ_i are eigenvalues of rate of strain tensor.

Collision is induced only by the normal components of transformed rate of strain tensor. Figure 2 illustrates the collision process in response to the principal rate of strain tensor. The negative components of the principal rate of strain are able to lead to collision between two particles as shown in (a) and (b) of figure 2. However, the collision due to deformation of a fluid element is sensitive to the direction of a vector, $\vec{r}_i - \vec{r}_j$. If this vector is aligned with the negative components of the principal rate of strain tensor, the deformation results in the collision regardless of the direction of other components of rate of strain tensor and the collision rate will be determined by the negative components only. Considering randomly distributed dense particles in a fluid element, it is difficult to obtain the information of this vector. Therefore, ignoring the effect of positive components may result in less accurate collision rate. When only positive components of rate of strain tensor exist like (c) in figure 2, two particles existing in a fluid element will result in no collision.

The next step is to calculate the total flux across the surface of the collision sphere including the positive components of rate of strain tensor without the assumption of incompressibility. Figure 3 illustrates the components of relative velocities induced by normal strain rates in three dimensional view with negative components in principal x' and z' directions and a positive component in principal y' direction. The velocity induced by normal strains in radial direction is given by:

$$\begin{aligned} W_{S,r} &= s'_{xx} R_c \sin^2\phi\cos^2\theta + s'_{yy} R_c \cos^2\phi + s'_{zz} R_c \sin^2\phi\sin^2\theta \\ &= R_c \sin^2\phi\left(s'_{xx}\cos^2\theta + s'_{zz}\sin^2\theta\right) + s'_{yy} R_c \cos^2\phi \end{aligned} \tag{13}$$

Performing integration over the collision sphere while $W_{S,r} < 0$ requires identifying the range where $W_{S,r} < 0$. The direction of $W_{S,r}$ is determined by the direction of s'_{ii}. After setting the direction of $s'_{xx}\cos^2\theta + s'_{zz}\sin^2\theta$ and s'_{ii}, the range of θ and ϕ satisfying $W_{S,r} < 0$ can be easily obtained from comparing $\tan^2\phi$ with $\pm s'_{yy}/\left(s'_{xx}\cos^2\theta + s'_{zz}\sin^2\theta\right)$ and $\tan^2\theta$ with $\pm s'_{xx}/s'_{zz}$. Performing lengthy calculation but straightforward, the hydrodynamic collision frequency

function for 3-dimensional case in laminar flow that is same as the inwardly normal flux across the collision sphere can be divided into two terms:

$$\beta_{l,S} = \beta_{l,S}^{C} + \beta_{l,S}^{IC}$$ (14)

where $\beta_{l,S}^{C}$ is the linear sum of the collision frequencies induced by the velocity components in x', y', and z' directions which is expressed by:

$$\beta_{l,S}^{C} = -\frac{4}{3}\pi R_{c}^{3}\left(s_{xx}' + s_{yy}' + s_{zz}'\right)$$ (15)

More details on the derivation are provided in Park [25]. This term vanishes for incompressible flow ($s_{xx}' + s_{yy}' + s_{zz}' = 0$), and therefore this term reflects compressibility effects on the collision frequency. Accordingly, the second term, $\beta_{l,S}^{IC}$ accounts for the incompressible effects. The second term represents the collision frequency function induced by differential shear between two or three principal components of strain rate tensor according to their direction. Therefore, the second term has different values according to the corresponding range of principal strain rate tensor:
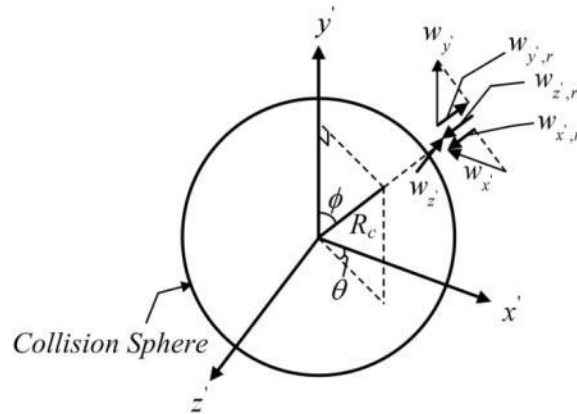

Fig. 3 Schematic of relative velocity components induced by normal strain rate

$$\beta_{l,S}^{IC} = \begin{cases} \text{I. all of principal strain tensors are same direction} \\ \quad -\beta_{l,S}^{C} \qquad for \quad s_{xx}' \geq 0, \ s_{yy}' \geq 0, \ s_{zz}' \geq 0 \\ \quad 0 \qquad\quad for \quad s_{xx}' \leq 0, \ s_{yy}' \leq 0, \ s_{zz}' \leq 0 \\ \text{II. one of principal strain tensors is zero} \\ \qquad\qquad \beta_{l,S}^{IC,2} \\ \text{III. none of principal strain tensors are zero} \\ \quad \beta_{l,S}^{IC,3(1)} \qquad for \quad s_{ii}' > 0, \ s_{jj}' > 0, \ s_{kk}' < 0 \\ \quad \beta_{l,S}^{IC,3(2)} \qquad for \quad s_{ii}' < 0, \ s_{jj}' < 0, \ s_{kk}' > 0 \end{cases}$$

(16)

where $\quad s_{max}' = \max\left(s_{xx}', s_{yy}', s_{zz}'\right) \qquad s_{min}' = \min\left(s_{xx}', s_{yy}', s_{zz}'\right)$

$$\beta_{l,S}^{IC,2} = (8/3) R_c^3 s_{max}' \left[\arctan\left(\sqrt{-\frac{s_{max}'}{s_{min}'}}\right) + \frac{s_{min}'}{s_{min}' - s_{max}'}\sqrt{-\frac{s_{max}'}{s_{min}'}}\right]$$

$$+ (8/3) R_c^3 s_{min}' \left[\arctan\left(\sqrt{-\frac{s_{max}'}{s_{min}'}}\right) - \frac{s_{min}'}{s_{min}' - s_{max}'}\sqrt{-\frac{s_{max}'}{s_{min}'}}\right]$$

$$\beta_{l,S}^{IC,3(1)} = (16/3) R_c^3 \int_0^{\pi/2} \left(s_{ii}' \cos^2\theta + s_{jj}' \sin^2\theta \right)\left(\frac{s_{ii}' \cos^2\theta + s_{jj}' \sin^2\theta}{s_{ii}' \cos^2\theta + s_{jj}' \sin^2\theta - s_{kk}'}\right)^{1/2} d\theta$$

$$\beta_{l,S}^{IC,3(2)} = (16/3) R_c^3 \int_0^{\arctan\left(\sqrt{-s_{kk}'/s_{ii}'}\right)} \left(s_{kk}' \cos^2\theta + s_{ii}' \sin^2\theta \right)\left(\frac{s_{kk}' \cos^2\theta + s_{ii}' \sin^2\theta}{s_{kk}' \cos^2\theta + s_{ii}' \sin^2\theta - s_{jj}'}\right)^{1/2} d\theta$$

where s_{ii}', s_{jj}', and s_{kk}' represents values of principal rate of strain tensors (s_{xx}', s_{yy}', and s_{zz}')

which is corresponding to the given applicable range while $ii \neq jj \neq kk$. When two of the

components of principal rate of strain tensor are zero, Kramer and Clark's [5] single component

of the strain rate tensor, $-4/3\pi R_c^3 s_{ii}'$, which is 1-dimensional collision frequency function based

on spherical approach, is recovered. Accordingly, when all of principal rate of strain tensors are

negative, only $\beta_{l,S}^{C}$ exists in the collision frequency function. Thus, $\beta_{l,S}$ becomes the linear sum

of the collision frequencies in each direction as explained above. The $\beta_{l,S}^{IC,2}$ represents the

components of collision frequency function induced between two nonzero components of strain

rate tensor. The $\beta_{l,S}^{IC,3(1)}$ and $\beta_{l,S}^{IC,3(2)}$ represent the components of collision frequency function

induced by differential shear between three nonzero principal components of strain rate tensor.

In order to assess the behavior of the collision kernels, consider a case where the collision

radius is one micron. Figure 4 illustrates the collision frequency function for $s_{zz}' = 0$ and

$s_{zz}' = -500$ 1/s. As it is explained above, while the fluid element displays a positive principal rate

of strain tensor for both directions while $s'_{zz} = 0$, a dilatation process is present and no collisions occur. When a negative principal rate of strain tensor exists, the collision frequency function is symmetric on $s'_{xx} = s'_{yy}$. Due to existence of negative s'_{zz}, the collision process occurs even if s'_{xx} and s'_{yy} are positive as illustrated in (b) of figure 4. The negative s'_{zz} also cause a larger collision frequency function than $s'_{zz} = 0$ for the range of s'_{xx} and s'_{yy} values considered.

COMPARISONS OF SHEARING COLLISION KERNEL OF MEAN FLOW WITH PREVIOUS STUDIES

The first consideration of particle collision rate due to shearing motion in a laminar flow is due to Smoluchowski [4] in 1917. He considered a uniform laminar shear flow, which is a special case in which only one directional velocity component of the fluid exists and it varies linearly. He assumed that the particles follow the exact flow streamlines so that the shear rate, G (=dU/dx), of the flow motion is responsible for the relative motion between two particles. In this case, the total flux towards the effective collision area on a cylinder (which is the collision frequency function) is given by:

$$\beta_{l,S} = (4/3) G R_c^3 \qquad (17)$$
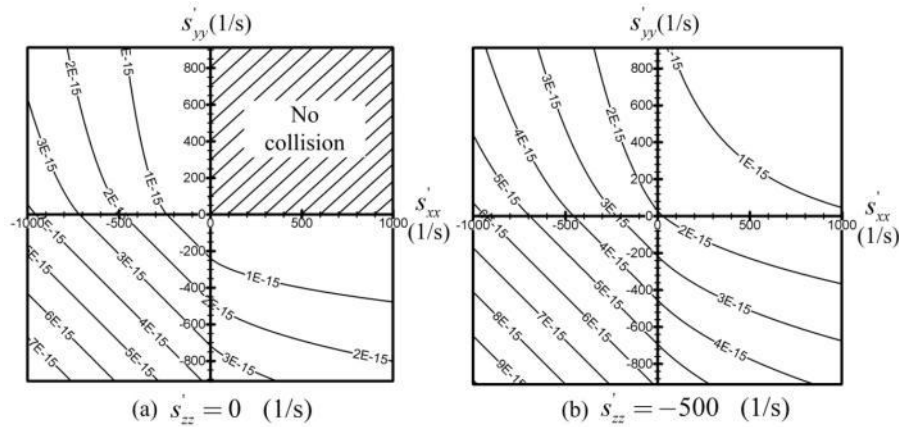
Fig. 4 The shearing collision frequency function contours for $R_c = 1$ μm (units: m^3/s); (a) $s'_{zz} = 0$ and (b) $s'_{zz} = -500$ 1/s

It is desirable to take into account more complex motion of flow and accurate amount of flux across the surface of a sphere in spherical formulation of collision frequency function. Recently, this problem was considered by Kramer and Clark [5]. They obtained the orthokinetic collision frequency for the laminar incompressible flow considering the strain rates acting within the fluid and ignoring dilatation effect as follows:

$$\beta_{l,S} = (4/3)\pi |s'_{max}| R_c^3 \tag{18}$$

where $|s'_{max}|$ is the absolute maximum value of principal rate of strain tensors in each directions.

As discussed earlier, Kramer and Clark's analysis did not consider the dilatation effect of a fluid element on collision frequency due to neglecting the positive strain rate tensors. More recently, Pedocchi and Piedra-Cueva [6] take into account the dilatation effect on the collision frequency function in a laminar incompressible flow. The result is given by:

$$\beta_{l,S} = k_\alpha |s'_{max}| R_c^3 \quad (k_{1/2} \le k_\alpha \le (k_0 = k_1))$$
$$\text{where} \quad k_{1/2} = 4\pi / \sqrt{27} \quad \text{and} \quad k_0 = k_1 = 8/3 \tag{19}$$

The parameter k_α varies for particular local flow conditions, and it can be characterized by the term α. However, the explicit expression on α is not available in their paper.

The comparisons between Smoulchowski [4], Kramer and Clark [5], Pedocchi and Piedra-Cueva [6], and current modeling for the shearing collision frequency function due to mean flow effect in incompressible flow are presented in figure 5. Supposing that s'_{xx} varies from -500 to zero, $s'_{yy} = 500$, and $s'_{xx} + s'_{yy} + s'_{zz} = 0$, $|s'_{max}|$ and G are set to be 500 1/s for Kramer and Clark's and Smoulchowski's model, respectively. Kramer and Clark's model shows the highest value over all range of collision radius because it ignores the mass flux coming out of the collision sphere while Smoulchowski's model considering 1-D shear in cylindrical topology has the lowest value over the entire collision radius range. The current model provides values somewhere between Kramer and Clark's and Smoulchowski's due to dilatation effects. The upper limit of the current model while $|s'_{max}| = 500$ is corresponding to $s'_{xx} = -500$, and $s'_{xx} = 0$ and it shows the same value as Pedocchi and Piedra-Cueva's $\alpha=0$ or 1 case. The lower limit of the current model is corresponding to $s'_{xx} = -250$, $s'_{yy} = -500$, and $s'_{zz} = -250$ and it is same as $\alpha=1/2$ case of Pedocchi and Piedra-Cueva. Accordingly, the current model follows the similar approach as Pedocchi and Piedra-Cueva, but it is not required to define the arbitrary value of α. The current model takes values between its upper and lower limits under the given local flow condition. As mentioned in Pedocchi and Piedra-Cueva [6], the variation between upper and lower limits is small and it may be negligible.

The comparisons between the collision frequency functions in compressible and incompressible flow are provided in figure 6. The s'_{yy} and s'_{zz} are chosen to satisfy $s'_{yy} + s'_{zz} = 0$ 1/s. As it is shown, the effect of contraction and dilatation of a fluid element in compressible flow is significant comparing to an incompressible flow and results in much larger or smaller value of collision frequency function.
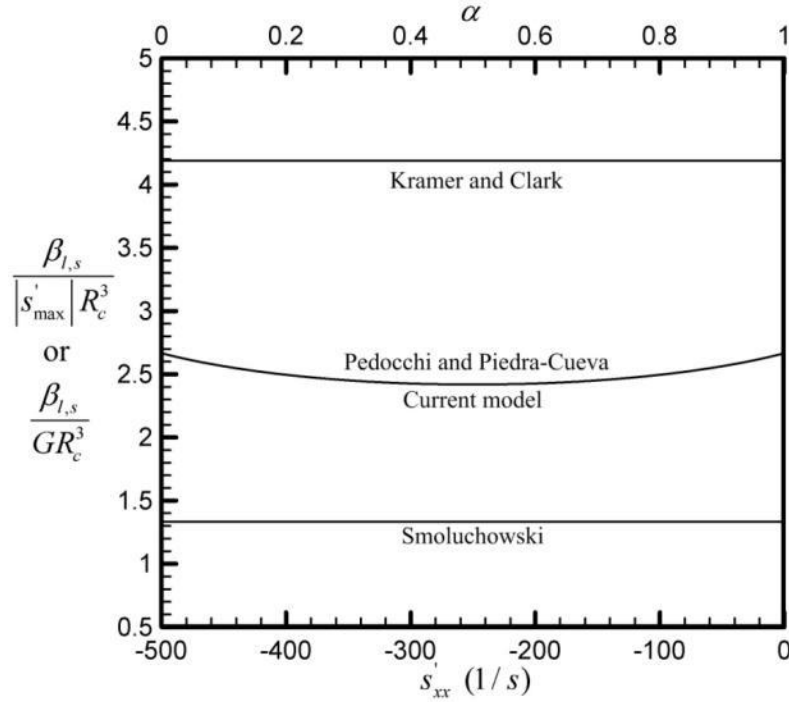

Fig. 5 Comparisons of shearing collision frequency functions for incompressible flows

$$(s'_{yy} = 500 \ 1/s, \ s'_{xx} + s'_{yy} + s'_{zz} = 0, \ |s'_{max}| = G = 500 \ 1/s)$$
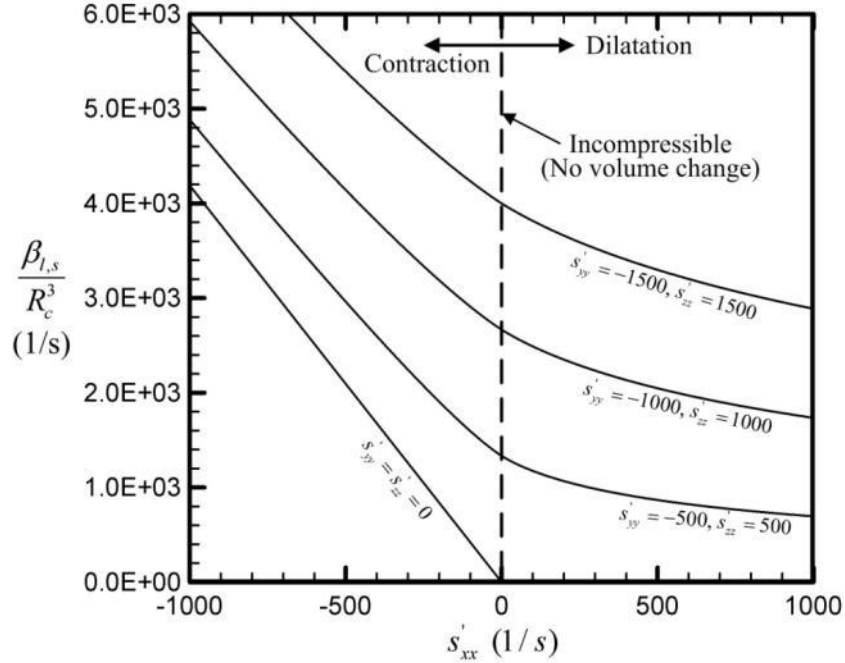
Fig. 6 Comparisons of shearing collision frequency functions for compressible flows

INERTIAL COLLISION KERNEL INCLUDINGMEAN FLOW

The consideration of velocity difference between two particles as a source for the collision can be found in differential sedimentation collision in Friedlander [14] and Elimelech et al.[15]. Considering the difference of terminal velocity between two differently sized particles in air as a collision source, the cylindrical collision formulation for 1-D flow gives:

$$\beta_{DS} = \pi R_c^2 \left| v_{t,i} - v_{t,j} \right| \quad \text{where} \quad v_{t,i} = \frac{2R_i^2 \left(\rho_p - \rho \right)}{9\mu} \tag{20}$$

However, a 1-D cylindrical formulation for collision frequency function is not suitable to take into account more complex motion of flow. Here we derive a more general three-dimensional result suitable for application in multidimensional CFD codes.

We presume that a two-phase flow solution is available such that instantaneous velocity vectors are computed for both the dispersed and continuous phases. As an example, we have employed the fast (or equilibrium) Eulerian approach [16] which presumes a one-way momentum coupling to obtain local particle velocities from a single-phase CFD computation. Fundamentally, this allows us to consider slip between phases in the model and the resultant aerodynamic forces

on droplets that may lead to collisional processes and/or breakup. In the fast Eulerian approach, the particle phase velocity is handled as a field variable with a limitation of small size and large density of particles such that the relative velocity between the particle and the surrounding fluid is given by:

$$\vec{Q}_i = \vec{U}_{p,i} - \vec{U} = -(1-\gamma)\tau_i \frac{D\vec{U}}{Dt}$$

$$\text{where} \quad \gamma = \frac{3\rho}{2\rho_p + \rho} \quad \tau_i = \frac{(2\rho_p + \rho)R_i^2}{9\mu}$$

(21)

where $\vec{U}_{p,i}$ and $\vec{U}$ are the particle phase and gaseous phase velocity vectors, respectively. The term τ_i is the relaxation time of the particle and D/Dt is the material derivative in Eulerian view point. Other Eulerian/Lagrangian approaches can be utilized to give similar information.

In analogy with Saffman and Turner [9], assuming that the carrier fluid velocities near two adjacent particles are same, the velocity difference of the carrier fluid between two close points is neglected (this velocity difference is already considered in the shearing collision frequency function) and then the relative slip velocity assuming $\gamma = 0$ and $\tau_i = 2\rho_p R_i^2 / (9\mu)$ for gas-liquid system is given by:

$$\vec{W}_I = (\tau_i - \tau_j)\frac{D\vec{U}}{Dt}$$

(22)

As in differential sedimentation, a collision frequency function for randomly distributed moving particles around a fixed central particle can be obtained by assuming the relative slip velocity which is responsible for the collision is the relative velocity holding negative components in each direction:

$$\beta_{l,I} = \pi R_c^2 |\vec{W}_I|$$

(23)

Accordingly, the accuracy of collision frequency highly depends on the slip velocity. As it employs one-way momentum coupling,he fast Eulerian method is limited to small particles [16,17]. The limitation is that the particle relaxation time is smaller than the time scale of the flow. The modified fast Eulerian method is available by Ferry et al. [17] which minimize errors on larger particle and still treat the particle velocity as a field variable. The modified fast Eulerian method extends the range of validity to tau_i< 3 tau_j .

Figure 7 illustrates the collision frequency function for $\left|\vec{W}_{I,z}\right|=0$ and $\left|\vec{W}_{I,z}\right|=50$ m/s. As expected, the $\beta_{I,I}$ contours show a circular shape since the magnitude (and not the direction) of the relative velocity determines the collision frequency. Similarly to the shearing collision frequency function, the inertial collision frequency function in (b) of figure 7 shows larger value than (a) for the entire range due to existence of z-direction component in slip velocity.

(a) $\left|W_{I,z}\right|=0$ (m/s)   (b) $\left|W_{I,z}\right|=50$ (m/s)
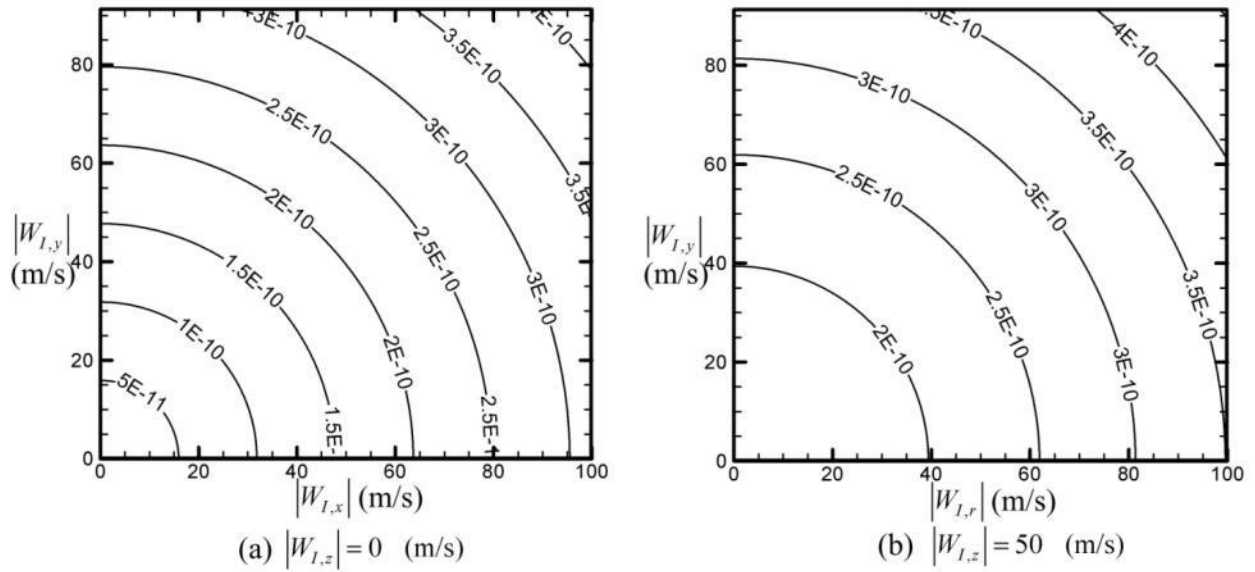
Fig. 7 The inertial collision frequency function contours for $R_c = 1$ μm (units: m³/s); (a) $\left|\vec{W}_{I,z}\right|=0$ and (b) $\left|\vec{W}_{I,z}\right|=50$ m/s

TOTAL COLLISION KERNEL OF MEAN FLOW

Following Han and Lawler [11], collision mechanisms for perikinetic, orthokinetic coagulation, and differential sedimentation are assumed to be statistically independent. Therefore, the total collision frequency function is simply the sum of values from each of these effects;

$$\beta_{l,total} = \beta_{l,S} + \beta_{l,I} + \beta_{l,B} \tag{24}$$

For comparison between the shearing and inertial collision frequency functions, assuming steady state, $s_{xx} = s_{yy} = s_{zz}$ ($s_{xx} < 0$), and $W_{I,x} = W_{I,y} = W_{I,z}$ ($W_{I,x} > 0$) for gas-liquid system, the inertial collision frequency function can be expressed in terms of s_{xx}' as follows:

$$\beta_{l,I} = St \pi R_c^2 \left| R_i - R_j \right| \left| s_{xx}' \right| \qquad \text{where} \quad St = \frac{2\sqrt{2}\rho_p R_c \left| U_x + U_y + U_z \right|}{9\mu} \tag{25}$$

Please note that the Stokes number in Eq. (25) is expressed slightly different than the conventional definition.

The collision frequency function induced by Brownian motion is given by [14]

$$\beta_{l,B} = \left(\frac{2k_B T}{3\mu} \right) \left(\frac{R_c}{2R_i R_j} \right) \tag{26}$$

where k_B is Boltzmann's constant which is 1.380e-23 J/K.

The total collision frequency function for mean flow is presented in figure 8 and 9 supposing that 1 μm particle is colliding with particles from 10 nm to 10 μm. As described by Saffman and Turner [9] for the inertial collision in turbulent flow, similar results are observed for the collision of same size particles. Due to the part, $\left(\tau_i - \tau_j \right)$, in fast Eulerian method and the assumption neglecting the velocity difference of the carrier fluid between two close points, no inertial collision is obtained for same size particles.

In figure 9, when St has small value (St=1), the shearing collision mechanism is dominant over the entire range of interest. When St=10 and 100, the inertial collision mechanism is dominant for smaller and larger particles while the shearing collision mechanism is dominant in the regions where particles are of similar size. The behavior noted is consistent with Stokes law in that low Stokes number (St << 1), particles follow the carrier fluid so that inertial collision is diminished and shearing collision is dominant. For large Stokes number (St >> 1), particles can detach (slip) from the carrier fluid streamlines, particularly when the carrier fluid is accelerating

or decelerating abruptly, and this slip results in the inertial collision. Therefore, for compressible flow at high Reynolds numbers, the Stokes number could be large enough to create the inertial collision over wide range of particle sizes. In contrast, the low velocity motion in boundary layers, combined with higher shearing effects can result in shearing collisions dominating this portion of the flow.

Accordingly, for small Stokes number flow, an accurate shearing collision kernel is required and one-dimensional treatments may generate substantial errors. Three negative components of principal rate of strain tensor can result in a larger flux over the entire collision sphere than a single component employed in a 1-D treatment. We have noted the importance of these multidimensional effects in shear layers between slower and faster moving fluid [25]. Our modeling of shearing collision kernel including contraction effects gives larger values over the entire range of interest as compared to Kramer and Clark's and Smoulchowski's for conditions of $s_{xx}' = s_{yy}' = s_{zz}' = -1000$ 1/s and $|s_{max}'| = G = 1000$ 1/s. As shown in figure 8, the shearing collision kernel results show the greatest disparity when colliding particles are nearly the same size. Again, in case of incompressible flow, our results lie between Kramer and Clark's and Smoulchowski's because of the positive component of principal rate of strain tensor.
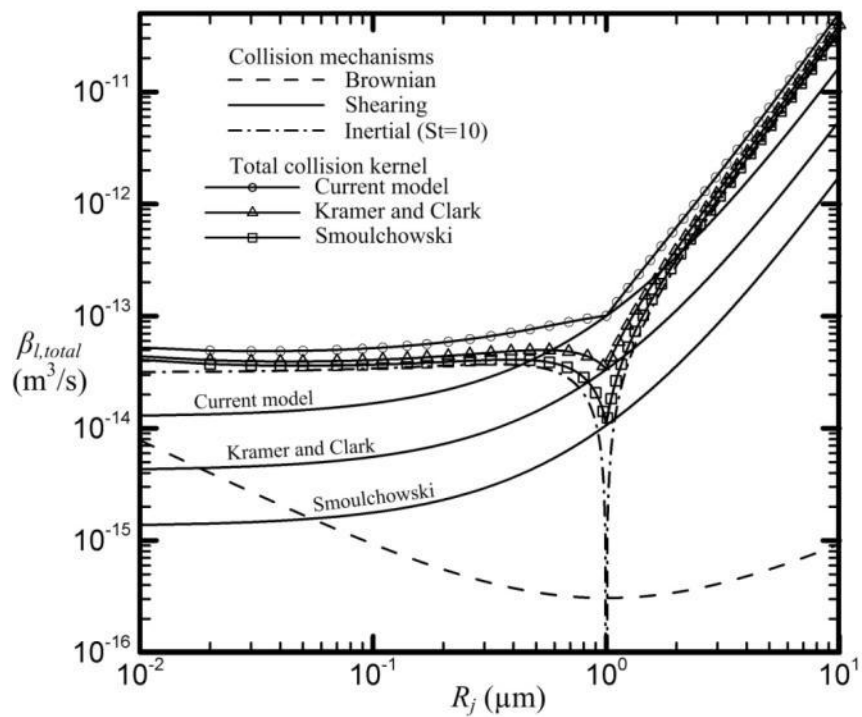
Fig. 8 Comparisons of total collision frequency functions for various shearing collision kernel
(R_i= 1 μm, T = 3000 K, μ=36e-5 kg/m-s, ρ_p=1000 kg/m^3,
$s'_{xx} = s'_{yy} = s'_{zz} = -1000$ 1/s, $\left| s'_{max} \right| = G = 1000$ 1/s)
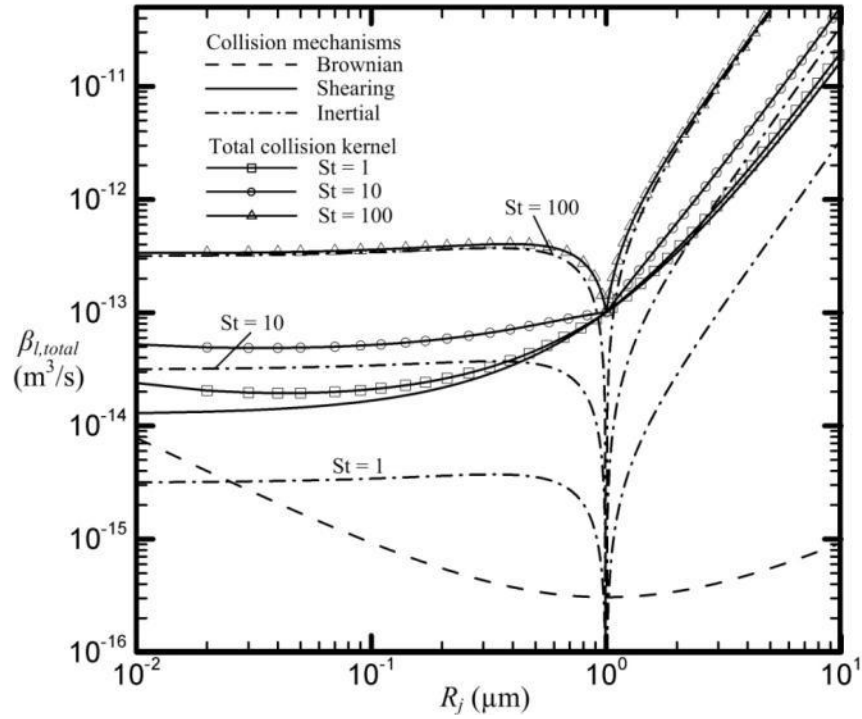
Fig. 9 Comparisons of total collision frequency functions for various Stokes numbers (R_i = 1 μm,
T = 3000 K, μ=36e-5 kg/m-s, ρ_p=1000 kg/m^3, $s'_{xx} = s'_{yy} = s'_{zz} = -1000$ 1/s)

COLLISION KERNEL IN TURBULENT FLOW

Based on previous collision studies considering the classes of particle with energy cascade in turbulent flow, it is widely assumed that the particle which is much smaller than Kolmogorov's micro length scale has a well correlated velocity with the carrier fluid and the particle which is larger than the integral time scale has a less-correlated velocity with the carrier fluid. In these two limits, the widely used collision frequency results are given by Saffman and Turner[9] and Abramson[18], respectively. Supposing the widely distributed particles in turbulent flow, the particles corresponding to inertial subrange of turbulent flow may have a less correlated velocity than the particle in viscous subrange and more correlated velocity than the particle in energy containing eddy. Numerous authors [9,12,19, and 20] have assessed the collision mechanism in the inertial subrange and several models are available. We employ the model from Williams and Crane [12] which is the considered the first theory addressing the inertial collision on arbitrary particle sizes and added the shearing term from Saffman and Turner [9] to the total collision kernel to compare it with laminar effects.

The collision radius or the relaxation time of the particle of collision radius might be employed as criteria for deciding if two different particles are in the viscous or inertial subrange. When the collision radius of two different particles is smaller than Kolmogorov's length scale, or its relaxation time is smaller than Kolmogorov's time scale, the collision occurs in viscous subrange. Thus, considering the formulation of Kolmogorov's length scale ($\eta = \left(\nu^3 / \varepsilon\right)^{1/4}$), time scale ($\tau_\eta = \left(\nu/\varepsilon\right)^{1/2}$), and particle relaxation time ($\tau_{Rc} = 2\rho_p R_c^2 / \left(9\mu\right)$), a more strict criterion would be the comparison between the particle relaxation time and Kolmogorov's time scale. Thus, in this study, when a drop/particle has a larger relaxation time than Kolmogorov's time scale, it is considered to be in the inertial subrange.

SHEARING COLLISION KERNEL IN TURBULENT FLOW

Considering a turbulent flow, the mean square of the relative fluctuating velocity is given by [9]

$$\langle \vec{w} \cdot \vec{w} \rangle = \langle \vec{w}_S \cdot \vec{w}_S \rangle + \langle \vec{w}_I \cdot \vec{w}_I \rangle \tag{27}$$

Using the mean square of the velocity gradient in viscous subrange which is given by

$$\left\langle \left(\frac{\partial u}{\partial x} \right)^2 \right\rangle = \frac{1}{15} \frac{\varepsilon}{v} \quad [22] \tag{28}$$

For isotropic turbulence, it has been shown that [21]

$$\left\langle \left(\frac{\partial u}{\partial x} \right)^2 \right\rangle = \frac{1}{2} \left\langle \left(\frac{\partial u}{\partial y} \right)^2 \right\rangle = \frac{1}{2} \left\langle \left(\frac{\partial u}{\partial z} \right)^2 \right\rangle \tag{29}$$

Thus,

$$\langle w_{S,x}^2 \rangle = R_c^2 \left\langle \left(\frac{\partial u}{\partial x} \right)^2 \right\rangle = \frac{R_c^2}{15} \frac{\varepsilon}{v} \tag{30}$$

Assuming that x-axis is aligned with radial direction ($\langle w_{S,r}^2 \rangle = \langle w_{S,x}^2 \rangle$) and $w_{S,r}$ is normally distributed ($\langle |w_{S,r}| \rangle = (2/\pi)^{1/2} \langle w_{S,r}^2 \rangle^{1/2}$), the shearing collision frequency function for turbulent flow in viscous subrange is:

$$\beta_{t,S}^v = \left(\frac{8\pi}{15} \right)^{1/2} R_c^3 \left(\frac{\varepsilon}{v} \right)^{1/2} \tag{31}$$

This form is same as the collision frequency function in the analysis of Saffman and Turner [9]. For inertial subrange, the relative velocity between two colliding particles is given by [23]

$$\langle w_{S,x}^2 \rangle = 1.37^2 R_c^{2/3} \varepsilon^{2/3} \tag{32}$$

Thus, assuming that x-axis is aligned with radial direction and the relative velocity is normally distributed, the shearing collision frequency function for turbulent flow in inertial subrange is given by

$$\beta_{t,S}^i = 1.37 (8\pi)^{1/2} R_c^{7/3} (\varepsilon)^{1/3} \tag{33}$$

INERTIAL COLLISION KERNEL IN TURBUELNT FLOW

To evaluate the inertial effect term $\langle \vec{w}_I \cdot \vec{w}_I \rangle$, it is assumed that adjacent particles see the same carrier fluid velocity as was assumed by Saffman and Turner [9]. This assumption implies that the correlation coefficient between $\vec{q}_1$ and $\vec{q}_2$ is unity where $\vec{q}_1$ and $\vec{q}_2$ are the fluctuating

parts of the relative velocity between particle and its surrounding fluid of particle 1 and 2 respectively. Thus, the inertial effect term can be expressed:

$$\left\langle \vec{w}_I \cdot \vec{w}_I \right\rangle = \left\langle \vec{u}_{p,2} - \vec{u}_{p,1} \cdot \vec{u}_{p,2} - \vec{u}_{p,1} \right\rangle \tag{34}$$

If the correlation coefficient is assumed to be unity, the inertial collision frequency function of Saffman and Turner can be obtained. The assumption that the correlation coefficient is unity is can be applied only to the small particles in viscous subrange. Therefore, considering that the turbulence level is widely distributed in real application, Williams and Crane [12] considered the following i-direction mean square relative velocity between two particles:

$$\left\langle w_{I,i}^2 \right\rangle = \left\langle u_{p,1,i}^2 \right\rangle + \left\langle u_{p,2,i}^2 \right\rangle - 2\left\langle u_{p,1,i} u_{p,2,i} \right\rangle \tag{35}$$

In Williams and Crane [12]'s analysis, the particle motion is described by the simplified Tchen [24]'s force balance equation ignoring the added mass, Basset history, and gravitational acceleration terms. For $\rho_p \gg \rho_g$, using simple form of drag coefficient and the covariance $\left\langle u_{p,1,i} u_{p,2,i} \right\rangle$ derived from the more accurate wavenumber spectrum, the i-direction mean square relative velocity between two particles $\left\langle w_{I,i}^2 \right\rangle^v$ for viscous subrange ($\theta \ll 1$) is expressed [12]:

$$\left\langle w_{I,i}^2 \right\rangle^v = \left\langle u_i^2 \right\rangle \frac{\gamma}{\gamma-1} \frac{(\theta_1 - \theta_2)^2}{\theta_1 + \theta_2} \left\{ \frac{1}{(1+\theta_1)(1+\theta_2)} - \frac{1}{(1+\gamma\theta_1)(1+\gamma\theta_2)} \right\} \tag{36}$$

where $\theta_1 = \dfrac{\tau_1}{T_L}$ $\theta_2 = \dfrac{\tau_2}{T_L}$ $T_L = \dfrac{L_f}{\left\langle u^2 \right\rangle^{1/2}}$ $\gamma = 2\left(\dfrac{L_f}{\lambda}\right)^2$ $\lambda = \left\langle u^2 \right\rangle^{1/2}\left(\dfrac{15v}{\varepsilon}\right)^{1/2}$ $\left\langle u^2 \right\rangle = \dfrac{2}{3}k$

The mean square fluctuating velocity $\left\langle u^2 \right\rangle$ is given in terms of turbulent kinetic energy k assuming isotropic turbulence. Here, θ_1 and θ_2 are non-dimensional relaxation times of drops of radii R_1 and R_2, where τ is the particle relaxation time. Also, L_f is the longitudinal integral length scale which is approximated by $0.5L$ where L is the integral length scale of the largest energy-containing eddy (approximated by $k^{1/2}/(B^*\omega)$ in $k-\omega$ model). Finally, λ is the Taylor's microscale length.

Williams and Crane have shown that the mean square relative velocity for viscous subrange approaches Saffman and Turner [9]'s inertial term in the limit of small relaxation time. They also derived the mean square relative velocity for large particles which satisfy the condition $\theta \gg 1$ (which imposes the particle is in energy containing region). The mean square relative velocity for energy containing region of turbulence goes to Abrahamson [18]'s term at the large particle

size limit. They interpolated the mean square relative velocities for viscous subrange and energy containing region and derived the universal solution which can be used in inertial subrange [12]:

$$\left\langle w_{I,i}^2 \right\rangle^i = \left\langle u_i^2 \right\rangle \frac{(\theta_1 + \theta_2)^2 - 4\theta_1\theta_2 \sqrt{\frac{1 + \theta_1 + \theta_2}{(1 + \theta_1)(1 + \theta_2)}}}{(\theta_1 + \theta_2)(1 + \theta_1)(1 + \theta_2)} \tag{37}$$

While Williams and Crane's solution approaches Abrahmson's [18] mean square relative velocity for higher-limit energies, it should be noted here that their solution does not approach Saffman and Turner's inertial term as explained in Kuris and Kusters [19]. However, the divergence for very small particle is not appreciable as indicated by Williams and Crane [12].

Finally, the mean square relative velocity induced by the different inertial response, $\left\langle \vec{w}_I \cdot \vec{w}_I \right\rangle$, can be calculated assuming the mean square relative velocities are same in an arbitrary direction which implies $\left\langle w_{I,x}^2 \right\rangle = \left\langle w_{I,y}^2 \right\rangle = \left\langle w_{I,z}^2 \right\rangle$. Saffman and Turner [9] have shown that only small error is introduced in the collision frequency due to this assumption. In addition, the mean value of radial relative velocity $\left\langle |w_r| \right\rangle$ is independent of the orientation of radial direction in isotropic turbulence. In analogy with Saffman and Turner [9], it is assumed that w_r is aligned with the x-axis so that $\left\langle |w_r| \right\rangle = \left\langle |w_x| \right\rangle$. The illustration of w_r and w_x is also available in figure 3. Assuming that the relative velocity in radial direction obeys a Gaussian distribution, the mean of absolute relative velocity is the first order moment of $|w_r|$ given by:

$$\begin{aligned} \left\langle |w_r| \right\rangle &= \int_{-\infty}^{\infty} |w_r| P(w_r) d(w_r) \\ &= \left(\frac{2}{\pi} \right)^{1/2} \left\langle w_r^2 \right\rangle^{1/2} \end{aligned} \tag{38}$$

Accordingly, the collision frequency function for the viscous and inertial subrange is:

$$\beta_{t,I}^v = (8\pi)^{1/2} R_c^2 \left[\frac{2}{3} k \frac{\gamma}{\gamma - 1} \frac{(\theta_1 - \theta_2)^2}{\theta_1 + \theta_2} \left\{ \frac{1}{(1 + \theta_1)(1 + \theta_2)} - \frac{1}{(1 + \gamma\theta_1)(1 + \gamma\theta_2)} \right\} \right]^{1/2} \tag{39}$$

$$\beta_{t,I}^i = (8\pi)^{1/2} R_c^2 \left[\frac{2}{3} k \frac{(\theta_1 + \theta_2)^2 - 4\theta_1\theta_2 \sqrt{\frac{1 + \theta_1 + \theta_2}{(1 + \theta_1)(1 + \theta_2)}}}{(\theta_1 + \theta_2)(1 + \theta_1)(1 + \theta_2)} \right]^{1/2} \tag{40}$$

respectively.

TOTAL COLLISION KERNEL IN TURBULENT FLOW AND COMPARISONS WITH MEAN FLOW EFFECTS

The mean square relative velocity, $\langle \vec{w} \cdot \vec{w} \rangle$, can be calculated assuming the fluctuations are the same in an arbitrary direction which implies $\langle w_x^2 \rangle = \langle w_y^2 \rangle = \langle w_z^2 \rangle$ except for the shearing term in viscous subrange which implies $2\langle w_{S,x}^2 \rangle^v = \langle w_{S,y}^2 \rangle^v = \langle w_{S,z}^2 \rangle^v$. Saffman and Turner [9] have shown that only a small error is introduced in the collision frequency due to this anomaly. Accordingly, assuming that w_r is aligned with the x-axis, the mean square relative velocities in radial direction for viscous and inertial subrange are given by putting equations (30), (36), (32), and (37) into (27):

$$\langle w_r^2 \rangle^v = \frac{2}{3} k \frac{\gamma}{\gamma - 1} \frac{(\theta_1 - \theta_2)^2}{\theta_1 + \theta_2} \left\{ \frac{1}{(1+\theta_1)(1+\theta_2)} - \frac{1}{(1+\gamma\theta_1)(1+\gamma\theta_2)} \right\} + \frac{1}{9} R_c^2 \frac{\varepsilon}{\nu} \tag{41}$$

$$\langle w_r^2 \rangle^i = \frac{2}{3} k \frac{(\theta_1 + \theta_2)^2 - 4\theta_1\theta_2 \sqrt{\dfrac{1 + \theta_1 + \theta_2}{(1+\theta_1)(1+\theta_2)}}}{(\theta_1 + \theta_2)(1+\theta_1)(1+\theta_2)} + 1.37^2 R_c^{2/3} \varepsilon^{2/3} \tag{42}$$

respectively. Assuming that the relative velocity in radial direction spreads by a Gaussian distribution, the spherical formulation for the total collision frequency functions for viscous subrange and inertial subrange are given by:

$$\beta_{t,total}^v = (8\pi)^{1/2} R_c^2 \left[\frac{2}{3} k \frac{\gamma}{\gamma - 1} \frac{(\theta_1 - \theta_2)^2}{\theta_1 + \theta_2} \left\{ \frac{1}{(1+\theta_1)(1+\theta_2)} - \frac{1}{(1+\gamma\theta_1)(1+\gamma\theta_2)} \right\} + \frac{1}{9} R_c^2 \frac{\varepsilon}{\nu} \right]^{1/2} \tag{43}$$

$$\beta_{t,total}^i = (8\pi)^{1/2} R_c^2 \left[\frac{2}{3} k \frac{(\theta_1 + \theta_2)^2 - 4\theta_1\theta_2 \sqrt{\dfrac{1 + \theta_1 + \theta_2}{(1+\theta_1)(1+\theta_2)}}}{(\theta_1 + \theta_2)(1+\theta_1)(1+\theta_2)} + 1.37^2 R_c^{2/3} \varepsilon^{2/3} \right]^{1/2} \tag{44}$$

respectively. Using these results, the same discrepancy with Saffman and Turner [9]'s model is observed. When the drops are identical (inertial effects of two adjacent drops confined in the smallest eddy are same), the constant becomes 1.671 whereas the constant in the model concerning the shear mechanism only is 1.294. This discrepancy is caused by the different

approximation in defining isotropy as explained by Saffman and Turner and the error is considered as small [9].

For comparison between the mean flow and turbulent flow effects on the collision, defining Stokes number in turbulent flow in terms of fluctuating velocity only makes it easy to obtain the turbulent intensity (*I*):

$$St_t = \frac{2\sqrt{2}\rho_p R_c \left\langle u^2 \right\rangle^{1/2}}{9\mu} \qquad\qquad I = \frac{St_t}{St_l} \qquad (45)$$

The total collision frequency functions in turbulent flow are compared for various St_t and ε in Figure 10. Stokes number and energy dissipation rate are carefully chosen in order to retain the criterion, $\sqrt{\theta_i \theta_j} < 10$ which is used to determine the inertial subrange by Williams and Crane [12]. For $\theta_i \theta_j$ above this criterion, the particles should be considered as they are in energy containing region. At a constant energy dissipation rate, increasing Stokes number from very small value (1) to moderate value (100) in (a) of Figure 10 leads to an increase in the collision frequency over the whole range of particle size except in the region of identical particle collision. Further increasing Stokes number does not lead to any major change of collision frequency over the whole R_j range. An upper limit is clearly observed at around $St_t = 1000$. Comparing (a), (b) and (c) in Figure 10, increasing the energy dissipation rate does not result in the increase of upper limit Stokes number. Thus, the upper limit Stokes number at which collision frequency is constant lies in the range of 100~150. Beyond this point, increasing the turbulent level will not lead to the increase of collision frequency at a certain dissipation rate.

Part (d) of Figure 10 shows the sensitivity of collision frequency to the dissipation rate. Sensitivity is mainly due to the shearing term in total collision frequency. At $St_t = 100$ increasing the energy dissipation rate results in large numbers of shearing collisions. In this case, the collision frequency for nearly identical particles is smoothed at high energy dissipation rate.
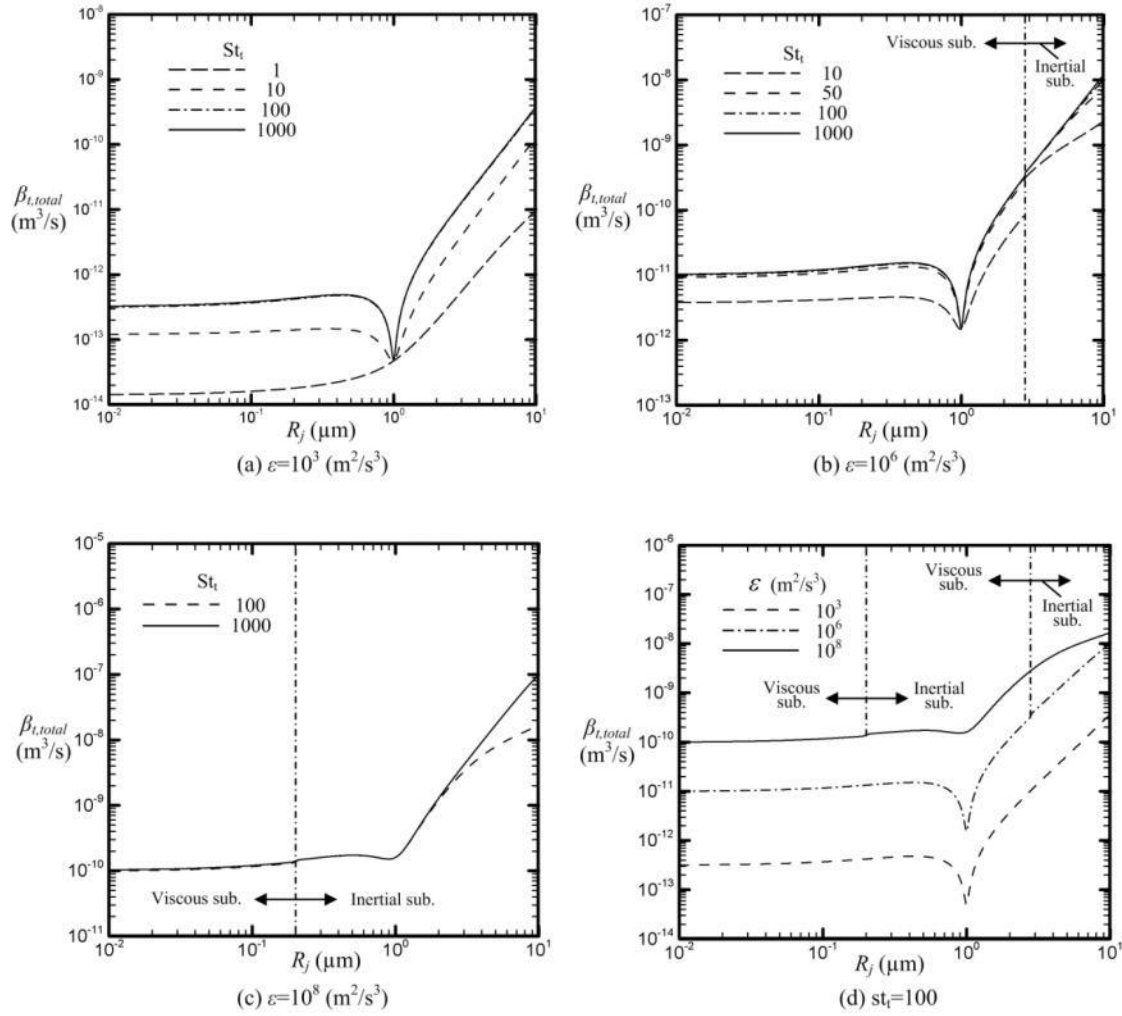
Fig. 10 Comparisons of total turbulent collision frequency function (R_i = 1 µm, µ=36e-5 kg/m-s, ρ=4.5 kg/m³, ρ$_p$=1000 kg/m³)

Finally, the comparisons between mean flow and turbulent effects are shown in Figures 11-13. Mean flow induced collision frequency is dominant in lower left portion of all three plots. This behavior is attributed to both smaller particles at the competitive conditions between laminar and turbulent effects on collision frequency. The upper left portion in Figs. 11-13 is a region where laminar and turbulent effects are of similar importance and the turbulent collision is dominant in upper right portion of these figures. Thus, when two large particles are colliding, the turbulent collision could be a dominant mechanism and the collision mechanisms are of similar importance when a small particle collides with a larger particle.

Sensitivity to the shear rate s'_{xx} and the energy dissipation rate ε are presented in Figures 11 and 13 respectively. As assumed above for the purpose of comparison, both of the inertial collision (St_l) and shear rate (s'_{xx}) are linearly dependant to the inertial collision in mean flow. Thus sensitivity to St_l should be similar to the sensitivity to shear rate. As expected, the boundary between mean flow and turbulent effect dominant regions changes nearly linearly as reflected in Figs. 11 and 13. As shown above, the boundary of dominant regions is not changed much when the turbulent intensities are above 0.1 in figure 12.
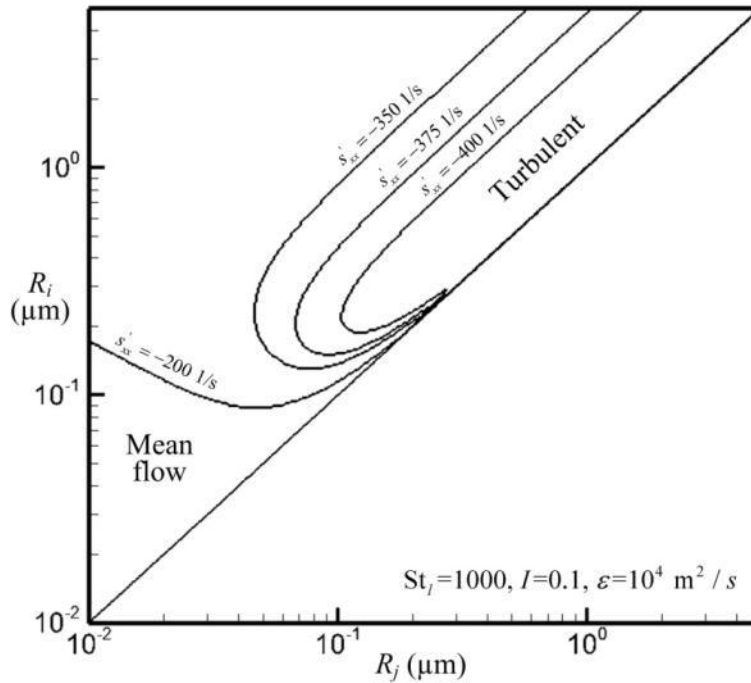
Fig. 11 Effect of s'_{xx} on dominant regions for collision frequency functions of mean and turbulent flow (μ=36e-5 kg/m-s, ρ=4.5 kg/m^3, ρ_p=1000 kg/m^3)
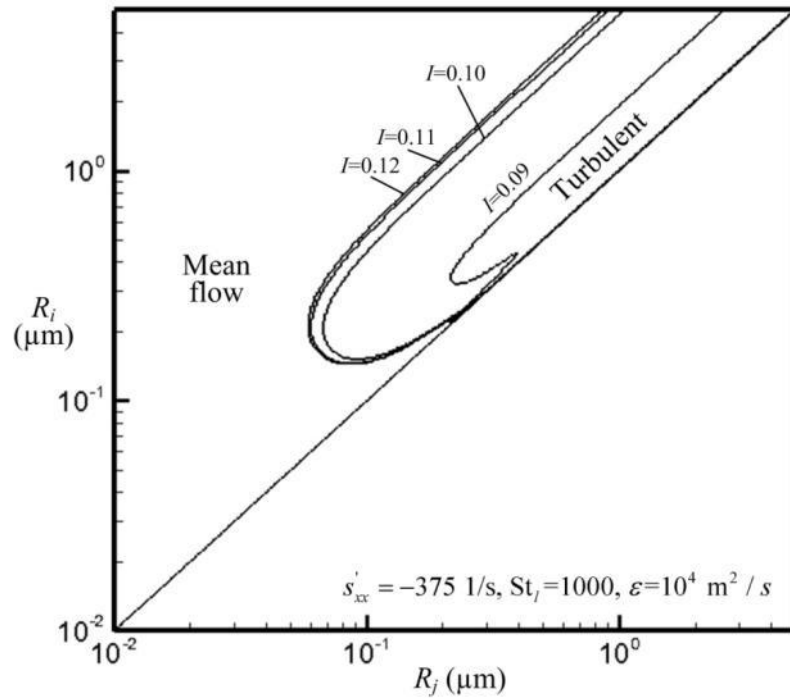
Fig. 12 Effect of Strouhal ratio I on dominant regions for collision frequency functions of mean and turbulent flow (μ=36e-5 kg/m-s, ρ=4.5 kg/m^3, ρ_p=1000 kg/m^3)
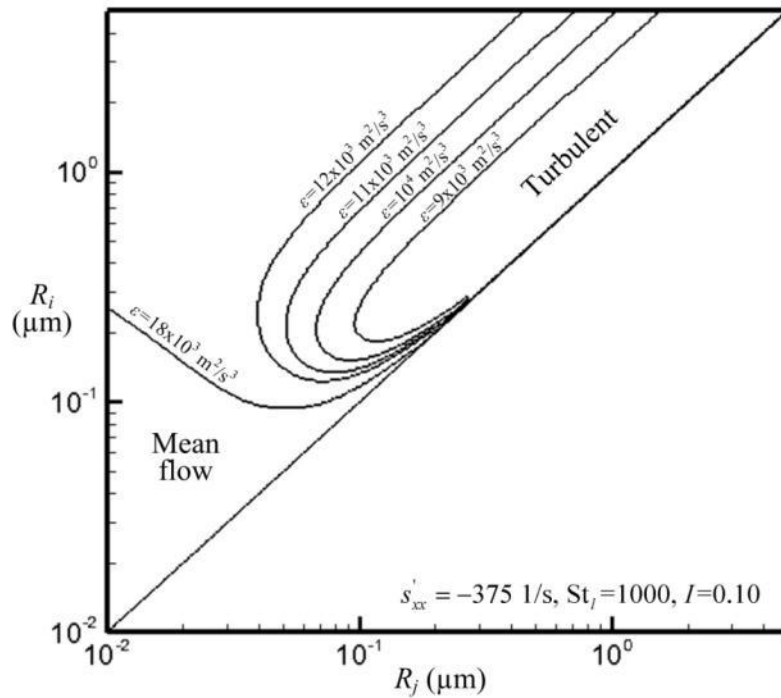

Fig. 13 Effect of ε on dominant regions for collision frequency functions of mean and turbulent flow (μ=36e-5 kg/m-s, ρ=4.5 kg/m^3, ρ_p=1000 kg/m^3)

CONCLUSIONS

Collision frequency kernels are derived for application to high speed (high Reynolds number) flows. The influence of multidimensional and mean flow (inertial collision) behavior permits application to flows in which shear layers are present and extension to compressible flow permits solution in a variety of high-speed flow applications. Collision kernels have been derived for laminar flows and extended to turbulent conditions using the approach of Williams and Crane.

The new models agree well with prior incompressible formulations in this limit. The compressible part of new shearing collision frequency has a significant effect on the collision kernel due to the contraction and dilatation effects of a fluid element. High Reynolds number flow which experiences a rapid change of density, like a subsonic to supersonic transition flow in a rocket nozzle, will result in significantly different numbers of collisions than the incompressible approach due to local deformation of a fluid element.

The collision frequency function which takes into account the high Reynolds number flow effect on the dispersed phase with inertia was also suggested using spherical formulation of collision frequency. The resultant aerodynamic collision frequency function had the similar form with the collision kernel in differential sedimentation except that the expression to the amount of slip was the magnitude of vector. The accuracy of aerodynamic collision frequency function is highly dependent on the accuracy of estimation to slip velocity. The current model was implemented using the fast Eulerian method which is limited to small particles. The results are also applicable to alternative Lagrangian/Eulerian two-phase flow approaches for computing particle and fluid velocity fields.

When colliding particles are nearly the same size, the current model shows more continuous behavior than prior studies. It was difficult to directly compare the total laminar collision rate to total turbulent collision rate because those effects are widely distributed along with the given flow condition. At certain flow conditions considered here, it was observed that smaller particles are more susceptible to laminar collision.

V. ACKNOWLEDGMENTS

VI.

VII. REFERENCES

[1] Coulaloglou, C. A., and Tavlarides, L. L., Description of Interaction Processes in Agitated Liquid-Liquid Dispersions, *Chemical Engineering Science*, Vol. 32, 1977, pp. 1289-1297.

[2] Tsouris, C., and Tavlarides, L. L., Breakage and Coalescence Models for Drops in Turbulent Dispersions, *AlChE Journal*, Vol. 40, No. 3, 1994, pp. 395-406.

[3] Prince, M. J., and Blanch, H. W., Bubble Coalescence and Break-up in Air-Sparged Bubble Columns, *AlChE Journal*, Vol. 36, No. 10, 1990, pp. 1485-1499.

[4] Smoluchowski, M. v., Versuch einer Mathematischen Theorie der Koagulationskinetik Kolloider Losungen, *Zeitschrift fur Physikalische Chemie*, Vol. 92, 1917, pp. 129-168.

[5] Kramer, T. A. and Clark, M. M., Influence of Strain-Rate on Coagulation Kinetics, *Journal of Environmental Engineering*, Vol. 123, No. 5, 1997, pp. 444-452.

[6] Pedocchi, F. and Piedra-Cueva, I., Camp and Stein's Velocity Gradient Formalization, *Journal of Environmental Engineering*, Vol. 131, No. 10, 2005, pp. 1369-1376.

[7] Randolph, A. D., and Larson, M. A., *Theory of Particulate Process*, 2nd ed., Academic Press, New York, 1988.

[8] Marchisio, D. L., and Fox, R. O., Solution of Population Balance Equations using the Direct Quadrature Method of Moments, *Aerosol Science*, Vol. 36, 2005, pp. 43-73.

[9] Saffman, P. G., and Turner, J. S., On the Collision of Drops in Turbulent Clouds, *Journal of Fluid Mechanics*, Vol.1, 1956, pp. 16-30.

[10] Wang, L., Wexler, A. S., and Zhou, Y., Statistical Mechanical Descriptions of Turbulent Coagulation, *Physics of Fluids*, Vol. 10, No. 10, 1998, pp. 2647-2651.

[11] Han, M., and Lawler, D. F., The (Relative) Insignificance of G in Flocculation, *Journal American Water Works Association*, 1992, Vol. 84, Issue 10, pp. 79-91.

[12] Williams, J. J. E., and Crane, R. I., Particle Collision Rate in Turbulent Flow, *International Journal of Multiphase Flow*, Vol. 9, No. 4, pp. 421-435.

[13] Clark, M. M., Critique of Camp and Stein's RMS velocity-gradient., *Journal of Environment. Engineering Div., ASCE*, Vol. 111, No. 3, 1985, pp.741-754.

[14] S. K. Friedlander, *Smoke, Dust, and Haze (Fundamentals of Aerosol Dynamics)*, 2nd edition, Oxford University Press, 2000, Nework and Oxford

[15] M. Elimelech, J. Gregory, X. Jia, and R. A. Williams, *Particle Deposition and Aggregation (Measurement, Modelling and Simulation)*, Butterworth-Heinemann, 1995,

[16] Ferry, J., and Balachandar, S., A fast Eulerian method for disperse tow-phase flow, *International Journal of Multiphase Flow,* Vol. 27, 2001, pp. 1199-1225.

[17] Ferry, J., and Rani, S. L., and Balachandar, S., A locally implicit improvement of the equilibrium Eulerian method, *International Journal of Multiphase Flow*, Vol. 29, 2003, pp. 869-891

[18] Abrahamson, J., Collision Rates of Small Particles in a Vigorously Turbulent Flow, *Chem. Eng. Sci.*, Vol. 30, 1975, pp. 1371-1379.

[19] F. E., Kruis and K. A., Kusters, The collision rate of particles in turbulent media, *Journal of Aerosol Science*, Vol. 27, 1996, pp. 263-264.

[20] L. Pan and P. PADOAN, Relative velocity of inertial particles in turbulent flows, *Journal of Fluid Mechanics*, vol. 661, 2010, pp. 73-107

[21] Batchelor, G. K., *The Theory of Homogeneous Turbulence*, Cambridge University Press., 1953, p. 110.

[22] Taylor, G. I., Statistical Theory of Turbulence, *Proc. Roy. SOCA.,* Vol. 151, 1935, pp. 421-478.

[23] Rotta, J. C., *Turbulente Stromungen*, B. G. Teubner, Stuttgart, 1972, pp. 96.

[24] Tchen, C., *Mean Value and Correlation Problems Connected with the Motion of Small Particles Suspended in a Turbulent Fluid*, PhD thesis, Delft Univ. of Technology, 1947.

[25] Park, K. S., Modeling of Two-Phase Flow with Stochastic Coalescence/Breakage Models, PhD thesis, Purdue Univ., 2012.

Agglomeration/Breakup Studies on Radial Slot Flows in Solid Rocket Motor

Ki Sun Park[1] and Stephen D. Heister[2]
Purdue University,W. Lafayette, IN 47907-2045

      Gas-particle flow simulations for liquid metal oxide droplets dispersed within the gas phase are performed to assess particle agglomeration/breakup processes in a solid rocket motor with radial slot. The one-way coupled population balance equation (PBE) is solved using the direct quadrature method of moments (DQMOM) assumption along with Reynolds averaged Navier-Stokes equation (RANS). Parametric studies are performed on various radial slot geometries with inhibitors. The effect of cross flow is assessed with respect to Mach number (or pressure difference), mass flow ratio between main and slot flows, step height behind the slot, and mass fraction of the dispersed phase.

I. Introduction

Radial slots are utilized in many segmented Solid Rocket Motors (SRMs) to control the motor thrust or facilitate motor manufacture. Salient features of a radial slot flow within SRM are illustrated in Figure 1. Within the slot, the burning propellant creates a radial flow that interacts with the main core flow. As pointed out by previous researchers[1], the presence of the slot can lead to substantial stagnation pressure loss and large aerodynamic forces on the propellant. The interacting streams create a vena-contracta that exhibits a recirulating flow and effectively reduces the flow area for the main stream. The interaction of the two flows also creates turbulence and leads to the formation of vortices behind the slot. Once the vortices are formed, the vortex shedding to the downstream may occur. The vortex shedding phenomena can create large scale unsteadiness in the overall flowfield.

The shearing motion induced by rapid change of flow velocities at the slot-main flow interface can be a strong source of collision of droplets. Vortices develop along the shear layer formed between the two streams. Particle collisions occur in this region, the resultant agglomerated particles are formed in the thin shear layer.
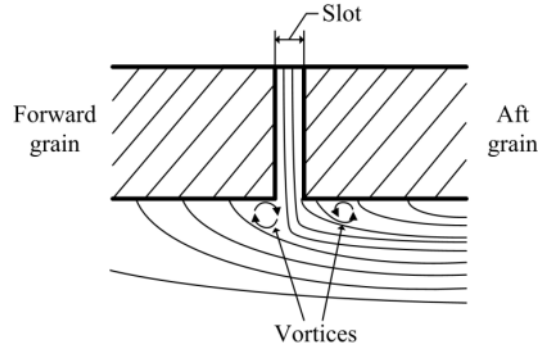
Figure 1. Conceptual features of radial slot flow

The recently developed and validated droplet coalescence and breakup models[3] are used to simulate radial slot flows. In the model, The one-way coupled population balance equation describing the evolution of number concentration due to particle-particle interactions and aerodynamic forces is solved using the direct quadrature method of moments (DQMOM) along with Reynolds averaged Navier-Stokes equation (RANS). The turbulent feature is assessed by Wilcox's $k - \omega$ equations. The fast Eulerian method is used to assess the slip velocity of the dispersed phase which holds a significant inertia. Accordingly, effects of shearing motion of carrier fluid and inertia of drops are included in coalescence/breakage kernels. Both laminar (mean flow) and turbulent effects on the coalescence/breakages of drops are also evaluated by modification of coalescence/breakage kernels. The effect of compressibility is also included in laminar collision kernel.

II. Baseline simulation

A. Boundary conditions

Figure 2 illustrates the entire computational domain and geometry used for the study. An axisymmetric geometry is assumed and is representative of a radial slot in Space Shuttle SRM. Following Sabnis et al.[2], to reduce the disturbances propagating upstream/downstream from the vicinity of the slot, the inflow and outflow boundary are located about 3.66 and 4.57 m from the slot edges in either direction, respectively. The slot width is 3.81 cm (1.5 in) as illustrated in Figure 3. The inhibitors are located in both edges in slot region. According to the simulated cases, the inhibitors are removed to increase mass flow rate from the slot. At the inhibitor surfaces, no-

slip conditions were used as boundary conditions, whereas the normal mass flow injection at the propellant surface was modeled assuming that propellant burning obeys St. Robert's law:

$$r_b = aP^n \tag{1}$$

where r_b is the regression rate, a is the regression rate coefficient and n is the regression rate exponent. For the Space Shuttle SRM[1], the coefficient and exponent are given by

$$a = 0.561 \qquad n = 0.35 \tag{2}$$

Using the Space Shuttle propellant density, which is 1.76 kg/m^3, the mass flux of gases from the propellant surface is given by

$$\rho u = 9.874 P^{0.35} \qquad (\text{kg/m}^2\text{-s}) \tag{3}$$

where the local pressure P is given in MPa.

At inflow and outflow, pressure inlet and pressure outlet boundary conditions are used, respectively. The constant inlet kinetic energy k and specific dissipation rate ω are chosen. The inlet kinetic energy k at pressure inlet and mass flow inlet are 37.5 and 0.06 m^2/s^2, respectively, which are approximately corresponding to the turbulent intensity I of 2.5% of gas velocities at inlet faces. The inlet specific dissipation rate ω for k-ω model is determined as follows:

$$\omega = \frac{k^{1/2}}{0.09^{1/4} \ell} \tag{4}$$

where ℓ is the turbulence length scale and it is given by $\ell = 0.07 D_h$. The D_h is the hydraulic diameter of the chamber. The gas mixture properties are summarized in Table 1. Sutherland's law is used for the viscosity.

The log-normal particle number distribution or exponential distribution can be used following Najjar et al.[4], Crowe and Willoughby[5] and Fein[6], respectively. Najjar et al. have referred other researcher's finding of lognormal and bimodal size distribution of droplets entering the chamber from the solid propellant surface. We choose a log-normal particle number distribution. Table 2 summarizes the inlet particle phase condition and we used this condition on both of propellant surface and inflow. At this particle inlet conditions, the mass fraction of particle phase at inlet face is about 0.32 for all simulated cases because the gas density variation is minimal along the chamber in these slow flow conditions.

Table 1. Gas mixture properties and pressure boundary conditions

Quantity	Value
MW (kg/kmol)	27.76
C_p (J/kg · K)	2439.04
μ_{ref} (kg/m · s)	36.0e-05
$T_{inlet} = T_{ref}$ (K)	3279
S_{ref} (K)	120
P_{in} (MPa)	6.205
P_{out} (N/m^2)	varying by cases

Table 2. Particle phase inlet boundary conditions

| Quantity	Value
n_{total}	5e15
D_m (μm)	0.536
σ_s (μm)	0.456
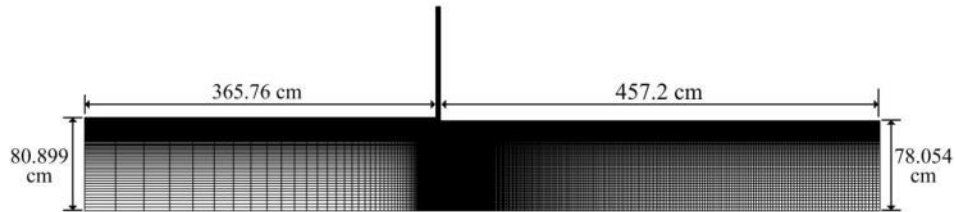


Figure 2. Typical computational grid
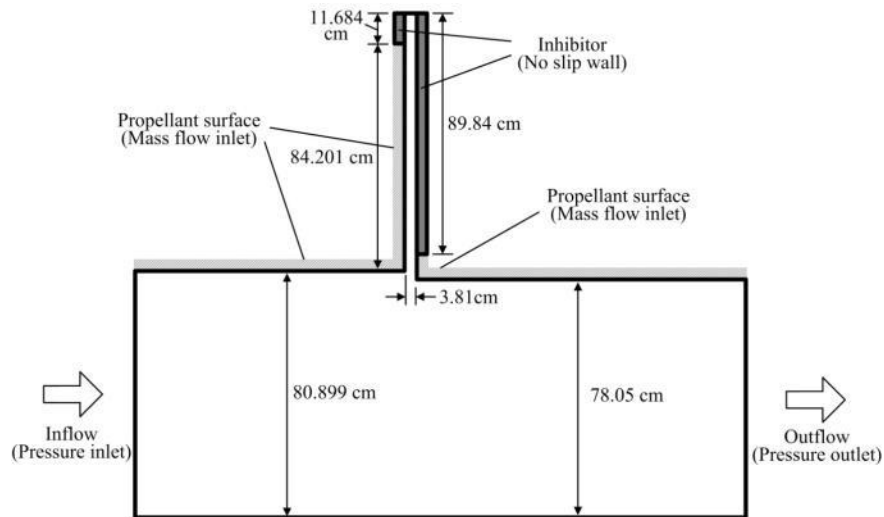
Figure 3. Zoomed view near slot exit and boundary setup

B. Grid convergence study

A grid convergence study was performed on the geometry given above including the short inhibitor on the upstream side of the slot. The details of grid configuration for coarse, intermediate, and dense grids are provided in Table 3. The mesh is highly stretched axially to the slot region from the inlet and outlet to match with the first grid size at the inhibitor surface and resolve the flow field accurately in these high gradient regions. The number of total cell elements on coarse grid is 22,500, and 45,990 and 75,850 on intermediate and dense grids, respectively. The computational times required to obtain the converged solution were 1 week and 2 weeks for coarse and intermediate grids, respectively, on dual 12-core AMD Opteron 6172 processors and 2 weeks for dense grid on 48 cores.

Table 4 summarizes the results from grid the convergence studies. The mass averaged Mach number is obtained at the face just in front of the slot. The mass flow ratio and momentum ratio are calculated based on the area averaged mass flow rate at the face just in front of the slot and the slot outlet. The stagnation pressure loss is obtained as the difference between the value at the face just in front of the slot and the value at 10 slot widths downstream from the rear slot face. The amount of difference between two faces are divided by the upstream value. The mass fraction (α_f) of dispersed phase and mass mean diameter (D_{43}) is obtained at the face located 10 times slot width behind the slot.

As shown in Table 4, Mach number and stagnation pressure loss are almost identical for all considered grid sizes and vary by at most 0.28 and 0.3%, respectively. The momentum ratio and mass fraction converges to 1.56% and 0.32, respectively, as the grid size increases. The highest mass flow ratio is 4.02% at intermediate grid size but the difference is only about 2%. The mass mean diameters for dense and intermediate grids are 2.37 and 2.24 µm, respectively, and the difference is 5.5%. Therefore, regarding the mass mean diameter, the dense grid can be the best choice, but the intermediate grid is chosen considering the computational efficiency.

Table 3. Details of grid configuration for grid convergence studies

	Coarse	Intermediate	Dense
Total cell no.	22,500	45,990	75,850
Forward slot region	90x70	130x100	155x146
Slot area region	30x100	55x130	55x216
Backward slot region	220x60	340x76	390x106

Table 4. Averaged characteristics of gas and particle phase for grid convergence studies

	Coarse	Intermediate	Dense
Mach number[1]	0.279	0.280	0.280
Mass flow ratio[2] $(\dot{m}_s / \dot{m})$	3.90%	4.02%	3.93%
Momentum ratio[2] $(\dot{m}_s V_s / \dot{m}V)$	1.53%	1.55%	1.56%
Stagnation pressure loss[3] $(\Delta P / P)$	0.30%	0.30%	0.29%
α_f[4]	0.29	0.32	0.32
D_{43} (µm)[4]	2.12	2.24	2.37

[1] evaluated at the face just before the slot
[2] evaluated between the face just before the slot and slot outlet
[3] defined as the difference between the value at the face just in front of the slot and the value at the face located 10 times slot width behind the slot.
[4] evaluated at the face located 10 times slot width behind the slot

C. Gas phase flow fields

Under the given boundary conditions in section A, the baseline case simulation is performed. The simulation result showed the highly stretched flow behind the slot but no vortex is observed. Accordingly, the case with a high slot mass flow rate is chosen as a baseline case (case no. M-1-2). The outlet pressure is given by 5.75 MPa. Based on one-way coupling approach, the gas flow field is not disturbed by the particle phase.

Initially, an unsteady simulation was performed. Vortices are shed periodically from the vena-contracta downstream of the slot. Large agglomerates are created inside the vortex in vena-contracta and are periodically shed to downstream. However, the flow rapidly becomes steady and the steady bound vortex is created like the simulation of orifice internal flows which were performed by Xu[7] using k - ω turbulence model. The combination of slow motion of flow and long geometry behind the slot with dissipation created by the turbulence model possibly leads to this steady vortex as indicated by Xu[7]. A steady solution was deemed suitable to provide insight on particle agglomeration effects that are the main emphasis of this study. Therefore, only steady simulations are performed throughout cases in this paper.

The contours of static pressure, Mach number, and, turbulent parameters of kinetic energy k and specific dissipation rate ω for the baseline are given in Figure 4. As given in table 5, the averaged Mach number is 0.272, the mass flow ratio is 8.14%, and the momentum ratio is 6.31%. A significant pressure drop behind the slot is present as highlighted in Figure 4(a) and the

stagnation pressure loss difference between the locations just before the slot and 10 slot widths downstream is 0.4%. The contraction of the main flow after the slot, accelerates the main flow as shown in Figure 4(b). The turbulent kinetic energy and dissipation rate grow significantly as the flow passes through the slot region as shown in (c) and (d) of Figure 4. Figure 5 shows the streamlines of the baseline case. In this case, the vena-contracta is evident at the downstream edge of the slot. The contraction of main flow area results in a venturi effect[1] and the flow velocity passing through this region increases rapidly. The vortex and the reversed axial velocity region approximately extends to ten slot widths along the axis as can be seen in Figure 5.

Table 5. Averaged characteristics of gas phase for baseline case

Variables	values
Mach number[1]	0.272
Mass flow ratio[2] $(\dot{m}_s / \dot{m})$	8.14%
Momentum ratio[2] $(\dot{m}_s V_s / \dot{m}V)$	6.31%
Stagnation pressure loss[3] $(\Delta P / P)$	0.40%

[1] evaluated at the face just before the slot
[2] evaluated between the face just before the slot and slot outlet
[3] defined as the difference between the value at the face just in front of the slot and the value at the face located 10 times slot width behind the slot.
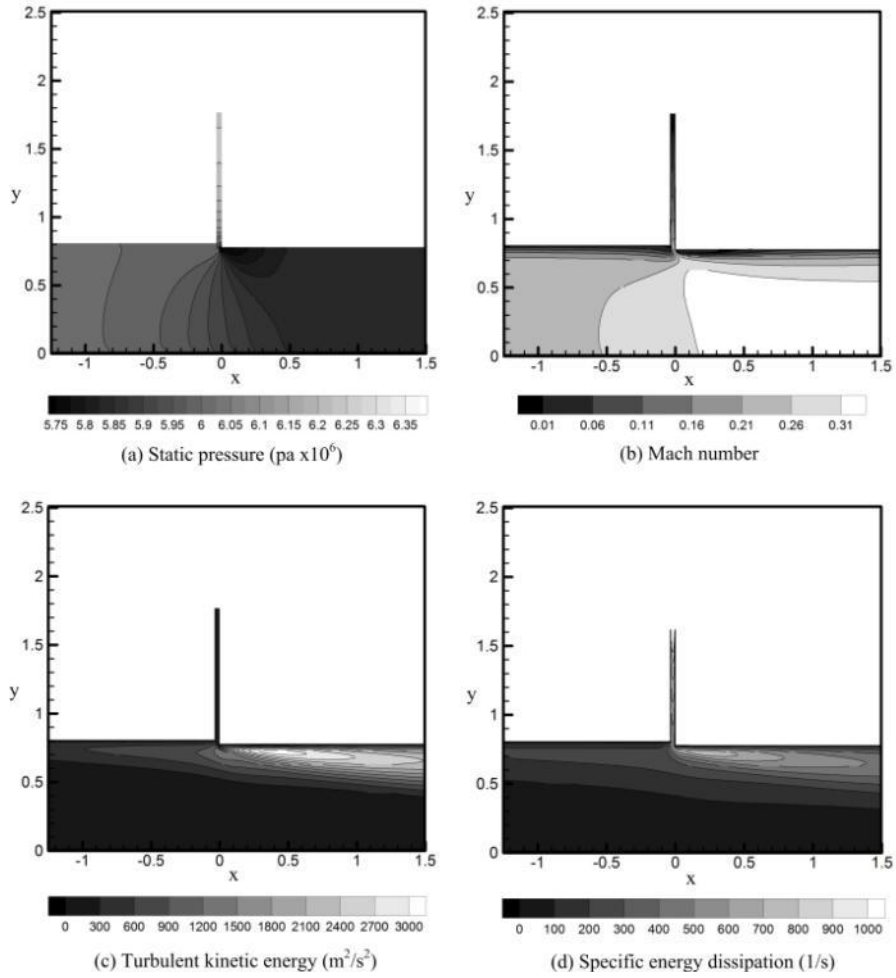
Figure 4. Gas phase flow variation in a SRM near radial slot; (a) static pressure (pa x 10^6), (b) mach number, (c) turbulent kinetic energy k (m^2/s^2), and (d) specific dissipation rate ω (1/s)
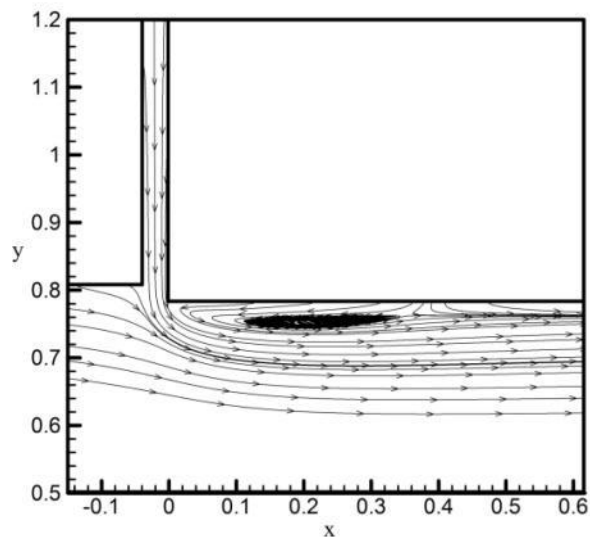

Figure 5. Streamlines near radial slot for baseline case

D. Dispersed phase characteristics

   The mass mean diameter and mass fraction contours for the baseline case over the entire domain are presented in Figure 6. The D_{43} in Figure 6(a) and 7(a) indicates the growth of particles starts from the forward section from the slot near the propellant surface due to the interaction between the axial flow and the flow vertically dispatched from the propellant surface. While these agglomerated particles pass through the slot region, the interaction with the cross-flow coming out of the slot containing large agglomerates leads to the formation of very large agglomerates behind the slot. The agglomerates created in the slot region are still closely located to the propellant surface due to the existence of axial flow in the main stream. While these agglomerates move downstream, the interaction with particles coming from the propellant surface with relatively low speed flow causes a continuous growth and collision of particles along the shear layer between the two streams. Accordingly, a thin band of large agglomerates are created along the axial direction. As shown in Figure 8(a), it is located at about 5% of downstream chamber radius below the propellant surface at $x/x_s = 10$, 10% at $x/x_s =30$, and 15% at $x/x_s =60$. The thickness of this band is about 10% of downstream chamber radius at $x/x_s =10$, 30% at $x/x_s =30$, and 40% at $x/x_s =60$. The location x=0 is defined at the backward slot face and x_s is the slot width. Part (b) of Figures 6, 7, and 8 shows the variation of mass fraction. The collision of particles and transport of large agglomerates in this band lead to decrease of mass fraction of particles and this clearly indicates that the amount of large particles is very small.

   In the baseline case and all other simulated cases, no clear signs of breakup is observed. The low relative velocities in the SRM chamber and high viscosity of liquid drops even inhibit breakup of very large particles of 100 μm size. The calculated mean particle velocities using Fast Eulerian method shows very small difference of 0.05 % from the gas phase velocities. This indicates that the currently considered particle phase falls in the limit of Fast Eulerian method. In addition, it was observed that the large amount of particle growth in the SRM is mostly induced by the turbulence effects from the comparison simulations between the calculations only with mean flow effect and with total effect including mean flow and turbulent effects. The averaged D_{43} of mean flow case at $x/x_s = 60$ is about 1.5 μm which is very small comparing to 6.19 μm of total effect case. Regarding the mean flow in a motor, it holds the relatively slow mean velocity of flow, no high mean velocity divergence region such as boundary layer, and a very small amount of mean velocity difference between the particle and surrounding gas. Instead, the shear

layer holds the significant amount of fluctuation due to turbulent motion and it results in the creation of large agglomerates.

Table 6 summarizes details of predicted characteristics of particle phase at various planes. The slot outlet is defined at the horizontal face located at upstream propellant surface height. Due to the existence of large agglomerates, the standard deviation clearly increases in axial direction after the slot. However, the amount of large agglomerates is small and therefore the averaged D_{43} is much smaller than the maximum value along the radial direction. The $\Delta D_{43}/D_{43,inlet}$, shows very large increases values downstream of the slot. The inlet D_{43} is 1.09 μm. It is 58.6% at slot outlet, 54.2% at just before slot, and 57.9% at just after slot. Accordingly, it can be identified that the location of large agglomerates build up is the location at behind the slot where the shear layer present.

Table 6. characteristics of particle phase for baseline case at various locations

Variables	x-location (x/x$_s$)					Slot outlet
	-10	**0^1**	**10**	**30**	**60**	
v_f	0.995e-3	0.988e-3	0.969e-3	0.935e-3	0.876e-3	0.968e-3
α_f	0.320	0.320	0.318	0.307	0.289	0.309
D_m (μm)	0.430	0.430	0.397	0.151	0.061	0.348
σ_s (μm)	0.624	0.629	0.682	0.948	1.149	0.684
D_{43} (μm)	1.681	1.721	2.026	3.508	6.187	1.792
$\Delta D_{43}/D_{43,inlet}$	54.2%	57.9%	85.9%	180.6%	467.6%	58.6%

[1] evaluated at the face just after the slot

(a) D_{43} (μm)
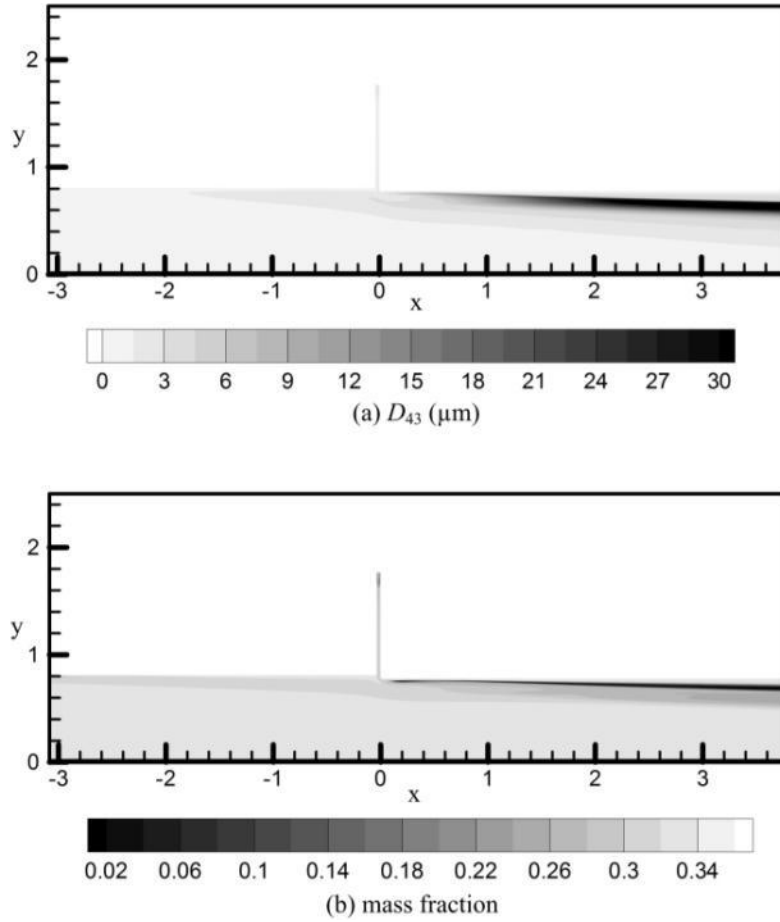
(b) mass fraction

Figure 6. Predicted (a) mass mean diameter (D_{43}) and (b) mass fraction for baseline case

Particles entrainment in vortex of vena contracta and large agglomerates creating   Keep adding particles and shear field increases D_{43}

Flow acceleration over the vena contracta and large agglomerates creating

(a) D_{43} (μm)
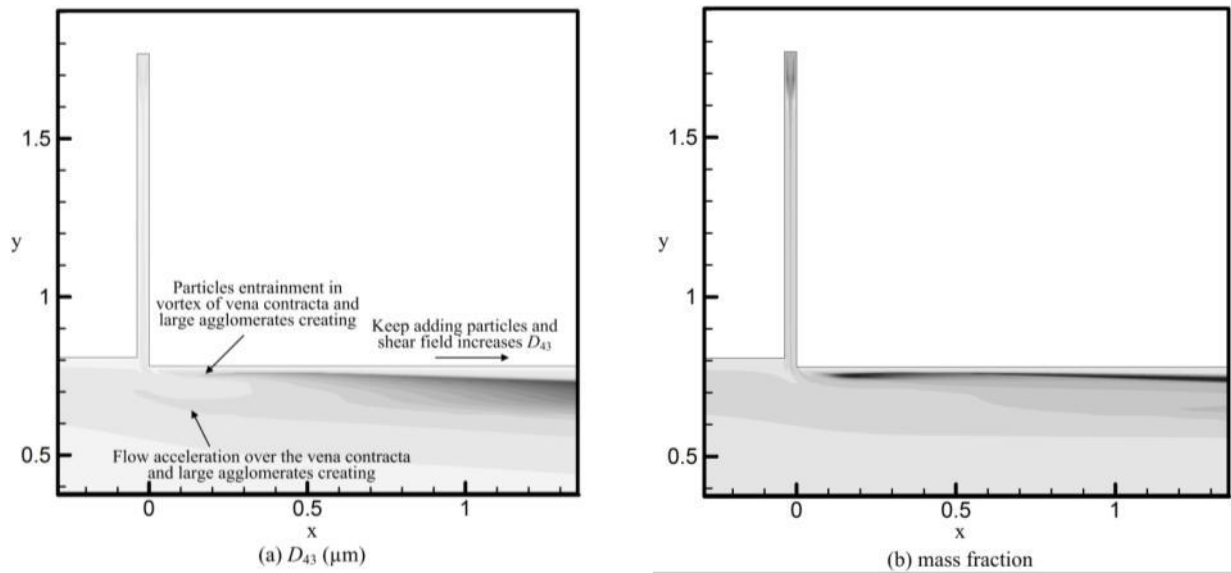
(b) mass fraction

Figure 7. Zoomed view of radial slot region for baseline case; (a) mass mean diameter (D_{43}) and (b) mass fraction
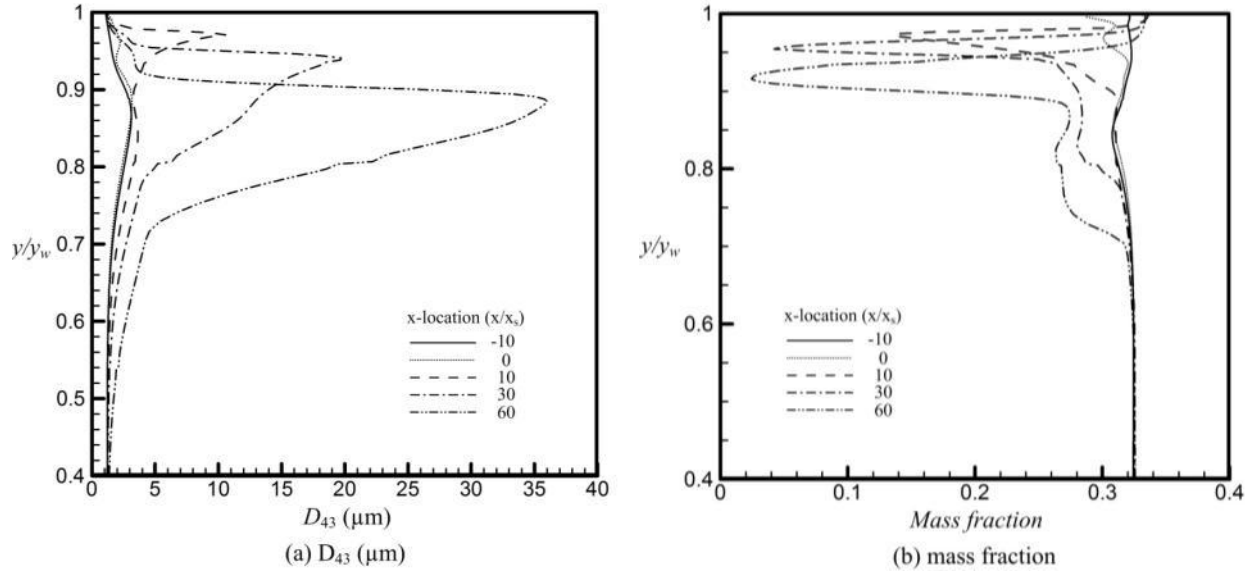
Figure 8. Predicted radial variation at various axial locations of (a) mass mean diameter (D_{43}) and (b) mass fraction for the baseline case

III. Parametric studies

A. Boundary conditions and slot configurations

A total of 19 simulations are performed to investigate the influence of core Mach number (or pressure), mass flow ratio (or momentum ratio), step height (or area ratio), and mass fraction of particle phase. To vary the mach number, the various exit pressures at the outlet are chosen. Specification of the outlet pressure sets the Mach number as well as the mass flow rate of main flow stream. Here, the Mach number is defined the average value just in front of the slot.

The mass flow ratio between the main stream and slot flow is controlled by varying the inhibited region inside the slot. Figure 9 shows the currently simulated inhibitor configurations. While the size of inhibitor on the left face of the slot is not changed, the size of inhibitor is varied. Accordingly, the bare propellant surface on the right face is varied by 87.05, 47.97, and 8,89 cm for high, mid, and low mass flow ratios for a given mach numbers, respectively. The 13 simulations are performed to assess the effect of outlet pressure and mass flow ratio. Table 7 summarizes boundary conditions.

To assess the effect of downstream propellant height (defined as step height), 3 additional simulations are performed under the low mass flow slot configuration and the same outlet pressure as the baseline case. The step heights are adjusted to 0, 2.849, 5.698, and 8.547 cm as summarized in Table 8.

The effect of mass fraction on the particle agglomeration is assessed by adjusting the total number of particles. Table 9 summarizes the inflow boundary conditions for various mass fraction of particles. The slot geometry M-1 is used for these parametric studies and 3 additional simulations were performed. The effect of particle size (D_m and α_s) is not assessed here because it is more likely controlled by the combustion process at the propellant surface.

As described above, the mass flow ratio and momentum ratio are calculated based on the area averaged mass flow rate at the face just in front of the slot and the slot outlet at upstream propellant surface height. The stagnation pressure loss is obtained as the difference between the value at the face just in front of the slot and the value at the face located 10 times slot width behind the slot. The mass fraction (α_f) of dispersed phase and mass mean diameter (D_{43}) is obtained at the face located 10, 30, and 60 slot widths downstream.

Table 7. Gas and particle phase boundary conditions for parametric studies assessing the effect of mach number and mass flow ratio

Case no.	Gas Phase				Particle phase		
	P_{in} (Pa)	P_{out} (Pa)	Slot configuration	Step height	D_m (µm)	α_s (µm)	n_{total}
M-1-1		6000000					
M-1-2 (baseline)		5750000	M-1				
M-1-3		5500000					
M-1-4		5250000					
M-2-1		6000000					
M-2-2	6205282	5750000	M-2	2.849 cm	0.536	0.456	5e15
M-2-3		5500000					
M-2-4		5250000					
M-3-1		6000000					
M-3-2		5750000					
M-3-3		5500000	M-3				
M-3-4		5250000					
M-3-5		5000000					

Table 8. Gas and particle phase boundary conditions for parametric studies assessing the effect of step height

Case no.	Gas Phase				Particle phase		
	P_{in} (Pa)	P_{out} (Pa)	Slot configuration	Step height	D_m (μm)	$α_s$ (μm)	n_{total}
S-1				0			
S-2 (M-3-2)	6205282	5750000	M-3	2.849	0.536	0.456	5e15
S-3				5.698			
S-4				8.547			

Table 9. Gas and particle phase boundary conditions for parametric studies assessing the effect of mass fraction

| Case no.	Gas Phase				Particle phase		
	P_{in} (Pa)	P_{out} (Pa)	Slot configuration	Step height	D_m (μm)	$α_s$ (μm)	n_{total}
P-1							0.78e15
P-2							2.34e15
P-3	6205282	5750000	M-1	2.849	0.536	0.456	3.9e15
P-4 (M-1-2)							5e15
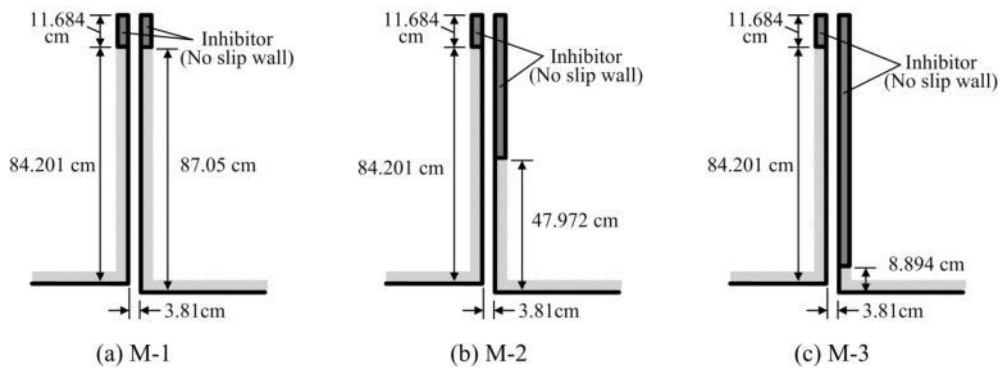
Figure 9. Slot inhibitor configurations for the variation of mass flow ratio

B. The effect of Mach number and mass flow ratio

Table 10 shows the results from all simulations performed to assess the effect of Mach number and mass flow ratio. The existence of a bound vortex at the slot lip is mainly dependent on the mass flow ratio as this structure is formed under higher slot flowrate conditions. Figure 10 shows the vortex and no vortex zone for various Mach numbers and mass flow ratios. Figure 11 show the streamlines near the slot lip for the various mach number and mass flow ratio combinations. Increasing Mach number permits formation of the structure at lower slot flow rates. However, at the highest Mach/slot mass flow condition the flow behind the slot is highly stretched due to the strong reverse axial velocity and no bound vortex is created as shown in Figure 11(b). At this condition, the strong cross-flow increases the axial length of vena-contracta, therefore, the pressure difference along the axial direction is small (small dp/dx) and it is not enough to create the vortex motion. However, only one simulation point reveals this result as shown in Figure 10 and additional simulations would be required to fully map the topological changes.

As shown in Figure 11(a), the very large vena-contracta is created when the Mach number is relatively low and mass flow ratio is relatively high (M-1-1) comparing to Figure 11(c). As describe above, no vortex is created when the mass flow ratio is relatively high (M-1-4) and the mass flow ratio is relatively low (M-3-1) as shown in (b) and (d) of Figure 11.

The correlation presented in Table 10 is given by Hilbing[1] as follows:

$$\frac{\Delta P}{P} = 1.457 M^{1.293} \left(\frac{\dot{m}_s V_s}{\dot{m} V} \right)^{0.888} \tag{5}$$

The current simulation and correlation shows the noticeable difference as the current simulation calculated the stagnation pressure loss at 10 slot width from the slot (3.82 cm downstream) and Hilbing calculated at one motor radius from the slot (80.899 cm downstream). One interesting difference between the current simulation and Hilbing's correlation is that the stagnation pressure loss varies conversely with the variation of outlet pressure at the same slot configuration. Increasing the outlet pressure, the stagnation pressure loss is increasing in current simulations. However, Hilbing's correlation shows the decrease of stagnation pressure loss as the outlet pressure increases. One possible reason of this difference is that Hilbing varies the area ratio to control the mass flow ratio. As presented in Hilbing[1], Kays[8] has a term of (1-A_1/A_2) in his correlation for the stagnation pressure loss. According to Kays' correlation, increasing step

height results in increasing of stagnation pressure loss. Although Hilbing derived the correlation without the term of A_1/A_2, the comparisons of current simulations with his correlation shows the necessity of the term in the correlation.

Table 10. Averaged characteristics of gas phase

| Case no.	vortex	Mach number	Mass flow ratio	Momentum ratio	Stagnation pressure loss	Correlation*
M-1-1	o	0.164	13.92%	17.64%	0.22%	1.80%
M-1-2	o	0.272	8.14%	6.31%	0.40%	1.39%
M-1-3	o	0.353	6.28%	3.82%	0.53%	1.25%
M-1-4	x	0.420	5.33%	2.78%	0.64%	1.18%
M-2-1	o	0.167	9.53%	8.43%	0.20%	0.96%
M-2-2	o	0.277	5.61%	3.06%	0.36%	0.75%
M-2-3	o	0.359	4.34%	1.86%	0.48%	0.67%
M-2-4	o	0.428	3.68%	1.36%	0.59%	0.64%
M-3-1	x	0.170	6.63%	4.15%	0.16%	0.52%
M-3-2	x	0.279	3.94%	1.55%	0.30%	0.41%
M-3-3	x	0.362	3.05%	0.95%	0.40%	0.37%
M-3-4	x	0.432	2.60%	0.70%	0.49%	0.36%
M-3-5	x	0.492	2.31%	0.56%	0.57%	0.35%

* Hilbing[1]
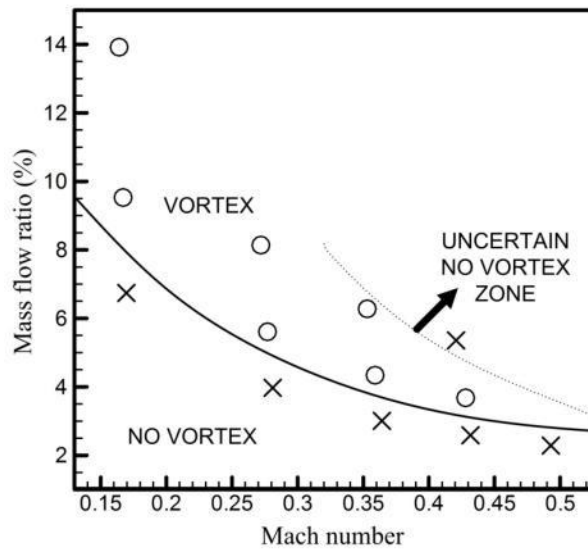
Figure 10. Vortex and no vortex zone identification according to the various mach number and mass flow ratio
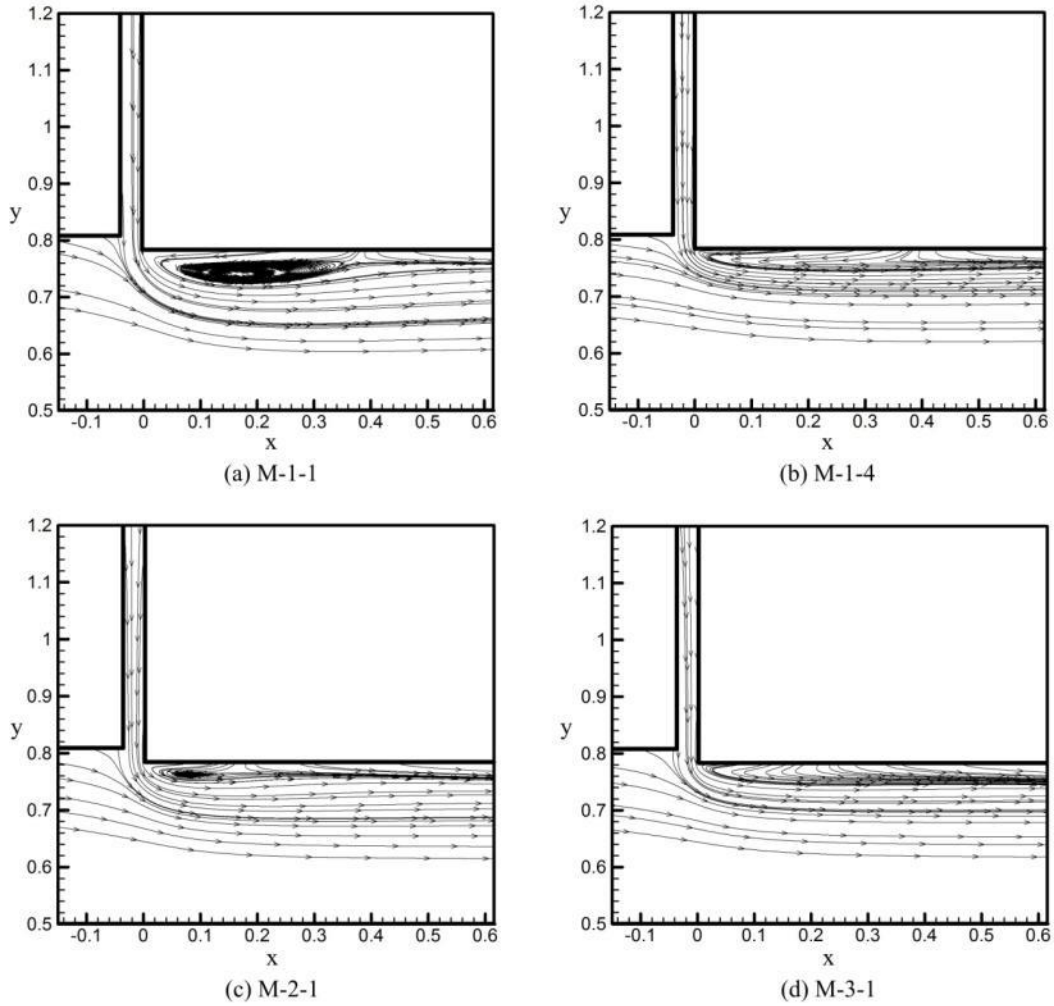
Figure 11. The streamlines for cases (a) M-1-1 (low mach number, high mass flow ratio), (b) M-1-4 (high mach number, high mass flow ratio), (c) M-2-1 (low mach number, mid mass flow ratio), and (d) M-3-1 (low mach number, low mass flow ratio)

Table 11 summarizes details of predicted characteristics of particle phase just before the slot (x=-0.038 m), at the slot outlet and 10 and 60 slot widths downstream (x=0.382 m,x=2.292 m). In all cases investigated, no signs of particle break up are observed and particle growth occurs monotonically in the core streamwise direction.

While holding the same slot configuration, decreasing the outlet pressure results in decreasing of mass mean diameter at all x-locations considered here along the bore. Interestingly, the mass mean diameter at slot outlet increases as the outlet pressure decreases. However, the variation of outlet pressure involves the variation of mass flow ratio, therefore, Figure 12 is plotted with respect to Mach number and mass flow ratio. As shown in (a) and (b) of Figure 12,

it is observed that the maximum averaged D_{43} is obtained at mid mass flow ratio with a constant Mach number. Accordingly, at a given Mach number, the low and high mass flow ratios can result in the reduction of agglomeration at slot outlet and the vena-contracta region. In addition, the variation of maximum agglomerate size over the considered mach numbers can be identified. The maximum D_{43} at slot outlet is nearly constant over the entire Mach numbers range assessed, as the slot flow is less perturbed by the variation of main stream conditions. Within the vena-contracta region, the maximum D_{43} increases as the mach number increases.

Figures 12(c) and 12(d) shows the variation of D_{43} with respect to Mach number and mass flow ratio just before the slot and 60 slot widths downstream. Just before the slot, mass mean diameter at a given mach number is insensitive to the mass flow ratio. Therefore, it can be concluded that the cross-flow has a very little effect on the upstream agglomeration. At 60 slot width downstream, the variation of D_{43} is complex, and additional study will be required to clearly identify the D_{43} variation trends. The information presented here about the agglomeration process in radial slot flow can be a valuable design consideration for the nozzle wall and throat erosion in a solid rocket motor.

Table 11. Averaged characteristics of particle phase for baseline case at various locations

| Case no. | x-location (x/x_s) | | | | | | Slot exit | |
| | -10 | | 10 | | 60 | | | |
	f	D_{43}	f	D_{43}	f	D_{43}	f	D_{43}
M-1-1	0.314	1.944	0.307	2.475	0.261	9.492	0.302	1.785
M-1-2	0.321	1.681	0.318	2.026	0.289	6.187	0.309	1.792
M-1-3	0.329	1.558	0.328	1.843	0.308	4.541	0.316	1.800
M-1-4	0.337	1.487	0.337	1.745	0.325	3.351	0.324	1.808
M-2-1	0.314	1.906	0.303	2.832	0.254	8.732	0.300	2.029
M-2-2	0.322	1.641	0.314	2.381	0.274	9.210	0.308	2.042
M-2-3	0.330	1.520	0.325	2.166	0.290	8.085	0.316	2.055
M-2-4	0.339	1.451	0.335	2.011	0.304	7.056	0.325	2.070
M-3-1	0.315	1.876	0.306	2.396	0.260	7.476	0.300	1.687
M-3-2	0.323	1.618	0.315	2.237	0.274	8.801	0.307	1.718
M-3-3	0.331	1.499	0.324	2.112	0.287	8.400	0.316	1.744
M-3-4	0.340	1.430	0.334	1.987	0.300	7.897	0.325	1.764
M-3-5	0.349	1.386	0.344	1.872	0.312	7.437	0.334	1.783
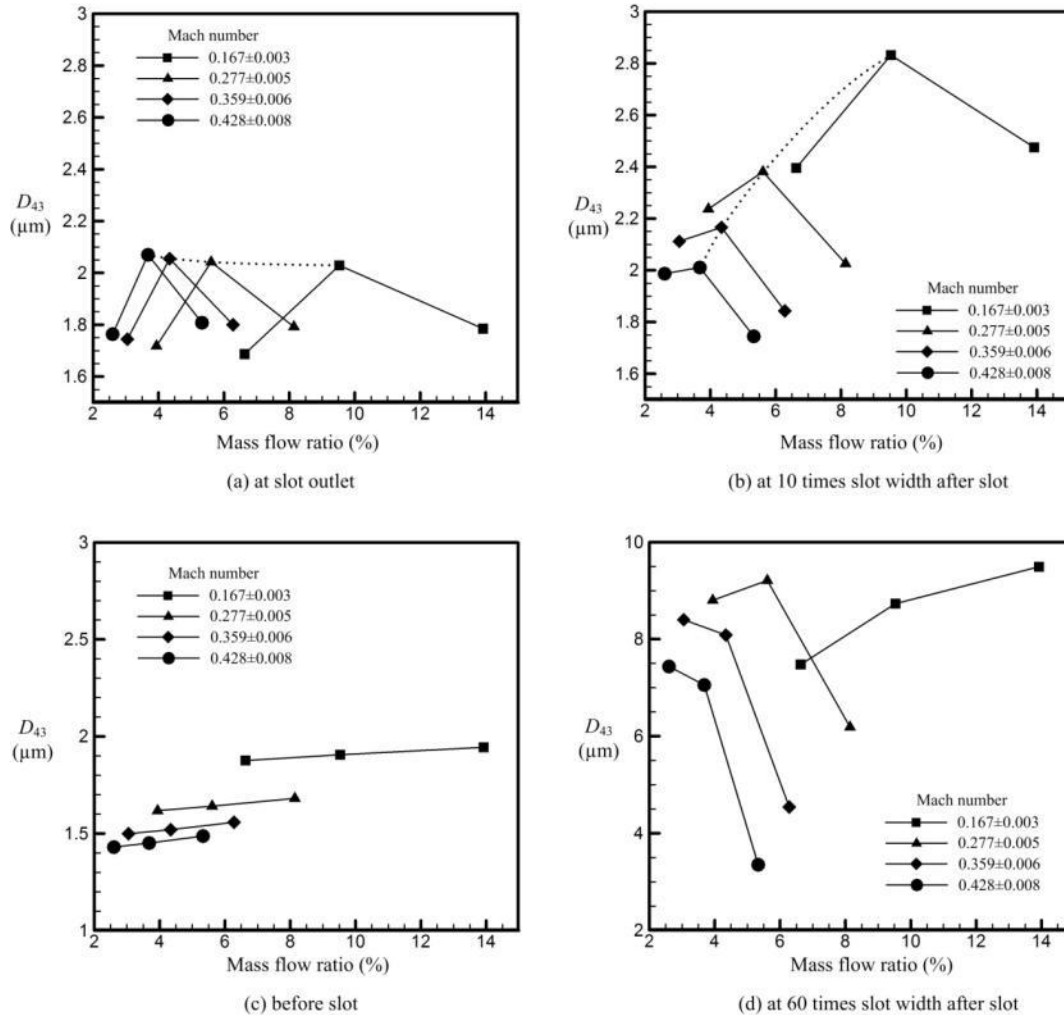
Figure 12. Mass mean diameter variations for the various mach numbers and mass flow ratios at (a) slot outlet, (b) 10 slot width downstream from the slot, (c) just before the slot, and (d) 60 slot width downstream from the slot

C. The effect of step height

Under a given outlet pressure which is 5.75 MPa and M-3 configuration, the effect of step height is assessed by varying the step height from 0 to 8.547 cm with a difference of 2.849 cm. Because the variation of step height varies the upstream condition, the mach number and mass flow ratio changes over small ranges. The resultant gas phase conditions are presented in Table 12. When the step height is low, the Mach number is large and the mass flow ratio is small. As the step height increases, the Mach number decreases and the mass flow ratio increases. The

vortex is created only at low Mach number and high mass flow ratio with the highest step height. While the mass flow ratio varies in the amount of approximately 0.3%, the stagnation pressure loss is changed in the amount of 0.03% when there is no vortex. Due to the existence of vortex, the amount of increase of stagnation pressure loss is 0.05% comparing S-4 with S-3.

The particle phase characteristics are summarized in Table 13. The mass mean diameter increases as the step height increases at just before the slot and just after the vena-contracta region. At the slot exit and far downstream of $x/x_s=60$, the D_{43} decreases until the step height of 5.698 cm. When the step height is increased to 8.547 from 5.698 cm, D_{43} increases about 0.5 and 17 % at the slot exit and far downstream, respectively.

Therefore, it is shown here that the vortex can be created without additional mass addition to the main stream. When the vortex exists behind the slot, additional stagnation pressure loss and agglomeration of particles tends to occur. Unfortunately, due to the variation of Mach number and mass flow ration with the variation of step height, the more careful flow boundary condition should be used to assess the sole effect of step height.

Table 12. Averaged characteristics of gas phase for the various step heights

Case no.	vortex	Mach number	Mass flow ratio	Momentum ratio	Stagnation pressure loss	Correlation
S-1	x	0.292	3.69%	1.55%	0.28%	0.44%
S-2	x	0.279	3.94%	1.55%	0.30%	0.41%
S-3	x	0.271	4.21%	1.65%	0.33%	0.42%
S-4	o	0.263	4.53%	1.77%	0.38%	0.43%

Table 13. Averaged characteristics of particle phase for the various step heights at various locations

Case no.	x-location (x/x_s)						Slot exit	
	-10		10		60			
	f	D_{43}	f	D_{43}	f	D_{43}	f	D_{43}
S-1	0.325	1.555	0.319	2.118	0.284	10.433	0.310	1.725
S-2	0.323	1.618	0.315	2.237	0.274	8.801	0.307	1.718
S-3	0.321	1.681	0.312	2.428	0.270	9.546	0.307	1.685
S-4	0.319	1.750	0.309	2.613	0.266	11.165	0.307	1.693

D. The effect of mass fraction

The effect of mass fraction of particle phase on the agglomeration process is assessed here by varying the total number of particles at inlet from 0.78e15 to 5e15 and 4 simulation results are obtained. The mass fractions at inlet are given by 0.05, 0.15, 0.25, and 0.32. The details of results are presented in Table 14 and the results are plotted in Figure 13. As expected, the increase of inlet mass fraction results in the increase of D_{43} over the entire domain. It is found that the amount of increase is large at far downstream comparing to the upstream and slot region as shown in Figure 13.

The radial variation of D_{43} in the vena-contracta region which is defined at 10 slot width behind the slot is plotted in Figure 14. The overall shape of each case is very similar but it is noticed that the agglomeration over the vortex becomes significant and clearly noticeable when the inlet mass fraction is large. Accordingly, two peaks located at 5 and 15% of motor radius from the downstream propellant surface are observed in the radial direction.
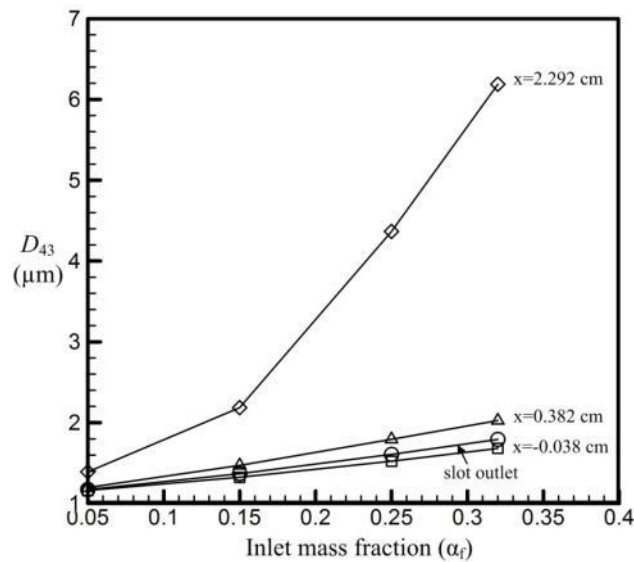

Figure 13. Predicted mass mean diameters according to the various inlet mass fractions at various locations
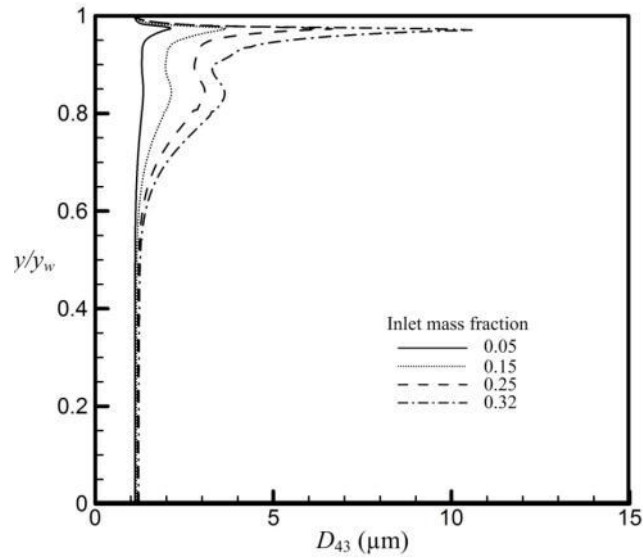
Figure 14. Predicted radial variation of mass mean diameter at 10 slot width from the slot

Table 14. Averaged characteristics of particle phase for the various mass fractions at various locations

Case no.	x-location						Slot exit	
	-0.038		0.382		2.292			
	f	D_{43}	f	D_{43}	f	D_{43}	f	D_{43}
P-1	0.050	1.161	0.050	1.197	0.050	1.391	0.491	1.172
P-2	0.151	1.324	0.151	1.471	0.150	2.186	0.146	1.368
P-3	0.251	1.523	0.250	1.794	0.233	4.366	0.242	1.607
P-4	0.321	1.681	0.318	2.026	0.289	6.187	0.309	1.792

IV. Summary and conclusions

A series of numerical simulations were performed to study the gas flow and particle agglomeration in a solid rocket motor with a radial slot which produce a strong cross-flow into the main stream. The effect of radial slot was examined with respect to the mach number, mass flow ratio, step heights of downstream propellant, and inlet mass fraction of particle phase. The important parameters controlling the vena-contracta behind the slot is the mach number and mass flow ratio. Regarding the vortex in vena-contracta, it was found that the vortex is created at very high mass flow ratio when the mach number is small while the vortex is created at relatively small mass flow ratio when the mach number is relatively large.

The effect of step height on the vortex was also assessed by changing the downstream propellant geometry. The decrease of mach number and increase of mass flow ratio and stagnation pressure loss were observed as the step height increases. It was also observed that the vortex is created only when the considered step height is maximum. Unfortunately, the variation of step height yields the variation of the mach number and mass flow ratio, so the complete decoupling of step height with the mach number and mass flow ratio has not been made in the current simulations. The more careful configuration will be required to assess the independent effect of step height.

The D_{43} distribution over the entire domain showed the increase along the axial direction. More specifically, it was observed that the strong agglomeration of particles starts at vena-contracta region. The particles entrained in vena-contracta region experience the strong shearing motion between the reversed axial flow and normal axial flow and result in the formation of large agglomerates. Also, the contraction of area due to vena-contracta result in the significant agglomeration while particles passing over the vena-contracta in an axial direction.

The effect of Mach number and mass flow ratio was also examined and the interesting results were found that the maximum averaged D_{43} is obtained at mid mass flow ratio with a constant mach number at slot outlet and just after the vena-contracta. Accordingly, at a given mach number, the low and high mass flow ratios can result in the reduction of agglomeration at slot outlet and vena-contracta region. In the vena-contracta region, the maximum D_{43} over the wide range of mass flow ratios increased as the mach number increased. In addition, the maximum D_{43} at slot outlet showed an almost constant value over all mach numbers as the slot flow is less perturbed by the variation of main stream conditions. Therefore, it was concluded that the cross-flow has a very little effect on the upstream agglomeration.

As the rocket nozzle and wall experience a serious erosion due to the existence of Al_2O_3, the current simulation using the validated agglomeration/breakup models can provide the valuable information for the design consideration. It is expected that a few more simulations in addition to current simulated cases will strengthen the conclusions made in this paper.

VIII.   Acknowledgments

IX.   References

[1]Hilbing, J. and Heister, S., "Radial Slot Flows in Solid Rocket Motors", AIAA 93-2309, *29th Joint Propulsion Conference and Exhibit*, June, 1993

[2]Sabnis, J. S., Gibeling, H. J., and McDonald, H., "Navier-Stokes Analysis of Solid Propellant Rocket Motor Internal Flows", *Journal of Propulsion and Power*, Vol. 5, No. 6, 1989, pp. 657-664

[3]Park, K. S., "Modeling Two-phase Flow with Stochastic Coalescence/Breakage Model", Ph.D thesis, Purdue Univ. 2012

[4]Najjar, F. M., Ferry, J. P., Haselbacher, A., and Balachandar, S., "Simulations of Solid-Propellant Rockets: Effects of Aluminum Droplet Size Distribution", *Journal of Spacecraft and Rockets*, Vol. 43, No. 6, 2006, pp. 1258-1270.

[5]Crowe, C. T. and Willoughby, P. G., "A study of Particle Growth in a Rocket Nozzle", *AIAA Journal*, Vol. 5, No. 7, 1967, pp. 1300-1304

[6]Fein, H. L., "A Theoretical Model for Predicting Aluminum Oxide Particle Size Distributions in Rocket Exhausts", *AIAA paper*, No. 65-10, 1965.

[7]Xu, C., "Simulation of orifice internal flows including cavitation and turbulence", Ph.D thesis, Purdue Univ. 2001

[8]Kays, W. M., "Loss Coefficients for Abrupt Changes in Flow Cross Section with Low Reynolds Number Flow in Single and Multiple Tube Systems", *Transactions of the ASME*, Vol.72, 1950, pp. 1067-1074